The XY-Scanner

A Versatile Method for the Absolute End-to-End Calibration of Fluorescence Detectors

Zur Erlangung des akademischen Grades eines

Doktors der Naturwissenschaften (Dr. rer. nat.)

von der KIT-Fakultät für Physik des
Karlsruher Institut für Technologie (KIT)

genehmigte

Dissertation

von

M. Sc. Christoph Meinhard Schäfer

aus Bruchsal

CONTENTS

CHAPTER I

INTRODUCTION

The top of the atmosphere of the earth is constantly hit by particles of extraterrestrial and extra-galactic origin – these particles are known as *cosmic rays*. The energy of these cosmic rays can exceed the energy reached by any human-made accelerators by many orders of magnitude. At the highest energies, these cosmic rays are typically observed indirectly via particle cascades they induce in interactions with the atmosphere. Above a certain energy threshold, particles produced within these cascades (often referred to as *air showers*) can reach the surface of the earth. Therefore, earth-based observatories equip large areas with detector systems to measure these secondary particles and use the gained information to estimate the energy, mass, and arrival direction of the cosmic rays.

The largest cosmic-ray observatory ever constructed is the Pierre Auger Observatory located in Argentina. This observatory employs an array of ~1700 surface-detector stations distributed across an area of ~3000 km^2, which measure the lateral distribution of particles contained in air showers at the ground. In addition, the observatory uses 27 large-aperture wide-angle Schmidt telescopes to measure the longitudinal profile of air showers using the air-fluorescence technique. The measurements with the fluorescence telescopes are used to derive a calorimetric and model-independent estimate of the primary cosmic-ray energy. However, the fluorescence telescopes can only be operated during clear and moonless nights, which limits the duty cycle of observations with the telescopes to ~15%. On the other hand, the surface detector has no limitations to measuring times and thus an almost 100% duty cycle. To combine the advantages of both techniques, the energy calibration of the fluorescence telescopes is transferred to the surface detector, which otherwise has to rely on air-shower simulations to obtain an energy calibration. Therefore, the energy scale of the entire Pierre Auger Observatory is set by the fluorescence detector, which makes the accurate calibration of the fluorescence telescopes of utmost importance.

Up to the year 2013, the absolute calibration of the telescopes was performed by mounting a uniform large-diameter light source on each telescope and illuminating the entire aperture with a known photon flux. The uncertainty of this absolute calibration method is estimated to be on the order of 9%. Due to large time requirements and the high amount of work, the absolute calibration was only performed roughly once every three years while a relative calibration system tracks changes in the telescopes for the time between the absolute calibration campaigns. However, since 2013 no absolute calibration of the telescope was carried out and the observatory relies only on the relative calibration of each telescope.

In this thesis we present the *XY-Scanner*, a novel and versatile technique for the absolute end-to-end calibration of the fluorescence telescopes. The XY-Scanner consists of a motorized rail system, which is installed at the aperture of each fluorescence telescope. After the travel restrictions due to the pandemic were lifted and we were able to travel again to Argentina, we finished equipping all telescopes of the Pierre Auger Observatory with such a rail system in spring of 2023. Onto this rail system an uniformly emitting and absolutely calibrated light source

is mounted and moved across the aperture of each telescope. We mimic the illumination of the entire aperture by flashing the light source at ~1700 positions, evenly distributed across the telescope aperture. For the absolute calibration of the light source, we built a dedicated setup, which employs a NIST-calibrated photodiode to measure the average photon flux per light pulse and PMTs to track the pulse-to-pulse stability. We show that this new technique is a viable solution to replace the cumbersome calibration with the large-diameter light source, which was performed in the past. With the XY-Scanner we reach an uncertainty for the absolute calibration of the fluorescence telescopes of below 6%, which, in the future, could be reduced to ~4% by improving the setup for the calibration of the light sources.

This thesis is structured as follows. We introduce cosmic rays, the phenomenon of extensive air showers, and the Pierre Auger Observatory in Chapter 2. In Chapter 3 we give a detailed description of the telescopes of the fluorescence detector employed by the Pierre Auger Observatory and discuss the current techniques and methods to calibrate these telescopes. We introduce the mechanical setup of the XY-Scanner and describe the calibration measurement procedure in Chapter 4. In this Chapter we also validate our understanding of the XY-Scanner measurements at the telescopes via ray-tracing simulations. We present our observations regarding different optical properties of the telescopes in Chapter 5. This includes studies of the influence of cleaning telescope components and the first measurements performed with a collimated-beam source to study the point-spread-function of telescopes. In Chapter 6 we give an overview of the various light sources we employed for the XY-Scanner measurements. In addition, we discuss the technique and measurements to characterize the emission profiles of the calibration-light source. We also describe the setup and method to measure and estimate the calibration of these light sources. In Chapter 7 we describe the analysis of the measurements at the telescopes at the observatory site and derive a method to evaluate the absolute end-to-end calibration constants. Furthermore, we present the results of the latest XY-Scanner calibration campaigns. Finally, we summarize and give an outlook for possible improvements in Chapter 8.

COSMIC RAYS AND THE PIERRE AUGER OBSERVATORY

Contents

In the following chapter we briefly introduce cosmic rays and the phenomenon induced by their interaction with molecules in the atmosphere of the earth, so called air showers. We then discuss most popular indirect detection methods and finish this chapter with a description of the largest ever constructed cosmic ray observatory, the Pierre Auger Observatory.

2.1. COSMIC RAYS

Primary cosmic rays are high-energy particles – mostly protons or mainly lighter, but also heavier nuclei – traveling through space and perpetually arriving at the top of the earth's atmosphere at a rate of $\sim$1000 m^{-2} s^{-1} [1]. The energies of primary cosmic rays span over 12 decades and reach higher than 10^{20} eV. We discuss the energy spectrum of cosmic rays in Section 2.1.3. The origin of most cosmic rays is within our Galaxy, but outside of the solar system. There are cosmic rays originating from the sun, however these are in temporal correlation with violent events on the sun. For higher energies $E_{CR} \gtrsim 10^{18}$ eV, the gyroradius of the cosmic-ray particle within the typical magnetic field of the Galaxy is larger than the Galaxy itself and therefore these cosmic rays may have their origin in extragalactic sources.

Cosmic rays with energies above $\sim 10^{18}$ eV = 1 EeV are most commonly referred to as *Ultra-High-Energy-Cosmic-Rays* (UHECRs) and are the result of the most powerful acceleration processes in the universe. However their origin, nature, acceleration mechanisms, and propagation through the universe are one of the main open question of the contemporary astroparticle physics.

The detection and measurement of cosmic rays is generally split into two different approaches, namely direct and indirect detection. For the direct detection one measures, as the name suggests, the primary cosmic-ray particle directly. Such experiments are usually located as payload on balloons at high altitudes or in satellites in space. The design of direct cosmic-ray observatories is similar to most detector systems in high-energy physics. They usually employ several detector
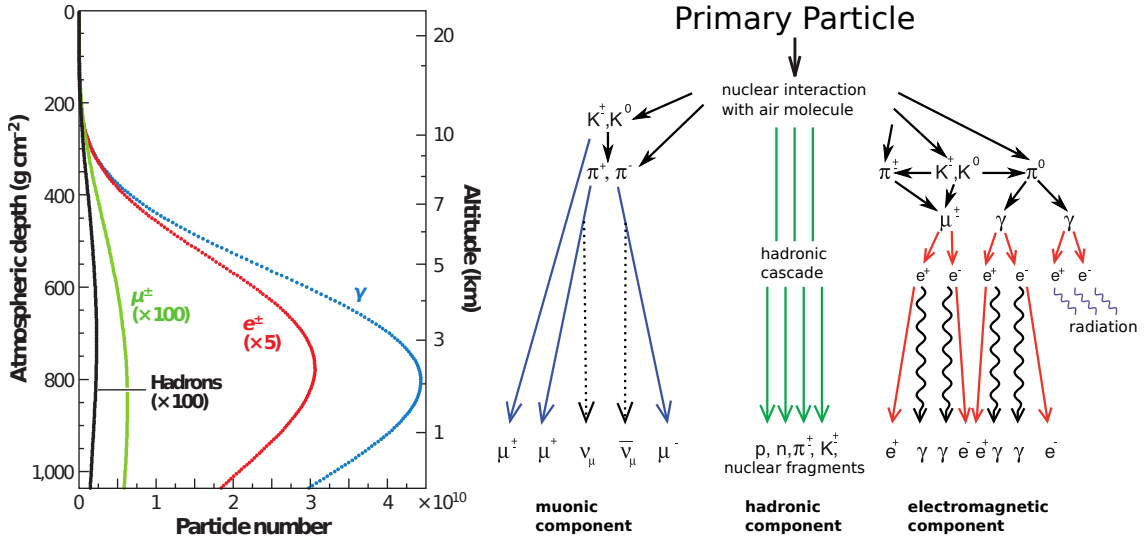
Figure 2.1: *Left:* Longitudinal profile of a simulated shower. The primary cosmic ray is a proton with a energy of 10^{19} eV. Plot taken from Ref. [2]. *Right:* Schematic drawing of the development of a hadron-induced air shower. Three different components of the air shower is illustrated. Modified version from Ref. [3].

layers, which estimate the energy of the particle or discriminate between different particle types passing through the detectors. Since the flux of cosmic rays decreases very rapidly with increasing energy and the volume of instrumentation on a balloon or satellite experiment is rather limited, only cosmic rays typically with energies up to $\sim 10^{13}$ eV are measured directly. At these energies the rate of cosmic rays is roughly one particle per $1\,\mathrm{m}^2$ in $\sim 10\,\mathrm{min}$. For higher energies the rate is too low to measure cosmic rays with an adequate statistic.

Due to this steeply falling rate of cosmic rays, the cosmic rays at higher energies are typically detected indirectly. The interaction between the primary cosmic ray and particles of the atmosphere leads to cascade of secondary particles, which travel towards the surface of the earth and can be detected even on the ground level. Such events are called *Extensive Air Showers* (EAS) and we discuss their evolution in Section 2.1.1. To detect such air showers, large areas on the surface of the earth are equipped with detector systems, which measure these secondary products of the interaction of the primary cosmic ray with the atmosphere of the earth.

2.1.1. EXTENSIVE AIR SHOWERS

After the first interaction of the primary cosmic ray with an air molecule of the atmosphere, a cascade of secondary particles and interactions develops. These secondary particles "rain" down on the earth and therefore this phenomenon is referred to as an (extensive) air shower and for convenience often simply called shower. The development of an air shower can be described by three components: the electromagnetic, the hadronic, and the muonic component. The most abundant particles in an air shower are the particles of the electromagnetic component, most prominent are photons γ followed by electrons $e^{\pm}$. We show the longitudinal profiles of different shower components for a simulated air shower in Fig. 2.1-left. The particle numbers contained in the hadronic or muonic component are approximately a factor ~ 400 less abundant compared to the electromagnetic component. We show a schematic of an air shower development in Fig. 2.1-right and briefly discuss the individual components in the following.

The shower of high-energy hadrons develops mostly close to the core axis of the shower. In each interaction between these hadrons and the air molecules new particles are produced, provided the energy of the particle is sufficient. The development of the hadronic shower can be in a simplified form described by the Heitler-Matthews splitting model [4]. This model assumes

that at each interaction point, charged (for this model only π^+ and π^-) and neutral (π^0) particles are produced in the ratio 2:1. While the charge particles may continue to interact and thus contribute to the further development of the hadronic shower, the neutral particles promptly decay ($\pi^0 \to \gamma\gamma$). Therefore, at each interaction step one third of the energy is carried away by photons, which induce subsequent electromagnetic showers. Thus, after n interaction steps, the total energy E_n^{em} contained in the electromagnetic component is approximately

$$E_n^{\text{em}} = \left[1 - \left(\frac{2}{3} \right)^n \right] E_0 \tag{2.1}$$

with E_0 the energy of the primary particle. According to this model, most of the primary energy will be eventually transferred into the electromagnetic component. The interaction of the charged particles stops as soon as their interaction length λ_i becomes smaller than their decay length λ_d. After this point the charged particles mostly decay and do not further contribute to the hadronic component. We assume most hadrons of the shower are pions or other mesons which eventually decay into pions. The charged pions weakly decay into muons and neutrinos, $\pi^\pm \to \mu^\pm \nu_\mu$, which compose the muonic component of the air shower. According to the Heitler-Matthews splitting model, the number of muons N_μ contained in an air shower can be estimated as

$$N_\mu = \left(\frac{E_0}{E_{\text{dec}}} \right)^\alpha \tag{2.2}$$

with the decay energy of charged pions $E_{\text{dec}} \approx 30\,\text{GeV}$, again the energy E_0 of the primary particle, and $\alpha = \ln n_{\text{ch}} / \ln n_{\text{tot}} \approx 0.9$, where n_{ch} and n_{tot} are the multiplicities of the charged pions and the total number of pions, respectively. Assuming heavier particles are made of A independent nucleons, the energy of each nucleon is $E_{\text{nuc}} = E_0/A$, and we can estimate the muon number as

$$N_\mu^{(A)} = A \left(\frac{E_0/A}{E_{\text{dec}}} \right)^\alpha = A^{1-\alpha} N_\mu^{(1)} \tag{2.3}$$

which makes the muon number a powerful observable sensitive to the cosmic-ray mass.

Electromagnetic sub-showers are started and continuously fed by hadronic component through the decay of neutral pions into two photons. If the photon energy is large enough, these photons produce electrons and positions via pair production, which then on their part generate more photons through bremsstrahlung. This leads to a development of an electromagnetic sub-shower. The most simple description of a purely electromagnetic shower is the Heitler model [5], which assumes that each particle of the shower is split into two particles after a certain interaction length λ_{em}. The number of particles N_n and the energy E_n of each particle after n interaction steps is then calculated to be

$$N_n = 2^n \qquad \text{and} \qquad E_n = \frac{E_0}{2^n} \tag{2.4}$$

with the energy E_0 of the particle starting the electromagnetic cascade. In the further development of the electromagnetic sub-shower the number of particles increases until a critical energy E_c is reached. At this point the maximal number N_{max} of particles is produced and the resulting energy is too low to produce any new particles. The remaining particles then lose energy until they get absorbed and thus, the particle number of the electromagnetic component is decreasing. The maximal particle number N_{max} of the electromagnetic shower and the slant depth X_{max} where this number is reached can be respectively expressed by

$$N_{\text{max}} = \frac{E_0}{E_c} \qquad \text{and} \qquad X_{\text{max}} \propto \lambda_{\text{em}} \ln \frac{E_0}{E_c} \tag{2.5}$$

with the starting particle energy E_0, the critical energy E_c, and the interaction length λ_{em}. The atmospheric or slant depth X is typically defined as

$$X(h) = \int_h^\infty \rho_{\text{air}}(h') \, \mathrm{d}h' \tag{2.6}$$

with the density of air ρ_{air}. Again, assuming heavier particles are made of A independent nucleons, the depth X_{max} of the shower maximum becomes sensitive to the mass A of the primary particle,

$$X_{\mathrm{max}}^{(A)} = X_{\mathrm{max}}^{(1)} - D_{\mathrm{e}} \ln A \tag{2.7}$$

with the elongation rate $D_{\mathrm{e}} = \Delta \langle X_{\mathrm{max}} \rangle / \Delta \ln E \approx 28\,\mathrm{g\,cm^{-2}}$ in air. A fairly accurate description for the number of particles within the electromagnetic shower as a function of the slant depth was introduced by Gaisser and Hillas [6] as

$$N(X) = N_{\mathrm{max}} \left(\frac{X - X_1}{X_{\mathrm{max}} - X_1} \right)^{(X_{\mathrm{max}} - X_1)/\Lambda} \exp \left(-\frac{X - X_{\mathrm{max}}}{\Lambda} \right) \tag{2.8}$$

with the maximal number of particles in the shower N_{max}, which is reached at the depth X_{max}, X_1 and $\Lambda \approx 55$ to $65\,\mathrm{g/cm^2}$ are shape parameters, while $X_1 > 0$ can be interpreted as the atmospheric depth of the first interaction.

2.1.2. DETECTION OF EXTENDED AIR SHOWERS

On Ground Level. For air showers initiated by a high-energy cosmic rays ($E_{\mathrm{CR}} \gtrsim 10^{14}\,\mathrm{eV}$), secondary particles can reach surface of the earth. Depending on the energy and type of the primary cosmic ray the size of this footprint on the earth's surface varies. For a $10^{19}\,\mathrm{eV}$ proton the shower footprint on the ground level is approximately ~4 km in radius, while the particle density decreases from more than 10 000 particles per square meter for electrons and photons (~10 m^{-2} for hadrons) close to the shower core to below 0.01 particle per square meter at a distance of ~4 km to the core axis. Air showers reaching down to the ground level can be measured by an array of particle detector stations. Typically these detector stations are distributed over large areas (several km^2) to enable the detection of a reasonable number of air shower candidates for the steeply falling spectrum of primary cosmic rays. Due to the high density of particles within the shower, the distance between detector stations can be of the order of ~1000 m. For example, for the $10^{19}\,\mathrm{eV}$-proton shower discussed above, the particle densities at a radius of ~500 m are roughly ~5 hadrons, ~10 muons, ~100 electrons, and more than ~1000 photons per square meter.

In such ground-based measuring methods, shower events are identified by the temporal and spatial coincidence in the detector array. The signal strength of individual stations, the timing delay between different stations, and the accurate knowledge of the position of each station is then used to reconstruct the arrival direction and the energy of the primary cosmic ray. However, this technique only measures the particle density in the ground-level plane and thus observes the air shower at fixed stage of its development. To estimate the energy of the primary cosmic ray out of such a measurement, one has to either accurately simulate the shower development and the detector response or use a hybrid approach. For a hybrid approach, another different detector system, which is able to directly estimate the energy of the cosmic ray, is installed. Possible systems are the detection of radio or fluorescence light emission induced by the air shower. We discuss the air fluorescence technique below. This second system simultaneously observes the same shower as the ground array and thus provides an energy measurement. A correlation between the energy measurement and an energy sensitive observable (shower size) of the ground array (e.g. the signal strength at a given distance to the shower core) is then used to obtain the energy of the cosmic ray from the array measurement only.

Air Fluorescence Technique. During the propagation of an air shower through the atmosphere, charged particles contained within the shower (mainly electrons and positrons) can excite air molecules. The de-excitation of these molecules leads to an isotropic emission of fluorescence light. In the air the most prominent fluorescence emission is produced by nitrogen molecules (N_2 and N_2^+). The wavelength of this emission is in the range from 300 to 400 nm. We show the spectrum of the air fluorescence emission as measured by the AIRFLY experiment [7] in Fig. 2.2. In the label nomenclature of that figure, the 2P label corresponds to neutral nitrogen N_2 and 1N
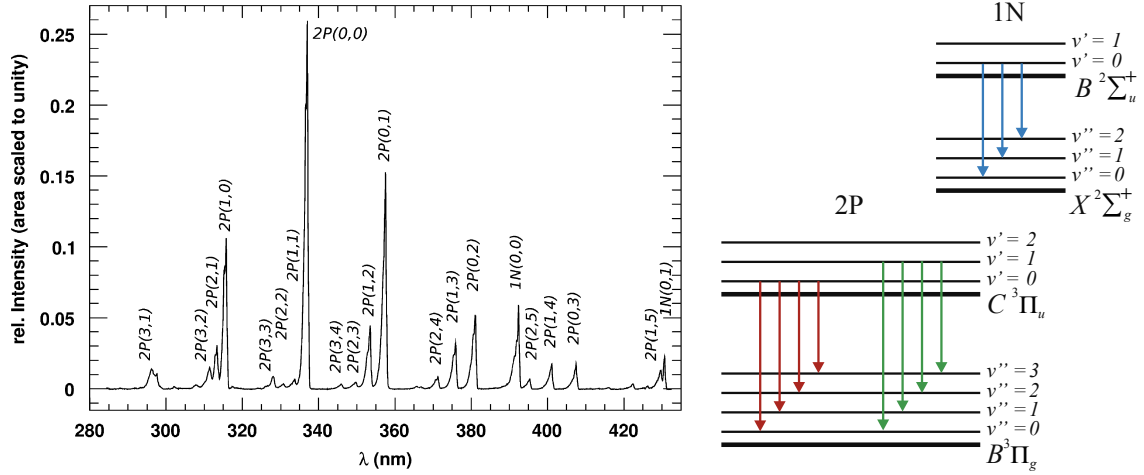
Figure 2.2: *Left:* Air fluorescence spectrum measured by the AIRFLY experiment [7]. The air was excited by 3 MeV electrons at an air temperature of $T = 293$ K and air pressure of $p = 800$ hPa. Labels indicate the major emission lines. *Right:* Scheme of the energy states of the 2P and 1N systems of N_2 and N_2^+. Adapted from Ref. [9].

corresponds to the positively charged nitrogen molecule N_2^+. The number in brackets indicate the initial (v') and final (v'') vibrational state. On the right side of Fig. 2.2 we show a schema of the energy states within the nitrogen molecules. For further details on air fluorescence emission see e.g. Refs. [7, 8, 9].

Since the emitted air fluorescence light is very faint, it can only be detected in low background environments. For ground-based telescopes this limits the observation time to clear moonless nights, which, as a direct consequence, limits the duty circle of such observations to less than ~15%. Nevertheless, the isotropic emission of the fluorescence light enables a single telescope to observe large volumes and detect showers in distances up to several tens of kilometers. Since the fluorescence emission depends on the condition of the atmosphere like the air temperature, humidity, and pressure and the propagation of the fluorescence photons from their emission point to a telescope is influenced by the atmospheric attenuation and scattering, an accurate knowledge of atmosphere conditions including the aerosol concentration is essential. We define the total transmission of the atmosphere, including all losses due to absorption and scattering, as $T_{atm}(\lambda, X)$. The number of emitted fluorescence photons per deposited energy and traversed matter is called the fluorescence light yield and is described by the function $Y(\lambda, T, p)$.

Observing air showers with the air-fluorescence technique benefits from the fact that such telescopes can record the entire development of the shower through the atmosphere. In contrast, a ground-level detector array can only sample the air shower at the ground plane. Fig. 2.3 illustrates two detector systems (a surface detector and a fluorescence detector) observing an air shower. The observed longitudinal profile of a shower development is used to estimate the position of the shower maximum X_{max}, where the air shower reaches its maximal particle content. This observable X_{max} is sensitive to the mass of the primary cosmic ray. In the bottom part of Fig. 2.3 we show typical shower profiles measured by a fluorescence telescope.

The bottom left profile of Fig. 2.3 shows the photon density detected by the telescope. The first step of the reconstruction of such an event is to find the shower-detector plane and to determine the geometry of the air shower. This procedure is not discussed here, but a description can be found in e.g. Ref. [10]. Then the signal detected by each camera pixel of the telescope is converted to the corresponding energy deposit $(dE_{cal}/dX)(X)$ as a function of the atmospheric depth X. In general the amount of deposited calorimetric energy dE_{cal} per traversed matter dX can be
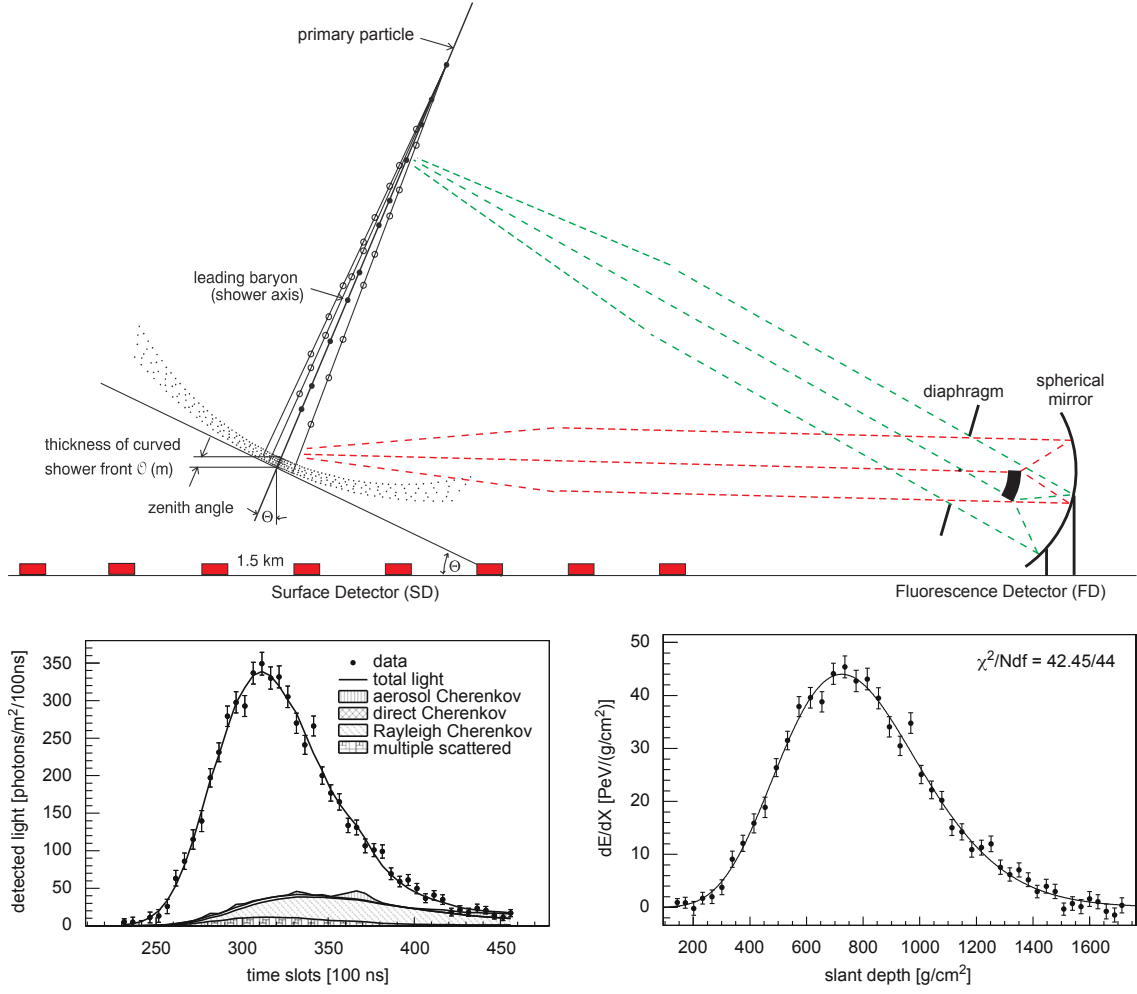
Figure 2.3: *Top:* Schematic drawing of a fluorescence detector and a surface array observing an air shower. Adapted from Ref. [8]. *Bottom:* Examples of shower profiles. Both plots are taken from Ref. [10]. *Left:* Typical light measurement of an FD telescope, individual light contributions are depicted as hatched areas. *Right:* Reconstructed energy deposit from the measurement on the left. The line represents the fit of a Gaisser–Hillas function to the profile.

expressed as

$$\frac{\mathrm{d}E_{\mathrm{cal}}}{\mathrm{d}X} = \int Y(\lambda, T, p)\, T_{\mathrm{atm}}(\lambda, X)\, \epsilon_{\mathrm{FD}}\, \mathrm{d}\lambda = \frac{\mathrm{d}N_\gamma}{\mathrm{d}X} \propto S_{\mathrm{FD}}\, C_{\mathrm{abs}} \tag{2.9}$$

with the aforementioned fluorescence light yield $Y(\lambda, T, p)$ and transmission of the atmosphere $T_{\mathrm{atm}}(\lambda, X)$. ϵ_{FD} accounts for the efficiency of the detector, the number of observed photons per traversed matter is given by $\mathrm{d}N_\gamma/\mathrm{d}X$. S_{FD} and C_{abs} are the signal and the absolute calibration of the FD telescope pixels, respectively. This estimate of the deposited calorimetric energy is directly proportional to the absolute calibration of the telescope camera which makes the accurate calibration of the detector a crucial ingredient in an accurate measurement of this energy deposit.

Assuming the number of particles produced in an air shower is proportional to the deposited energy we can express the Gaisser-Hillas function, Eq. (2.8), as

$$f_{\mathrm{GH}}(X) = \left(\frac{\mathrm{d}E_{\mathrm{cal}}}{\mathrm{d}X}\right)_{\mathrm{max}} \left(\frac{X - X_1}{X_{\mathrm{max}} - X_1}\right)^{(X_{\mathrm{max}} - X_1)/\Lambda} \exp\left(-\frac{X - X_{\mathrm{max}}}{\Lambda}\right) \tag{2.10}$$

where $(dE_{cal}/dX)_{max}$ denotes the maximum of the energy deposit. This function in Eq. (2.10) is then fitted to the measurements. In Fig. 2.3 on the bottom right plot, we show the measured profile of the deposited energy together with the Gaisser-Hillas fit. If the telescope, due to its limited field of view, only observes a part of the shower profile, we still can use Eq. (2.10) to extrapolate the profile into unobserved atmospheric depths. The total calorimetric energy E_{cal} deposited by an air shower is then calculated as the integral over the measured and the extrapolated profile as

$$E_{cal} = \int_0^\infty f_{GH}(X)\,dX \qquad (2.11)$$

where $f_{GH}(X)$ is the Gaisser-Hillas function fitted to the measured shower profile.

However, for the estimation of the energy of the primary cosmic ray E_{CR}, we have to take into account, that not the entire energy is deposited in the atmosphere. Particularly the energy carried by the muonic component of the air shower (muons and neutrinos) does not significantly contribute to the air fluorescence emission and therefore this part of the shower is invisible in relation to the fluorescence observations. The consequential correction of the energy is called invisible-energy correction $F_{inv}(E_{CR})$ and is of the order of ~15% of the primary cosmic-ray energy. The fraction of invisible energy can be estimated either with simulations or with a data-driven approach [11], but will not be discussed here.

Concluding, we express the energy E_{CR} of the primary cosmic ray as

$$E_{CR} = \frac{E_{cal}}{1 - F_{inv}} \qquad (2.12)$$

with the invisible energy fraction F_{inv} and the energy E_{cal} estimated from the fluorescence observation. Note that this energy estimate E_{cal} directly depends on the absolute calibration C_{abs} of the telescope.

2.1.3. Energy Spectrum of Cosmic Rays

The cosmic-ray energy spectrum describes the flux of cosmic rays arriving at the earth as a function of energy. We show the measured flux of several air-shower experiments covering energies between 10^{13} eV and 10^{20} eV in Fig. 2.4. Overall the entire spectrum of cosmic rays, also outside the energy range of Fig. 2.4, is well approximated by a power law

$$\frac{dN}{dE} \propto E^{-\gamma} \qquad (2.13)$$

with the spectral index γ being close to 3. However, detailed studies of the energy spectrum revealed a non-constant spectral index of the spectrum. Therefore, we refer to the energy spectrum as composed of broken power laws. The most prominent breaking points (indicating a change in the spectral index γ) are labeled in Fig. 2.4 as the *knee*, *2nd knee*, and *ankle* in some vague analogy to the human leg. The knee is located at a energy of ~3×10^{15} eV where the spectral index starts to change and the spectrum steepens. The spectrum slightly further steepens at the 2nd knee at energies around ~10^{17} eV, before it flattens again at the region of the ankle close to ~3×10^{18} eV. For energies below the knee the spectral index is $\gamma \approx 2.7$, it then increases up to $\gamma \approx 3.1$ at energies right below the ankle. An interpretation of these features (breaking points in the spectrum) is not given here, but can be found in e.g. Ref. [1].

Measurements of the cosmic-ray flux at the highest energies are mainly performed by the two largest observatories currently in operation. These are the Pierre Auger Observatory [14] in Argentina and the Telescope Array (TA) [15, 16, 17] in the United States. We show the cosmic-ray flux measured by these two experiments in Fig. 2.5. Comparing the two measurements we observe a similar spectral shape up to energies of ~2×10^{19} eV, but with a systematic difference of ~9% in the absolute energy scale. By re-scaling the energy of the Auger measurement upwards by 4.5% and the TA measurement downwards by the same amount, the two spectra are in a good
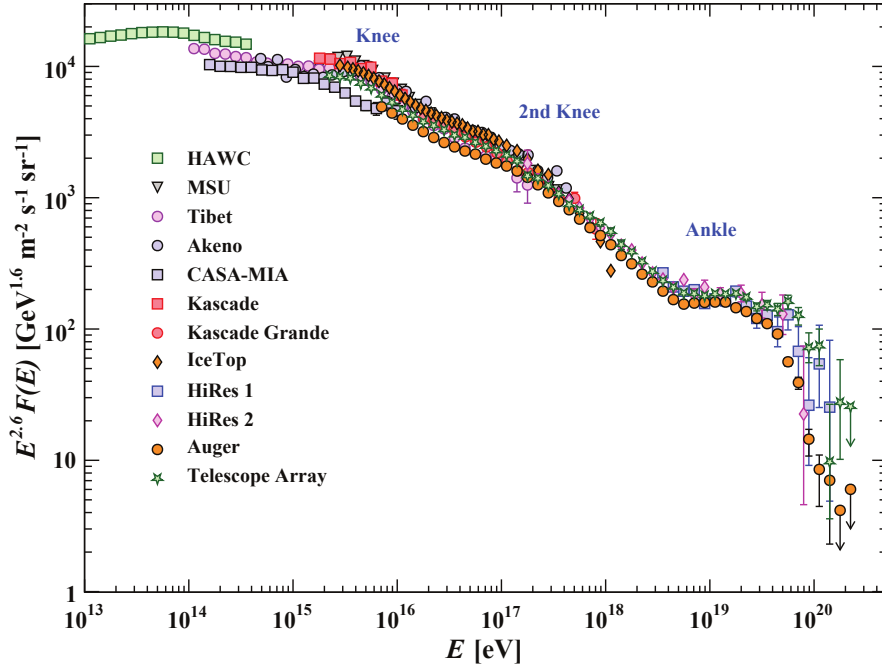
Figure 2.4: Flux of cosmic rays at highest energies measured by a variety of different air-shower experiments. For a visual enhancement of the breaking points in the power law, the flux F is scaled with $E^{2.6}$. Figure taken from [12].

agreement within their systematic uncertainties up to energies of ~2×10^{19} eV [13]. We show the rescaled spectra on the right side of Fig. 2.5.

Due to their different locations on the earth, the two observatories observe a different declination band δ of the sky. The Pierre Auger Observatory has a field of view of $-90° < \delta < +24.8°$, while the TA covers $-15.7° < \delta < +90°$. However, selecting the common declination band does not solve the ~9% difference on the absolute energy scale. A possible explanation for this discrepancy is an inaccurate absolute energy scale of either or both of the two observatories. Therefore, an independent validation of the energy scale of both experiments is appropriate, which motivates us to perform this absolute energy calibration of the Pierre Auger Observatory with the novel technique presented in this work.

2.2. PIERRE AUGER OBSERVATORY

Figure 2.6: The location of the Pierre Auger Observatory in southern America is indicated by the blue circle. Modified from Ref. [18].

The Pierre Auger Observatory [14] is the largest observatory for cosmic rays ever built. It is located near the city of Malargüe in the province Mendoza in Argentina and is on the southern hemisphere of the earth. See Fig. 2.6 for its approximate location within southern America. The observatory is located on a high plateau with an average elevation of 1400 m above sea level, which corresponds to an atmosphere depth of $X_{\text{obs}} \approx 875 \, \text{g/cm}^2$ [14]. The observatory was started in 1999, while the main construction was performed between 2004 and 2008. Since then the observatory continuously records cosmic-ray data.

The observatory is designed as a hybrid detector system and is thus composed of several different detector systems. The two largest systems are the surface detector array (SD) [19] and the fluorescence detector (FD) [10], which are explained in the following.

The SD consists of ~1660 self-sustaining detector stations distributed over an area of ~3000 km^2. These stations are arranged on a triangular grid with a spacing of 1.5 km with additional more dense stations deployed in the north-west of the SD array. In the dense region the distance

10
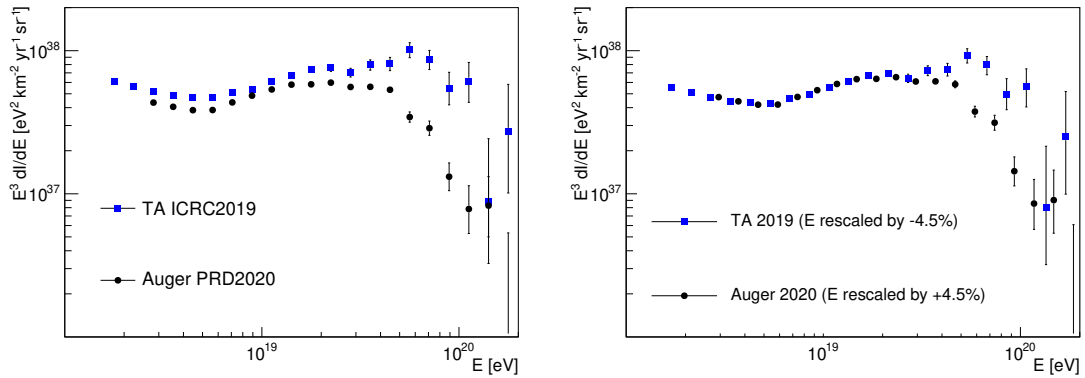
Figure 2.5: *Left:* Cosmic-ray energy spectra as measured by the Pierre Auger Observatory (Auger) and the Telescope Array (TA). *Right:* Similar spectra as on the right but the energies are rescaled by ±4.5% for both measurements. Both plots are adapted from Ref. [13].
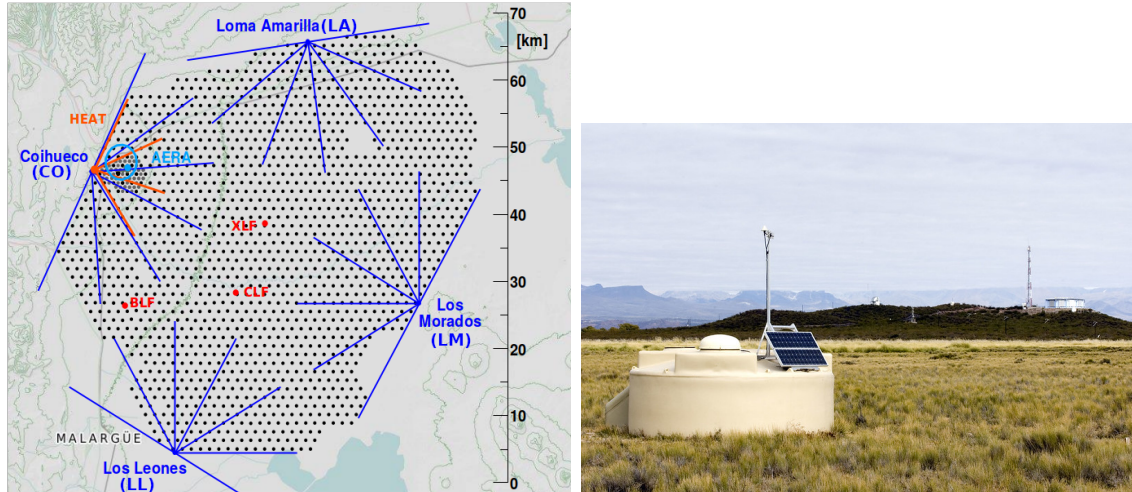
Figure 2.7: *Left:* Schematic map of the Pierre Auger observatory. Each black dot represents one SD station. The field of views of FD telescopes are indicated by the blue (red for HEAT) lines. Locations of the Auger Engineering Radio Array (AERA), the eXtreme Laser Facility (XLF), the Central Laser Facility (CLF) and, the Ballon Launching Facility (BLF) are also marked. *Right:* Photograph of an SD station (in the foreground) and an FD telescope building (in the background) [20].

between the stations is reduced to 750 m and therefore this (infilled) region is referred to as the SD-750 array. Similarly, the main array is called SD-1500 array. The entire area covered by the SD is overlooked by the 27 fluorescence telescopes of the FD located at four sites on the perimeter of the SD array. A map of the Pierre Auger Observatory is shown in Fig. 2.7-left. Each SD station consists of a water-Cherenkov detector (WCD), required electronics, and antennas for communication, timing, and position. Power is provided by a solar panel in combination with a battery. The WCD employs a cylindrical tank of 3.4 m diameter and has a height of ~1.5 m holding 12 t of clean water. Three photomultiplier tubes (PMTs), 9 inch in diameter, are symmetrically placed at the top of the station, looking downwards into the water. These PMTs record the Cherenkov light induced by relativistic charged particles passing through the water. A photograph of an SD station is shown in Fig. 2.7-right. Each SD station is designed to operate 24 h per day (100% duty cycle) and the entire SD has a full trigger efficiency for air showers of

Figure 2.8: Photographs of the FD telescope building in Coihueco. Communication tower is visible on the right. *Top:* During day time. *Bottom:* During night time. The Milky Way appears in the background.

primary particles with energies above ∼ 3×10^{18} eV falling anywhere in the array.

At the moment a major upgrade, called AugerPrime, of the entire observatory is performed. In the upgrade, each SD station will be additionally equipped with scintillation surface detector (SSD) which is mounted on top of the WCD tank. The SSD allows for a better discrimination between electrons and muons measured by the SD station. Furthermore, the electronics of each station is upgraded, an additional smaller PMT is included into the WCD, radio antennas are added to all SD stations with an SSD, and a selection of stations are equipped with underground muon detectors. A detailed description of all aspects of the upgrade is not included in this work, but can be found in Ref. [21],

The FD of the Pierre Auger Observatory employs 27 fluorescence telescopes which are distributed over four locations as indicated in the map in Fig. 2.7. Three of these telescopes take a special role, since they are installed in custom designed housings which can be tiled by 29°. These

event 12018427 06/27/2011 05:10:23 UTC
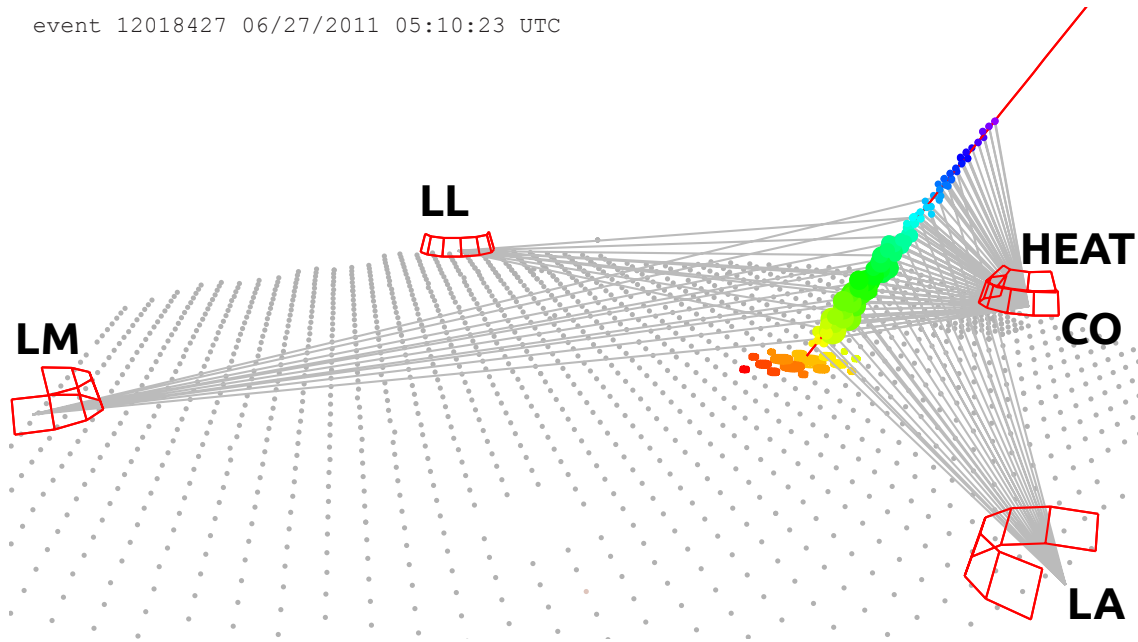
Figure 2.10: An example of an air-shower event measured by the SD and all FD telescopes, including HEAT. The red rectangles illustrate the field of view of the FD telescopes. Timing is encoded by color. The marker size of the SD stations corresponds to the magnitude of the measured signal. Average reconstructed FD energy of this event is $E_{\mathrm{FD}} = (47 \pm 1)\,\mathrm{EeV}$ and the depth of the shower maximum is $X_{\mathrm{max}} = (730 \pm 3)\,\mathrm{g/cm^2}$. Modified version from Ref. [23].

telescopes observe the night sky under higher elevations as the standard telescopes. The three telescopes assemble the High-Elevation Auger Telescopes, short HEAT. The main 24 telescopes are installed within four telescope buildings, each hosting six telescopes. We show photographs of one of the FD telescope buildings in Fig. 2.8 and a technical drawing of a telescope building layout in Fig. 2.9. We give a detailed description of the telescope design, operation, and calibration in Chapter 3.

The four sites of the FD are labeled starting in the South and going counter-clock wise: Los Leones (LL), Los Morados (LM), Loma Amarilla (LA), and Coihueco (CO). HEAT (HE) is located at the FD site of Coihueco. Each telescope is operated independently and has a field of view of $30° \times 30°$ in azimuth and elevation. An entire building containing six telescopes has a $180°$ coverage in azimuth. With such an arrangement of telescopes the FD reaches full trigger efficiency for air showers with energy above ~10^{19} eV over the entire area of the SD array. However, the observations with the FD are limited to dark, moonless nights and appropriate weather conditions. This limits the duty cycle of the FD to ~14%.

The attenuation due to aerosols contained within the atmosphere is continuously monitored by two laser facilities located close to the center of the observatory [22]. Both, the Central Laser Facility (CLF) and eXtreme Laser Facility (XLF), are marked as red points in the map of Fig. 2.7. Several LIDAR station are installed close to each FD site, which can be used to study the atmospheric conditions close to the telescopes. Additionally, each FD site employs a weather station and cloud detectors.

Figure 2.9: Technical drawing of an FD building hosting six telescopes. Taken from Ref. [10].

Since the Pierre Auger Observatory is build as a hybrid detector we are able to observe air showers independently with several detectors systems. We show a typical air-shower event observed from all four FD sites and the SD array in Fig. 2.10. Events which are observed by both the SD and FD are labeled hybrid events. We use these hybrid events to relate the direct energy measurement of the FD to an energy calibration of the SD. For this purpose we define an energy

Figure 2.11: Correlation between the energy estimators of the SD and the measured energy of FD. Different energy estimators are plotted in different colors. Plot is adapted from Ref. [27].

estimator S_{SD} for the signal recorded by the SD. We then obtain the SD energy calibration with the correlation between S_{SD} and the energy E_{FD} measured by the FD with a simple power-law ansatz

$$E_{FD} = A\, S_{SD}^{B} \tag{2.14}$$

where A and B are the calibration parameters. Depending on the SD (sub-)array and the zenith angle of the arriving air shower, different reconstruction algorithm are used and each algorithm provides its own energy estimator. For vertical showers with zenith angles $0° \le \theta \le 60°$, we use the shower-size parameters S_{38} and S_{35} as energy estimators for the SD-1500 and the SD-750 array, respectively [24]. These parameters correspond to the mean signal a station at a distance of $r = 1000\,\text{m}$ ($r = 450\,\text{m}$) to the shower core would detect if the shower with the same energy would arrive under the zenith angle of $\theta = 38°$ (35°). For inclined showers ($\theta > 60°$) we use N_{19}, which corresponds to the relative muon content with respect to a simulated proton shower with a primary energy of 10^{19} eV, as an energy estimator [25]. We will not further discuss how these energy estimators are determined, more details can be found in e.g. Refs. [24, 25, 26, 27].

In Fig. 2.11 we show the correlation between the SD energy estimators and the measured FD energy. The different colors in the plot correspond to the different energy estimators as introduced above. We use these correlations to perform an energy calibration of the SD. With this procedure we compensate for the rather low duty cycle of the FD (~14%) by relating this energy scale to the SD (100% duty cycle), which would otherwise have to rely on simulations to obtain an energy measurement. However, this implies that the energy scale of the entire Pierre Auger Observatory is set by the energy estimation of the FD. This makes the accuracy of the absolute calibration of all FD telescopes of utmost importance.

FLUORESCENCE TELESCOPES OF PIERRE AUGER OBSERVATORY

Contents

In the following chapter we introduce the telescopes of the fluorescence detector system of the Pierre Auger Observatory. We first give a technical description of the telescope design and the data acquisition, and then we discuss the current techniques and methods to absolutely and relatively calibrate these fluorescence telescopes.

3.1. DESIGN OF TELESCOPES

The optical setup of the fluorescence telescopes of the Pierre Auger Observatory is based on a modified Schmidt telescope design which provides a large aperture and a wide field of view. A schematic drawing of the design with its individual components and a photograph of the interior of one fluorescence telescope is presented in Fig. 3.1. We provide a more detailed technical drawing in Fig. A.1 of the appendix. The working principle of the telescope is that the light, which enters through the aperture system, is focused by a spherical mirror onto a camera, which is located between the entrance window and the mirror. We describe the individual components of the telescope briefly in the following, but for more detailed descriptions see e.g. Refs. [14, 10].

Starting from the left edge in the drawing of Fig. 3.1, the first, leftmost part of the telescope is the shutter. The shutter obscures the entire telescope aperture while closed. During no data-taking periods, e.g. daytime, rain, high winds, or moon in the field of view, these shutters are closed to protect other components of the telescope from any damage.

While the shutter is open, the light enters the telescope through a 2.2 m diameter aperture which is entirely covered by a UV filter made of 3.25 mm-thick M-UG 6 dark-violet tinted silicate-glass [28]. This kind of glass has a high absorption in the visible and infrared region while still allowing the transmission of photons with wavelengths between ~290 nm and ~410 nm, which is essential to reduce the background for the detection of fluorescence light of nitrogen. The
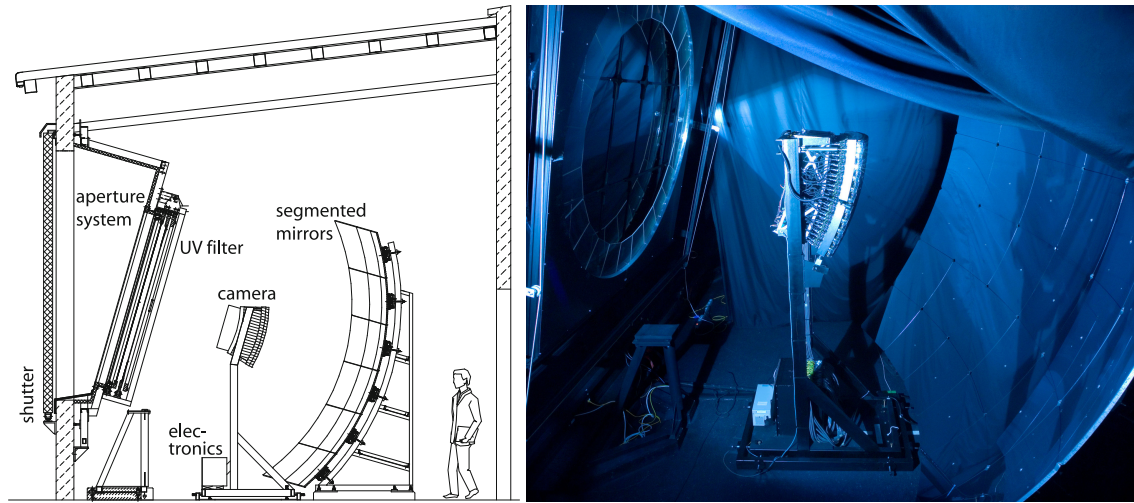
Figure 3.1: *Left:* Schematic drawing of the components of a fluorescence telescope of the Pierre Auger Observatory. Adapted from Ref. [10]. *Right:* Photograph of the interior of one of the telescopes [20].

transmission of the filter in the relevant part of the wavelength spectrum is shown in Fig. 3.2. Since it is quite difficult and expensive to produce the whole filter (~3.8 m^2) in a single piece of glass, the filters at the telescopes are assembled out of segments with sizes of roughly (45×76) cm^2. In addition, the filter glass protects the interior parts of the telescope from dust, dirt, and wind.

Following further the path of photons entering the telescope, the next part they encounter is the corrector lens which is located ~12 cm behind the filter glass. The purpose of this lens is to reduce the spherical aberrations of the telescope. For cost optimization, only a corrector ring with inner and outer radius of 0.85 m and 1.1 m, respectively, is installed at the telescopes, instead of a 3.8 m^2 lens covering the entire aperture window. Since the production and transportation of a ring with external diameter of 2.2 m is still rather difficult and quite expensive, the whole corrector ring is divided into segments. The corrector rings for the FD telescopes are assembled out of 24 segments and are made of either BK7 glass or Borofloat [14]. By installing such a corrector-ring lens an improvement of a factor ~2 in the effective light-collection area is gained for FD telescopes [29]. The measured transmittance of the corrector ring is shown in Fig. 3.2. The segmented corrector ring is visible in the left side of the photograph in Fig. 3.1-right.

Behind the filter and the corrector ring there is a safety mechanism installed, which protects the very sensitive camera hardware against destruction by focused sun light. If the light intensity on the camera increases above a certain threshold, a curtain closes and covers the entrance window at the inner side and thus prevents light from reaching the sensitive camera. The curtain is also automatically closed any time a power cut occurs. When the shutters are opened during daytime, it is mandatory to close the curtain or otherwise the bright daylight gets focused on the camera and can destroy it, even when the camera is in a standby mode. During regular data-taking periods this curtain is left opened.

Following along the path of incident light, for most of the photons the next component they encounter is the mirror. Some photons will hit the back of the camera support structure and will probably get absorbed or reflected there. However, we will not focus on these photons for now. The focusing mirror is of a spherical shape ($r_{\mathrm{mirror}} = 3.4$ m) and spans an area of $A_{\mathrm{mirror}} \approx 13$ m^2. Due to this large area, the mirror is segmented to again reduce the cost of the production and ease the assembly and installation. For faster and more cost effective production the mirror segments were manufactured in different laboratories across several countries. Each of the laboratories was specialized in different kind of mirrors, which resulted in two types of telescope mirrors finally employed at the observatory. The first type of the mirror is assembled of 60 hexagonal glass-

16
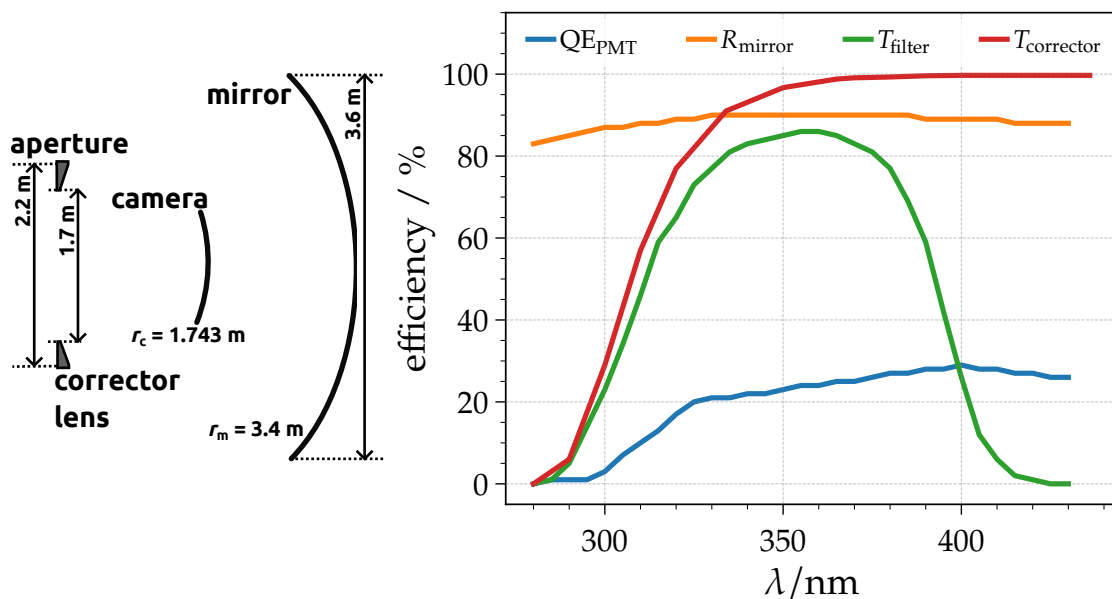
Figure 3.2: *Left:* Illustration of the geometry of a fluorescence telescope. Figure is adapted from Ref. [10]. *Right:* Efficiency of the individual optical components of a fluorescence telescope. Quantum efficiency of the PMTs, QE_{PMT}, is shown in blue, reflectivity R_{mirror} of the mirrors in orange and the transmission T_{filter} of the filter in green, and the corrector ring $T_{corrector}$ in red. Data for the plot is taken from the analysis tool of the Pierre Auger Collaboration ($\overline{\text{Offline}}$ `FModelConfig.xml`).

mirror segments of four different shapes and sizes. These segments have a thickness of 12 mm and are made of a borosilicate glass SIMAX, which has good mechanical and thermal stability. Onto the glass segments a reflection coating of one 90 nm-layer Al and one 110 nm-layer SiO$_2$ is vacuum-deposited. The use of these materials is motivated by the high reflectivity of aluminium and the high mechanical resistance of silica. At the observatory site 15 telescopes are equipped with the hexagonal glass-mirror setup, these are the each six telescopes at the sites of Coihueco and Loma Amarilla, and the three telescopes of HEAT. The second mirror type is installed in the remaining telescopes at the FD sites of Los Leones and Los Morados. This mirror type is constructed out of 36 segments of rectangular shape, which are arranged in a 6 by 6 matrix. The height $h \approx 65$ cm is the same for all elements, while the width is decreasing from $w_1 \approx 65$ cm to $w_2 \approx 55$ cm going up or down from the equator of the mirror. These mirror elements are made by diamond milling 2 cm-thick aluminum blocks to the desired spherical form. Onto the inner surface of each element a 2 mm-thick layer of AlMgSiO$_5$ is glued to create the reflecting surface. This surface is again diamond milled and a roughness smaller than 10 nm is archived in this procedure. For additional protection of the mirror elements a 90 nm aluminum-oxide layer was applied via chemical anodization.

After being reflected and focused by the mirror, the photons travel towards the camera of the telescope, which is described in more detail in the following Section 3.2.

3.2. CAMERAS OF FLUORESCENCE TELESCOPES

In the following section we introduce and describe the camera of an FD telescope which is arguably the most crucial part of the telescope. We focus on giving an overview of the camera setup and operation, for greater detail on this topic see e.g. Refs. [10, 30].

The camera of each FD telescope consists of 440 pixels arranged in a 20 (columns) by 22 (rows)
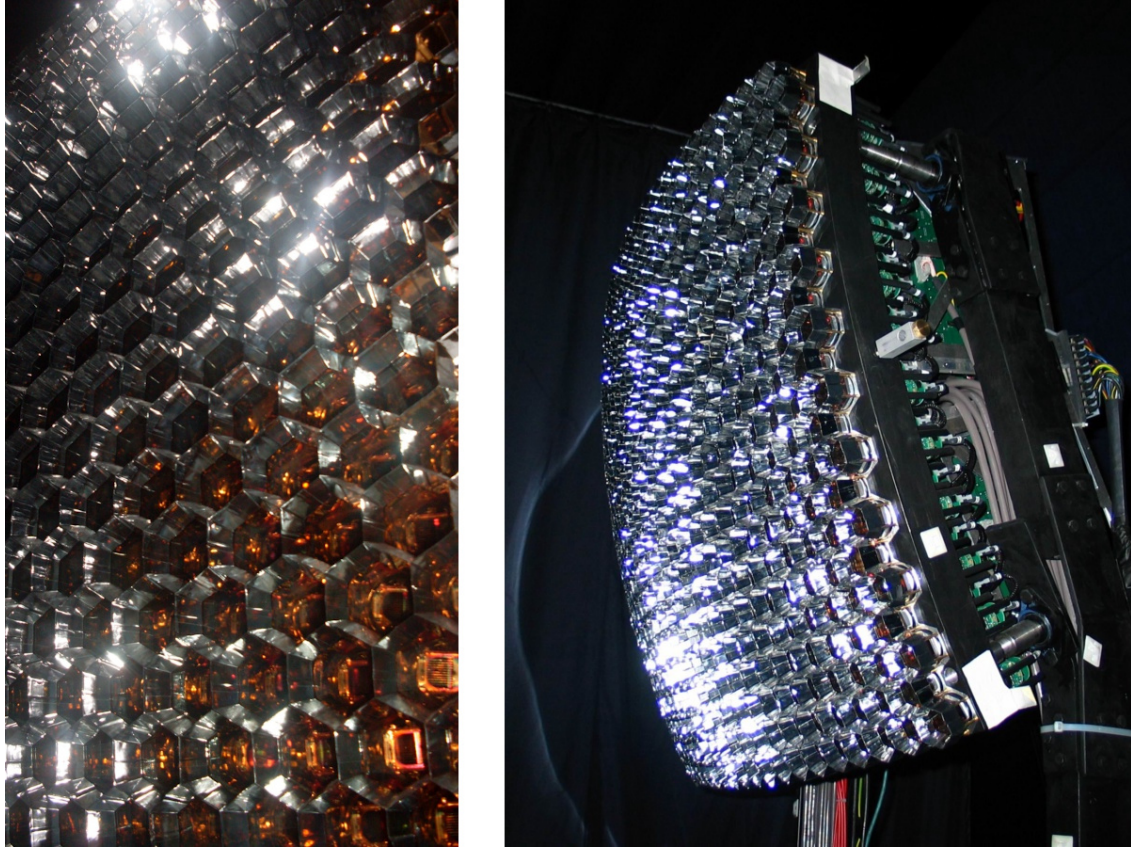
Figure 3.3: Photographs of the PMT camera of a fluorescence telescope. *Left:* Closeup view showing the light collectors on top of the PMTs. *Right:* Photograph of the entire camera. Both photographs are taken from Ref. [20].

matrix. More details on the construction of the camera are given below. Each pixel of the camera is made of a hexagonally-shaped photomultiplier tube (PMT) made by the company Photonis [31]. The type of the PMT is XP3062. This type of a PMT has a size of ~40 mm, measured from side to side. The PMTs employ a standard bialkaline photocathode which is sensitive to photons with wavelength between ~300 nm and ~600 nm. The maximal quantum efficiency of ~30% is reached at a wavelengths of ~400 nm. In Fig. 3.2 the quantum efficiency of this type of PMTs is shown together with efficiency of other optical components of the telescope. The electron multiplier of the XP3062 tube has 8 dynode stages and the operating voltage is applied in the way that the photocathode lies on ground potential and the anode is supplied with a positive high voltage. The operating high-voltage of the pixel-PMTs were chosen to be $U \approx 800 - 900$ V, which results in a overall gain $G \approx 5\times10^4$ for each PMT. To increase the cost efficiency, the PMTs of one camera are organized into groups of 44 units. Each of the 10 groups is then powered by a single high-voltage channel. The PMTs within the group were selected to have a maximal gain differences of about ±10%.

The symmetry of the whole telescope results in a spherical shape of the focal surface, which is concentric with the mirror sphere and has a radius r_{focal} = 1.743 m slightly larger than half the radius of the mirror. An ideal camera would map this spherical shape perfectly. Since this spherical focal surface cannot be completely covered by hexagonal PMTs, there are several possibilities of positioning the pixels across the focal surface. The solution employed in the FD telescopes of the Pierre Auger Observatory is described in Ref. [30] and summarized in the following.

18
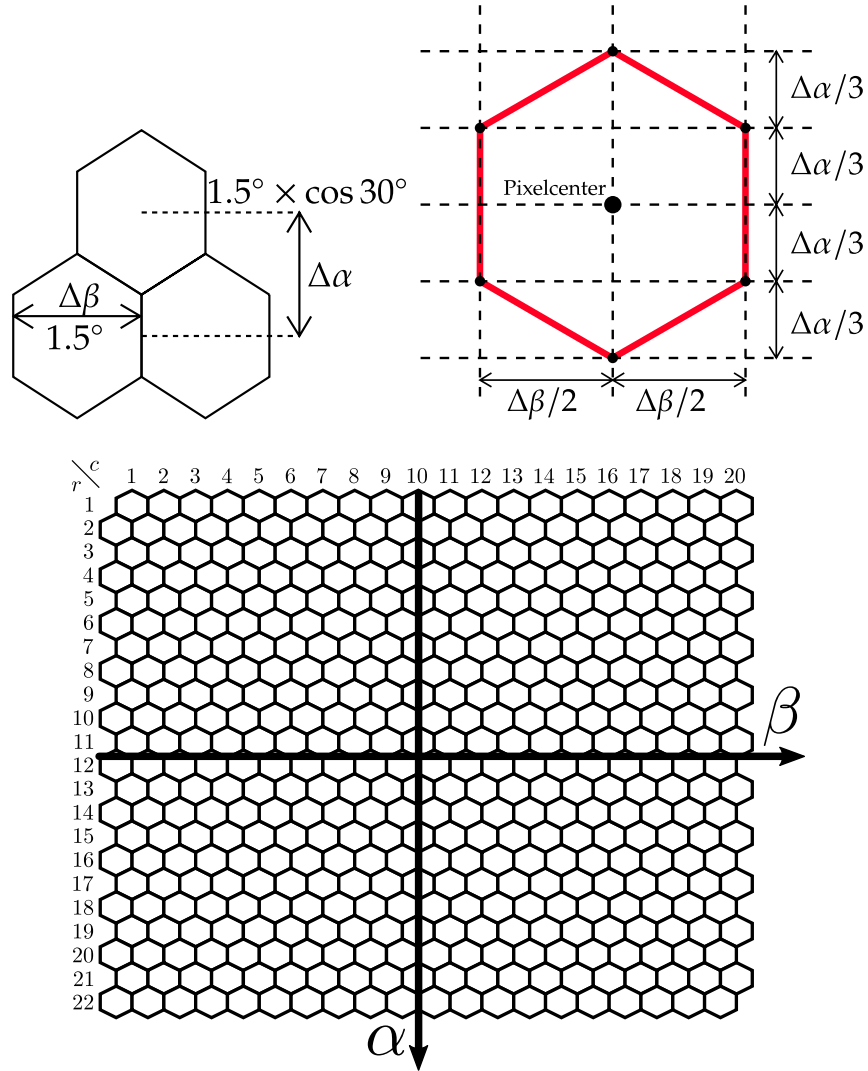
Figure 3.4: *Top:* Dimensions of the pixels of the camera. Drawings adapted and modified from Ref. [30]. *Bottom:* Angles (α, β) on the camera sphere viewed from the back side of the camera (concave side). Figure adapted from Ref. [32].

The pixels of the camera are arranged in 22 rows and 20 columns as illustrated in Fig. 3.4. The size of a hexagonal pixel (~45.6 mm, side-to-side) at the focal surface r_{focal} corresponds to an angle of $\Delta\beta = 1.5°$. The pixel centers within the same row of the camera are $\Delta\beta = 1.5°$ apart. For neighboring pixels in different rows, the distance $\Delta\alpha$ between their centers is calculated to be $\Delta\alpha = \Delta\beta \cos 30° \approx 1.3°$, as illustrated in Fig. 3.4-top. For the construction of the camera, the centers of pixels are obtained by applying steps of $\Delta\beta$ and $\Delta\alpha$, while each row is moved by $\pm\Delta\beta/2$ with respect to the previous row. We illustrate this geometry in Fig. 3.4. Following this procedure, we calculate the coordinates of the centers for each individual pixel on the focal surface as the two angles

$$\alpha = \Delta\alpha \, (r - r_{\text{center}}) \tag{3.1}$$

$$= 1.5° \times \cos 30° \, (r - r_{\text{center}}) = 1.5° \times \frac{\sqrt{3}}{2} \, (r - r_{\text{center}}) \tag{3.2}$$

$$\approx 1.3° \, (r - r_{\text{center}}) \tag{3.3}$$

19

and

$$\beta = \Delta\beta \, (c - c_{\text{center}}) \tag{3.4}$$

$$= 1.5° \, (c - c_{\text{center}}) \tag{3.5}$$

with column number c and row number r. The center column and center row of the camera are given as $r_{\text{center}} = 35/3 \approx 11.667$ and $c_{\text{center}} = 10$ for odd rows and $c_{\text{center}} = 21/2$ for even rows, respectively. In Fig. 3.4-bottom the pixel matrix and the two angles are drawn. After the pixel centers are obtained the vertices between pixels are determined by moving from each pixel center in steps of $\Delta\beta/2$ and $\Delta\alpha/3$. An illustration for one pixel is shown in Fig. 3.4-top.

For a safe mechanical construction of the camera, the PMTs have to be installed in the camera frame with some remaining space left between them. This space results in a significant area between the PMTs, which remains insensitive, although the hexagonal shape of the XP3062 PMT allows for a dense arrangement of the latter. In addition, the effective cathode area of a PMT is smaller than the area covered by the glass tube. To compensate for this insensitive area and to ensure a sharp transition between neighboring pixels, light collectors are installed in the space between the PMTs. These light collectors assemble an equivalent of an *Winston cone* and are constructed of specially designed elements. Each element has three arms which are oriented at angular steps of 120° and because of their shape, these elements are called *Mercedes stars*. The height of the Mercedes elements is ~18 mm and the length of each arm is half the side length of a PMT. The cross-sectional area of an arm is an isosceles triangle with a base length of ~9.5 mm. This base length is chosen to be large enough to cover the insensitive outer parts of the PMTs (~2 mm) and the maximal space between adjacent PMTs (~5 mm). The Mercedes stars themselves are made of a plastic material covered by an aluminized polyester film, known as *Mylar foil*. Each element for the light collector is installed at a vertex for three PMTs, thus the light for one PMT is collected by six Mercedes stars. A photograph of the FD camera with the installed light collectors is presented in Fig. 3.3.

The pixels of a FD telescope are defined on the focal surface and the focal surface is located exactly where the edges of the light collectors are. This means that the top edges of the Mercedes stars divide the FD camera into pixels and hence the PMT photo-cathodes are placed ~18 mm behind the focal surface.

Viewing Direction of Telescope Pixels in the Sky. The procedure of calculating the actual viewing direction of a pixel in the sky is described in Ref. [32]. In the following we summarize the most important (in context of this thesis) details and formulas. We calculate the viewing direction of each individual pixel with the coordinates α and β on the camera sphere by applying the sine theorem for spherical triangles. Thus, we estimate the elevation angle δ of a given pixel as

$$\frac{\sin\delta}{\sin(\alpha + \alpha_{\text{m}})} = \frac{\sin(90° - \beta)}{\sin 90°} = \cos\beta \tag{3.6}$$

with the corresponding angles marked in blue and orange in Fig. 3.5. Similarly, for the azimuth φ we get

$$\frac{\sin\beta}{\sin\varphi} = \frac{\sin(90° - \delta)}{\sin 90°} = \cos\delta \tag{3.7}$$

with the red and green marked angles in Fig. 3.5. By combining Eqs. (3.6) and (3.7) we express the elevation δ as

$$\sin\delta = \sin(\alpha + \alpha_{\text{m}}) \cos\beta \tag{3.8}$$

and azimuth φ as

$$\sin\varphi = \frac{\sin\beta}{\cos\delta} \tag{3.9}$$

for each individual pixel with the coordinates (α, β) of the camera surface. The angle α_{m} describes the elevation of the optical axis of the telescope. The optical axis of the standard telescopes is elevated by $\alpha_{\text{m}}^{\text{FD}} \approx 16°$ and for HEAT by $\alpha_{\text{m}}^{\text{HEAT}} \approx 45°$.
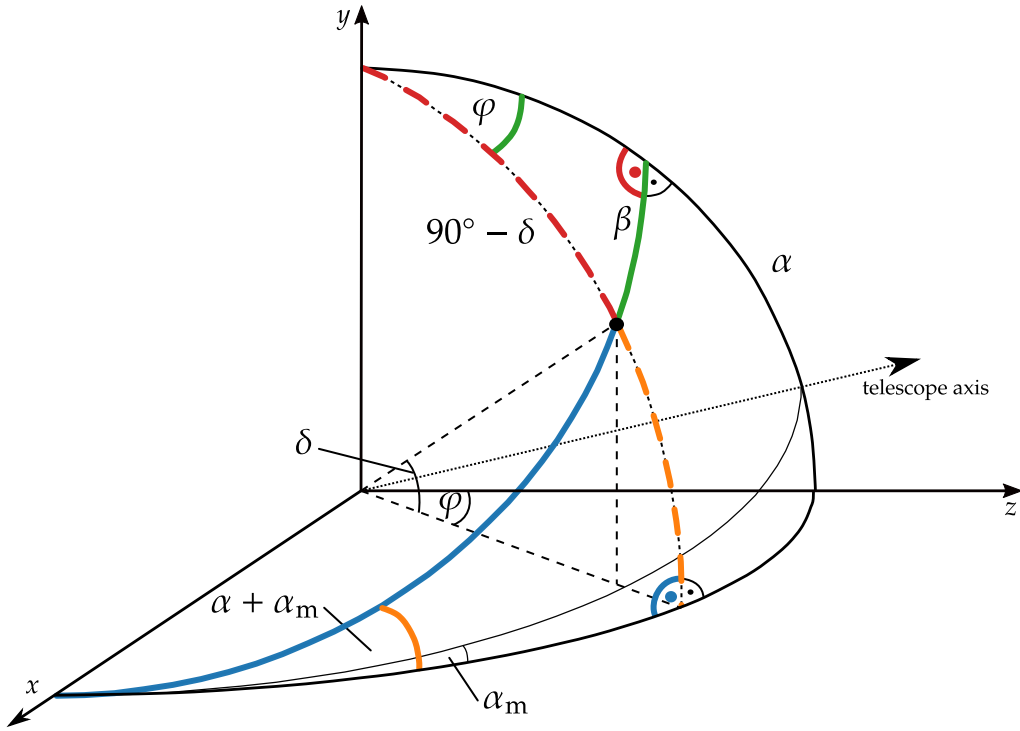
Figure 3.5: Conversion of pixel centers in camera coordinates (α, β) to an elevation δ and azimuth φ of the viewing angle in the sky. The telescope axis is elevated by α_m and is drawn as the dotted line. Figure is adapted from Ref. [32].

Solid Angle of Camera Pixel. In general the solid angle observed by a pixel is calculated as

$$\Omega_\mathrm{pixel} = \frac{A_\mathrm{pixel}}{r_\mathrm{focal}^2} \tag{3.10}$$

with the pixel surface area A_pixel on the camera sphere with radius r_focal.

The equal steps in angles used for the pixel positions in the construction of the camera lead to different linear dimensions and thus the actual size of the pixels varies across the camera. Therefore, not all pixels are regular, planar hexagons. Furthermore, a different area A_pixel of a pixel implies also a different solid angle Ω_pixel covered by that particular pixel according to Eq. (3.10). The difference is the largest between pixels on the edge and in the center of the camera and has a magnitude of ~4%. Compared to the mean solid angle of all pixels, the deviation of these extreme cases (edge and center pixels) becomes of the order of ~2%.

In the analysis software framework $\overline{\text{Off}\underline{\text{line}}}$, the values of the pixel solid angles are hard-coded and were obtained once via simulations. In the following part we describe a procedure of geometrically calculating the solid angle of each individual pixel.

Therefore, we split the area of the pixel hexagon into six triangles as shown in Fig. 3.6. The area of the hexagon is then simply the sum of the areas of all six triangles. The positions of the pixel centers and vertices between pixels can be calculated as explained above and thus the length of all triangle sides are known as well. With the assumption that the triangles can be treated as planar triangles, we use Heron's formula

$$A = \sqrt{s\,(s - a)\,(s - b)\,(s - c)} \tag{3.11}$$

for a triangle with the side lengths (a, b, and c) and $s = (a + b + c)/2$ to calculate the area of each triangle and consequently of the hexagon.
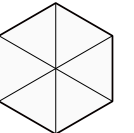
Figure 3.6: Hexagonal pixel split into six triangles.
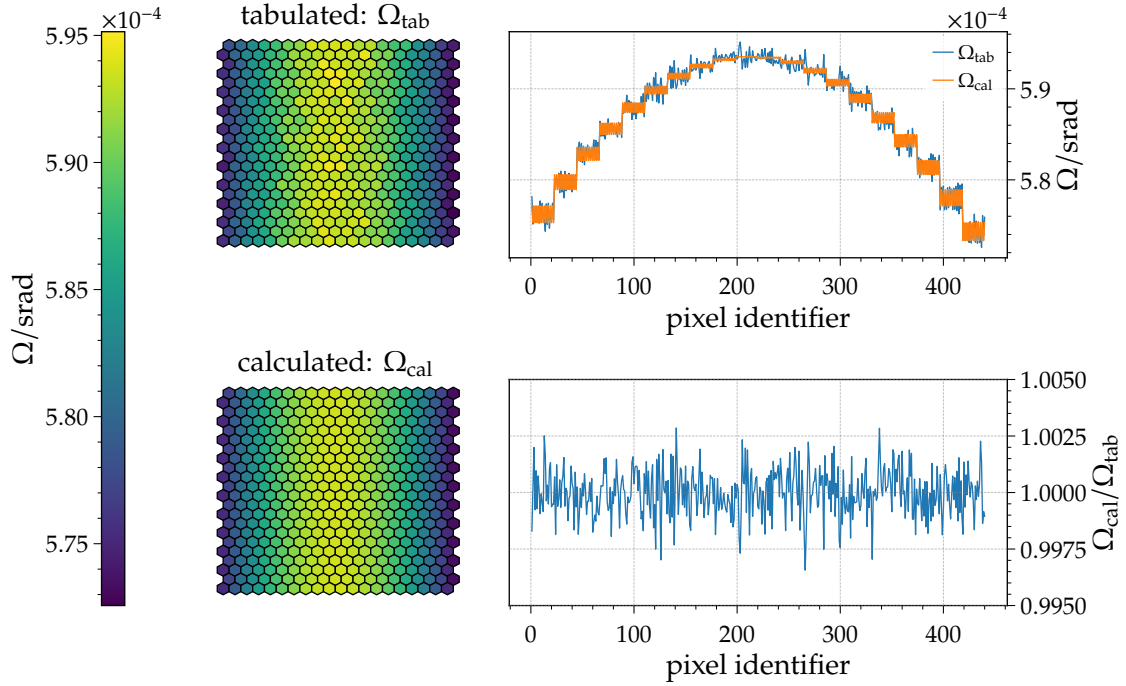
Figure 3.7: Solid angles of the FD camera pixels. *Left:* Illustration of the pixel solid-angles tabulated in $\overline{\text{Off}}\underline{\text{line}}$ (top) and calculated as described in the text (bottom) as pixel matrix. *Right:* Plot of the tabulated and calculated solid angles of pixels (top) and the ratio between the latter two (bottom) as a function of the pixel number.

In Fig. 3.7 we show the pixel solid angles as tabulated in the $\overline{\text{Off}}\underline{\text{line}}$ framework together with the geometrical estimate. The left part of that figure illustrates the solid angles, while on the right side we show the solid angles as a function of the pixel number. Additionally, we plot the ratio between the calculated and the tabulated values in the lower right plot. We observe a maximal deviation of less than 0.35% and we thus conclude that the geometrical estimation of the pixel solid angle is in agreement with the tabulated values. This validates the approach to calculate the solid angles.
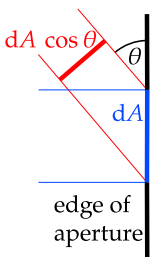
Figure 3.8: Illustration of the area projection for an FD aperture.

Aperture of Telescopes. The area of the aperture for all fluorescence telescopes of the Pierre Auger Observatory is defined to be a fixed value of $A_{\text{aperture}} = \pi \, (1.1 \, \text{m})^2 \approx 3.8 \, \text{m}^2$. For historic reasons this nominal aperture area is included in the calibration constant of each telescope pixel, meaning that the calibration constant gives the number of photons per nominal aperture per adc. In the reconstruction the measured ADC signal is then converted first into a photon number at the aperture via the absolute calibration and then to a photon density by multiplying it with the nominal aperture area A_{aperture}. Therefore, it would be much more convenient to directly estimate and use the calibration constant as a photon density at the aperture rather than a photon number. Nevertheless, as long as the calibration and the reconstruction use the identical value for the nominal aperture A_{aperture} its contribution cancels out and the actual value of A_{aperture} becomes irrelevant. Therefore, including the aperture area in both calibration and reconstruction or in neither of them is just a form of convention.

Another property of the telescopes, which is included in the calibration constants, is the aperture-area projection. For light that enters the telescope under a zenith angle θ the effective area

$$\mathrm{d}A' = \mathrm{d}A \cos \theta \tag{3.12}$$

of the aperture decreases with the zenith angle θ as illustrated in Fig. 3.8. This projection effect

is maximal for the pixels at the corners of the telescope camera. These pixels have zenith angles of $\theta \approx 20°$ and consequently their effective aperture area is of the order of 6% ($\cos 20° \approx 0.94$) smaller than for the central pixels of the camera. When calculating the photon density at the aperture this area projection effect has to be taken into account. But again due to historic reasons, this aperture effect is incorporated into the calibration constant of each individual pixel.

Moreover, if we use a calibration light source that has a directional emission according to the Lambert's cosine law,

$$I(\theta) \propto I_0 \cos\theta, \tag{3.13}$$

with the emission along the surface normal I_0, the cosines of the aperture-area projection and the emission of the light source cancel and can therefore be dropped in the estimation of the calibration constants.

3.3. Fluorescence Detector Electronics and Data Acquisition

The electronics of the FD telescopes is designed to handle a large dynamic range which is required for air fluorescence measurements. In addition, the electronics does provide a strong background rejection.

In the following we summarize the main parts of the FD electronics and data acquisition. A schematic drawing for the readout system is found in Fig. A.2 of the appendix. For a much more detailed discussions of the FD electronics the reader is referred to e.g. Refs. [10, 34, 35].

Each PMT of the telescope camera has its own head electronics which is connected via a distribution board to the front-end electronics of the telescope. The front-end electronics houses 20 analog boards (AB), each receiving the signal from a group of 22 PMTs (one column of the FD camera). The AB adjusts the gain of each channel. Each PMT is set up with a high-gain and a low-gain channel. The low-gain signals of each 11 non-adjacent PMTs are summed up in one virtual channel. If the high-gain channel of a PMT is saturated, the signal can be recovered by taking the virtual-channel signal into account. The de-saturation of channels is described in Ref. [36]. In short, the de-saturated signal s_i for each time bin of the i-th channel is calculated as

$$s_i = \left[\frac{s_{\mathrm{v}}}{g_{\mathrm{v}}} - \sum_{j \neq i} \left(\frac{s_j}{g_j} \right) \right] g_i \tag{3.14}$$

Figure 3.9: Five topologically different patterns regarded as straight track segments for the SLT. Taken from Ref. [33].

with s_{v} the signal of the corresponding virtual channel, g_{v} the gain of that virtual channel, s_j the signals of the high-gain channels within the virtual-channel group, g_j are their gains and g_i the gain of the i-th channel.

Each output of an AB is forwarded to a first level trigger (FLT) board, which is the main component of the front-end electronics. These boards are continuously digitizing the output signals of the analog boards at a frequency of $f_{\mathrm{sample}} = 10\,\mathrm{MHz}$. The digitized data is stored in the memory of the FLT board for the subsequent readout and additionally the FLT board adjusts the individual trigger thresholds for all PMTs to keep their trigger rate at a constant ~100 Hz. With this precautionary measure an increasing random trigger rate due to slowly changing night-sky background light is prevented. For a detailed description of the FLT boards, see Ref. [37].

Also included in the front-end electronics is the second level trigger (SLT) module which reads out the pixel triggers generated by the FLT. The duty of the SLT is to identify track shapes on the entire camera by searching for various patterns of at least five pixels. For the geometry of the FD camera five topologically different patterns exist for a straight track segment of five pixels as shown in Fig. 3.9. To account for tracks, which may not pass through the centers of all five pixels and to be robust against possibly faulty PMTs, the algorithm requires only four out of the five PMTs of a pattern to have triggered. However, ~37 000 combinations of arranging these four-coincidence patterns (including rotating and mirroring) exist on the 22×20 pixel matrix of the FD camera. For
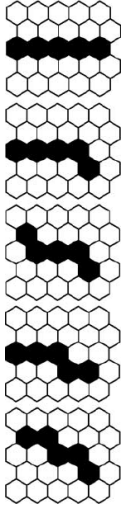
performance reasons the SLT logic searches continuously in a smaller 22×5 sub-matrix. Every 100 ns the FLT triggers of two neighboring columns are read into the SLT memory and thus a full SLT scan of the entire FD camera takes ~1 μs. In addition to the track identification, the SLT board provides each found pattern with a time stamp obtained via a dedicated GPS module and stores the recorded data as an event candidate. More details and information on the SLT module are given in Ref. [33].

Each front-end electronics (containing 20 AB, 20 FLT boards and one SLT board) of a FD telescope is connected to a MirrorPC via a FireWire interface. Furthermore, all the MirrorPCs of one FD site are linked to one EyePC via Ethernet. Since not all events passing through the two layers of hardware triggers (FLT and SLT) are actual shower events, a further software trigger is implemented on each MirrorPC. Naturally, this software trigger is called the third level trigger (TLT), its detailed description is given in Ref. [38]. Background events which trigger the hardware are mostly distant lightning events, direct hits of muons on the camera, or random triggers caused by noisy PMTs. The TLT algorithm for identifying these background events works on the multiplicity of triggered pixels rather than on captured ADC traces. Thus, only on rare occasions the captured ADC traces of pixels are read out. For most events the multiplicity signal directly obtained from the hardware (FLT, SLT) is sufficient to identify background events, which allows for a very fast trigger decision of the TLT. A more detailed discussion of the TLT algorithm is not given here, but can be found in Ref. [38]. The filtering performance of the TLT was validated with simulated and recorded data during different night/weather conditions. The TLT algorithm correctly identifies ~94% of the background events while only falsely rejecting ~0.7% of real showers [10]. The event rate per telescope after the three layers of triggers is ~0.01 Hz.

Events passing all three trigger layers are transferred to the EyePC, on which the event builder is running. This builder merges temporally coinciding events from neighboring telescopes and additionally sends a hybrid trigger (T3) to the Central Data Acquisition System (CDAS) of the observatory in Malargüe. For each arriving T3 the CDAS triggers the readout of the surface-detector stations which are closest to the FD site issuing the T3 trigger, approximately one quarter of the SD array is read out of a single hybrid T3 [10].

3.4. CALIBRATION OF FLUORESCENCE TELESCOPES

As discussed in Section 2.1.2, the deposited energy dE_{cal}/dX per traversed matter dX by an air shower in the atmosphere is proportional to the number of photons N_γ detected by a fluorescence telescope. The number of photons N_γ^{pixel} detected by a pixel of the FD camera during an air-shower event is estimated to be

$$N_\gamma^{pixel} \propto S_{ADC}^{pixel} \, C_{abs}^{pixel} \tag{3.15}$$

with the captured pixel signal S_{ADC}^{pixel} in adc and absolute calibration constant of that pixel C_{abs}^{pixel} in γ/adc. Thus, for the estimation of the energy $E_{CR}(\propto E_{cal})$ of a primary cosmic ray, it is mandatory to know the conversion factor C_{abs}^{pixel} (absolute calibration constant) between the captured pixel signal S_{ADC}^{pixel} and the number of photons N_γ^{pixel} arriving at the aperture of the FD telescope during an air-shower event. These absolute end-to-end calibration constants C_{abs}^{pixel} for every pixel of the FD telescopes are thus of great importance for the Pierre Auger collaboration.

In general, the absolute end-to-end calibration constants are obtained by exposing the entire telescope to a precisely known flux of photons and measuring the response of each individual PMT-pixel. Accordingly, all telescope effects like the transmittance and the reflectivity of each individual optical component and all PMT effects like quantum efficiency, gain, dynode collection efficiency, and digital conversion factors are directly included in these absolute end-to-end calibration constants. For the sake of simplicity, we will refer in the following to the absolute end-to-end calibration as the absolute calibration.

As we explained above, the absolute calibration constants for the FD telescopes of the Pierre Auger Observatory are used to convert the pixel signals to the number of photons at the nominal-size telescope aperture opening. Therefore, it is mandatory that the calibration and reconstruction use the identical aperture area. Additionally, the cosine dependence of the effective aperture-area projection is included in the calibration constants.

In the following we summarize the currently employed calibration systems and techniques for the FD telescopes. Generally, the systems are split into an absolute and a relative component. The absolute calibration gives the conversion factors between pixel signals and incident photon number (absolute calibration constant) and is performed, due to high workload requirements, roughly once every three years. On the other hand, the relative calibration is used to track the calibration constants for each data-taking night and is therefore performed during each measurement night. We introduce the current absolute calibration technique in Section 3.4.1 and give a overview of the relative calibration system in Section 3.4.2.

3.4.1. ABSOLUTE CALIBRATION WITH LARGE-DIAMETER LIGHT SOURCE

The standard procedure of the end-to-end absolute calibration of the FD telescopes of the Pierre Auger Observatory employs a large-diameter light source [41, 42]. The cylindrical shape of this particular light source (diameter of 2.5 m, depth of 1.4 m) reminds of a drum and thus provided the name for this calibration method – the *drum calibration*. For the calibration measurements this portable large-diameter light source (in the following drum) is mounted in front of an FD telescope aperture in a way that it entirely covers the entrance window of that telescope. A schematic drawing and a photograph of the installed drum as well as a photograph of the installation process are shown in Fig. 3.10.

The drum itself is a large metal cylinder. The interior of the drum is covered with Tyvek which is a diffusely reflecting material in the range of visible and UV wavelengths. The part of the drum which faces towards the telescope entry window is covered by a 0.38 mm thick Teflon sheet which is a diffuse transmitter. The actual light source of the drum is a pair of UV LEDs with a wavelength λ_{drum} = 365 nm [43, 44] and which are located at the center of the Teflon sheet facing towards the inside of the drum. In addition, various light sources of different wavelengths can be mounted into the drum and thus the relative spectral response of the telescopes can be measured [45, 46]. Therefore, it is sufficient to perform the absolute calibration at a single wavelength and account for the measured relative spectral response in the analysis.

The combination of diffusively transmitting and reflecting materials leads to a uniform light emission of the front disk of the drum. Here, we only very briefly describe the structure of the drum, a more detailed description of the drum can be found in e.g. Ref. [41]. While the drum is attached to the aperture of an FD telescope for calibration measurements, the LEDs within the drum are flashed with a frequency of $f_{\mathrm{drum}} \approx 1\,\mathrm{Hz}$ and a pulse length of $\Delta t = 5\,\mu\mathrm{s}$.

The total light output of the drum is designed to approximately match the light intensity of a typical EAS observed at the FD. This very low intensity makes it difficult to precisely calibrate the drum. Since the flux is too low for a direct measurement with a photodiode and too high to use a PMT in a single-photon counting mode, the calibration of the drum light source uses the $1/r^2$ law of the attenuation of light. The technique of the absolute calibration of the drum is described in Ref. [42]. With this method a total uncertainty of the absolute calibration of the drum intensity of 2.1% is achieved. An older method of calibration actually using a PMT is explained in Ref. [41], reaching a ~6% uncertainty. Calibration and uniformity measurements of the drum were performed in a special dark room at the central campus of the Pierre Auger Observatory. For the uniformity measurements a CCD camera was used to take pictures of the drum emitting surface at a distance of 14.4 m. In these pictures six concentric circles were drawn splitting the emitting surface into five annular regions. Comparing the intensity within the inner four regions a variation of the mean intensity of ~2% was found [41]. The directional emission from the drum was measured to be sufficiently close to that of an ideal Lambertian emitter [10, 41].

One disadvantage of the drum calibration method is that it takes a lot of person-power to install the drum at the FD telescopes and perform the calibration measurements. Consequently,
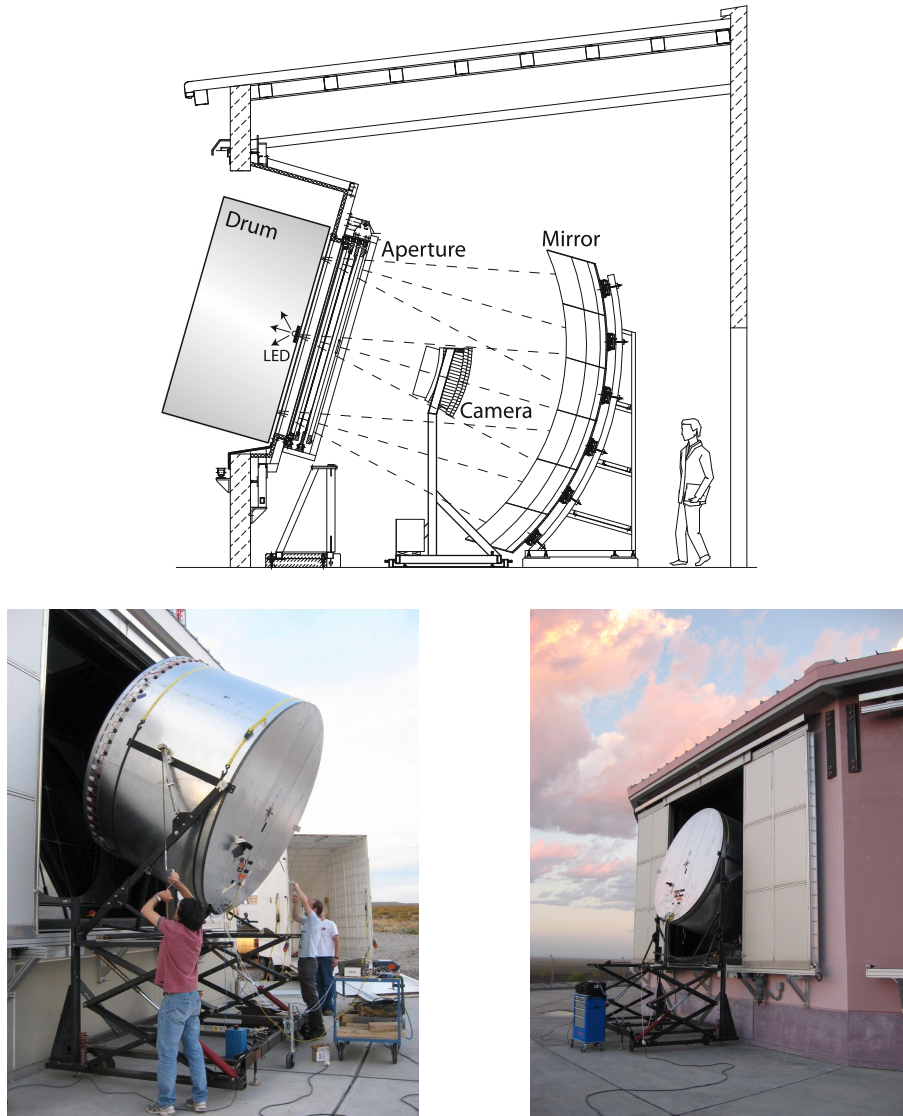
Figure 3.10: *Top:* Schematic drawing of the large-diameter calibration light-source (drum) installed at a telescope, adapted from Ref. [10]. *Bottom:* Photographs of the installation process (left, [39]) and the complete installation (right, [40]) of the drum.

the time required to calibrate a telescope is roughly half a night and therefore a whole FD site (six telescopes) needs three nights to be calibrated [10].

Another weakness, which actually influences the results of the calibration measurements, is back-reflection. Since the drum covers the entire aperture opening of the telescope all photons possibly reflected on the filter or in the interior of the telescope and leaving the telescope again through the filter, will be re-injected into the drum. Then, again the whole interior of the drum is covered with highly reflective materials and thus the photon will most likely leave the drum again in direction of the telescope. This process makes the drum appear brighter while installed on the FD telescopes than for the measurements in the dark room. The effect was estimated to be on the order of 4% [47].

The most recent absolute calibration measurements of the fluorescence telescopes with the drum technique, excluding the three telescopes of HEAT and telescope six at Loma Amarilla, were performed in 2013 [44]. The campaign before that was done in 2010 [43, 48]. For the 2010 drum
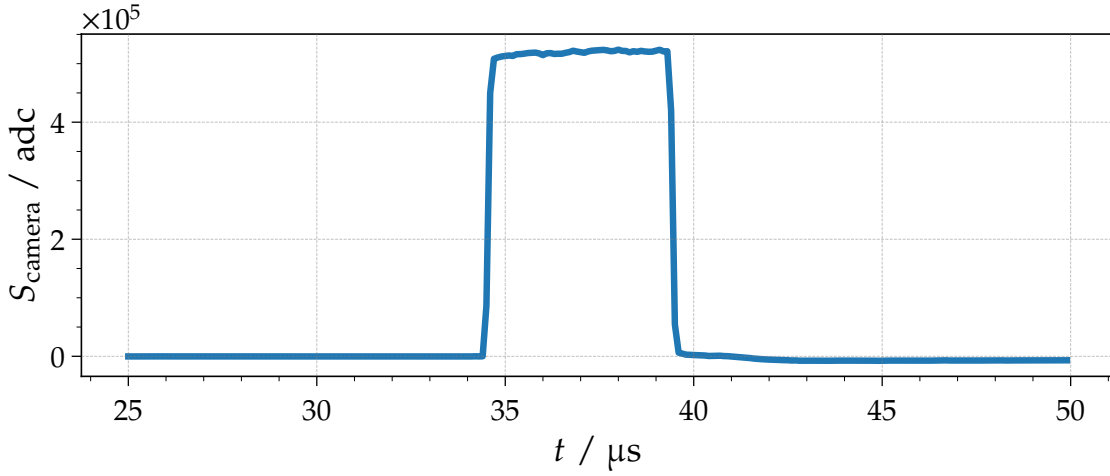
Figure 3.11: Trace captured by the entire camera (sum of 440 pixels) of the CO4 fluorescence telescope during a light flash emitted by the drum. Data was taken during the drum campaign in January 2010.

campaign the uncertainty for the absolute calibration of the drum intensity was estimated to be 3.5% [43]. Including the uncertainties from the data analysis and aperture effects, the absolute calibration constant for each telescope pixel is estimated with an accuracy of 5.0% for the 2010 drum calibration campaign [43].

The calibration results of the drum campaign in 2013 revealed an average offset per FD site (six telescopes) of ~0.8% in comparison with the tracked calibration constants from 2010 via the relative calibration system (the relative calibration system is introduced in Section 3.4.2). However, individual pixels show offsets on the order of ~5% [44]. Nevertheless, at that time the Pierre Auger collaboration decided not to update or change the calibration constants and instead keep the relative tracking starting from the 2010 absolute calibration. Since 2013 no absolute calibration with the drum at any FD telescope was performed.

Reproducing Drum Calibration Constants from 2010. For the drum calibration, the absolute calibration constant of each individual pixel is defined as the ratio between the number of photons injected by the drum into the angular acceptance of a pixel $N_{\gamma,\mathrm{drum}}^{\mathrm{pixel}}$ and the integrated response $S_{\mathrm{ADC}}^{\mathrm{pixel}}$ of this pixel during the light flash emitted from the drum. Consequently, the calibration constant of a pixel is defined as

$$C_{\mathrm{abs,\ drum}}^{\mathrm{pixel}} = \frac{N_{\gamma,\mathrm{drum}}^{\mathrm{pixel}}}{S_{\mathrm{ADC}}^{\mathrm{pixel}}}. \tag{3.16}$$

The drum itself was absolutely calibrated in 2010 (see Ref. [43]) and the number of emitted photons per pixel and pulse was estimated to be

$$N_{\gamma,\mathrm{drum}}^{\mathrm{pixel}} = I_{\mathrm{drum}}\, \Omega_{\mathrm{pixel}}$$
$$\approx 2.6{\times}10^5\, \gamma \tag{3.17}$$

with the mean solid angle $\Omega_{\mathrm{pixel}} \approx 5.85{\times}10^{-4}$ sr covered by a telescope pixel. For the drum calibration measurements, the drum emitted 400 light flashes and for each flash all pixels of the telescope camera were triggered for readout. An example of the captured readout trace as a sum over all pixels for a single light flash emitted from the drum is plotted in Fig. 3.11.

The analysis of the captured data from the telescopes is described in Ref. [43] and also shortly summarized in the following. To obtain the total signal S_{pixel} accumulated in a pixel during a
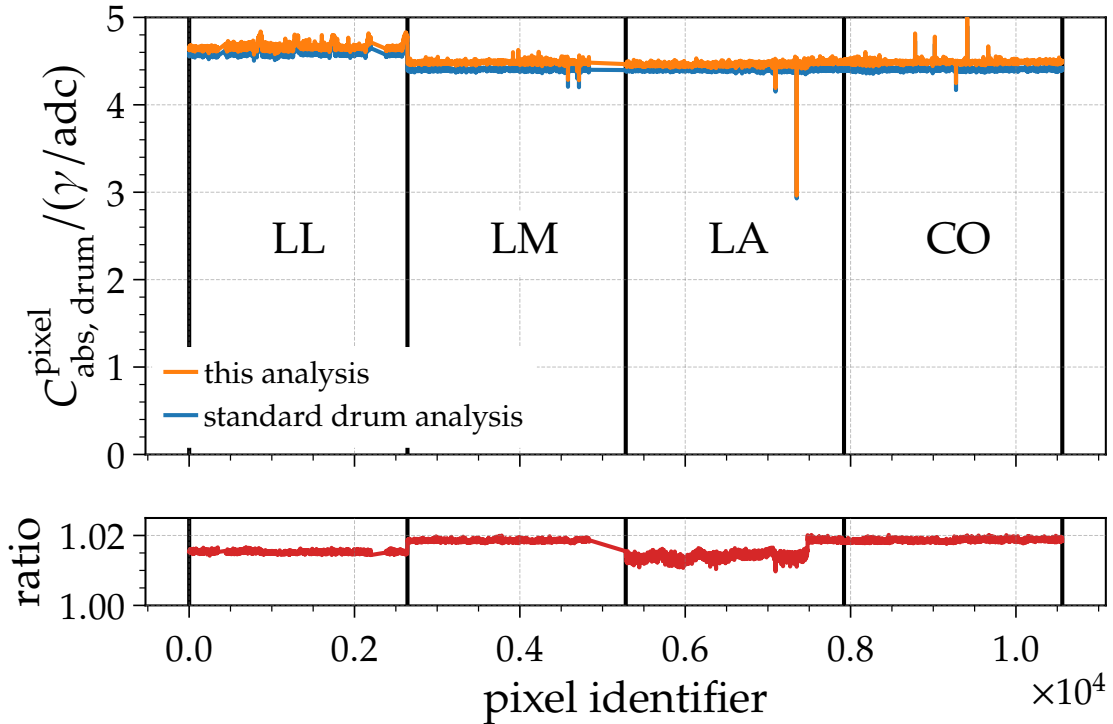
Figure 3.12: Absolute calibration constants for all the telescopes obtained from the drum measurements in 2010. The blue line shows the constants estimated by the standard drum calibration procedure and the orange line illustrates the calibration calculated with our new implementation of the algorithm. The bottom plot displays the ratio of the calibration constants shown above.

drum flash, first the pedestal of the captured trace is subtracted. Then, as a second step, the total signal S_{pixel} is estimated as the sum of all positive values of the entire trace. With this technique any after-pulsing or undershoots are ignored.

We independently implemented this procedure and then analyzed a large fraction of the dataset of the 2010 drum-calibration campaign containing measurements at all standard FD telescopes except for LM6. We did not analyze the drum measurements performed at HEAT. We present the results in Fig. 3.12, which shows the obtained absolute calibration constants (this analysis) together with the values estimated by the standard drum analysis [43]. In the bottom plot of Fig. 3.12 we show the ratio between these two results. We observe an almost constant difference on the order of ~2% between this analysis and the standard values for all telescopes of LM and CO and telescope six of LA. However for the remaining telescopes of LA and all telescopes of LL we find a ratio smaller than ~2%. We attribute this offset to an unknown (at the time of writing) correction applied in the standard analysis.

In conclusion, we are able to reproduce the absolute calibration constants delivered by the standard drum analysis for the 2010 measurement campaign to a level of 2%.

3.4.2. RELATIVE CALIBRATION SYSTEM

Since the absolute calibration of the FD telescopes with either the drum (large-diameter light source, Section 3.4.1) or the XY-Scanner (Section 4.2) is a rather time and workforce consuming procedure, it is not feasible to perform the absolute calibration of each telescope during every measuring night. To overcome this, a relative calibration of the telescope camera is performed during these nights. We use this relative calibration to propagate the latest absolute calibration
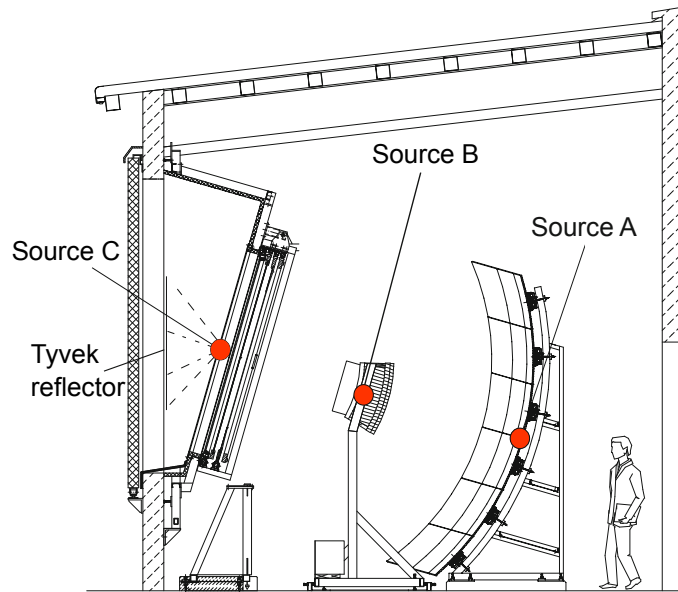
Figure 3.13: Drawing of the locations of the three light sources of the relative calibration system of an FD telescope. Drawing adapted from Ref. [10].

constants through time. In the following we introduce and describe this relative calibration system.

The relative calibration system of each FD telescope of the Pierre Auger Observatory consists of several light sources installed at three different locations within the telescope. First, the calibration source A (short: Cal A) is located at the center of the telescope mirror and points directly towards the telescope camera. It is used to track only changes of each PMT within the camera and is blind to any influence of other components within the telescope. The second source, calibration B (Cal B), is actually made out of two sources which are placed on both the left and right edge of the camera and are pointing towards the mirror. In addition to Cal A, this setup enables us to track the condition of the mirror e.g. the change of its reflectivity due to dust accumulation on its surface. The remaining calibration source (Cal C) is mounted in the aperture box in front of the filter. It again consists of two sources, located left and right of the aperture opening. These light sources illuminate two ~60 cm × ~60 cm Tyvek sheets which are attached to the backside of the telescope shutter. With this relative calibration system, changes in almost all components of the telescope can be tracked, starting with the filter, corrector lens, and ending with the PMTs of the camera. The mounting points of the three parts of the relative calibration system are indicated in drawing in Fig. 3.13.

Since the operation of Cal B and Cal C was terminated by the end of 2019, these sources of the relative calibration system are not discussed any further and we focus the following section on Cal A.

Calibration System A. The actual light source of the Cal A system is a (365 ± 5) nm UV LED NCSU033B from Nichia [49], which is located in a dedicated calibration room. See Fig. 2.9 for the ground plan of an FD telescope building. In the past we used super bright LED arrays of the type Luxeon Star V from Lumiled with a wavelength of (470 ± 25) nm [49], but they were replaced between December 2011 and January 2012 (depending on the telescope building) by the aforementioned LEDs. The Cal A light source is coupled to seven optical fibers, six of them guide the light to the six telescopes of one building, while the seventh fiber leads back to the LED Calibration Unit (LCU). The fiber ends are mounted in the center of each telescope mirror. The LCU does not only provide the power for the LED, but it also employs a photodiode which samples the LED signal through the seventh fiber for monitoring. Each FD building has one
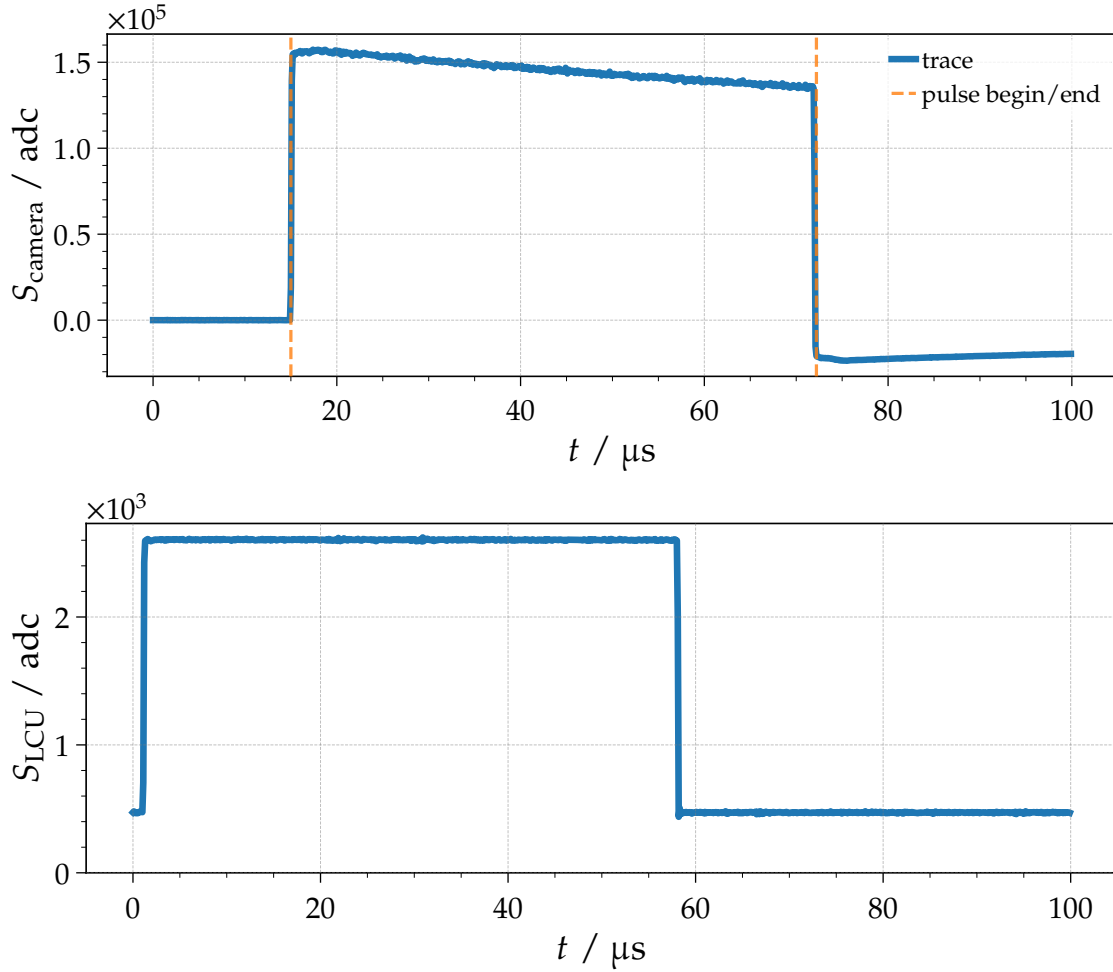
Figure 3.14: *Top:* Typical trace captured by the entire FD camera during a Cal A calibration run. We plot the summed trace of 440 pixel PMTs. *Bottom:* Typical trace digitized by the LCU.

single LCU, except for HEAT. The three telescopes of HEAT each have their own separate LCU. For more details on the LCU see e.g. Refs. [49, 50, 51].

During each FD data-taking night the standard Cal A procedure is executed. This procedure is performed immediately before the start of the observation measurements, alas while the shutters of the telescopes are still closed. At the end of the night and after the telescope shutters are closed again, another Cal A procedure is performed. The difference in the captured FD signal for Cal A with open or closed shutter is negligible, as we shortly discus in Appendix A.5.

During the Cal A operation 50 light flashes with a duration of ~57 μs are fired from the Cal A source at a frequency of ~0.3 Hz (0.5 Hz for HEAT). For each light pulse the readout of all telescope cameras within one building is triggered and the response of each individual PMT is digitized and stored. The signal trace captured by an entire telescope camera (bin-wise summed traces of 440 pixels) during a Cal A light flash is plotted in Fig. 3.14-top, for example for a measurement at the CO4 telescope. The bottom part of the Fig. 3.14 displays a typical trace captured by the photodiode inside the LCU coupled to the seventh fiber, as explained above. These traces together with additional information are then used to track the absolute calibration of each individual pixel throughout the time. We explain the tracking algorithm in the following.
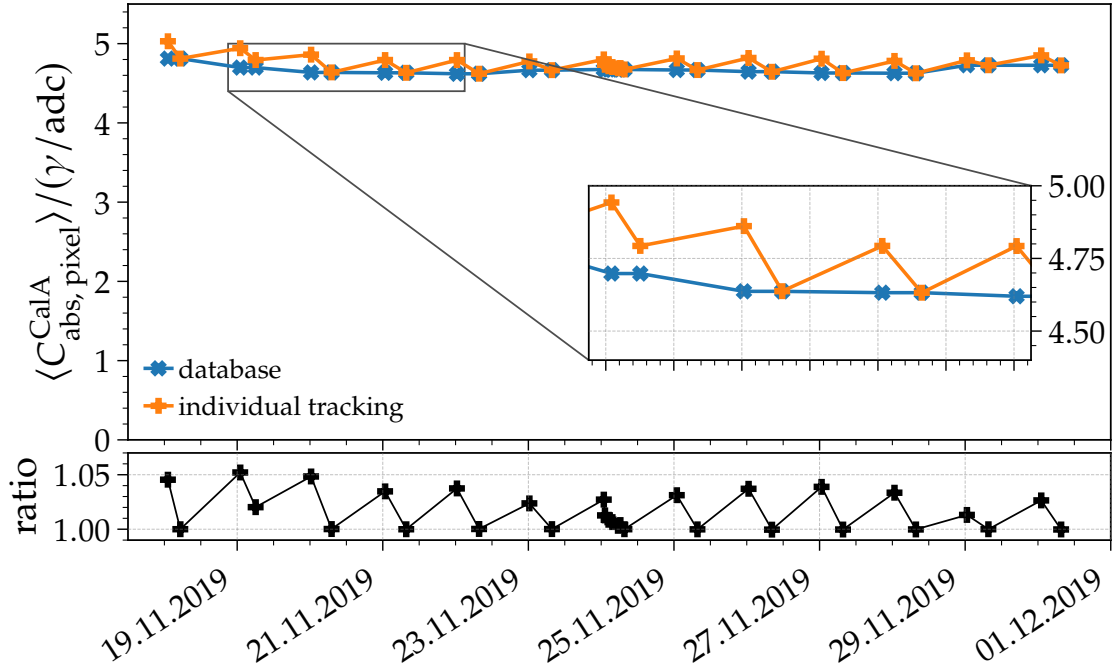
Figure 3.15: *Top:* Absolute calibration constants of telescope CO3 during the partial November 2019 data-taking shift. Each data point represents the camera average of one Cal A measurement. Plotted are the constants from the FD calibration database (blue) and the constants obtained via tracking every Cal A measurement individually (orange). *Bottom:* Ratio of the individually tracked calibration and the database values.

Tracking Absolute Calibration with Cal A System. In the following we introduce an algorithm for tracking of the absolute calibration constants via the relative calibration measurements of the Cal A system. First, we define the night during which the latest absolute calibration of the telescope was performed as the reference night n^*. This night also marks the starting point of the calibration tracking. During the reference night n^* and in very close temporal proximity to the absolute calibration an additional Cal A procedure is executed, usually right before and/or after the absolute calibration measurement is performed.

We define, according to e.g. Ref. [52], the absolute calibration C_{abs}^{CalA} tracked via Cal A to any night n as

$$C_{abs,pixel,n}^{CalA} = \frac{S_{LCU}^n}{S_{LCU}^{n^*}} c_{LCU}^{pixel} \frac{S_{FD,\,ADC}^{pixel,n^*}}{S_{FD,\,ADC}^{pixel,n}} c_{halo}^{pixel} C_{abs}^{pixel,n^*} \tag{3.18}$$

with the signal captured by each telescope pixel $S_{FD,\,ADC}^{pixel}$ and the signals collected by the LCU photodiode S_{LCU} during this night n and the reference night n^*. C_{abs}^{pixel,n^*} is the absolute calibration constant of each individual pixel obtained during the reference night. The factor c_{LCU}^{pixel} accounts for the change of the LED in the LCU as explained above, which only has to be applied if we want to track the absolute calibration across the LED change in the end of 2011. c_{halo}^{pixel} accounts for a correction for back-reflected photons between the pixel-PMT surfaces and the telescope mirror. We discuss the contribution of these reflections between in Section 4.4.5.

Even though several Cal A measurements are performed during a given night, usually only the latest measurement of every night is taken into account to track the absolute calibration constants of that night. On rare occasions, when for example the last Cal A of the night fails, another Cal A measurement enters the database. Nevertheless, we assume a constant calibration for each pixel

31

during the entire measuring night. The evaluated calibration constants for each telescope pixel and measuring night are stored in a database and requested for event reconstruction.

In Fig. 3.15 we plot the average absolute calibration constants of a typical telescope camera during the November 2019 shift. This Fig. 3.15 shows the calibration constants received from the database together with the constants obtained from individual tracking for every Cal A measurement, additionally their ratio is plotted in the bottom plot. The difference between calibration constants obtained from the database and from our implementation of the individual tracking is less than 0.5% for the Cal A measurements which are included in the database and on the order of ~3 to 5% otherwise. As mentioned above, typically only the last Cal A of a night is stored in the database. Since we analyze all Cal A measurements performed during this shift, we observe a saw-tooth-like behavior and only for roughly every second data point the database value and the individual tacking are in the agreement. From this observation we conclude that by implementing Eq. (3.18) we are able to reproduce the official calibration constants which are stored in the database.

Additionally, we can approximate the drift of the Cal A calibration during a data-taking night from this analysis. Comparing the difference between the individual tracking and the database for a Cal A performed at the begin of the night with the one taken at the end, we observe a drift roughly on the order of ~3 to 4% on average. For some nights the drift is on the order of up to 5%. These observations are compatible with former studies, which observed typical drifts of 1 to 3% [53] or 2 to 3% [54] in the response of the PMTs to the Cal A light pulses.

Chapter IV

The XY-Scanner

Contents

In the first part of the following chapter we introduce the mechanical system which is employed by the novel calibration technique – the XY-Scanner. We start by describing the individual components of the XY-Scanner stage. Then we explain the measurement procedure at the fluorescence telescopes. We close the first part of this chapter by giving an overview of the various installation and measurements campaigns performed so far. The second part of this chapter describes a variety of simulation studies we use to validate our understanding of the telescope setup and the measurement procedure.

4.1. XY-Scanner Stage

The aim of the novel calibration method, outlined throughout this thesis, is to drastically reduce the amount of work and person-power required to absolutely calibrate the FD telescopes of the Pierre Auger Observatory, but still deliver a reliable absolute end-to-end calibration of each telescope. In the past the absolute calibration was performed with a large-diameter light source as we describe in Section 3.4.1. Rather than using a very large light source covering the entire aperture of a telescope, we employ a portable light source of a much smaller physical size. The small size of the light sources (fitting into carry-on luggage) enables uncomplicated transport of the sources between (a) the different locations of the FD telescopes on the observatory site in Argentina and between (b) the optical laboratories on other continents to perform precise measurements of the source properties and characteristics. We introduce and discuss the employed light sources in
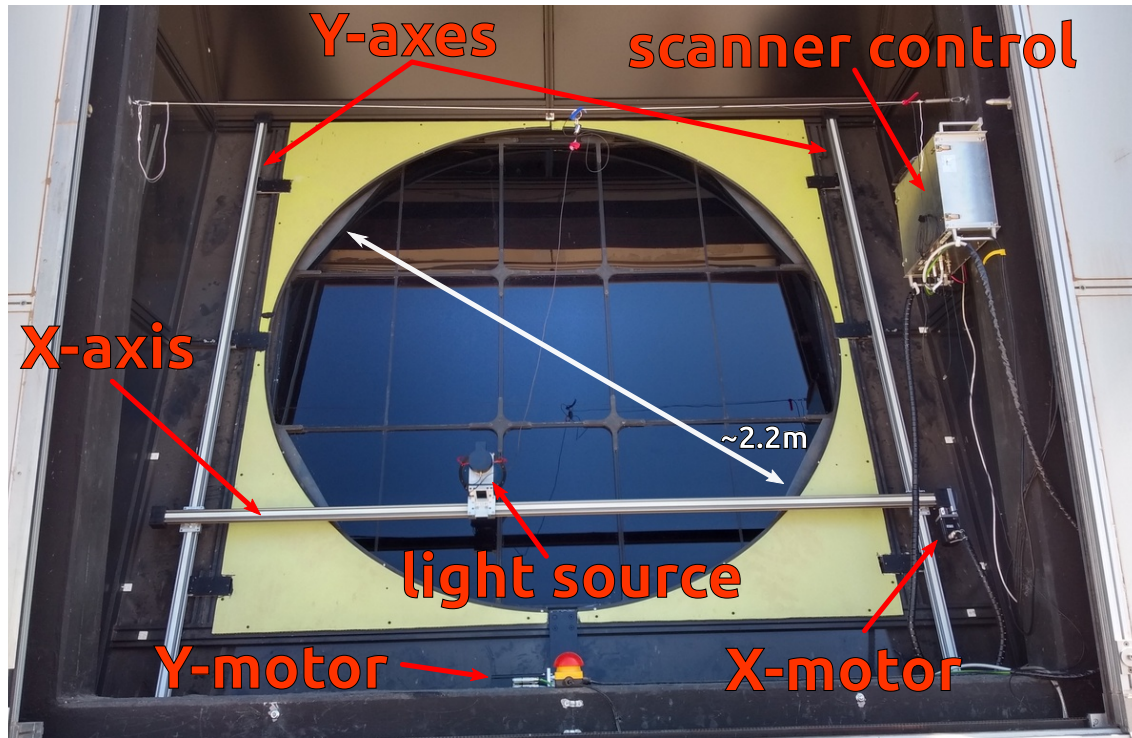
Figure 4.1: Photograph of a complete XY-Scanner system installed at a FD telescope. All crucial components are labeled within the photograph.

Chapter 6. As consequence of using a smaller light source, we cannot illuminate the entire aperture of the telescope at once. The emitting surface of the sources ($r_{src} \approx 2.54\,cm$) covers only ~0.05% of the aperture area ($r_{aperture} \approx 110\,cm$). We overcome this large difference in size by moving the light source across the telescope aperture window and thus mimicking the illumination of the entire aperture opening. The construction which carries and moves the light source in front of the telescope aperture is the *XY-Scanner*. In the following we introduce the hardware components and discuss the measurements procedure of the XY-Scanner.

The stage of a XY-Scanner system contains three motorized linear stages which are mounted outside the aperture window of each telescope. Two of them are mounted vertically on the left and right side of the aperture opening as Y-axes. These two linear stages are installed permanently at each telescope. To protect these axes from water, wind, and dust we cover them with a metal cover during times when no measurements with the XY-Scanner are performed, which is the case for most of the time. In Appendix A.2 we show the consequences of leaving the Y-axis uncovered and exposed to the environment. Distributed over several installation campaigns, we installed pairs of Y-axis permanently on all 27 FD telescopes of the Pierre Auger Observatory.

The third linear stage is mounted horizontally onto the sliding carriages of the two Y-axes. This horizontal linear stage builds the X-axis of the system. With this mechanical setup we are able to move the carriage of the X-axis to any position in front of the telescope aperture. We install the X-axis only for measurements with the XY-Scanner and otherwise this axis is stored inside the FD building. Fig. 4.1 shows a photograph of a complete, ready-to-measure installation of a XY-Scanner system. Although the photograph was taken during daytime, calibration measurements with the XY-Scanner are exclusively performed at nighttime. We usually perform the XY-Scanner measurements only during nights, which fulfill the data-taking requirements of the FD.

At each FD site there are two X-axes available which allows us the simultaneous preparation of two telescopes for calibration measurements. Nevertheless, for the three telescopes of HEAT only one X-axis exits. After the calibration measurements at one of these telescopes is finished

the only part we have to move to the next telescope is the light source. And while the calibration measurement proceeds on that second telescope, we can already mount the first X-axis onto another, third telescope. Thus, the time we need to calibrate a whole FD building with 6 telescopes is drastically reduced in contrast to the case when we would have only one X-axis available. With this procedure we are able to calibrate an entire FD site in one or two nights.

The hardware components of the linear stages are manufactured by the company *IGUS* [55], which is specialized in such motion products. All stages are of the type *drylin® linear guides*, which are designed to be maintenance-free and very insensitive to influences such as dirt, water, or heat [56]. These characteristics make the *drylin®* components an almost ideal fit for the rough environment of the Argentinian Pampa.

To evade the synchronous operation of two motors powering each of the Y-axes, we employ one single step motor to drive both axes simultaneously. This single step motor is located in the lower center of the aperture box and is mechanically connected to each Y-axis via a shaft. The X-axis is driven by a step motor which is directly mounted to its right end. Both motors are labeled in the photograph in Fig. 4.1. To minimize possible electromagnetic interference from the current flow within the motors, all motors are switched off once the light source reached its desired position. A brake system included in each motor holds the whole system in position until the measurement is completed. Both motors are equipped with encoders, which enables the system to automatically correct for missed or overdone steps. We estimate the relative accuracy of the positioning system as follows: one total rotation of the motor corresponds to a movement of 70 mm of the carriage on the axis. The step motor rotation is divided into 200 steps for a 360° rotation and we operate the motor in the quarter-step mode, thus one quarter step is equal to an axis movement of 0.0875 mm. Since the encoder counts the motor steps and the system corrects itself, we estimate the relative positioning precision of the XY-Scanner to $1/4$ step ≈ 0.0875 mm. This results in a relative position uncertainty of 0.15% for the typical distance between adjacent positions of 6 cm and below 0.1% for distance above 9 cm. Including a mechanical clearance of the order of 1 step ≈ 0.35 mm, we estimate the uncertainty on the distance between positions to be 0.7%.

The motors and encoders of all axes are controlled by the scanner control which is located in the aperture box (metal box on the right side of the photograph in Fig. 4.1). Inside the control box a Raspberry Pi single-board computer manages the steering of the scanner.

The scanner control also communicates with the light source to set up the flashing parameters and receive measured quantities of the source, like temperatures and the photodiode readout. More details in Chapter 6. Once the light source has reached its desired position, a trigger is sent to the source to emit a light flash and simultaneously to the telescope to readout the camera. After each flash the light source replies to the scanner control confirming the flash. If the scanner control does not receive any reply from the source after sending the trigger, we do not know whether the source flashed or not. A trigger to the telescopes is send either way and the camera is readout. If such an error occurs we have to stop this measurement and continue at the same (or some previous) light source position. We merge the data of such interrupted measurements offline after the data-taking is complete.

In the early campaigns the scanner control and the light source communicated via a special hosted WiFi network, but we observed a large number of connection losses between the latter two. In numbers: 9 out of 21 measurements performed in the autumn 2019 campaign had to be (partially) repeated due to a communication loss; in total we counted 39 communication errors. Therefore, we tested for the autumn 2022 campaign a wired communication system. For this purpose we installed an additional cable connecting the light source and the scanner control. With the wired communication solution we were able to reduce the number of failed measurements to 5 out of 33 and we observed only 8 communication losses for the entire campaign.

The actual reason for the communication loss is unknown. We performed several studies at a test XY-Scanner setup in a laboratory at KIT. This setup is assembled with the same components as the scanners at the telescopes. Even after performing extensive tests at this laboratory XY-Scanner, we never observed any communication loss neither with the wireless nor wired communication system. We thus cannot study the communication losses in our test setup.
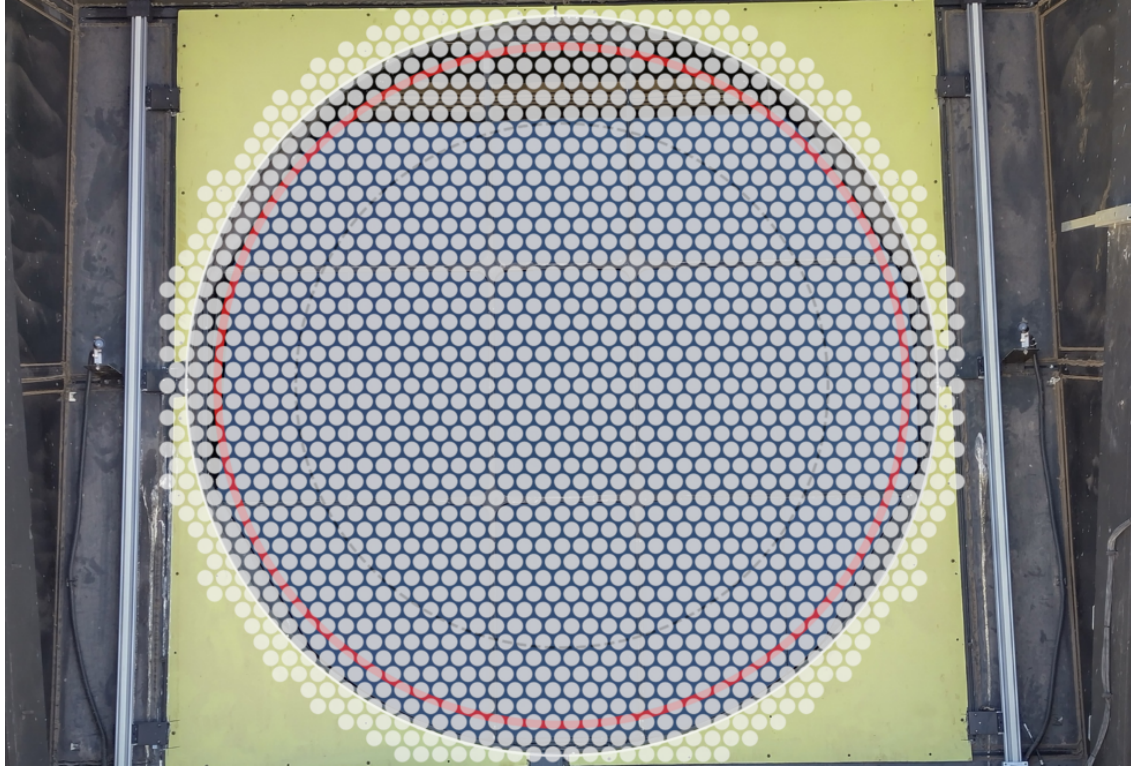
Figure 4.2: All positions of the light source (white dots) for a standard XY-Scanner calibration run. The background shows a photograph of the LL3 telescope. The edge of the aperture is drawn as a red circle.

However, at least for the autumn 2022 campaign, all communication losses occurred either at CO5, CO6, or at the HEAT telescopes. This may indicate a local problem. Note, CO5 and CO6 are the closest telescopes to HEAT. Nevertheless, a dedicated study on this issue was not possible during any of the past campaigns due to time constraints. We aim to address this problem in the future XY-Scanner campaigns.

4.2. CALIBRATION MEASUREMENT PROCEDURE

In the following we describe the standard measurement procedure of the FD telescope calibration employing the XY-Scanner. We perform calibration measurements for the FD telescopes only during night-time and during ordinary data-taking conditions. Similarly as for the standard data-taking procedure, we switch on the high voltages of the camera PMTs several hours before we start the actual measurements. Additionally to the standard relative calibration (Cal A) of the camera (see Section 3.4.2), at the begin and end of every measuring night, we execute the relative calibration procedure immediately before starting and after finishing an XY-Scanner measurements.

During the actual XY-Scanner calibration measurement the calibration light source is moved to numerous evenly distributed positions in front of the telescope aperture. Those positions are determined by a grid of equilateral triangles. Former simulation studies [57] concluded that the ideal side length of the triangular grid is 6 cm. In Fig. 4.2 all positions of a XY-Scanner run are shown as an overlay of a photograph of the LL3 telescope. The red circle in Fig. 4.2 marks the radius of the aperture opening.

Since not all telescope bays are constructed identically (some are prototypes or constructed
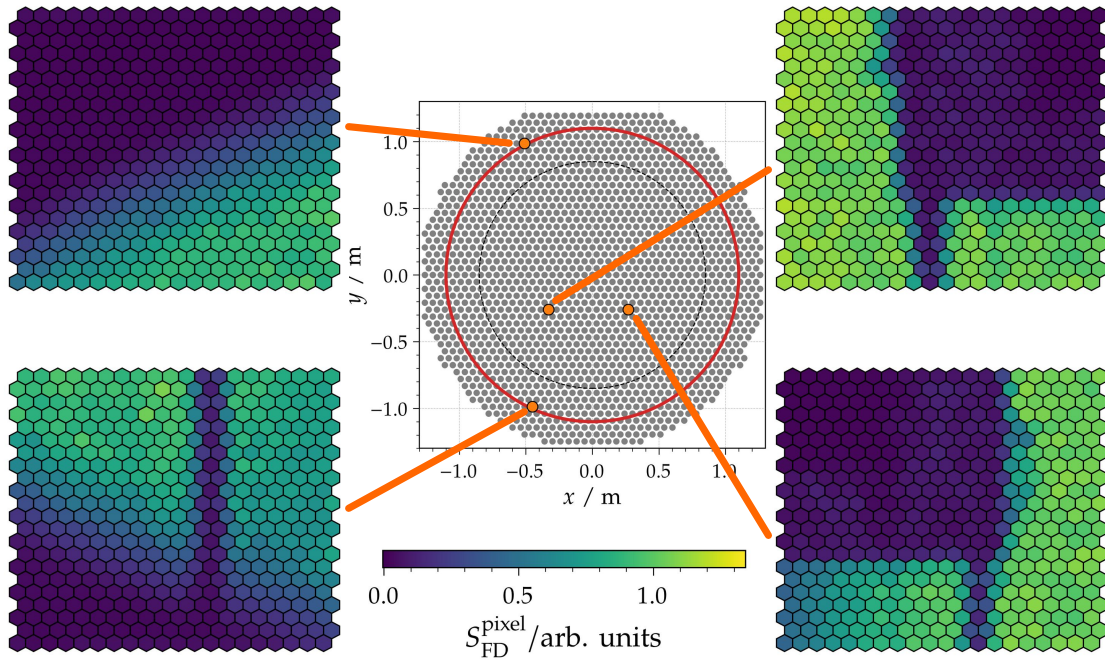
Figure 4.3: Typical events captured by the telescope camera for different positions of the light source. Each rectangle represents the 440 hexagonal pixels of the camera, the location of the source for each event is marked by the orange line.

and designed by different groups within the collaboration) the maximal and minimal height (y direction) the scanner can reach is slightly different for each telescope. This is especially the case for the HEAT since these telescopes are build with a completely different design. Additionally, in the prototype phase of the XY-Scanner we tested several designs of the carrying structure for the light sources which also gave, due to their dimensions, limits on the maximal reachable height. This results in a different total number of scan positions regarding the telescope and/or light source model. But irrespective of the telescope, the scanning grid of the XY-Scanner always covers the entire aperture.

For a standard XY-Scanner calibration run using the triangular grid with a step size of $\Delta s =$ 6 cm the light source travels through ~1700 positions. At each of these positions the light source emits a 5 µs long light flash and a trigger is sent to the telescope to capture and read out all pixel-PMTs of the camera. Each of the data-takings for such runs takes approximately 45 min to complete, while the telescope needs ~1 s to read out and store the signal traces of all pixel-PMTs. The time demand of one calibration measurement is larger, since we additionally need some time to install the X-axis, the scanner control box, and the light source. We could decrease the measuring time by increasing the step size and thus lowering the number of positions. However, this leads to an increased statistical uncertainty as discussed in Section 7.1.4.

4.2.1. Typical XY-Scanner Events

In Fig. 4.3 we illustrate a selection of typical XY-Scanner events captured at different positions of the light source in front of the telescope aperture. Depending on the light-source position, different features of the telescope become visible in the camera readout. We walk through the different features in the following.

The top-left event is captured while the light source is positioned at the upper edge of the telescope aperture. In the readout of the camera we observe a shadow in the top-left corner of the camera, which extents over more than half of the camera pixels. This shadow is cast by a
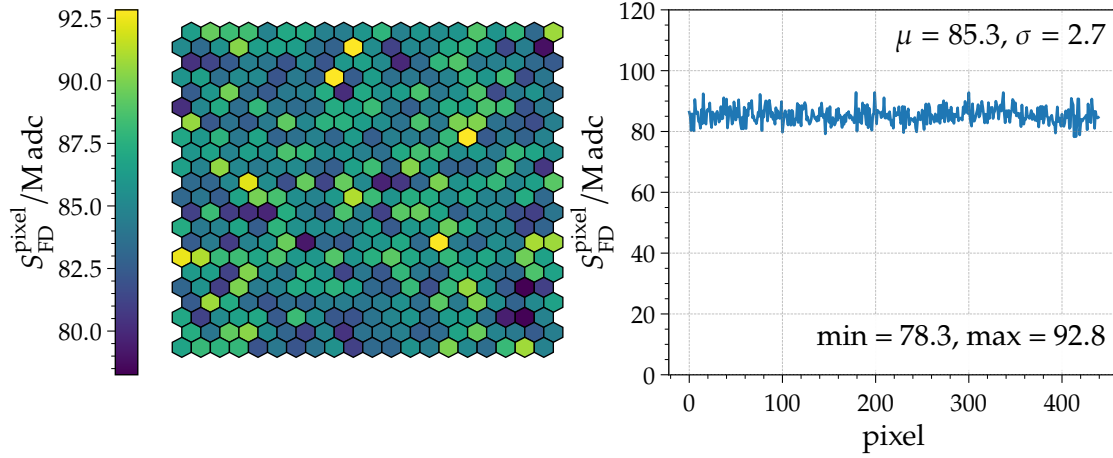
Figure 4.4: Signals captured by each pixel of the telescope camera for a complete XY-Scanner measurement. *Left:* Pixel matrix. *Right:* Signal plot as a function of the pixel number.

diaphragm surrounding the aperture opening of each telescope.

In the event below (bottom left) the edge of the aperture is again visible in the lower-right corner of the camera. Additionally, a vertical dark line appears, covering 1 to 2 pixels in horizontal direction. This dark line is a shadow cast by the left leg of the support structure carrying the telescope camera.

The two events on the right side of Fig. 4.3 are taken with the light source position in the same horizontal row of the scanning grid, but left and right (not symmetrical) of the central position. In both events we see a rectangular shape of darker pixels and a vertical darker line. These are again shadows cast by the camera itself and legs of its support structure. In addition we observe a bulge on the left and right edge of the camera shadow. The reasons for this are the light sources of the Cal B system. As we explain in Section 3.4.2, the Cal B consists of two sources mounted left and right of the camera body.

In the lower-right event we observe an additional darkening in the left part of the camera below the camera shadow. This is a consequence of the light source being partially obscured by a vertical bar of the filter support structure of the telescope. In fact we can use the XY-Scanner measurements to obtain the relative locations of that support structure as we point out in Section 5.5.

Additionally, we observe for the events on the left side of Fig. 4.3 on average a reduced pixel signal in comparison to the events on the right. The corrector lens installed on the outer rim of the telescope aperture adds additional absorbing layer resulting in a reduced number of photons reaching the camera for the positions of the light source behind this lens.

We estimate the signal in each individual pixel-PMT for a complete XY-Scanner measurement run as the sum over events of different light-source positions. In Fig. 4.4 we show the signals captured during such a complete measurement. We give a detailed description on the analysis of the XY-Scanner measurements in Chapter 7.

4.2.2. XY-SCANNER MONITORING TOOL

For the graphical illustration of the progress of a XY-Scanner calibration measurement at a telescope we developed a small monitoring tool. This tool is mainly used to follow the scanner movements from the inside of the FD building and to check the stability of the light source in real time. Therefore, the tool displays the temperatures of various components of the source, the signal captured by the internal photodiode of the source, and the position of the light source on
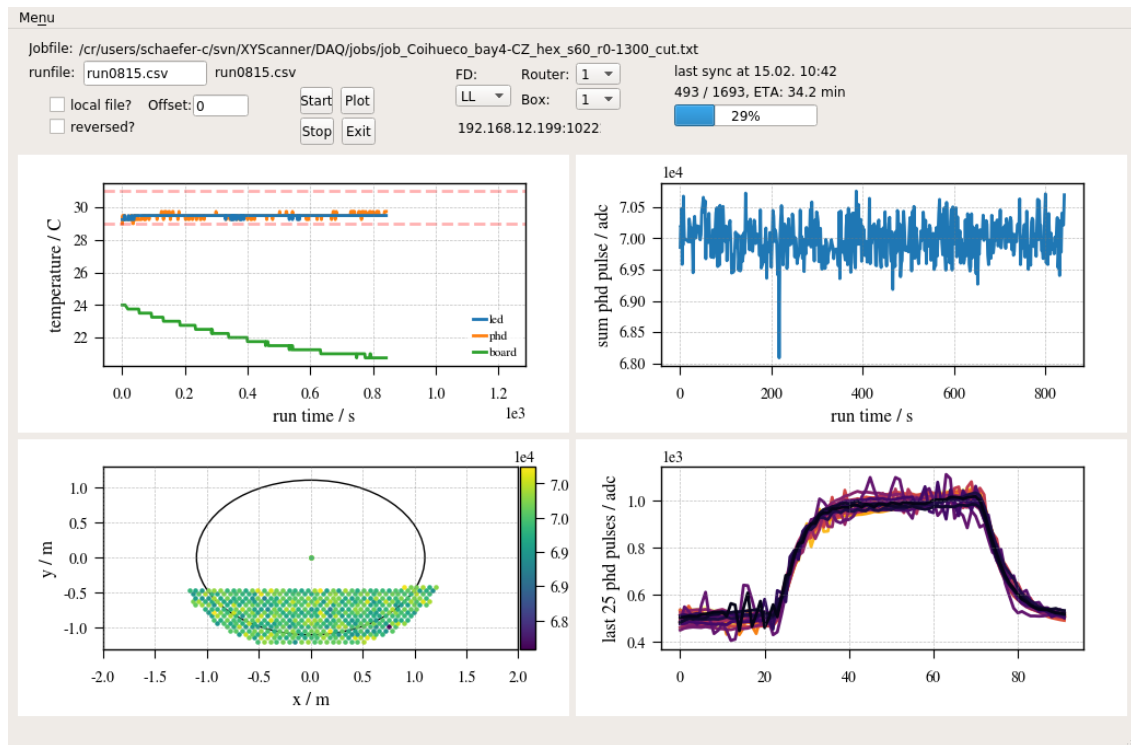
Figure 4.5: A graphical tool to monitor the status of the XY-Scanner during calibration runs in real time. The plots in the monitoring tool show the temperature of the LED, photodiode (PHD), and electronics board of the source *(top left)*. *Top right:* Integral readout of the PHD signal over the run time. *Bottom right:* Pulse shapes of the last 25 pulses recorded by the PHD. *Bottom left:* Position of the XY-Scanner in front of the aperture.

the scanner. We show a screenshot of the XY-Scanner monitoring tool in Fig. 4.5.

So far, this tool only supports the wireless communication between the scanner control and the light source. We plan to include the wired communication in the future updates.

4.3. Measurement and Instrumentation Campaigns

Below we give a timeline of the measurement and instrumentation campaigns, which were performed with the XY-Scanner so far.

Spring 2018 The first prototype of the scanner was installed at the bays CO4 and LL4. The main lesson from this campaign was that the installed prototype scanner was not large enough. More details are given in Ref. [57].

Autumn 2018 The measurements with the smaller scanner at CO4 were repeated to check and confirm the stability of the measurement on a larger timescale and improved scanners were installed at CO3 and HE1. The main improvement was the increased size of the horizontal axes. More details are given in Ref. [57].

Spring 2019 XY-Scanner systems were installed at the telescopes LA3, LL3, LL4, HE2, and HE3. Another scanner at LA4 was partly installed, but was not ready for operation at the end of that campaign. Calibration measurements were performed at seven telescopes: LL3, LL4, CO3, CO4,

HE1, HE2, and HE3. The filter and the mirror of LL4 were cleaned in order to check the influence of the accumulated dust on the mirror.

Autumn 2019 The scanner at LA4 was completed and one new scanner was installed at CO5. Calibration measurements were performed at ten telescopes: LL3, LL4, LA3, LA4, CO3, CO4, CO5, HE1, HE2, and HE3. First collimated beam (see Section 5.6) test measurements were performed at LL3, LL4, and CO5.

Spring 2020 Systems were partly installed at CO1, CO2, and CO6, but the work could not be finished, since we had to leave Malargüe rather fast due to strict travel restrictions against the global COVID-19 pandemic. Neither calibration nor collimated beam measurements could be performed during this campaign.

Autumn 2020 No campaigns possible due to the ongoing pandemic.

Spring 2021 No campaigns possible due to the ongoing pandemic.

Autumn 2021 No campaigns possible due to the ongoing pandemic.

Spring 2022 No campaigns possible due to the ongoing pandemic.

Autumn 2022 Nine new systems were installed, the complete FD site of LM (six telescopes) and three at CO (telescope 1, 2, and 6). Calibration measurements at 11 telescopes were performed. These measured telescopes were LL3, LL4, LA3, LA4, CO3, CO4, CO5, CO6, HE1, HE2, and HE3. No collimated beam measurements were performed.

Spring 2023 Remaining eight XY-Scanner systems were installed at the telescopes 1, 2, 5, 6 of the LL and LA sites. No measurements were performed during this campaign.

4.4. XY-SCANNER SIMULATION

For a detailed understanding and validation of the measurements we perform at the FD telescopes on site, we simulate the XY-Scanner measurements within the $\overline{\text{Off}\underline{\text{line}}}$ software framework [58] of the Pierre Auger collaboration. The modular design of the $\overline{\text{Off}\underline{\text{line}}}$ framework allows us the straightforward implementation of a module which is simulating the injection of photons from the XY-Scanner light sources into the telescopes. The module is called `XYScannerPhotonGenerator`. The `XYScannerPhotonGenerator` module is designed in a versatile way so that the module is able to simulate a variety of light-source geometries and emission patterns. Especially, we are able, in addition to the standard XY-Scanner calibration light sources, to effortlessly simulate the drum (discussed in Section 3.4.1) or collimated-beam light sources (introduced in Section 5.6) within the same `XYScannerPhotonGenerator` module.

For the standard FD telescope simulation, the trajectories of photons through the telescope are determined by the `TelescopeSimulatorKG` module via ray tracing. This module is aimed to deliver a fast simulation of air shower events, therefore the individual optical components of the telescopes are implemented in a rather rudimentary way and multiple reflections of photons inside the telescope are ignored. Another very detailed telescope simulator module, called `TelescopeSimulatorLX`, is based on Geant4 [59], but due software version incompatibilities this module cannot be complied with recent $\overline{\text{Off}\underline{\text{line}}}$ versions. To get a more realistic tracing of photons through the telescopes, the `TelescopeSimulatorKG` was further developed and improved under the name `TelescopeSimulatorKG_DEV` [60]. This simulator module is able to handle multiple
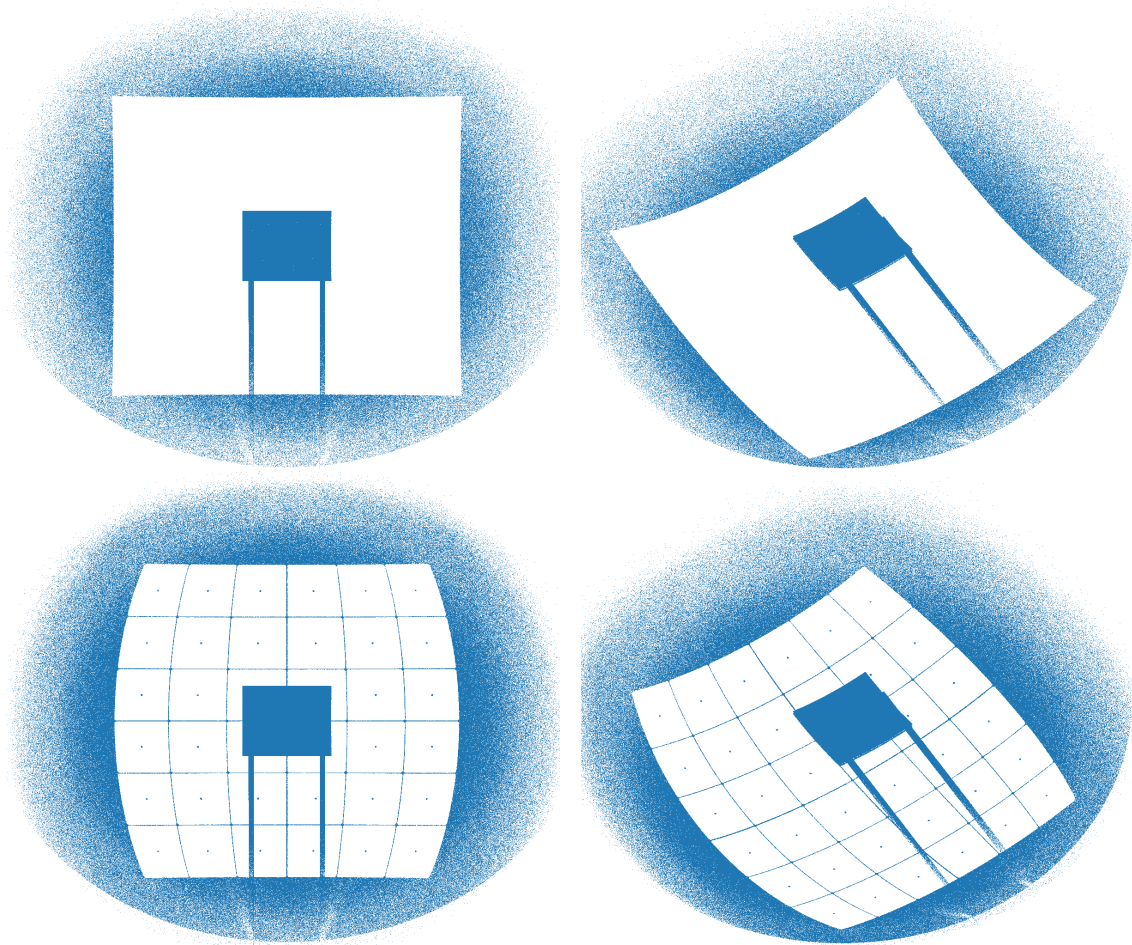
Figure 4.6: Illustrations of the different implementations of the mirror in the `TelescopeSimulator` modules. Each blue dot represents a simulated photon which gets absorbed by either the mirror or the camera. Thus, the images show the "shadow" of the two components. *Top row:* `TelescopeSimulatorKG_DEV`. The mirror is implemented as a simple cut of a sphere at longitude and latitude of 33.07°. *Bottom row:* `TelescopeSimulatorKG2` featuring detailed implementations of each mirror segment, including the gaps between the elements.

reflections of photons inside the telescope and the individual components are implemented in a much more detailed manor than for the `TelescopeSimulatorKG` module.

This development version (`TelescopeSimulatorKG_DEV`) of the telescope simulator is not part of the official $\overline{\text{Off}}\underline{\text{line}}$ repository. We further improved this module, as described in Section 4.4.1, and included it into the official $\overline{\text{Off}}\underline{\text{line}}$ repository as the `TelescopeSimulatorKG2` module.

4.4.1. Updates and Improvements to Telescope-Simulator Module

In the following we introduce the new features for the photon raytracing we implemented in the `TelescopeSimulatorKG2` module.

First, the telescope camera and its support structure were only implemented as a two-dimensional objects and thus the shadow of the camera (and the camera support structure) was not simulated correctly. We updated the geometry of the camera and the camera support and implemented these as three-dimensional objects.

In addition, we rotated the corrector lens by 7.5° around the optical axis of the telescope, so that the positions of the gaps between the individual lens elements match in reality and simulation.

As another larger improvement we include the gaps between the individual mirror segments. Therefore, we implemented the actual size and geometrical shape of each mirror segment. Up to now only the rectangular mirror segments are implemented, the hexagonal shaped segments of the Czech design are not yet included in the module. Therefore, the size of the total simulated mirror matches closer the size of a real mirror, while before (in the `TelescopeSimulatorKG_DEV` module) the mirror was implemented as simple angular cut of a sphere and thus overestimating the actual size of the total mirror. However, for the `TelescopeSimulatorKG` module the mirror is implemented as an entire sphere. The difference between the two implementations of the mirrors are illustrated in Fig. 4.6. Herein the location, where a photon is either not reflected by the mirror or absorbed by the camera or its support structure, is marked as a blue point. For the novel detailed implementation, the rectangular mirror segments and the mounting hole in the center of each mirror element appears in the bottom plots of Fig. 4.6, giving a more realistic image of the mirror.

4.4.2. Validation of XY-Scanner Simulation

To validate the simulation of the XY-Scanner measurements, we compare the simulated measurements with the real data from measurements performed at the FD telescopes. Therefore, we select a dataset containing XY-Scanner measurements with two different step sizes, namely 6 cm and 10 cm. These measurements were performed at the CO3 telescope in October 2022 employing the KIT integrating-sphere light source. A discussion of the XY-Scanner light sources is given in Chapter 6.

The top row of Fig. 4.7 presents the pixel-signal ratio between real XY-Scanner measurements with step sizes of 6 cm and 10 cm but with the identical light source. Since the two XY-Scanner measurements were performed within the duration of a few hours, we neglect any changes in the sensitivity of the pixel-PMTs between the two data-taking runs. In this measurement, we observe an average signal ratio per pixel of $\mu_{\mathrm{data}} \approx 2.75$ with a standard derivation of $\sigma_{\mathrm{data}} \approx 0.02$. This result is in an agreement with the purely geometrical expectation for the ratio given the two step sizes, $(10\,\mathrm{cm})^2/(6\,\mathrm{cm})^2 \approx 2.778$.

We simulated the equivalent geometry within $\overline{\mathrm{Off}\underline{\mathrm{line}}}$ using the above introduced `XYScanner-PhotonGenerator` and `TelescopeSimulatorKG2`. We show the results of the simulation in the central row of Fig. 4.7. Again, the plots show the pixel-signal ratio between 6 cm and 10 cm simulated XY-Scanner measurements. We observe a similar pattern in data and simulation, a brighter spot in the center of the camera surrounded by four darker spots. However, in the real measurement we notice a slightly larger signal ratio (~1 %) in the top and bottom pixel rows of the camera.

We validate the implementation of the entire XY-Scanner simulation chain by comparing the signal ratios between the two measurements of different step size for real FD measurements and simulations. We plot this absolute difference per pixel in the bottom row of Fig. 4.7. The average difference between the FD measurements and simulations of all pixels is compatible with zero and the maximal derivation for a pixel is on the order of 0.07. For the majority of pixels we observe a difference between measurement and simulation of less than 0.5%.

Therefore, we conclude that the implementations of the XY-Scanner photon generator (`XYScanner-PhotonGenerator`) and the FD telescope simulator (`TelescopeSimulatorKG2`) describe well the injection of the photons from the XY-Scanner into the telescope and describe the geometry of a real telescope in a sufficient way.

4.4.3. Simulation of Emission of Integrating-Sphere Source

We introduce the XY-Scanner calibration light sources in Chapter 6 and we describe the measurement of their emission profiles in Section 6.5. We used these measurements to implement a linear interpolation between the measured directional emission of each light source into the
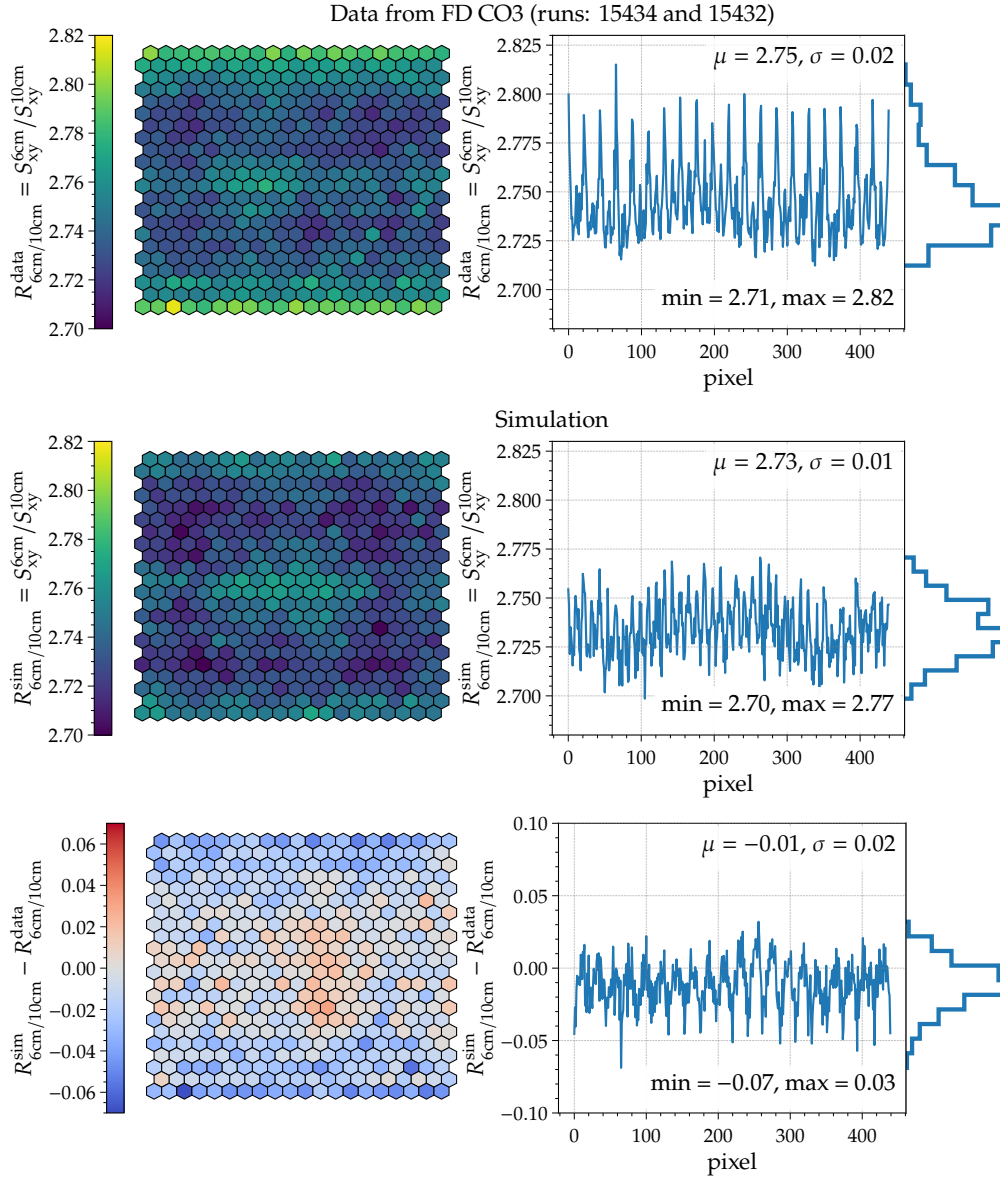
Figure 4.7: Validation of the XY-Scanner simulation chain. *Top:* Ratio of the pixel signals for XY-Scanner measurements with different step sizes at a real FD telescope. Left as pixel matrix and on the right as plot over pixel indices. *Center:* Similarly as the top plots, but the plots present simulated measurements. *Bottom:* Difference between the pixel-signal ratios obtained with simulation and from real measurements.

`XYScannerPhotonGenerator` module. For each generated photon this module adjusts the weight of the photon according to the measured emission. So far we implemented the emission for both integrating-sphere light sources (the KIT and the Olomouc sphere).

We validate this simulation by comparison with real XY-Scanner measurements performed at the FD telescopes on site. In Fig. 4.8-top we show the pixel-signal ratio between two XY-Scanner measurements performed at the same telescopes with the different light sources. These two measurements were performed during the same night with a ~1.5 h time interval between. In the center row of Fig. 4.8 we plot the results obtained via simulations of XY-Scanner measurements with the two light sources. For this simulations we used the `XYScannerPhotonGenerator` and the
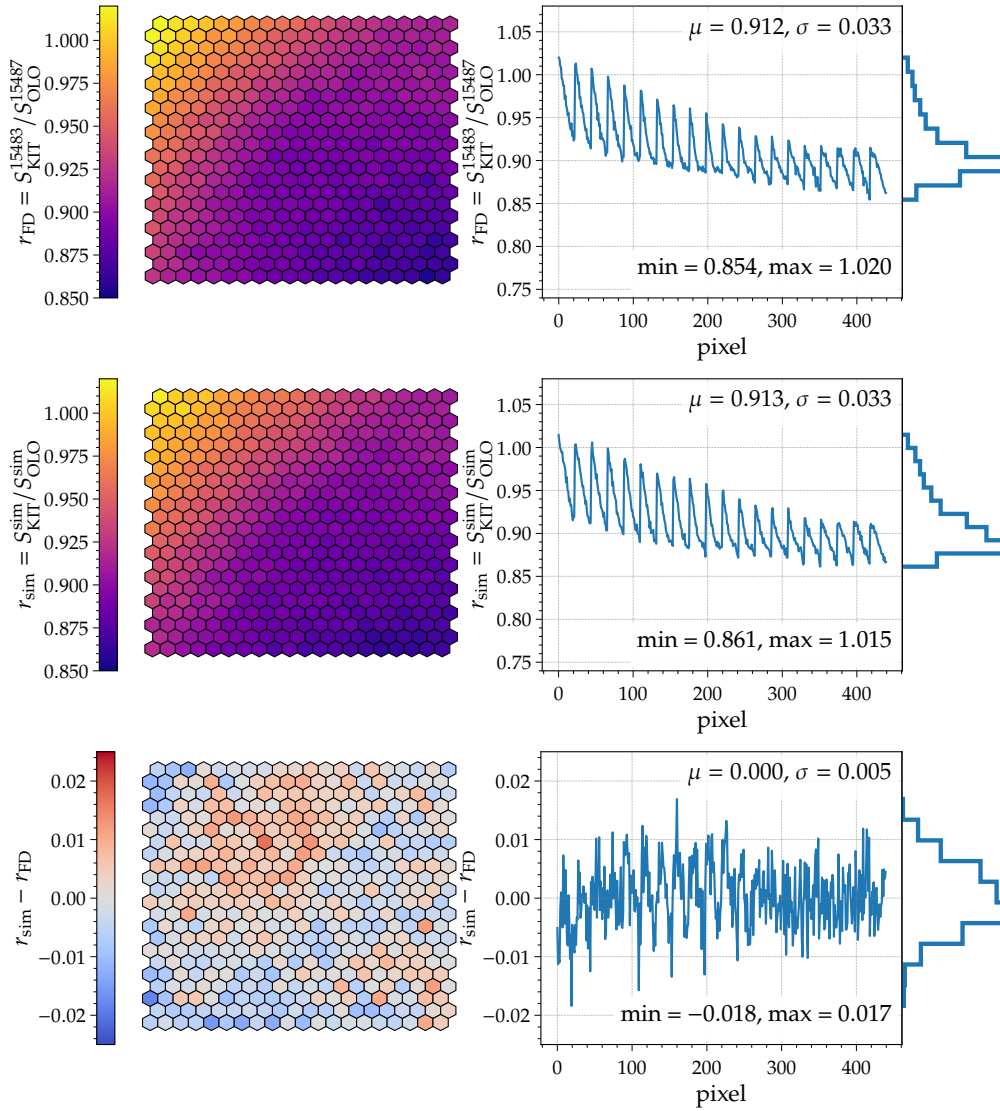
Figure 4.8: Validation of the implementation of the emission profiles for the integrating-sphere light sources. *Top:* Pixel-signal ratio between real measurements taken with the KIT and Olomouc (OLO) spheres at the CO3 telescope in October 2022. Left as pixel matrix and on the right as plot over pixel indices, the distribution of the data is attached to the right of the plot. *Center:* Similarly to the plots in the two row, but the simulated signal ratio is plotted. *Bottom:* Difference between the pixel-signal ratios obtained with simulation and from real measurements.

`TelescopeSimulatorKG2` modules. In both, the measured data and the simulation, we observe a diagonal gradient spanning the entire FD camera. This gradient is caused by the different emission profiles of the two sources, as we discuss in Section 6.5. The bottom row of Fig. 4.8 presents the absolute difference between the measured and simulated pixel-signal ratios.

We observe a maximal difference between the measured and simulated pixel-signal ratios of less than 2%, while the average difference is compatible with zero and most pixels show a difference of less than 1%.

We showed that the simulation of the XY-Scanner including the different light-source emission profiles are in agreement with the signal ratio measured at the FD telescopes.
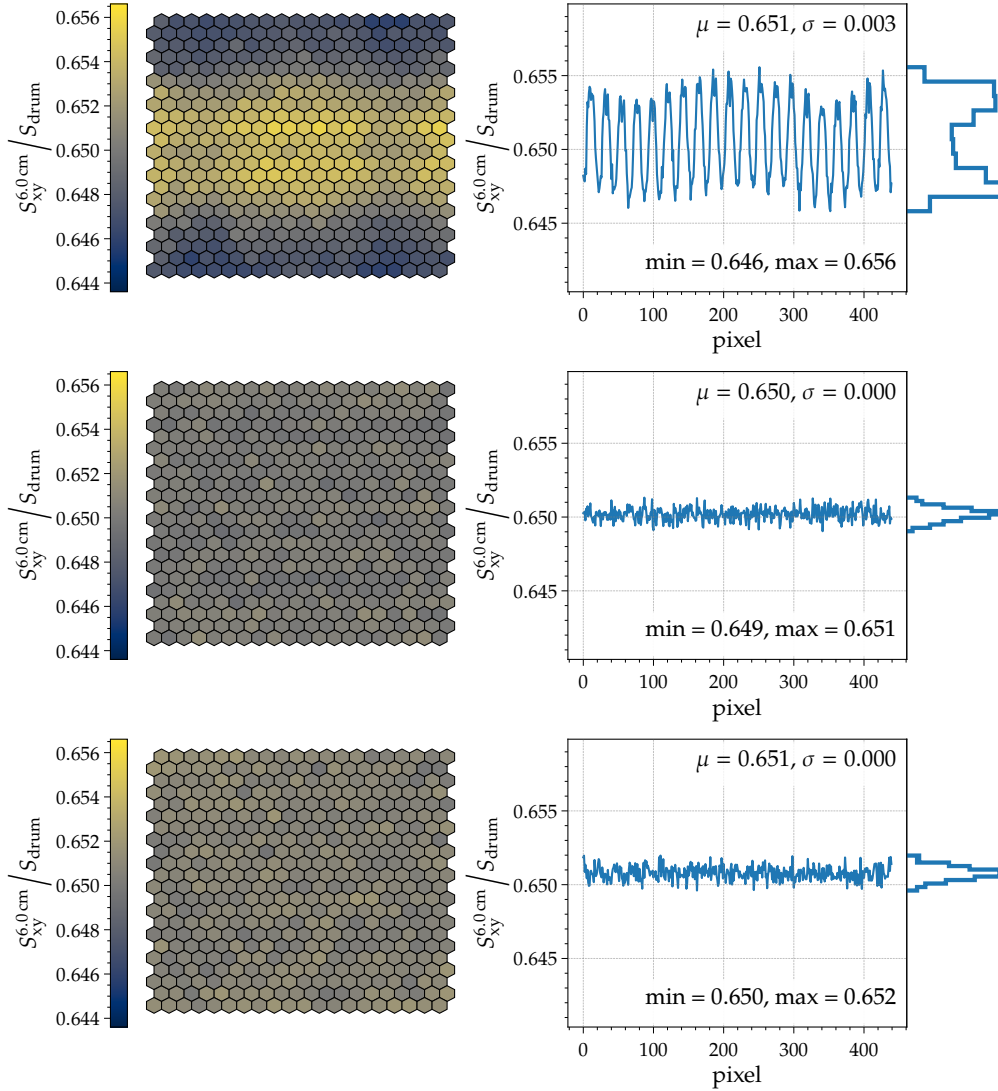
Figure 4.9: Simulation of the coverage factor. Shown is the ratio between XY-Scanner and drum simulations. Left as pixel matrix and right as a plots over the pixel indices. The distribution of the data is attached to the right plot. *Top:* Standard simulation. *Center:* Filter support structure is not simulated. *Bottom:* XY-Scanner grid rotated by 15° around the optical axis of the telescope.

4.4.4. Verification of Coverage Factor

For the estimation of the absolute calibration of the FD telescopes, as we describe in Section 7.4, we make use of a coverage factor f_{cov}, Eq. (7.18), to account for the partial illumination of the telescope aperture during the XY-Scanner calibration measurements.

The standard measurements presented within this thesis were performed with an integrating-sphere light source and a scanner step size $\Delta s = 6\,\text{cm}$. The exit ports of both integrating spheres are 2 inch (~5.08 cm) in diameter. Therefore, we calculate the coverage factor for such a standard XY-Scanner measurement to be

$$f_{\text{cov}} = \frac{A_{\text{src}}}{\Delta s^2 \, \sin 60°} = 0.650 \tag{4.1}$$

with the area of the light-source exit port $A_{src} = \pi\,(2.54\,\mathrm{cm})^2$. An illustration of the coverage factor is presented in Fig. 7.18. This purely geometrical estimation of f_{cov} does not explicitly account for any light-source positions on the edge of the aperture where the exit port is partially obscured. Thus, we validate f_{cov} with simulations. We compare the simulated signal of XY-Scanner measurements with simulations of the drum, which by design uniformly illuminates the entire aperture. We present the results of this simulation study in the top row of Fig. 4.9. Herein we plot the ratio of simulated photons reaching each pixel of the telescope camera between photons injected from the XY-Scanner and the drum.

We observe an average ratio per pixel of $\mu = 0.650$ with a standard deviation of $\sigma = 0.003$, which is in agreement with the purely geometrical estimation of Eq. (4.1). Nevertheless, in the simulated signal ratio a brighter (larger ratio) horizontal band in the central region of the camera appears. The pixels contained in this central band show a ~2% larger ratio than the pixels on top and bottom of the camera. This higher ratio band is caused by the shadow cast by the filter-support structure of the telescope. The scanning grid is oriented in a way that the light source is driven through a horizontal rows of positions at the same y coordinate. See Fig. 4.2 for a illustration of the scanning grid positions. We decided for this orientation to minimize the number of movements in y direction. But such a grid makes the XY-Scanner measurements sensitive to the horizontal bars of the filter support-structure, as we point out in the following. At the y coordinate close to the location of the horizontal filter-support bars, roughly ~40 light-source positions are contained within a single horizontal scanning row, this corresponds to ~2% of the total number of scanning positions. If at this particular scanning row the light-source emission into certain directions is blocked by the support structure, certain pixels will receive significantly less photons than others. This effect could thus explain the reduced simulated ratio at the top and bottom of the camera.

To verify this assumption, we performed a similar simulation study as above, but we disabled the filter-support structure in the telescope simulator. All other parameters were unchanged. We show the results in the central part of Fig. 4.9. We observe a narrower distribution of the simulated ratio and the horizontal band vanishes. Thus, we conclude that the observed pattern in the simulated signal ratio is indeed an effect caused by the filter-support structure of the telescopes.

One possible solution to reduce the influence of the filter-support structure on XY-Scanner measurements is to rotate the entire scanning grid around the optical axis of the telescope. By rotating the entire grid, all straight horizontal rows disappear and we become less sensitive to the horizontal structures. To avoid getting sensitive to the vertical components of the filter support, we have to avoid generating straight vertical columns of light-source positions and thus the rotation angle must not be a multiple of $30°$.

We tested the hypothesis of a rotated scanning grid in another simulation study. For this study we rotated the entire XY-Scanner grid by $15°$ around the optical axis of the telescope. All other parameters of the simulation were kept as for the simulations described above. In Fig. 4.9-bottom we present again the signal ratios between the XY-Scanner and the drum simulation. We observe a homogeneous ratio over the whole camera with a average value of $\mu = 0.651$ and a standard deviation of $\sigma = 0.003$.

Due to time limitations for this thesis, we could not study the rotated scanner grid at a real FD telescope on site. We plan to perform such measurements in the foreseeable future. However, we do not expect to observe any difference in the real data since the noise of the camera is significantly larger than ~2%, see Fig. 4.4.

4.4.5. REFLECTIONS ON CAMERA SURFACE

Former simulation studies have shown [61], that the absolute calibration constants obtained via the drum method (see Section 3.4.1) are underestimated by ~2.5 to 4% [47] due to reflected photons on the surfaces of the PMTs of the telescope camera.

The specular reflectivity of the FD PMTs were in a dedicated laboratory setup [62] measured to be ~20%. This reflectivity includes not only the front glass surface of the PMTs but also additional internal structures of the PMT, most prominently the photocathode. Therefore, some
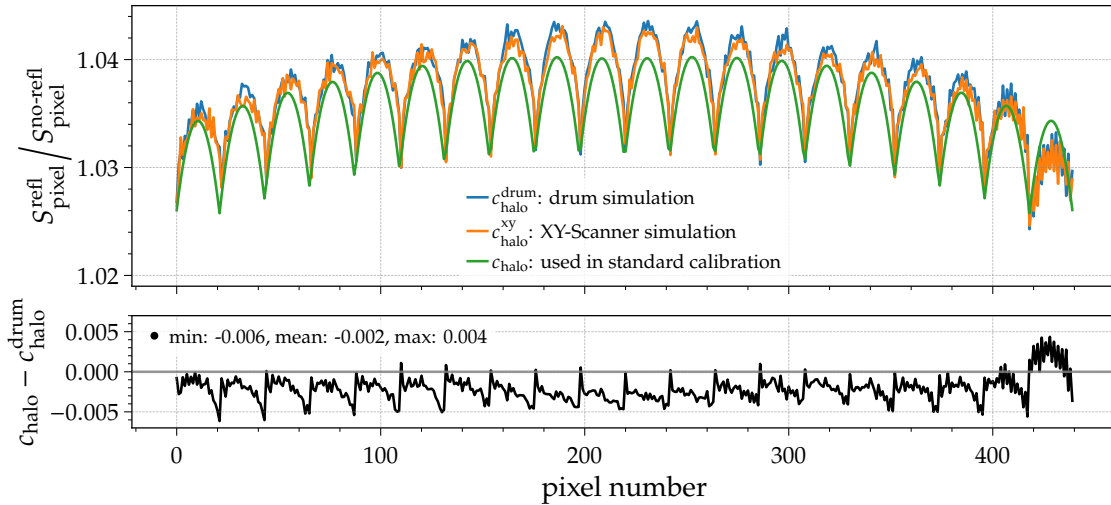
Figure 4.10: *Top:* Ratio of photons reaching a pixel between simulation studies with a reflecting or non-reflecting camera surface. Different colors depict different sources or methods. *Bottom:* Difference between these simulations and the currently used values for the calibration.

photons reaching the camera will get reflected on its surface and may travel back towards the telescope mirror. At the mirror these photons are again reflected and may make their way back to the camera where they most likely hit a different pixel-PMT. This situation is illustrated with the sketch in Fig. 4.11. We also present the first test measurements performed with a parallel collimated-beam source in Section 5.6.1, giving evidence to this situation.

This is a larger issue for calibration measurements than it is for air-shower data-taking. For the absolute calibration measurements we always capture and read out all pixels of the camera simultaneously. Therefore, all at the camera surface reflected photons that hit any other pixel do contribute to the total captured signal. However, for shower events only certain pixels close to the triggered pixel are read out and, therefore, photons in all other pixels do not contribute to the signal. We shortly explain the read out and trigger mechanism in Section 3.3.

The simulation study discussed in Ref. [61] used the `TelescopeSimulatorLX` to simulate photons through the telescope and to estimate a correction factor c_{halo} accounting for such reflected photons. In Fig. 4.10-top we show the values used in the standard drum analysis as green line. These values are not directly obtained from simulations, but calculated to match the simulated estimate by using a $\cos\theta$ expression with stretching and amplification factors, with the pixel viewing angle θ [47]. However, the actual formula is unknown to the author of this thesis. Due to historic reasons, this correction factor is not directly applied to the drum calibration, but rather incorporated within the relative Cal A tracking, see Eq. (3.18).

To validate these correction factors, we performed a dedicated simulation study using the `XYScannerPhotonGenerator` to generate and the `TelescopeSimulatorKG2` for ray-tracing photons in the telescope. We performed two simulation studies with different light sources. For the first study the photons were injected from the drum and, for the second study, from a integrating-sphere light source on the XY-Scanner. For both studies we simulated the number of photons reaching each pixel of the camera for (a) the reflectivity of the PMTs according to the measurements in Ref. [62] and for (b) non-reflecting PMT surfaces. For the second case a photon at the camera surface gets either detected or is removed from the ray tracer. While for the first case a photon can get reflected and is further propagated by the ray tracer. By building the ratio of detected
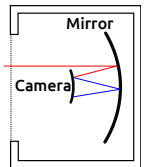
Figure 4.11: Reflections on the camera surface. Incoming (red) and reflected (blue) rays. Adapted from Ref. [63].
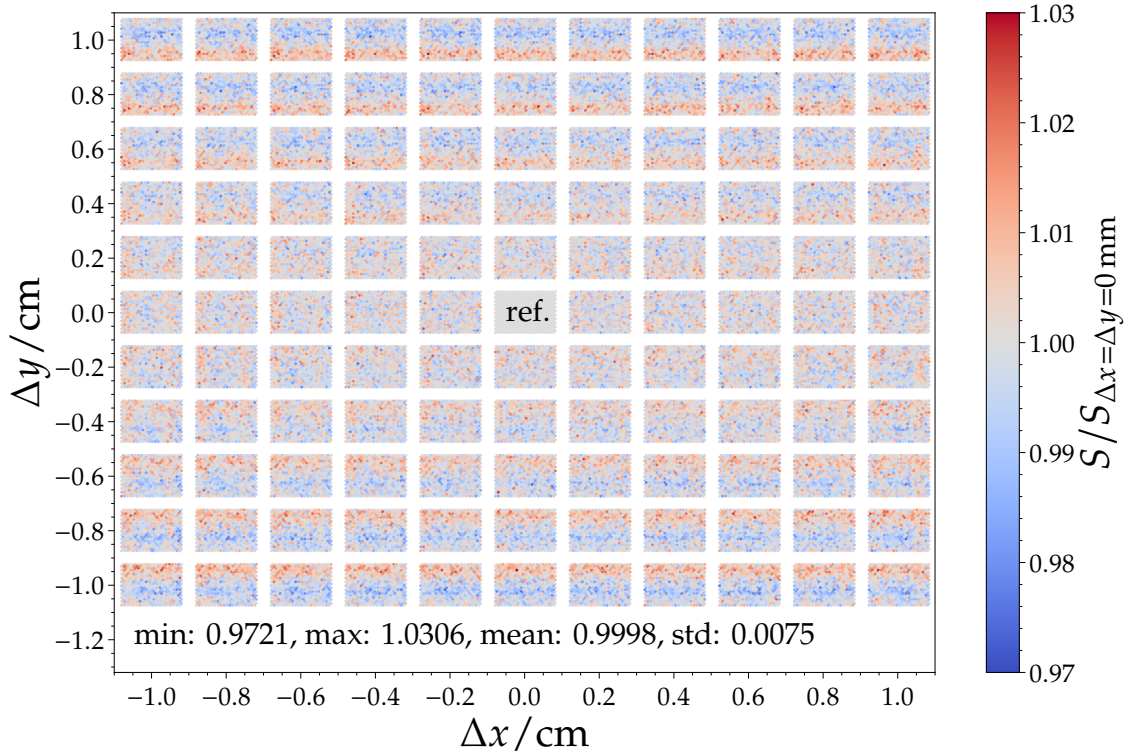
Figure 4.12: Influence of shifting the XY-Scanner positions in the plane parallel to the telescope filter. Plotted are the simulated pixel signal ratios (each rectangle represents the entire telescope camera) between shifted by $(\Delta x, \Delta y)$ scanner grids and the aligned one $(\Delta x = \Delta y = 0)$.

photons in each pixel between the scenarios (a) and (b) we directly obtain the correction factor as

$$c_{\text{halo}} = \frac{S_{\text{pixel}}^{\text{refl}}}{S_{\text{pixel}}^{\text{no-refl}}} \tag{4.2}$$

with the number of simulated photons reaching each pixel $S_{\text{pixel}}^{\text{refl}}$ and $S_{\text{pixel}}^{\text{no-refl}}$ for the scenario (a) and (b), respectively. We approximate the uncertainty on this estimate of the correction factor c_{halo} to be ~0.5% as the difference between measurement and simulation present in Section 4.4.2.

In Fig. 4.10-top we plot these ratios for the simulation of the drum $c_{\text{halo}}^{\text{drum}}$ and the XY-Scanner $c_{\text{halo}}^{\text{xy}}$. For both simulation studies, we observe the same saw-tooth trend of the ratio as in the estimate for the drum analysis. Nevertheless, the simulated ratio is slightly larger than the estimate for the drum analysis except for the last column of the camera. This effect is not yet understood. The studies for the drum and the XY-Scanner are in agreement and show a average difference of 0% with a maximum of 0.2%.

The bottom plot of Fig. 4.10 shows the absolute difference between the estimate for the drum analysis c_{halo} and the results of this simulation $c_{\text{halo}}^{\text{drum}}$ of the drum. We observe on average a difference of 0.2% (maximum 0.6%) between the estimate for the drum analysis and this simulation using the XYScannerPhotonGenerator and the TelescopeSimulatorKG2. Therefore, we conclude that both estimates are in good agreement.
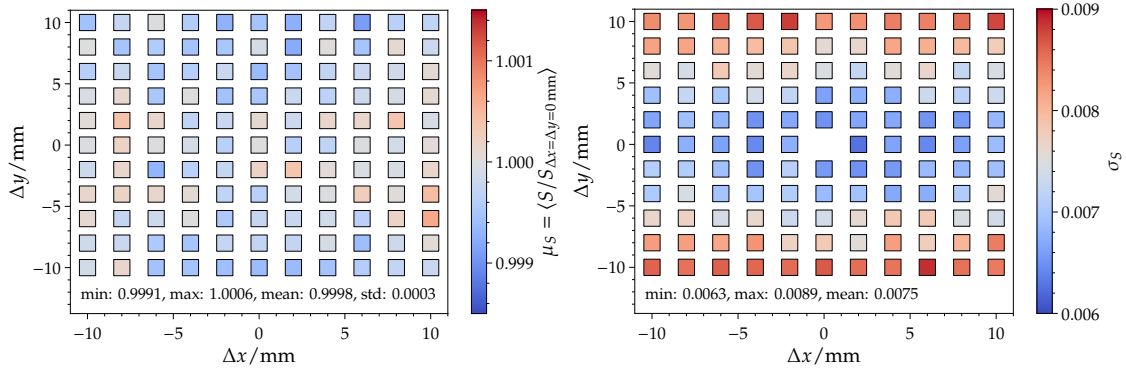
Figure 4.13: Similar to Fig. 4.12, but here we show for each shifted simulation the mean μ_S of the camera signal on the *left* and the standard derivation σ_S on the *right*, respectively.

4.4.6. Offsets of XY-Scanner Plane

We used the simulation of the XY-Scanner and the FD telescopes to study influences of a possibly shifted grid of the scanner. Therefore, we simulated the number of photons reaching the telescope camera while injecting photons from the XY-Scanner light-source with various offsets $(\Delta x, \Delta y)$ of the origin of the scanner grid.

xy-**direction.** First, we shift all grid positions of the light source for a simulation measurement in the two directions parallel to the filter plane of the telescope. We simulated shifts in Δx and Δy between ±1 cm in steps of 0.2 cm. Note that for $\Delta x = \Delta y = 0$ the optical axis of the telescope and the light source are aligned in the central position of the scanner grid ($x = y = 0$). For each pair of the 121 shifts in x and y direction, we simulated an injection of 10^5 photons at each of the ~1700 positions of the XY-Scanner and ray-traced them through the telescope. In Fig. 4.12 we present the results of this simulation study. Herein we show the ratio of the total number of photons reaching each a telescope pixel between each shifted scanner simulation and the central aligned reference. Each rectangle in Fig. 4.12 represents the entire telescope camera illustrating the signal ratios of the 440 pixels. We observe a maximal derivation of ~3% in the pixel-signal ratio while the average ratio is compatible with unity.

Moving along the Δy axis, horizontal bands containing a higher/lower ratio start to appear at $\Delta y \gtrsim 0.5$ cm. These bands are probably induced by different shadows cast by the filter support structure. Due to the geometry of the scanning grid we are more sensitive to the horizontal components of the filter support structure, as discussed in Section 4.4.4. Again, rotating the scanner grid may reduces the amplitude of the these observed structures.

To compute the corrections of a possibly shifted scanning grid on an individual pixel level, an accurate simulation of the filter support structure of each individual telescope is necessary. The geometry of the filter support structure differs between the telescopes. In Section 5.5 we present a method to obtain the geometry of the filter support structure directly from XY-Scanner measurements. Since the individual filter geometries are not yet included in any of the `TelescopeSimulator` modules, we ignore this possible correction for individual pixels for the time being.

However, building the average of all camera pixels for each shifted simulation, we observe a maximal difference of less than 0.1% between the shifted simulation and the central aligned reference. We show the camera averaged signals relative to the central aligned reference in Fig. 4.13-left. Additionally, on the right side of Fig. 4.13 we plot the standard derivation of the individual pixel signals for shifted simulation studies.

For the real XY-Scanner, we estimate the alignment of the central position ($x = y = 0$) to the optical axis of the telescope to be accurate within ±0.5 cm. Therefore, we conclude that, on camera average, we can neglect the influence of a possibly shifted scanning grid.
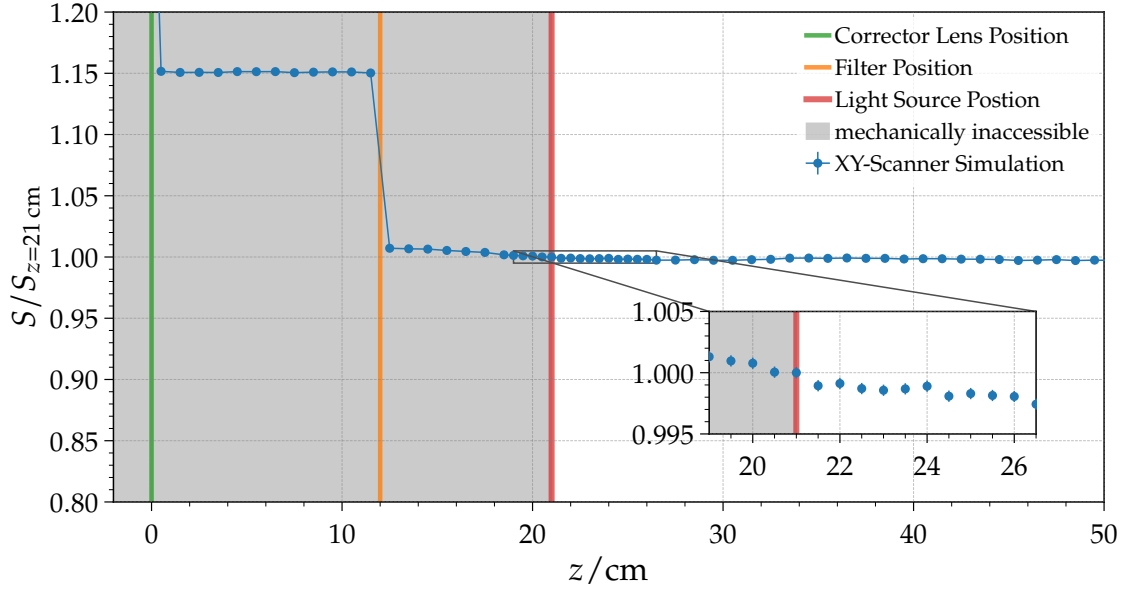
Figure 4.14: Offset of the XY-Scanner plane in z direction. The plot shows the ratio between the simulated signal at different z positions and the simulated signal at the actual position of the XY-Scanner plane, 9 cm in front of the filter. Locations of the corrector lens, the filter, and the light source are marked with vertical lines. The region which is mechanically not reachable is filled with gray.

z-direction. In another simulation study we investigate the effect of moving the light source along the optical axis of the telescope. Due to the geometry of the entrance windows of the FD telescopes, the closest distance between the filter and the scanning plane, where the light source can be mounted safely, is 9 cm. We simulated the trajectories of photons emitted from the same XY-Scanner grid shifted along the optical axis of the telescope. We shifted the grid plane from inside the telescope (behind the filter and the corrector lens) to ~40 cm in front of the filter plane. In Fig. 4.14 we plot the total number of photons S reaching the telescope camera scaled to the actual position of the scanner plane ($z = 21$ cm in the telescope coordinate system) for each shift of this scanner plane. We observe an expected ~15% drop of the number of photons S between the simulations on each side of the filter, due to its absorption. The region which is mechanically accessible with the current design of the XY-Scanner and light-source holding-structure is plotted as zoomed inlay in Fig. 4.14. Within this region we observe a change of the number of photons reaching the camera relative to the default scanner plane of less than ~0.3%. The change is below ~0.3% for distances up to 39 cm in front of the filter.

Therefore, we conclude that shifting the XY-Scanner plane even by several centimeters in z-direction does not significantly change the number of photons detected by the telescope camera.

Taking this results into account we consider to increase the distance between the telescope filter and the XY-Scanner plane by ~1 cm. In the current setup, we have to be very careful to avoid mechanical collisions between the light source and artifacts contained in the aperture box of the telescope. Due to different designs of the aperture boxes, for some telescopes we have to remove parts to be able to set a 9 cm-distance. Therefore, increasing the distance between the XY-Scanner plane and the filter would ease the installation process and thus reduce the overall time needed for the calibration.

CHAPTER V

OPTICAL PROPERTIES OF FLUORESCENCE TELESCOPES

Contents

In this chapter we discuss additional observations and measurements we performed with the XY-Scanner to study the optical characteristics of the fluorescence telescopes of the Pierre Auger Observatory. In addition we present the first measurements performed with a parallel and collimated light-beam source mounted onto the XY-Scanner.

5.1. EFFECT OF CLEANING COMPONENTS OF TELESCOPES

The accumulation of dust and other debris on the optical components of the telescopes alter their optical properties. Especially the transmission of the filter and the reflectivity of the mirror are reduced due to dirt and dust deposited on their surfaces [40, 64]. Measurements with the XY-Scanner enable us to observe and study the influence of dust on certain parts of a telescope. However, the calibration light sources illuminate all pixels of the FD camera simultaneously and thus these measurements are primarily sensitive to the light absorption on the dust layer and rather insensitive to the light scattering on dust. For the XY-Scanner measurements we always capture and read out the entire telescope camera, thus scattered photons on e.g. dust on the mirror, which miss their target pixel, probably end up in a different pixel, which nevertheless is read out.

Detailed studies of the light scattering on dust can be performed with a different light source. We introduce such a parallel and collimated beam source in Section 5.6 and discuss first measure-
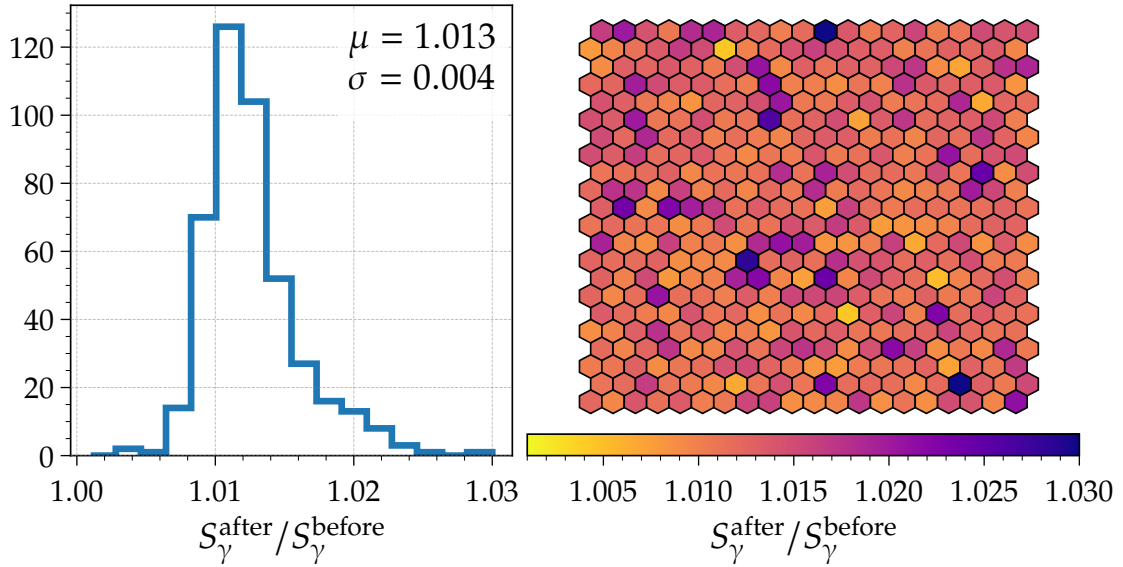
Figure 5.1: Ratios of the signals captured by each telescope pixel-PMT between XY-Scanner measurements performed before (S_γ^{before}) and after (S_γ^{after}) the UV filter of LL4 telescope was cleaned. The *left* plot displays the distribution of the obtained ratios, while the *right* side illustrates the same data in a form of a pixel matrix.

ments performed with this source with the XY-Scanner, but a detailed discussion on this matter is not the topic of this work.

In the following, we discuss measurements aimed to study the effect of cleaning different telescope components.

5.1.1. FILTER

To ensure the optimal operation of the FD telescopes, the UV filters of all telescopes of the Pierre Auger Observatory are cleaned of dust and dirt in regular time intervals. The 24 standard telescopes are cleaned once every ~4 months, while the high-elevation extension (HEAT) is cleaned roughly every month. The shorter cleaning interval for HEAT is due to its tilted operation, during which more dust and dirt is accumulated at the UV filter.

During the Spring 2019 XY-Scanner campaign we cleaned the UV filter at telescope 4 of Los Leones (LL4). Therefore, the unique opportunity arose to study the effect of cleaning the filters in terms of changes of the transmittance of the latter one. According to the FD task log [65] the last time the filter of LL4 was cleaned before the Spring 2019 campaign, was on 19th December 2018. We cleaned the filter on 2nd April 2019 which fits into the four-month cleaning schedule. However, the main reason for this particular filter cleaning was the increased dust debris on the filter surface which occurred during the installation process of the XY-Scanner at that particular telescope. Although the XY-Scanner was installed during daytime, the cleaning of the filter was performed during night time. We cleaned the filter rather rudimentary with a wet cloth only. We were able to perform XY-Scanner measurements immediately before and after the filter cleaning procedure. The general procedure of the XY-Scanner measurements is described in Section 4.2.

Both measurements were executed with identical parameter settings and the raw signals S_{ADC} were converted to photons by using the standard calibration $C_{\text{abs}}^{\text{CalA}}$ which was performed right before each of the XY-Scanner runs. The captured photon signal is estimated as

$$S_\gamma \propto S_{\text{ADC}} \, C_{\text{abs}}^{\text{CalA}} \tag{5.1}$$

for both XY-Scanner measurements. In Fig. 5.1 we plot the signal ratios of the two XY-Scanner
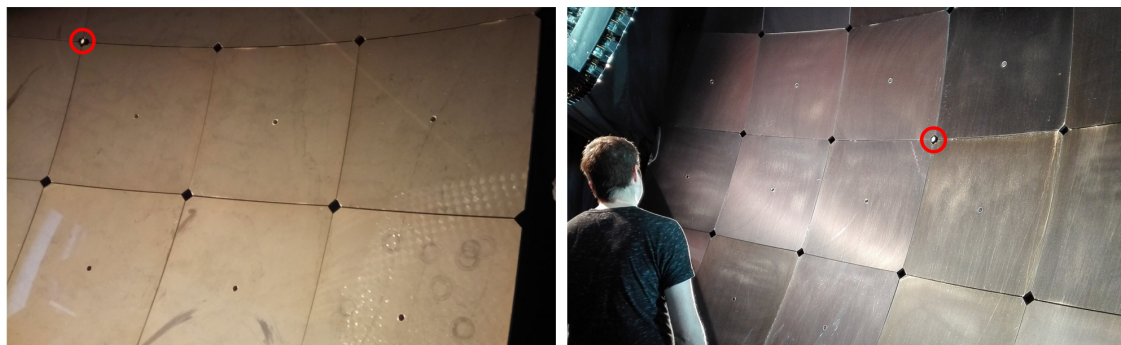
Figure 5.2: Photographs taken before (*left*) and after (*right*) cleaning the mirror of telescope LL4. For a better orientation the light source of the relative calibration system (Cal A) in the center of the mirror is marked with a red circle in both photographs.

measurements bracketing the filter cleaning. The right side of Fig. 5.1 displays the signal ratio per pixel as a pixel matrix, with the ratio being encoded by color. On the left side the identical data is shown as a distribution, mean and standard deviation are included within the plot.

On average we observe a change of ~1.3% in the captured pixel signals, we attribute this difference to a change in transmittance of the UV filter caused by the cleaning. Even with additional dust coverage due to the XY-Scanner installation process, we observe only a small change of ~1.3% in the filter transmittance. Therefore, we conclude that the intervals of ~4 months for cleaning the UV filters of the telescopes are sufficiently short.

5.1.2. Mirror

Even though the FD telescopes are located in an air-conditioned rooms, the accumulation of dust on the mirror and the consequent alteration of its optical properties are not insignificant. Detailed studies on the influence of dust sedimentation on the FD telescope mirrors can be found in e.g. Refs. [66, 67, 68].

Since the procedure of cleaning a telescope mirror is more complex and has a much higher workload than cleaning the filters, the mirrors are in general cleaned less frequently than the filters. In addition to that, each type of a mirror has a different procedure for cleaning. The hexagonal glass mirrors are fully disassembled and each element is washed separately, while the aluminum mirrors stay installed for the entire washing procedure. Since the aluminum mirrors are neither removed from their holding structure nor touched during the cleaning procedure, it is not necessary to realign each segment after the cleaning. This is not the case for the glass mirrors, since those are disassembled for the washing, a precise alignment of the mirror has to be performed after each cleaning procedure, which again heavily increases the workload for the cleaning of this type of a mirror.

We studied the effects of cleaning a telescope mirror with XY-Scanner measurements at the telescope 4 of Los Leones (LL4). Since this telescope is equipped with an aluminum mirror, a disassembly of the latter was not necessary before the cleaning.

Last time the mirror of LL4 was cleaned prior that was in October 2008 [69]. We cleaned the mirror on 5th April 2019 during the Spring 2019 XY-Scanner calibration campaign. This gave us the unique opportunity to study the effect of cleaning the telescope mirror on the XY-Scanner measurements. We performed standard XY-Scanner measurements (as described in Section 4.2) before and after the mirror-cleaning procedure was performed. We summarize the procedure of this particular cleaning in the following: In the first step coarse dust is removed from the mirror surface by blowing it with compressed nitrogen. Then, the mirror segments are washed with de-ionized water. The water is applied to the mirror surface by a special water sprayer. In the last step the mirror is dried by blowing it with nitrogen again. During all these steps we paid special
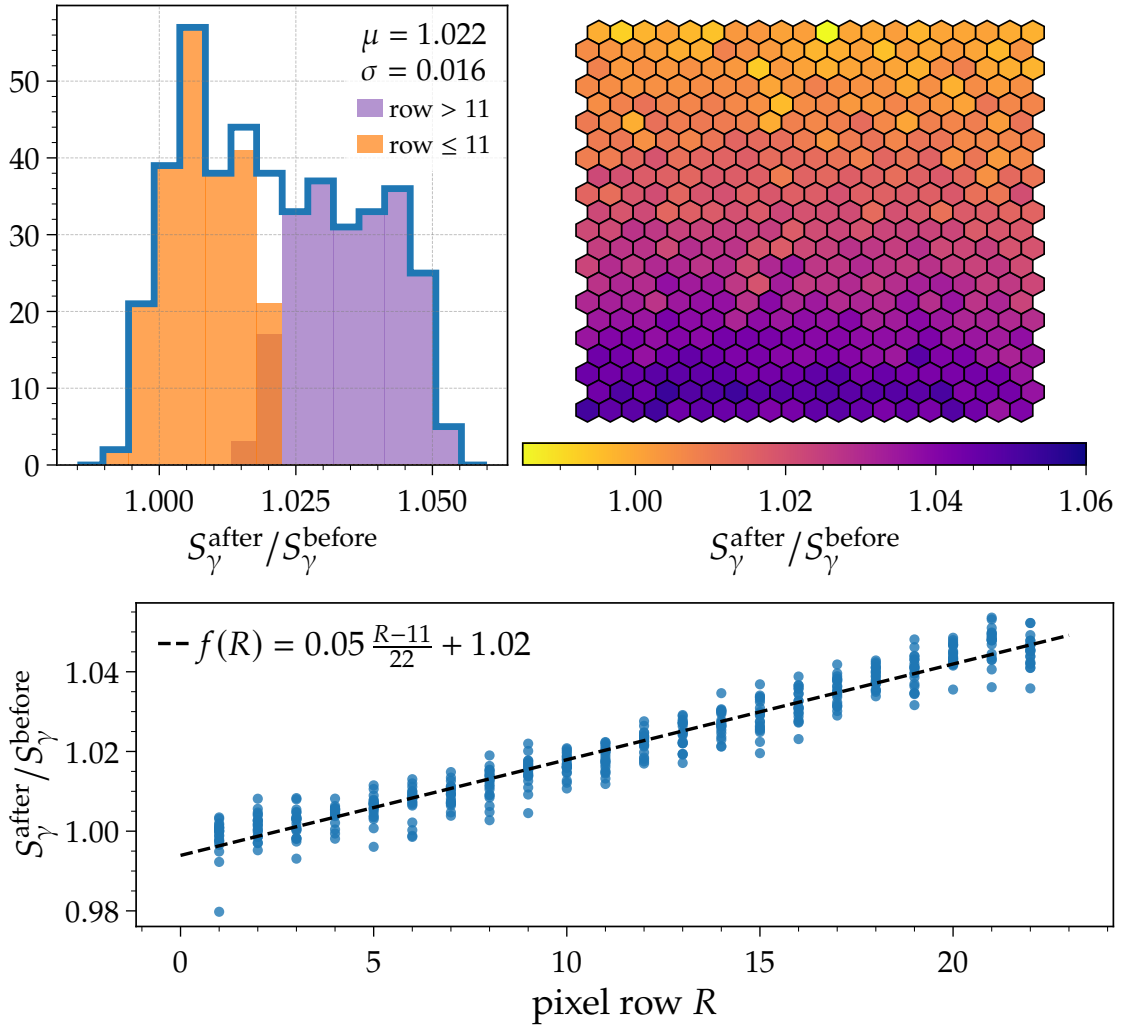
Figure 5.3: Observed effect of cleaning the mirror of telescope LL4. Per-pixel signal ratios between XY-Scanner measurements performed before and after the mirror of was cleaned. *Top left:* Distribution of the obtained ratios. Distributions of upper and lower half of the camera are indicated by different color. *Top right:* Illustration of the same data as pixel matrix. *Bottom:* Signal ratio as function of pixel row, together with a linear fit.

attention to avoid any direct mechanical contact with the mirror. Otherwise we would have to realign the individual mirror segments. We were able to remove most of the dust from the mirror with this procedure. In Fig. 5.2 we show photographs of the telescope mirror before and after the cleaning. Unfortunately a greasy contamination still remains on the mirror surface. To also remove this greasy layer a more aggressive cleansing agent may have to be applied. The cause of this greasy contamination of the mirrors is most probably the heating system of the FD buildings.

As mentioned above, we performed the XY-Scanner measurements in the nights before and after the telescope mirror was cleaned. The measurement before the cleaning was performed in the night of 4th April 2019 while the after-cleaning data was taken on 7th April 2019. We performed a similar analysis as for the filter cleaning mentioned above. The per-pixel ratios of the captured photon signal for the two XY-Scanner measurements bracketing the mirror cleaning are displayed in Fig. 5.3. Herein the left side shows the ratios as a distribution (where the mean and standard derivation are also shown within the plot) while the right side illustrates the same

data as a pixel matrix. The distribution on the left side of Fig. 5.3 is additionally split into upper and lower half of the camera as indicated by different colors. The upper half is defined as the pixels which are located in row 1 to 11 (orange), while the lower half contains the pixel rows 12 to 22 (purple). On average we observe an increase in the pixel signals on the order of ~2% due to the mirror cleaning. However, we observe a strong vertical gradient in the image of the camera. Therefore, the observed signal ratio depends on the vertical position of the pixel in the camera. We illustrate this gradient additionally in Fig. 5.3 where we plot the signal ratio as a function of the pixel row. Pixels in the upper rows ($R \lesssim 5$) of the camera show a ratio close to one, while for the pixels in the lower part of the camera we observe changes of up to ~5%.

We give an explanation for these observations in the following. From the design of the telescope it follows that the lower pixels of the camera mainly observe the lower part of the mirror and, likewise, the upper camera pixels mostly see the upper part of the mirror. Due to the spherical shape of the mirror and the geometry of the whole telescope, the upper part of the mirror is oriented almost vertically, which leads to hardly any dust accumulation there. The effect of cleaning the upper segments is thus rather small and the observed signal ratios are very close to one for the upper pixel rows of the camera. Moving further down the situation changes and the mirror segments are tilted towards more horizontal orientations, which results in a larger amount of accumulated dust. Therefore, cleaning the mirror does have a large impact on the lower mirror segments, which results in a larger signal ratio for the bottom camera-pixel rows.

In air shower observations, the unevenly accumulation of dust of the mirror potentially affects the estimation of the position of the shower maximum $X_{\max}$. A discussion on this topic can be found in e.g. Ref. [70].

The method we describe here is only sensitive to absorption of photons and mostly insensitive to diffuse scattering and refraction. A sensitivity to changes in the point-spread-function (PSF) can may be gained by using the collimated beam source, introduced in Section 5.6.

5.2. Covered Corrector-Lens Gaps in Los Leones

In this section we describe a noteworthy feature we observe in one of the XY-Scanner measurements at a particular telescope. The left part of Fig. 5.4 displays the signal recorded by the entire camera of the telescope for all positions of the calibration-light source during an ordinary XY-Scanner measurement run. Each marker illustrates the position of the light source on the scanning grid while the color indicates the summed signal strength of all 440 pixel-PMTs. The darker-appearing vertical lines in the horizontal center and two horizontal lines symmetrically around the vertical center are shadows cast by the support structure of the filter. The shape of this support structure is also visible in the photograph on the right side of Fig. 5.4. The shadow cast by the camera manifests itself as the dark diffuse area in the central region.

In this illustration we observe darker lines in the outer rim of the telescope aperture, which are similar to the tick markers of a clock. This feature is so far observed only at one telescope, namely at the Los Leones 4 (LL4) telescope. The positions of these shadows coincide with the expected locations of the gaps between the individual elements of the corrector lens. For more details on the assembly of the corrector lens see Section 3.1. One exception is the upper left part of the aperture, here it appears that two tick shadows are missing.

On the right part of Fig. 5.4 we show a photograph of the aperture window of LL4 taken from the inside of the telescope. In this photograph (and even better in the magnified inlay) black strips are visible, which are attached to the lens at the positions of the gaps between the elements. They are hardly visible since located at the side of the lens, which faces towards the filter. According to an FD task log [65] entry the gaps between the corrector-ring segments at LL4 were covered with a 19 mm-wide PVC tape on 28th November 2011. This was done to check whether the gaps between the lens elements are contributing to an unexpectedly large point-spread function (PSF). Since photons, which pass through one of these gaps, are not corrected for the spherical aberrations may widen the PSF. It turns out, this is most probably not the main reason and the increased PSF is probably due to tiny dust particles on the mirror surfaces, diffractively scatter the photons. The
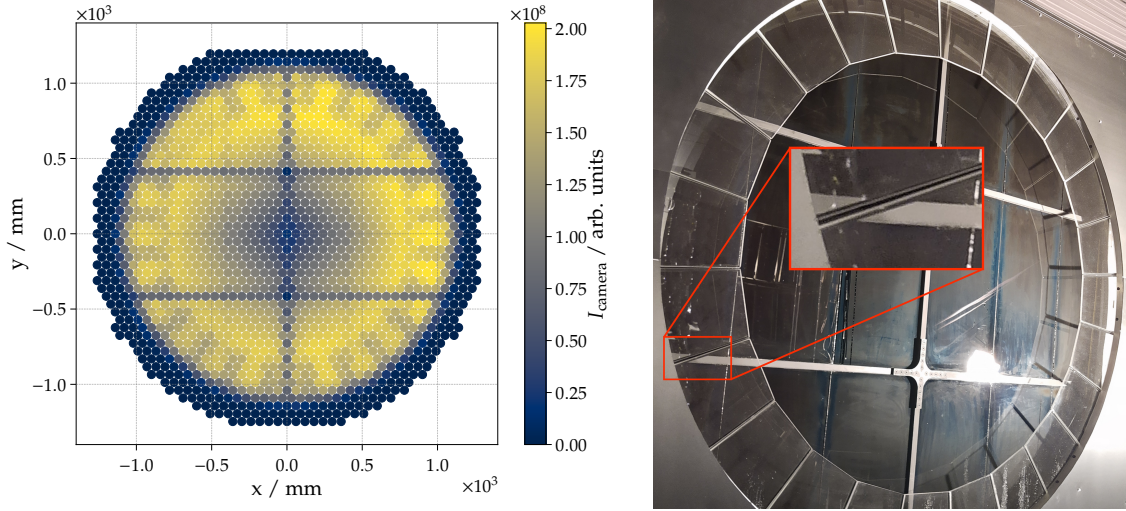
Figure 5.4: *Left:* For each position of the light source on the XY-Scanner grid (location of the dots) the intensity recorded by the entire telescope camera (color of the dots) is shown. Note the shadow ticks sticking in from the outer edge of the aperture. Data was taken at the Los Leones telescope 4 in November 2019 with the KIT sphere. *Right:* Photograph of the corrector lens of the LL4 telescope. The inlay displays an enlarged part of the photograph focused on a gap between the corrector-lens elements. Photograph was taken by Primo Vitale in September 2021.

studies on the PSF are not further discussed here. The same procedure was also performed at LL3 on 23th November 2011, but the tape at LL3 was removed on 7th November 2012, as written in the FD task log. No entry of the FD task log mentions that the tape from the gaps between the corrector-ring segments at LL4 were ever removed. In a visual inspection of the LL4 telescope in October 2022, we verified that most gaps are still covered by the black tape. For the two gaps in the upper left region the tape was missing. One explanation is that one segment of the corrector lens was replaced and the tape was not attached after that. Or that the tape simply fell off at some time during the last ~8 years, between the installation of the tape and time the XY-Scanner measurements were performed.

We conclude that the tick shadows observed during the measurements with the XY-Scanner are cast by this stripes of tape attached to the corrector lens. We did not observe such tick pattern in any other XY-Scanner measurements at any other telescope.

We roughly geometrically estimate the fraction of the aperture window which is obscured by the tape,

$$f_{\text{obsc}} = \frac{A_{\text{taped}}}{A_{\text{aperture}}} = \frac{24 \times 19\,\text{mm} \times 250\,\text{mm}}{\pi\,(1100\,\text{mm})^2} \approx 0.03 \tag{5.2}$$

assuming each of the 24 gaps is covered by a 19 mm-wide piece of tape. The length of the tape is the difference between the two corrector ring radii, $\ell = 1100\,\text{mm} - 850\,\text{mm} = 250\,\text{mm}$. Following this geometrical approach ~3% of the aperture opening is obscured by the tape covering all the corrector-ring gaps. In the actual situation at LL4 only 22 gaps are covered and thus the fraction is reduced to ~2.75%.

To confirm this rather rough geometrical approach mentioned above, we simulated the XY-Scanner measurements. General details on the XY-Scanner simulations are given in Section 4.4. Two XY-Scanner measurements were simulated with the only difference between the two simulation being a 19 mm-wide absorbing layer covering the gaps between the corrector-ring segments. For each measurement we simulated ~10^6 photons for each of the ~1700 positions and traced them trough the telescope. In Fig. 5.5 we show the signal ratio between the "taped" and "untaped" simulation for each pixel of the telescope camera. A pixel matrix indicating the ratio by color is

Figure 5.5: Ratio of the pixel signal obtained via XY-Scanner simulations. For the first simulation study the gaps between the lens elements were covered by an 19 mm-wide absorbing layer (taped). The second simulation was performed without this layer (untaped). The ratio is plotted as distribution on the *left* and as pixel matrix on the *right*.

displayed on the right side. The left plot of Fig. 5.5 shows the same data as a distribution, mean and standard deviation are also given within the plot. On average we observe a ~3.6% signal difference between simulation with and without absorbing layers on the gaps of the corrector lens. We thus conclude that the simulation supports the geometrical approach.

5.3. Reduced Aperture Window in HEAT

The analysis of particular XY-Scanner measurements at the first HEAT telescope (HE1), revealed an unusual situation. On the right side of Fig. 5.6 all positions of the light source on the scanning grid during an ordinary calibration measurement are drawn as filled circles. The color of each data point indicates the total signal captured by the entire telescope camera while the light source flashed at this given position. The red and black-dashed circles represent the edges of the aperture and the corrector ring, respectively. We observe in this illustration the shadows induced by the filter support structure as straight vertical and horizontal dark lines, and the shadow induced by the camera itself in the center of the aperture. Another feature, which we so far only observed at HE1 is a shadow appearing in the upper part of the aperture, reaching into the aperture opening (red circle). On the left side of that Fig. 5.6 the captured readout of the telescope camera for a particular position of the light source is shown as a pixel matrix. This position is located at the edge of the unexpected shadow in the upper part of the aperture and is marked by a blue cross in the plot on the right. With the light source at that particular position approximately one third of the camera pixels detected less than expected or barely any signal.

As it turned out, this shadow in the upper part if the aperture was caused by a mechanical issue within the telescope. Inside the telescope, right behind the corrector lens, the safety curtain is installed, as explained in Section 3.1. The upper stop switches of that particular curtain at HE1 were located ~25 cm lower than intended, which leads, judging from the XY-Scanner measurements, to obscuring the top $d \approx 15$ cm of the aperture. We calculated a geometrical
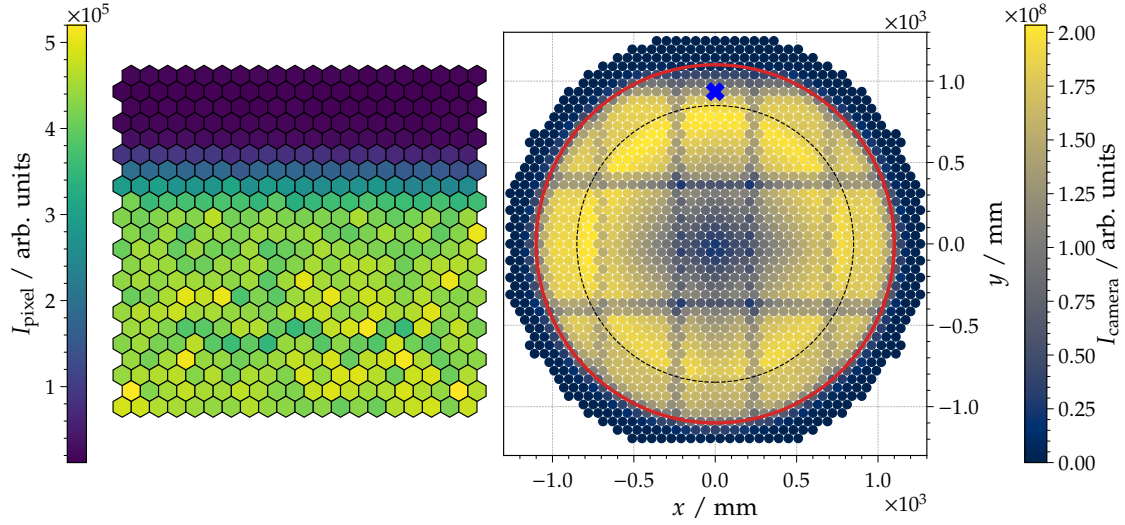
Figure 5.6: *Left:* The signal captured by the FD camera of HEAT1 with the XY-Scanner light-source flashing at a position in the upper center of the aperture opening. Position marked as blue cross on the right plot. *Right:* All positions of the light source during a XY-Scanner calibration run. The color of the data points indicate the total signal recorded in all telescope pixel-PMTs. Red and black-dashed circles represent the edges of the aperture opening and corrector ring respectively.

estimate of that obscured area as follows. Generally the area of a chord is given as

$$A_{\text{chord}} = A_{\text{sector}} - A_{\text{triangle}} \tag{5.3}$$

$$= \frac{r^2}{2}\theta - \frac{r^2}{2}\sin\theta = \frac{r^2}{2}(\theta - \sin\theta) = 0.1125\,\text{m}^2 \tag{5.4}$$

Figure 5.7: Sketch of partial areas of a circle.

with the angle $\theta = 2\arccos\left(\frac{r-d}{r}\right)$ and $r = 1.1\,\text{m}$ the radius of the aperture. See Fig. 5.7 for an illustration. Based on the XY-Scanner measurements we estimate the additional relative obscured area to be

$$f_{\text{obscured}} = \frac{A_{\text{chord}}}{A_{\text{aperture}}} \approx 0.03. \tag{5.5}$$

Since this issue is probably not visible in any other data of the telescope, it is probably impossible to estimate since when the upper part of the aperture was obscured by the lowered safety curtain. This particular curtain was probably installed around 2008. We observe this particular shadow in all measurements performed with the XY-Scanner at HE1, with the earliest data taken in November 2018.

In July 2020 the curtain stop switch was re-adjusted in a way that the curtain should completely open. For the measurements we performed during the Autumn 2022 campaign we do not observe any shadow obscuring the top fraction of the aperture anymore. We thus conclude that the issue with the lowered stop switch is fixed and the HE1 telescope has again the nominal aperture area.

5.4. DAMAGED MIRROR SEGMENT

One of the mirror segments at HEAT telescope 1 is damaged as shown in the photograph on the right side in Fig. 5.8. We observe this damage in the data taken during the XY-Scanner calibration measurements. The left side of Fig. 5.8 illustrates the signal captured by the telescope camera for various positions of the XY-Scanner light source. Within this illustration a rather bright c-shaped

Figure 5.8: *Left:* Captured readout of the telescope camera at different positions of the XY-Scanner light source. The reader of the digital version of this work is encouraged to zoom into this plot to see the detailed structure. *Right:* Photograph of a damaged mirror segment in the lower left part of the mirror of telescope HE1.

line does appear in the left part of several camera readouts. This increase in signal is probably due irregular reflections of the broken corner of the mirror segment as shown in the photograph in Fig. 5.8-right. We show this here for illustrative purposes.

5.5. GEOMETRY OF FILTER SUPPORT STRUCTURE

The measurements performed with the XY-Scanner at the FD telescopes also give us the unique opportunity to perform a kind of tomography of the telescopes. In the following we introduce a procedure of estimating the geometry and the positions of the filter support structure mounted at each telescope.

For ordinary XY-Scanner calibration measurements the light source is driven across the telescope aperture. By scanning in a triangular grid in steps of 6 cm, the light source is moved to and flashed at ~1700 positions uniformly distributed over an area slightly larger than the aperture window. The left side of Fig. 5.9 shows the signal captured by the entire camera for all positions of the light source during a complete XY-Scanner calibration measurement. Within this plot the positions of each filled circle correspond to the positions of the light source on the scanning grid while the signal strength captured by the telescope camera is indicated by different colors. The dark appearing horizontal and vertical lines are shadows cast by the filter support structure. In the two plots on the left and bottom side of the plot we show the projected signal onto the y-axis and x-axis, respectively. In these projections several dips (two in the y-projection and four in the x-projection) appear, which correspond to the positions of the aforementioned shadow of filter support structure. By estimating the position of the dips in this representation, we determine the relative position of the filter support structure with respect to the XY-Scanner origin.
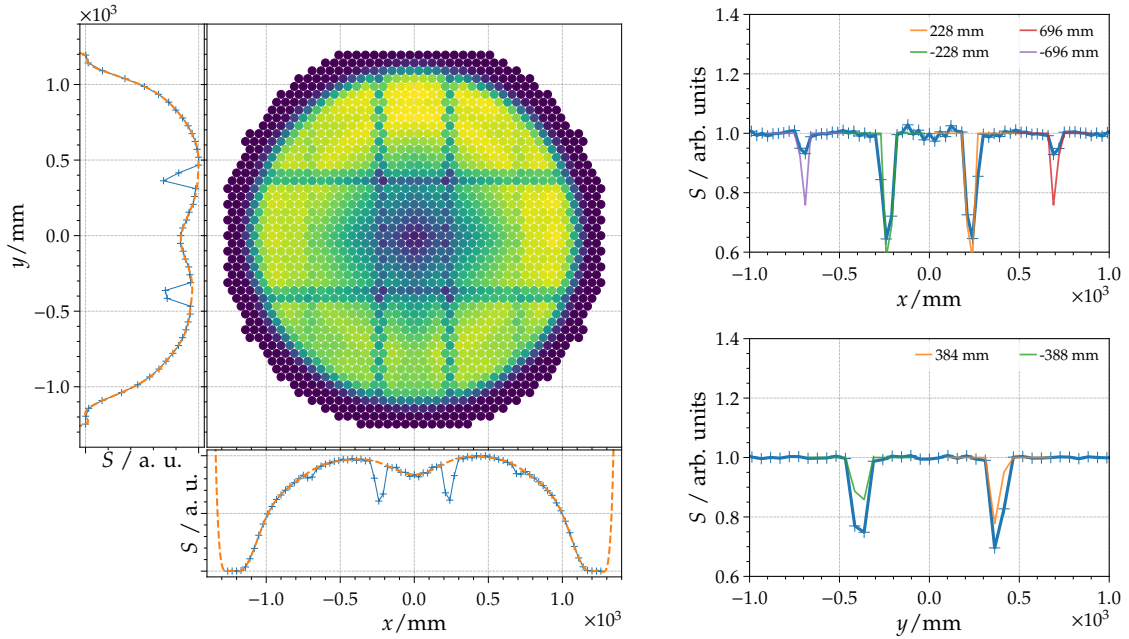
Figure 5.9: The data taken at Los Leones telescope 3 in April 2019. *Left:* Each point in the plot represents a position of the light source, the color indicates the signal strength captured by the whole telescope camera. Projections of the signal to the y- and x-axis are plotted on the left and bottom side as blue lines. The fit, explained in the text, is drawn in orange. *Right:* Ratio of the measured signal and the polynomial fit is shown in blue. The results of the position fit for each filter support bar are shown as well.

In a first step we fit a high-order polynomial to the projected data on the x- and y-axis, excluding the approximate locations of the dips form the fitting. The resulting fitted functions are drawn as orange dashed lines in the left/bottom plots of Fig. 5.9. On the right side of that same Fig. 5.9, we show the ratio of the measured data and the prediction of the obtained fits in blue. Again, the position of the filter support-structure corresponds to the positions of the dips in Fig. 5.9-right.

In a next step, we calculate the fractional area of the light-source exit port, which is obscured by any bars of the filter structure. In the following the distance between the exit port and the filter is neglected. We are assuming that the exit port of the light source is a circle with radius r centered at location $(x_0, y_0) = (0, 0)$, as illustrated in Fig. 5.10-left. If we start to move a secant line from above the circle to below the circle, the area enclosed by the circle and the secant line increases from $A_0 = 0$ to the entire circle area $A_1 = \pi r^2$. Now, for a secant line at any position x we calculate the area enclosed by the circle and this secant to be

$$A_s(x) = \begin{cases} \pi r^2, & \text{if } x \leq -1 \\ 0, & \text{if } x \geq 1 \\ \arccos(x) - x\sqrt{1 - x^2}, & \text{otherwise} \end{cases} \qquad (5.6)$$

as illustrated in Fig. 5.10-left. For any given bar of the filter support structure of a width w at position x_B we calculate its edges x_1 and x_2 relative to the source exit-port as

$$x_{1,2} = \frac{x_B \mp \frac{w}{2} - x_0}{r} \qquad (5.7)$$

with x_0 and r representing the position and radius of the exit port of the light source, respectively.
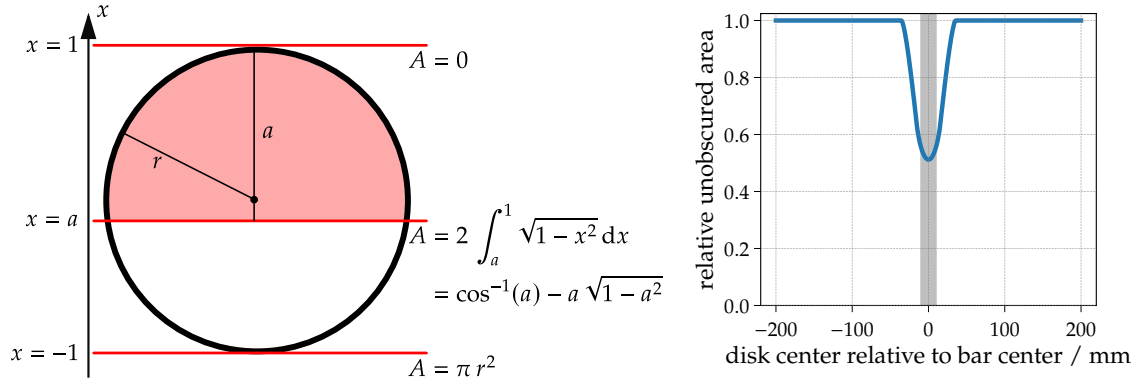
Figure 5.10: *Left:* Schematic drawing of the enclosed area by a circle and a secant line. *Right:* Relative not obscured area for various disk positions for a 20 mm bar (gray band) at 0 mm.

The relative unobscured area A_u of the exit port is

$$A_u(x_0, x_B) = A_s(x_2) + A_s(-x_1). \tag{5.8}$$

Assuming now that the intensity of the light source is proportional to the unobscured area A_u, the function in Eq. (5.8) is fitted to the scaled signal shown on the right side of Fig. 5.9. Since the actual width of the filter support bars is known, we fix this parameter to $w = 20$ mm. The resulting positions x_B for the support structure for each individual fit are shown within the Fig. 5.9-right.

With this procedure we estimate the location of the vertical bars to be $x_{B,fit} \approx \pm 22.8$ cm. This results differs only 8 mm (~3.5%) from the value in the technical drawing $x_B \approx \pm 23.6$ cm. The second vertical structure is only a sealing between the filter-glass plates and does not appear in the technical drawing, but we measured its real position at a telescope to be $x_{B,seal} \approx \pm 70$ cm. Here we observe a difference of only 4 mm.

For the two horizontal bars we observe a difference of 4 mm between the technical drawing and the data-driven method explained above. The positions are determined to be $y_{B+,fit} \approx 38.4$ cm and $y_{B-,fit} \approx 38.8$ cm. The technical drawing gives the position as $y_B \approx \pm 39.1$ cm. Thus, the observed differences for the horizontal structures are below 1 cm.

Concluding, by analyzing the standard calibration measurements of the XY-Scanner we are able to estimate the positions of the filter support-structure and we observe a difference of less than 1 cm between this method and the technical drawing of the telescopes. We discussed here only standard calibration XY-Scanner measurements, with dedicated XY-Scanner measurements containing denser positions closer to to the filter support-structures we may archive a more accurate estimation of the filter geometry.

In the future, the estimation of the filter geometry obtained with the XY-Scanner measurements can be implemented into the telescope simulation and thus provide a more realistic simulation.

5.6. Collimated-Beam Light Source

The versatile and modular setup of the XY-Scanner stage allows us the straightforward installation of basically any type of a light source, which does not exceed weight and space limits of the scanner. In the following, we introduce another type of a light source, a parallel collimated source, which serves a different purpose than the calibration light sources. First we describe the light source itself and then present the first test measurements performed with the source installed onto the XY-Scanner.

The collimated-beam light sources (CB) are additional light sources, which can be easily mounted onto the XY-Scanner system. These types of sources are still under development and so
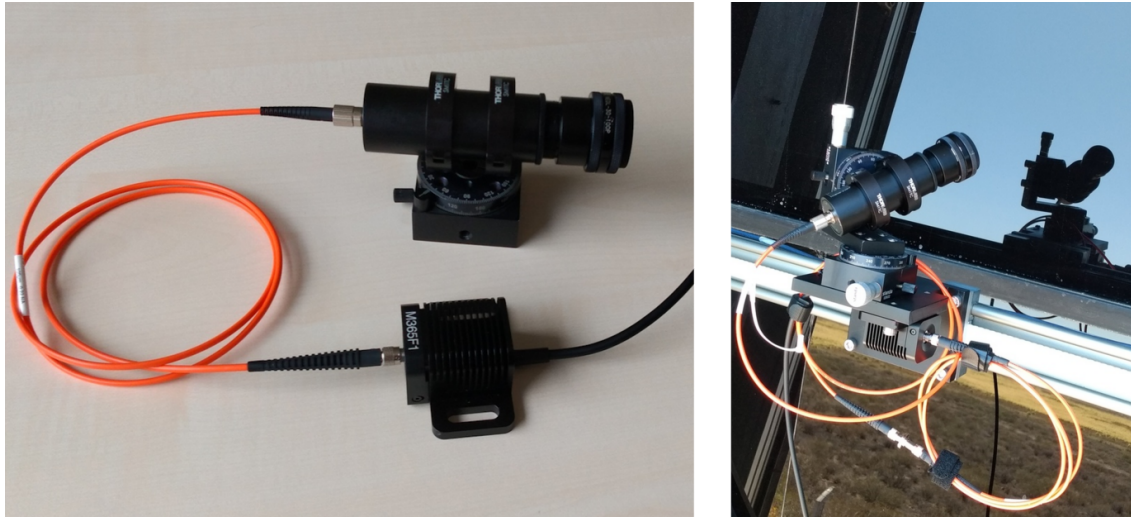
Figure 5.11: Photographs of the collimated-beam (CB) light source. *Left:* The collimator (black tube) is connected to the initial light source (LED, black box) with an optical fiber (orange). *Right:* The CB source installed on a XY-Scanner system at FD Los Leones.

far we only performed first test measurements with a prototype of the CB during the November 2019 XY-Scanner campaign. In contrast to the calibration light sources, the emission of the CB source consists of a rather parallel beam. The rays emitted from the CB source are not entirely parallel but show a small divergence. The beam-spread angle is chosen to be large enough so that the CB source illuminates a sufficiently large area of the mirror surface and that the spot size in the focal plane is not larger than one pixel.

The purpose of measurements performed with this CB source is not to calibrate the telescope, but rather to investigate the imaging properties of the telescope. With such a device the point-spread function (PSF) as well as the influence of dust or dirt on the optical parts of the telescopes can be studied in great detail. For such a measuring program the requirements on the light source are the following: the light emission of the source should consist of parallel light rays with a small beam-spread angle. In addition, the emission is required to be homogeneous over the entire light source surface. Next, the emitting window should not be too small in order to integrate over small impurities on the optical components like the dust or similar debris on the optical components like the filter and mirror. To fulfill all these requirements, a custom-made light source was developed and built. The development of the CB source was mainly performed by our colleagues from the Joint Laboratory of Optics of Palacký University and Institute of Physics of the Czech Academy of Sciences in Olomouc, Czech Republic. This collimating unit consists of a system of lenses with point-like light source placed in its focal point. In the CB the end of an optical fiber acts as a point-like source and the actual light source is a Thorlabs M365F1 LED with a wavelength of $\lambda_{CB} = 365\,\text{nm}$, which is connected with the optical fiber to the actual CB. Photographs of the light source and the CB are shown in Fig. 5.11. Other types of CB sources, mainly with different diameters, were developed and constructed, but these are not discussed here.

In the following we discuss the first measurements with the CB source performed with the XY-Scanner installed at the FD telescopes.

5.6.1. First Measurements with CB Light Source

For the here discussed proof-of-concept measurements the CB source is mounted to the XY-Scanner system as shown in the photograph on the right side of Fig. 5.11. Similarly to the calibration light sources, the CB sources are operated in a pulsed mode. For each light pulse emitted from the CB source the FD DAQ is triggered to capture and read out the entire FD
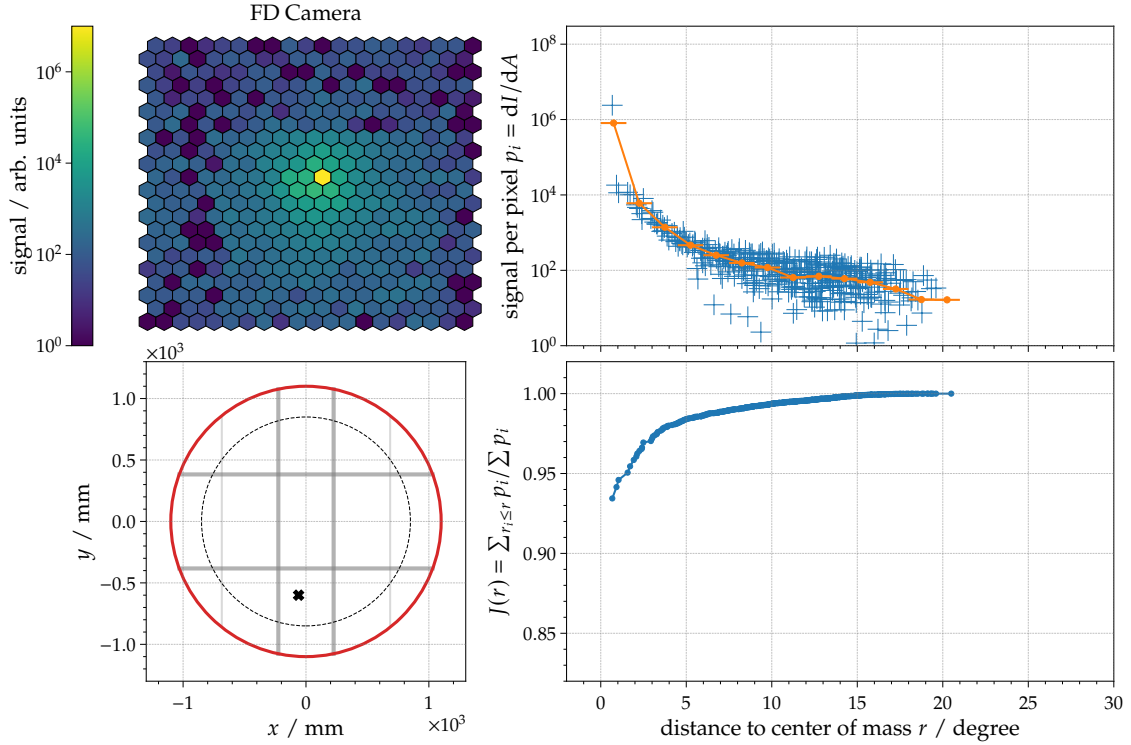
Figure 5.12: Typical event captured by the telescope camera during a light flash from the CB light source. *Left top:* Readout of the camera. *Left bottom:* Position of the XY-Scanner marked as a black cross. Edge of the aperture opening and the corrector ring are drawn as concentric red and dashed-black circles, respectively. Filter support structure is shown as gray lines. *Right top:* Signal per pixel (blue) as function of the radial distance to the center of gravity. The orange curve shows the mean in 1.5° bins. *Right bottom:* Cumulative sum of the pixel signal from the plot above.

camera. For the here discussed test measurements performed in November 2019 the pulse length was set to 5 μs, similar to the pulse length of the calibration source, and the intensity was adjusted to saturate the aimed pixel but not saturate the virtual channel, to which the pixel belongs. The virtual channels of the FD telescopes and their roles in recovering the signals of saturated pixels are explained in Section 3.3. We recover the actual signal of the saturated pixel according to Eq. (3.14). The pointing direction of the CB source was adjusted manually to maximize the signal in one particular pixel of the telescope camera. For this purpose the CB source is flashed a limited number of times and then the readout of the FD camera is analyzed. If more than one pixel shows a large signal, we readjusted the CB and the procedure is repeated until only one pixel captures a significant signal. With this procedure the pointing of the CB is not very accurate (the pixel may not be hit centrally) nor precisely reproducible. For future measurements two motorized rotation stages will be employed in the CB source mounting, allowing us to remotely steer its pointing direction. Therefore, the reproducibility and the accuracy of the pointing direction will significantly increase for future measurement campaigns.

Nevertheless, we present some of the first measurements in the following. We show a typical event of a CB flash at the CO5 telescope in Fig. 5.12. The position of the XY-Scanner is marked as a black cross in the lower left plot. The top left part of that Fig. 5.12 shows the signal captured by the telescope camera as a pixel matrix. For this particular event the CB light source is pointed into the direction of pixel #209 (column 10, row 11), which is one of three pixels closest to the center of the camera. In the top-right plot of Fig. 5.12 the signal captured by each individual pixel
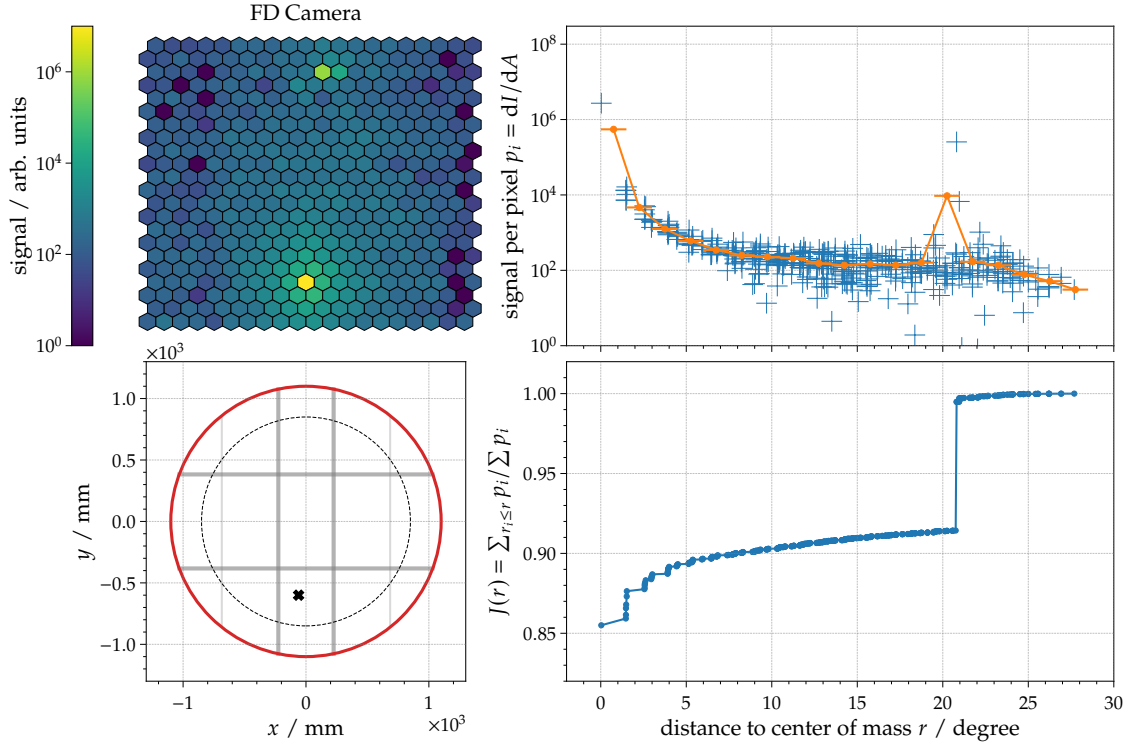
Figure 5.13: Another typical CB-induced event with a second signal spot caused by the internal telescope reflections. For a description of the individual plots see the caption of Fig. 5.12.

is plotted as a function of the radial distance of that pixel to the center of mass of the camera. The binned average of 1.5°-bins is drawn as an orange line in the same plot. As expected, the signal drastically decreases with increasing distance to the center of mass. The lower-right plot of Fig. 5.12 displays the cumulative sum of pixel signals over the given radial distance to the center of mass. Approximately 93% of the entire camera signal is detected by the pixel which the CB light source is pointed to and ~99% are contained within a circle of radius ~7.5° around the center of mass. A more detailed and sophisticated analysis of the CB data is not given here and left as subject for future investigations.

In Fig. 5.13 we present another interesting event where the CB light source is pointing towards a different pixel. The CB light source is adjusted to illuminate the pixel #217 in column 10 and row 19 in the lower center of the camera. The position of the XY-Scanner, the length of the light flash and the current of the LED are kept the same as for the previous event explained above. One notable feature visible in the event present in Fig. 5.13 is the satellite image appearing in the upper center of the FD camera. This or similar satellite images, often referred to as *ghosts*, were already observed before in various other measurements with e.g. a blimp [63] or an octocopter [40]. These satellite images have their origin in multiple reflections of photons at interior components of the telescopes. For the satellite images observed during the blimp measurements the signal contained within the ghost is of the order of ~0.5% of the total signal captured by the telescope camera [63]. An effect of such a magnitude may be explained by reflected photons of the camera surface hitting the mirror, then traveling towards the filter and getting reflected by the latter one, hitting again the mirror, and finally focused into a different pixel of the camera. This situation is depicted in the top sketch of Fig. 5.14. The reflectivity of the various optical components are roughly given as: $\rho_{\text{mirror}} \approx 0.85$, $\rho_{\text{filter}} \approx 0.15$, $\rho_{\text{PMT}} \approx 0.20$. This leads approximately to a probability of $p_4 \approx \rho_{\text{PMT}} \rho_{\text{mirror}} \rho_{\text{filter}} \rho_{\text{mirror}} \approx 2\%$ for a photon to be reflected four times between these

components. Nevertheless, the ghost observed in the CB event of Fig. 5.13 does carry a larger signal fraction of almost ~10% of the entire camera signal. Such a large signal fraction cannot be explained by the aforementioned fourfold reflections between camera, mirror, and filter. The better-fitting explanation is a reflection between camera and mirror only, as illustrated by the lower sketch of Fig. 5.14. The probability for a photon to be reflected off the camera and mirror is roughly $p_2 \approx \rho_{PMT} \rho_{mirror} \approx 17\%$, which may explain the observed larger signal fraction contained in the ghost image.

The explanations presented here are only very rough estimations and further investigations are required to fully understand the reflections within the telescope interiors.

5.6.2. REFLECTIONS AT CORRECTOR LENS

Photons, which enter the telescope in the outer regions of the aperture will cross the corrector lens, which has the purpose to reduce the spherical aberrations. We give more details on the design of the telescopes in Section 3.1. Nevertheless, a photon traveling through the corrector lens does also have the possibility to get reflected on the surface of that lens and thus will travel back towards the filter. Under this circumstances this photon, which was reflected at the corrector lens, will either leave the telescope through the filter or the photon gets reflected again on the filter glass. If the photon does not leave the telescope, but gets reflected at the filter and again travels towards the mirror, its direction might have changed in regard to a straight trough-going photon, since the surfaces of the filter and the corrector lens are not parallel.

This situation is illustrated in Fig. 5.15. In this sketch various trajectories of photons, which hit the aperture at different locations but under the same angle (here parallel to the optical axis of the telescope or 90° to the filter surface) are drawn in different colors and style. First, a photon, which does not pass through the corrector lens at all is drawn as a orange solid line. This photon travels straight towards the mirror and gets then reflected and focused into a certain pixel of the camera. A photon traveling through the corrector lens gets (by design and purpose of the lens) deflected by a small degree and then is focused by the mirror to the very same pixel, since all parallel incident photons will be focused to the same pixel of the camera by design of the telescope. The blue line in the sketch of Fig. 5.15 represents photons, which are first reflected at the corrector lens and then again at the filter, before the photons travel towards the mirror to get focused on the PMT camera. Because of this multiple reflections, the resulting trajectories (after the multiple reflection at the corrector lens and the filter) of the photons are not anymore parallel to their incident trajectories and therefore, the photons will be focused into a different pixel. Assuming the effect of the deflection via the multiple reflections is of the order of some degree, the photons will end up in one of the six adjacent pixels with regards to the pixel, which would have been hit if the photons were not deflected.

The consequence of these reflections between corrector lens and filter were already studied with simulations before, see for example Ref. [63].

We studied this effect in dedicated measurements with the CB source mounted on the XY-Scanner. We performed two dedicated measurements with the CB source at Los Leones in November 2019. At that time only the telescopes 3 and 4 of Los Leones were equipped with a XY-Scanner systems and we performed the measurement at the telescope 3. The positions of the light source for these two measurements were selected to be on two concentric circles with the two radii $r_{large} = 975$ mm (in the center of the corrector lens) and $r_{small} = 800$ mm (inner part of the aperture, outside of the corrector lens). In these circles the positions themselves were chosen in equal angular steps of 6° resulting in 60 positions on each of the two radii. In Fig. 5.15-top-right all positions of the CB light source for the two measurement runs are shown as blue/orange points of the larger/smaller radius. At each position of the two measurements, the CB was pulsed for $\Delta t = 5.0$ μs and the whole telescope camera was read out. The CB source was adjusted to point in the direction of pixel #209, which is located at column #10 and row #11 of the telescope camera. The pointing direction was not changed during or between these two measurements.

For each of the measurements the average signal S captured in each pixel of the camera is estimated and for a comparison we calculate the pixel-wise difference of the two measurements.
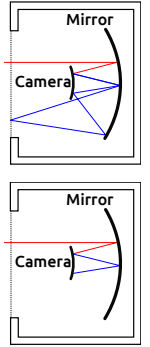
Figure 5.14: Sketches of light rays producing a satellite image on the FD camera. In red incoming and blue reflected rays. Adapted from Ref. [63].
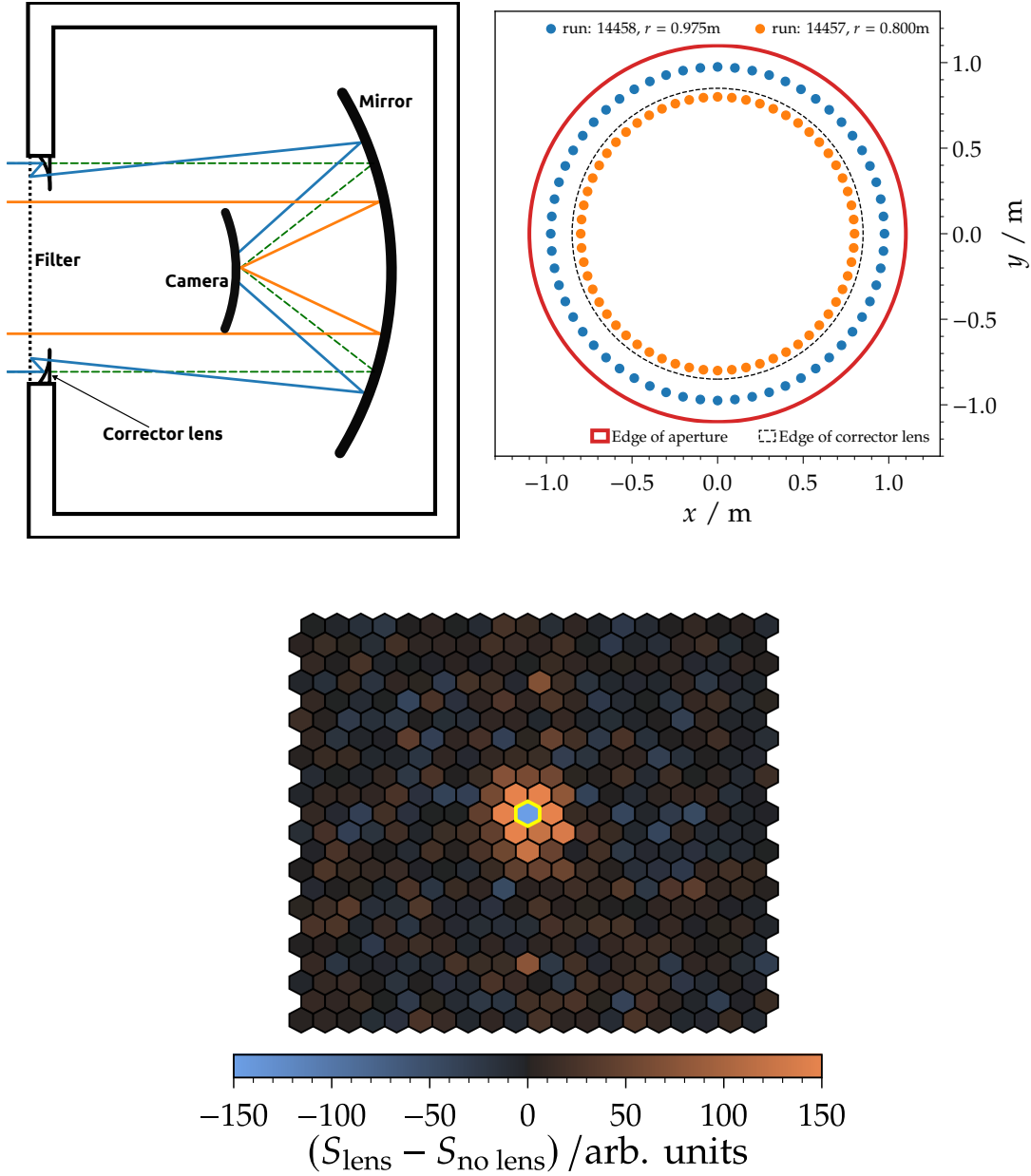
Figure 5.15: *Top left:* Illustration of the photon reflection between corrector lens and filter glass. The orange line represents a non-deflected photon. A photon, which gets diffracted by reflection is drawn in blue. Sketch is adapted from Ref. [63]. *Top right:* Positions of the CB source of the dedicated corrector-lens reflection study are drawn as orange and blue points. The red and black-dashed circles indicate the edges of aperture and corrector lens. *Bottom:* Difference of the signals S captured by each pixel between two CB measurements inside and outside of the corrector lens. The light-source positions of the two measurements are shown in the top-right plot. Pixel #209 is marked in yellow.

We show this difference in Fig. 5.15 as a pixel matrix.

Pixel #209, into which the CB source was pointed in both measurements, shows a significantly higher signal for the measurement of the CB outside of the corrector lens. This is either caused by the additional absorption of the corrector lens or different obscurance by the filter-holding structure at the different radii. Since this is not the main point of this small study, the actual reason was not investigated any further.

The main focus for this short study lies on the pixels, which surround pixel #209. We observe a larger signal in those pixels for the measurement where the CB source is moved on the larger radius inside the corrector lens.

We conclude that with this very small study we strengthen the effect of the lens-filter reflections, which was already studied in simulation [63].

CALIBRATION LIGHT SOURCES

Contents

In the following chapter we summarize the variety of calibration light sources employed by the XY-Scanner for the absolute calibration of the fluorescence telescopes. First we introduce the different light sources and explain their different characteristics, followed by a discussion of their emission properties. Finally we present a technique for the absolute calibration of the light sources.

6.1. IDEAL CALIBRATION LIGHT SOURCE FOR XY-SCANNER

The ideal light source for the FD calibration via the XY-Scanner technique is small enough to guarantee an uncomplicated transport of the source (a) between the different location of the telescope buildings on the observatory site and (b) between the observatory site in Argentina and laboratories in Europe for the characterization and the absolute calibration of the source itself. Ideally the light source fits into a carry-on luggage which ensures an uncomplicated and safe transport of the source by air traveling.

Even though a small physical size of the light source is desired, the emitting surface of the source is preferred to be as large as possible. With a large emitting surface the sensitivity to smaller impurities like dust or similar contamination of the optical components of the telescopes are reduced. Additionally, the required time for the scanning procedure of the telescope calibration measurements is inversely proportional to the area of the emitting surface, since a larger emitting surface requires less positions of the XY-Scanner to drive through to cover a sufficient fraction of the aperture area.

Furthermore, a homogeneous light emission across the entire emitting surface is desired, otherwise this calibration technique becomes sensitive to the impurities or features (like the support structure) of the telescope filter.

Next, the light source should be robust enough to withstand the rather rough measuring environment, but also light enough to be carried by the XY-Scanner systems. The weight limit of the XY-Scanner is on the order of ~2.5 kg [71].

Concerning the optical properties, the light output of the source is required to be very stable on a timescale of at least weeks, which is the typical duration of a on-site calibration campaign. Of course, the light source itself has to be absolutely calibrated. The directional emission of the source should ideally follow the Lambert's cosine law

$$I(\theta) \propto I_0 \cos \theta \tag{6.1}$$

with the emission along the optical axis being I_0 and the angle θ with respect to the optical axis. By design, in the FD data acquisition and reconstruction, the cosine dependence of the aperture-area projection is included into the calibration constant of each telescope pixel. If the light source has the same cosine dependence, these effects cancel and can therefore be ignored. See also the discussion in Section 3.2. Any deviation of the directional emission of the source away from the Lambert's cosine law has to be measured and has to be accounted for in the determination of the calibration constants of the telescope pixels.

6.2. Integrating Spheres as Light Sources

One type of light sources we employ for the calibration measurements with the XY-Scanner are sources assembled from general-purpose integrating spheres. Integrating spheres, often also called *Ulbircht spheres*[1], are hollow spheres, which have interiors coated with a diffuse and highly reflective material. Typical use-cases of integrating spheres are in reflectance and transmittance measurements of materials or in the studies of optical properties of other light sources, but they can also be employed as light sources themselves. Light entering such a integrating sphere is reflected by its interior walls and after several reflections within the sphere any spatial information of incident light is lost while, for an ideal sphere, the total number of incident photons is conserved. Due to these multiple reflections the flux of photons at any given area segment of the interior surface is the same everywhere. Therefore, the photon flux at any given small enough exit window is constant. The integrating sphere is thus a homogeneous extended uniform light source. For more details on integrating spheres, see e.g. Refs. [72, 73, 74]. The suitable utilization of a general-purpose integrating spheres as an extended uniform light sources is discussed in e.g. Ref. [75].

6.2.1. Integrating-Sphere Light Sources of XY-Scanner

The integrating spheres, adopted as light sources for the XY-Scanner calibration technique, are manufactured by the company Labsphere [76] and have an inner diameter of 5.3 inch (~13.5 cm). The interior surface of the integrating spheres is made of the diffuse reflecting material *Spectralon*, which shows a reflectance exceeding 98% for wavelengths between 500 and 700 nm [77]. In

---

[1]after the German engineer Richard Ulbricht
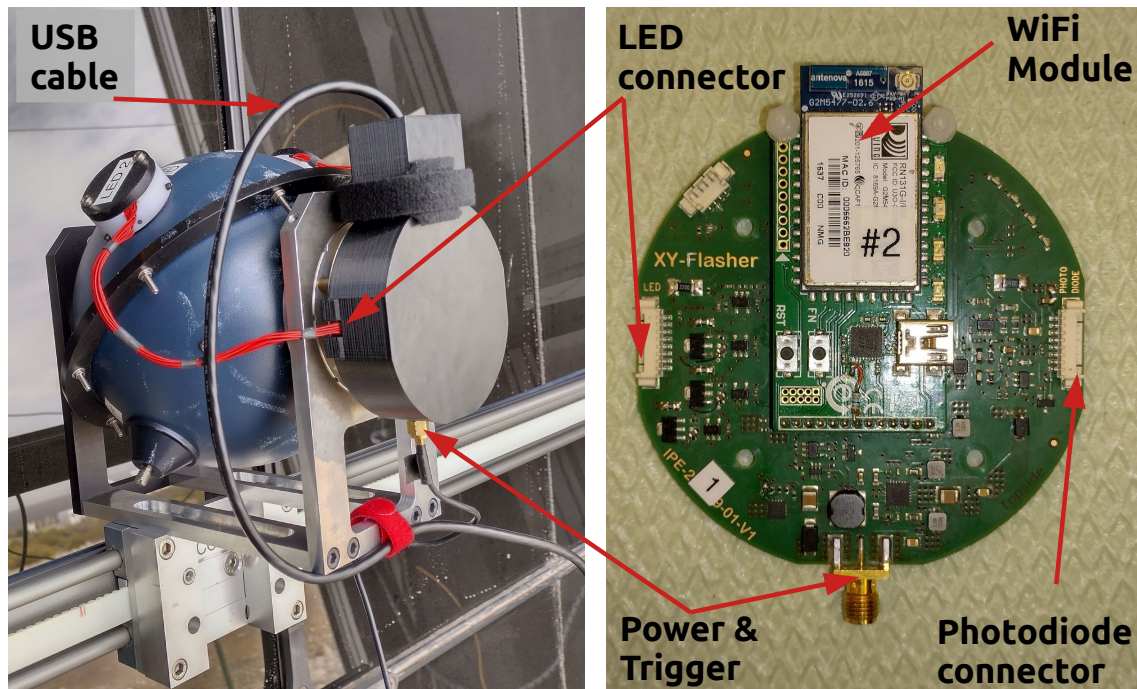
Figure 6.1: *Left:* Photograph of the integrating-sphere light source mounted in front of a telescope aperture on a XY-Scanner system. *Right:* Photograph of the light-source electronics. The electronics is located inside the black container on the back of the integrating sphere (left photograph). The standard electronics is equipped with a WiFi module, while this particular source on the left is equipped with a USB interface. More details can be found in the text.

the prototype phase of the XY-Scanner, we performed measurements with different integrating-sphere sources. These spheres are not only of different types and but also underwent different modifications and optimizations, as we explain below.

The first generation of spheres are of the type 4P-GPS-053-SL, while the type of the second generation of spheres is 3P-GPS-053-SL. Both generations of spheres are manufactured identically with the only difference being the number of exit ports. The first-generation sphere has an additional exit port which is not present in the models of the second generation. A more detailed discussion of the structural difference between the two sphere generations is given in Section 6.2.2.

The integrating spheres of all generations have one large exit port of 2.5 inch (~6.35 cm) diameter. According to Ref. [72] not more than 5% of the inner sphere surface should be covered by port openings. For this reason we decreased the exit port diameter to 2.0 inch (~5.08 cm) by means of a port reducer. The port reducer is a simple ring-shaped element, which is attached to the exit port of the integrating sphere to reduce the effective diameter of that port. There is also the possibility to further reduce the exit-port diameter to 1.0 inch but for the measurements discussed within this thesis, the exit ports were kept at 2.0 inch diameter. Additionally, two smaller ports with diameters of 1.0 inch (~2.54 cm) are positioned in a plane parallel to the exit port. During XY-Scanner calibration measurements at the telescopes these two smaller ports are equipped with the so called *heads* (explained below) while the exit port faces towards the aperture opening of the telescope. In Fig. 6.1-left we show a photograph of one calibration light source mounted onto the XY-Scanner stage. In the first generation of spheres an additional port of 1.0 inch diameter is present on the opposite side of the exit port. During most of the time and for all measurements discussed in the following this additional port was sealed with a port plug. The coating of the inner part of the port plug is the same material as the interior of the integrating sphere.

The aforementioned *heads* are plugs that carry various electronic components, which induce

light into the sphere and measure the light content inside of the integrating sphere. For all measurements and all integrating spheres discussed within this work, the integrating sphere is equipped with two different heads. To monitor the pulse-to-pulse stability of the integrating sphere itself, one head holds a Hamamatsu S1336-44BQ photodiode (PHD). The other head is equipped with two or three (depending on the head generation) light-emitting diodes (LEDs) of the type UVLED365-110E made by Roithner Lasertechnik [78]. According to the manufacturer [79], the peak emission of the LEDs is at a wavelength of $\lambda \approx 365$ nm with a spectrum half width of ~15 nm at $T = 25°$C. The change of the peak wavelength with temperature can be read-off a graph in Ref. [79] and is approximated to be $d\lambda/dT \approx 0.04$ nm/K. The LEDs installed within the LED head are not operated simultaneously since each of the LEDs has its own purpose. By design, the first LED is operated for test measurements in the laboratory, the second one works as tracker for ageing effects of the other LEDs as well as the interior material of the integrating sphere itself, and the third LED is the actual light source used for calibration measurements at the FD telescopes. For later generations of the LED heads the number of LEDs was reduced to two, as explained below. All components located in these heads, the LEDs and the PHD, are anchored into temperature stabilized copper disks which are heated and stabilized at 30°C. Heating of the cooper disks is performed by a common 2N2222A transistor and both copper disks are equipped with a TMP37F temperature sensor to constantly monitor and regulate the heating. The temperature setting is chosen to be well above the excepted ambient air temperature during night at the FD sites in the Argentinian Pampa and also above the typical temperature of laboratories in Europe. Thus, it is sufficient to provide heating to the heads to keep them at 30°C and the necessity to equip the heads with a cooling structure is eliminated. Including an additional cooling system into the heads would make their design much more complex while increasing drastically the overall power consumption of the light source.

Monitoring and regulating the temperatures, digitizing the PHD signal, as well as operating the LEDs is accomplished by a microcontroller of the MSP430 family. This microcontroller and all other required electrical components are installed onto a printed circuit board which is located outside the integrating sphere. The black plastic box attached to the back of the integration sphere in Fig. 6.1-left contains this circuit board and the microcontroller on it. A photograph of the source electronics is shown on the right side of Fig. 6.1. A single coaxial cable provides 24 V power to the board and in addition serves as trigger line. In addition the sphere electronics is equipped with a RN131 wireless LAN module, which allows communication with the sphere electronics without the need of additional cables. Setting up the parameters of the light source and transferring data is archived through this wireless connection. The wireless LAN module can easily be replaced with a USB serial interface. Due to wireless network restrictions in the laboratory and due to unstable wireless communications for measurements at the observatory site, after the November 2019 campaign we decided to completely switch to the USB serial interface for all calibration light sources. See the discussion in Section 4.1.

6.2.2. OPTIMIZATIONS OF INTEGRATING-SPHERE LIGHT SOURCES
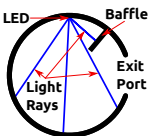
Figure 6.2: Sketch of the integrating sphere. Adapted from Ref. [80].

As mentioned above we used mainly two generations of integrating spheres as light sources for the measurements with the XY-Scanner at the telescopes of the observatory. In the following we discuss their constructional differences.

The first generation of spheres is an unmodified version of the 4-port integrating-sphere (type: 4P-GPS-053-SL) as bought and delivered from Labsphere. For the second generation of spheres a slightly different type was acquired. This 3P-GPS-053-SL type has, in contrast to the 4P-GPS-053-SL, only 3 ports but is otherwise identical.

The original versions of the general purpose integrating spheres (as manufactured by Labsphere) are equipped with an internal shielding structure which prevents all light induced from a light source mounted into one of the ports to directly leave the integrating sphere through the exit port without any internal reflections. This shielding, also called *baffle*, is illustrated in the sketch of the integrating sphere in Fig. 6.2 and is visible inside the sphere on the photographs in Fig. 6.3. The baffle is made of the same material as the other sphere interior and is mounted inside the
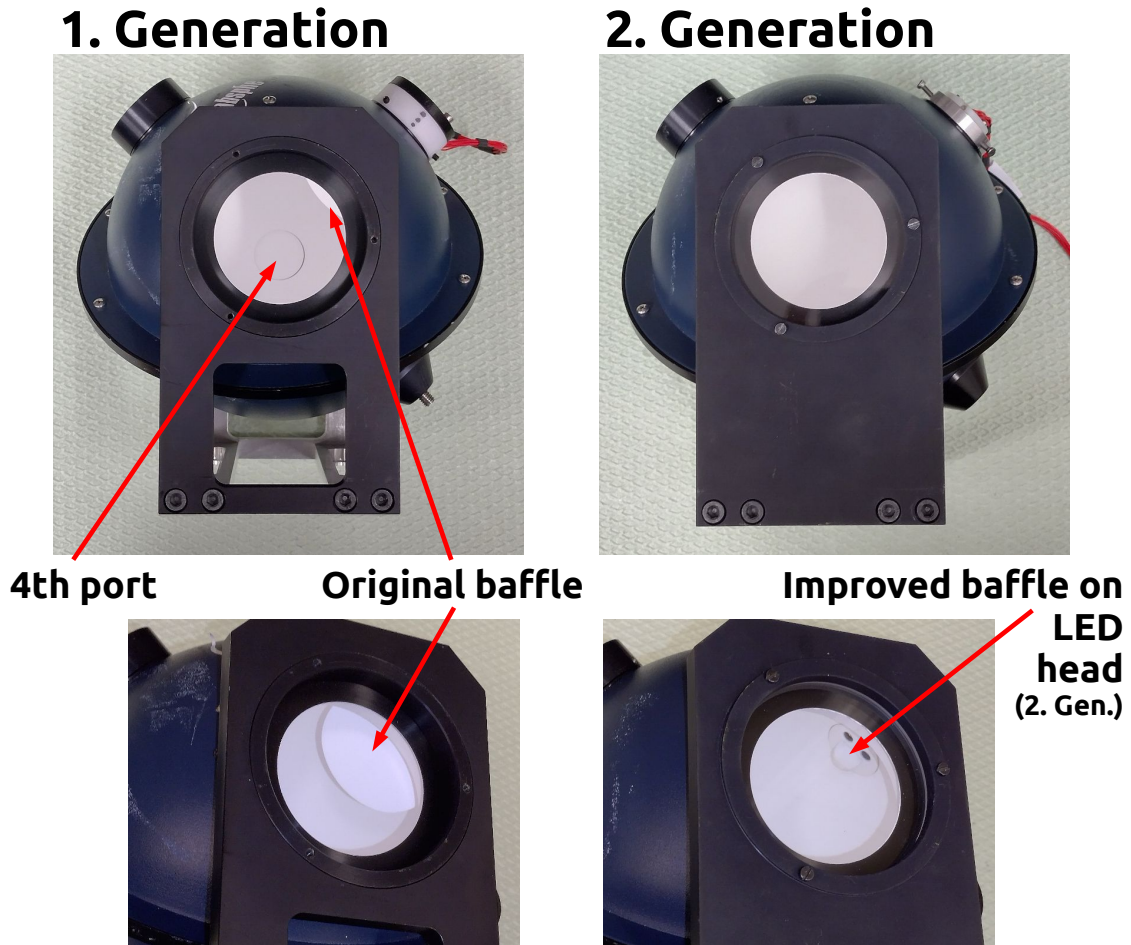
Figure 6.3: Photographs of the different generations of integrating-sphere light sources. The first-generation sphere with the original large baffle and the fourth port is displayed on the left. The right side shows the second generation of spheres including a second-generation LED head carrying the improved smaller baffle.

sphere next to the port into which the LED head plug is inserted. While this baffle is serving as a shield for direct light, it also introduces unfavorable side effects, as it is influencing the emission pattern of the integrating-sphere light source. We discussed the emission profiles of the sources in Section 6.5. Therefore, the second generation of spheres were mechanically modified to optimize their emission profiles. The optimal modifications were developed and performed by our collaborators at the Joint Laboratory of Optics of Palacký University and Institute of Physics of the Czech Academy of Sciences in Olomouc, Czech Republic and are summarized in the following.

First, to reduce the inhomogeneities induced by rather large physical size of the baffle, its size is reduced to a minimum and thereby the improved baffle shields the direct light emitted from only one of the LEDs carried by the LED head. Since only one LED is operated at the time, it is sufficient to only shield that LED and keep the remaining LEDs unshielded. Due to the much smaller size of the optimized baffle, it is possible to install this baffle directly onto the LED head next to one of the LEDs. The optimal size and position of the smaller baffle were estimated via simulations of the integrating sphere by our colleagues from Olomouc [80]. With this much smaller baffle planted next to one of the LEDs, the larger baffle of the original sphere design is removed completely for the second generation of the integrating-sphere light sources. The photographs in Fig. 6.3 show the different generations of integrating spheres. Another improvement made to the second

1. Generation

2. Generation
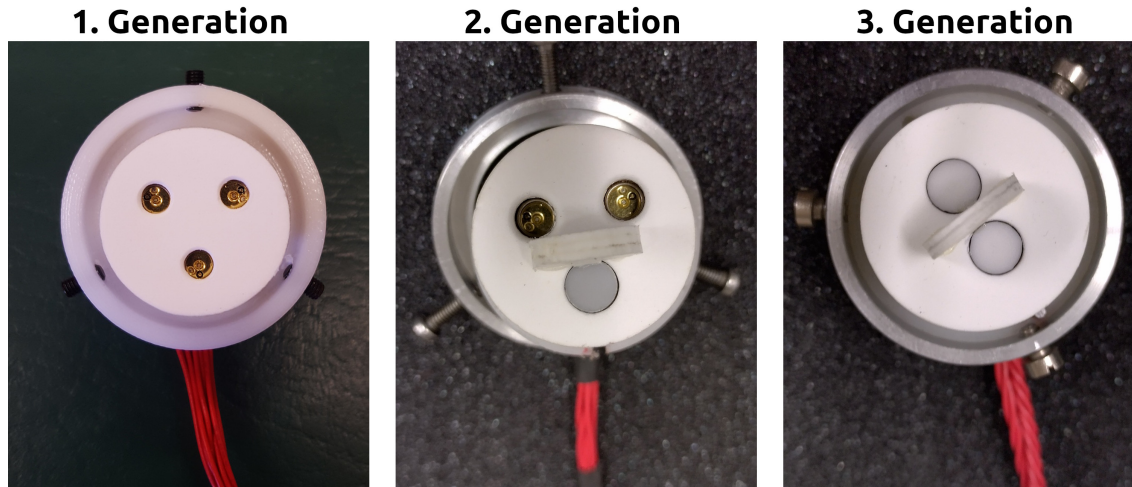
3. Generation

Figure 6.4: Photographs of the three different generations of LED heads for the integrating-sphere light sources employed for the XY-Scanner calibration measurements. A detailed description of each generation is given in the text.

generation of integrating spheres is to add a protective glass layer covering the exit port. With such a glass cover the interior of the integrating sphere is well protected against external contamination like dirt or dust.

As mentioned, the required size of the improved baffle is small enough to place it directly onto the LED head, as a consequence several generations of the LED heads were developed, designed, and constructed. In the following the different generations of LED heads are introduced and described. The basic components for all generations are the same, so far every generation employs LEDs of the type UVLED365-110E from Roithner Lasertechnik. Although, there are ongoing efforts to build additional LED heads employing LEDs emitting at different wavelengths, those efforts are not discussed further here. The heating element and the temperature sensor are also of the same type for all generations. In Fig. 6.4 photographs of the three generations of LED heads are shown.

Starting with the photograph on the left side of Fig. 6.4, the first generation of LED heads is shown. This generation employs three LEDs arranged in a triangle with a distance of ~20 mm between the LEDs. The heating transistor is located in the center of the triangle. A sketch of the layout for the first generation LED heads is displayed in Fig. 6.5-top. This transistor and the copper plate which holds it and the LEDs are not visible in the photograph since they are covered by the white masking. This first generation of LED heads is only used in combination with a first generation sphere, since the larger baffle inside the integrating sphere is mandatory to shield direct light emitted from the LEDs of the first generation heads leaving the sphere.

The second generation of LED heads is displayed in the center photograph of Fig. 6.4. Heads of this generation include also three LEDs planted in the same layout as for the first generation. But for this generation a shielding baffle is placed directly on the LED head. Additionally, to further advance the homogeneity of the emission profile of the sphere, a thin layer of a diffusive transmitting material (opal glass) is mounted into the LED head covering the LED shielded by the baffle. The other two LEDs are unmodified and kept as for the first generation. Since two of the three LEDs are not shielded by any baffle, only the one LED behind the baffle is used in measurements, which renders the other two LED more or less useless.

On the very right side of Fig. 6.4 we show a photograph of the third generation LED heads. Additionally, its layout is sketched in Fig. 6.5-bottom. For this third generation of heads the number of LEDs contained within the head is reduced to two, which are placed symmetrically to the center of the head. With such a design it is sufficient to mount a single baffle between the
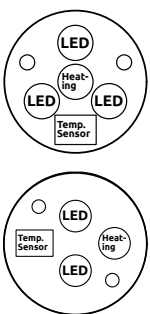
Figure 6.5: Sketches of the layouts for the different (*top*: 1st and 2nd, *bottom*: 3rd) generations of LED heads.

Figure 6.6: Photographs and schematic drawings of the tube source as an alternative approach of an uniform calibration light source for the XY-Scanner.

two LEDs and thus, depending on the orientation of the head within the sphere, one or the other LED is shielded. Again, both LEDs of the third-generation head are covered by thin layer of opal glass.

The integrating-sphere light sources we used for the measurements discussed throughout this thesis are: (a) the first generation sphere with a first generation LED head, the so called *KIT sphere* and (b) a second generation sphere equipped with a second generation LED head, which we will refer to as the *Olomouc sphere*. The names of the sources are given by the different groups who designed and constructed the sources. So far we performed no measurements employing a third generation LED head.

6.3. ALTERNATIVE APPROACH FOR UNIFORM LIGHT SOURCE

The most time-consuming factor for the XY-Scanner measurements at the FD telescopes is the readout of the camera, which takes more than ~1 s for all 440 pixels. Since the telescope camera is readout for every position where the light source is flashed on the XY-Scanner, reducing the number of positions will directly result in a shorter measuring time at the telescope, which is desired in general. If we want to reduce the number of positions but still keep a high coverage of the telescope aperture, we need to have a larger emitting surface of the light source. For integrating spheres the size of the exit port depends on the diameter of the entire sphere. To still get a homogeneous emission of the sphere the area of its exit port must not exceed a certain fraction of the inner sphere surface [75]. Due to limited space around the apertures of the Auger FD telescopes and transport limitations it is not possible for the XY-Scanner (in its current setup) to employ larger integrating spheres.

Therefore, in the following we present a different approach for a calibration light source. The aim of this alternative approach is to design and construct a light source with a significantly larger emitting surface, while still having a homogeneous emission across its entire surface and, more importantly, a directional emission following Lambert's cosine law as close as possible. The design of the alternative light source has the shape of a tube with a single LED on its optical axis on one side, while the other side of the tube is covered by a diffusive transmitting material. Because of its shape in the following we refer to this alternative light source as the *tube source*.

We tested several materials and found that the best fitting diffuser for our purpose was a white diffusing glass made by Edmund Optics [81]. The largest available white diffusing glass [82] from Edmund Optics has a diameter of 10 cm and thus, the area of the emitting surface of the prototype of the tube source was defined by the dimension of this diffuser.

For the LED of the tube source we used the same type of LEDs which are employed in the integrating-sphere light sources, the UVLED365-110E made by Roithner Lasertechnik [78]. According to the technical datasheet [79] of this LED the relative radiant intensity drops to below ~95% for radiation angles larger than ~22°. To archive a homogeneous illumination of the entire diffuser area while still keeping the source compact, we adjusted the distance between the LED and the diffuser to ~12 cm.

The tube itself as well as most parts of the source are made of a 3D-printed PLA (polylactic acid), which makes the manufacturing of this source much more cost efficient than for integrating-sphere sources. Because of its modular design we are able to basically mount any type of a diffuser or similar material onto the tube source as long as the material has a diameter of 10 cm. Mechanically, the source is designed to fit onto the same holding structure as the integrating spheres, which allows us the easy exchange of the different sources in all setups. Photographs of the tube source are shown in Fig. 6.6. The diffusing glass is mechanically held in place by a 3D-printed ring which is attached to the tube source and fixed by four screws. The black ring and the screws are also visible in the left photograph of Fig. 6.6. To hold the diffuser in its position an overlap between the ring and the diffuser disk is required, therefore the inner diameter of the ring is slightly smaller than the diameter of the diffuser disk. Therefore, the effective diameter of the emitting surface of the tube source is measured to be $d_{ts} = (97.3 \pm 0.2)$ mm and we thus calculate its area to be $A_{ts} = (74.4 \pm 0.3)$ cm^2. This is a factor ~3.5 larger than emitting surfaces of the integrating spheres.

To archive a more uniform emission across the surface of the tube source and to increase its total light output, we covered all interior walls of the source with a reflective paint. We applied three layers of the reflective paint EJ-510 [83] from Eljen Technology [84], which has an approximated reflectivity higher than ~50% at $\lambda \approx 365$ nm. The EJ-510 is not the ideal choice to cover the source interior, but it was available in the laboratory and easy to apply. Nevertheless, we observed an increase of ~35% in the total light output of the tube source after applying the reflective paint. A detailed study of the uniformity of emission across the emitting surface of the tube source was not yet performed, but is planned for the foreseeable future.

For a thermal stabilization, the LED is mounted and glued into a 6.0 cm diameter and up to 0.2 cm thick copper disk. This copper disk is equipped with a similar heating transistor and temperature sensor as the LED heads for the integrating-spheres, which allows us the straightforward use of the same light-source electronics for all calibration sources. The temperature-regulation algorithm in the source electronics firmware is custom-tailored for the heat reservoir of the cooper disks installed in the LED- and PHD-heads of the integrating-sphere light sources. Due to the different size of the heat reservoir in the tube source (copper disk with diameter ~2.5 cm vs. ~6.0 cm), we had to adjust and optimize the temperature regulation in the firmware of the light-source electronics.

We tested the behavior of the temperatures of the copper disks holding the LED in climate chamber in the laboratory. The climate chamber was set to temperatures $T = 0°C, 10°C, 20°C$ and we performed measurements with two different versions of electronics firmware, but identical hardware. The only difference between the firmware versions are a different implementations of the temperature control loop. The temperatures were measured by the internal temperature sensors glued onto the copper disk and are shown in Fig. 6.7, where each of the panels displays
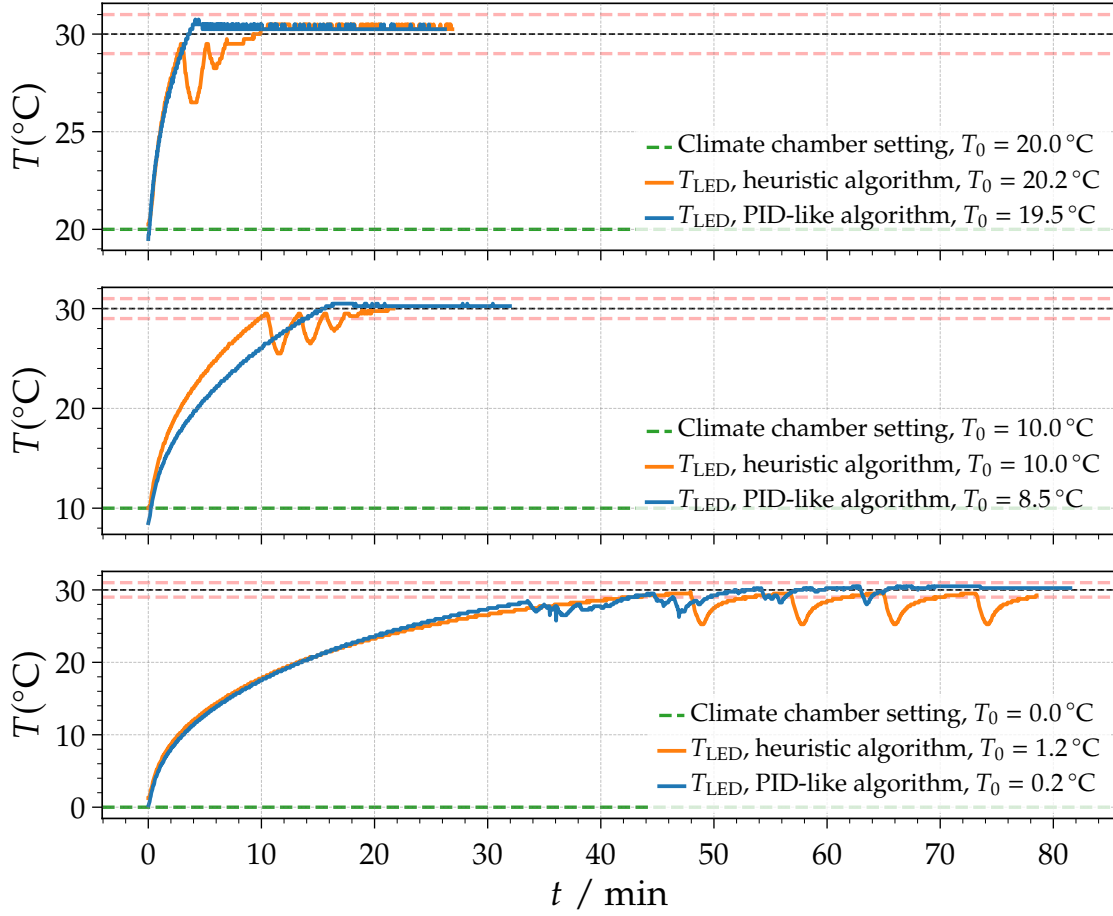
Figure 6.7: Temperatures of the LED copper disk for different temperature regulation algorithms. For these measurements the tube source was placed inside the climate chamber. Different temperature settings of the climate chamber are shown in the three panels.

the data for different temperature settings of the climate chamber.

Temperatures captured with the unmodified firmware, which uses a heuristic temperature control loop custom-made for copper disks within the LED (and PHD) heads of the integrating spheres, are shown as orange line in Fig. 6.7. For the lowest temperature setting of the climate chamber (0°C) this temperature regulation is able to heat the LED to the working point of 30°C, but it cannot keep the temperature stable at 30°C. We observe regular temperature drops of $\Delta T \approx 5\,\mathrm{K}$ every $\Delta t \approx 8\,\mathrm{min}$, as visible in the bottom panel of Fig. 6.7. To avoid these unstable temperatures of the LED, we implemented a different temperature-regulation algorithm in the electronics firmware. We implemented a control loop similar to a proportional-integral-derivative (PID) controller. Therefore, the heating power setting can be written as

$$P_{\mathrm{heat}} \propto K_{\mathrm{p}}\,T(t) + K_{\mathrm{i}} \int_0^t T(t')\,\mathrm{d}t' + K_{\mathrm{d}}\,\frac{\mathrm{d}T(t)}{\mathrm{d}t} \tag{6.2}$$

with the PID-coefficients K_{p}, K_{i}, and K_{d}. For the implemented algorithm we approximated the integral term of Eq. (6.2) by the sum of a certain fraction of previous temperature measurements and the derivative term by a parameter containing the difference between the current temperature and the previous measured one. After several iterations of tuning the PID-loop, we found suitable values for the parameters K_{p}, K_{i}, and K_{d}, for which the algorithm manages to heat and keep the

temperature of the LED at the working point. Additionally, we observe that the PID-like control loop reaches the working point faster than the heuristic algorithm and with hardly any transient oscillations.

Concluding, we designed and constructed a viable alternative approach of a uniform light source for the XY-Scanner which has an emitting surface ~3.5 times larger than the integrating-sphere light sources. Employing such a light source directly reduces the time we need to perform the calibration of a FD telescopes by approximately the same factor.

6.4. BRIEF OVERVIEW OF XY-SCANNER LIGHT SOURCES

KIT Sphere: Integrating sphere of the first generation. Was used in all campaigns, thus most data with this source is available. Type: 4P-GPS-053-SL. Unmodified, large baffle. Only first generation LED heads.

Olomouc Sphere: Integrating sphere of the second generation. Type: 3P-GPS-053-SL. Original baffle removed. Second and third generation of LED heads can be equipped. Exit port is covered by protective glass. Used in the Autumn 2019 and Autumn 2022 XY-Scanner campaigns, but only with second generation LED head.

KIT Sphere #2:   Integrating sphere of the second generation. Type: 3P-GPS-053-SL. Original baffle removed. Third generation of LED heads can be equipped. Exit port is covered by protective glass. So far never used in any measurements discussed within this thesis.

Tube Source: Not an integrating sphere, but 3D-printed alternative approach. Larger emitting surface than the integrating-sphere light sources. Developed in 2021/22 and first data taken at the observatory in the Autumn 2022 XY-Scanner campaign.

6.5. EMISSION PROFILE OF CALIBRATION LIGHT SOURCES

The light sources we employ for the calibration measurements with the XY-Scanner are introduced above in Section 6.2 and Section 6.3. For a closer study of the optical properties of the employed light sources and to estimate the emission pattern of the sources we designed and assembled a dedicated setup in a optical laboratory at KIT. In the following we present this setup, the performed measurements, and obtained results.

6.5.1. EXPERIMENTAL SETUP

For the underlying structure of the laboratory setup we use two optical benches. The two benches are of identical design, both are 2.5 m long and arranged in a straight horizontal line separated by a ~2.8 m gap. Thus, the two benches are equivalent to one larger optical bench of ~7.8 m, with the gap at its midpoint. We adjusted and confirmed the height of both benches and their horizontality via observations with a theodolite. The maximal deviation between various space points on both benches we observed is on the order of a millimeter.

To study the optical properties of the light sources, we equip one of the benches with a photomultiplier tube (PMT) as a light detector, while the light source is mounted at a distance of ~5.3 m on the other optical bench. We chose this particular distance to roughly match the distance between the light source installed on the XY-Scanner and a pixel-PMT of the telescope camera. Photographs and a schematic drawing of the setup are shown in Fig. 6.8.

We digitize the signal output of the PMT with a PicoScope 6404D digital oscilloscope [85]. This type of an oscilloscope has an analog-to-digital-converter (ADC) resolution of 8 bit and a bandwidth of 500 MHz. The voltage range of the PicoScope is set to ±100 mV and the baseline was moved by setting an analog offset to 70% of the voltage range, to obtain a better use of the
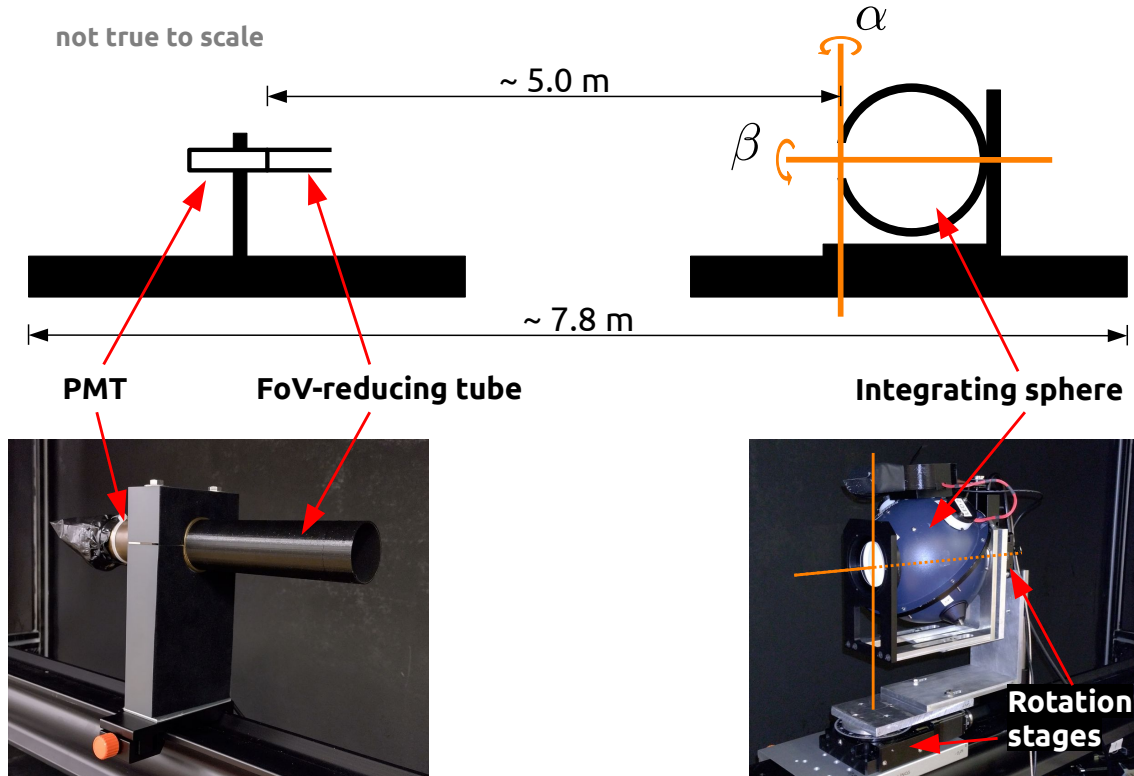
Figure 6.8: Schematics and photographs of the experimental setup for study of the optical properties of the light source. This setup was installed at the optics laboratory of IAP at KIT.

rather small ADC dynamic range. For each trigger arriving at the PicoScope a 1000-bin trace with a sampling period of 100 ns is captured. Thus, the resulting trace is 100 μs long, equal to the traces captured by the pixels of the FD telescopes. To ensure the entire pulse is captured within the trace the pre-trigger fraction of the trace is set to 15%. The PicoScope is connected to the data acquisition (DAQ) computer via USB. This DAQ computer does not only store the captured data, but also performs the steering of the mechanical components of the setup and manages the communication with the light-source electronics, as we explain below.

For cost optimizations, we did not acquire a new PMT for the setup, but we rather chose the PMT for the setup out of a variety of available PMTs at the laboratory. Due to the impossibility of the FD pixel-PMTs operation without the entire FD DAQ chain, which cannot be built for the setup here, the FD PMTs had to be discarded from the possible choices. We took two different types of PMTs into closer consideration. The first PMT is of the type 9107QB [86], manufactured by ET Enterprises [87], and was previously employed by the FUNK dark-matter experiment [88]. The second PMT is an EMI 9902KSB25FL tube, which is a remnant of the KASCADE experiment [89]. The company ET Enterprises nowadays manufactures also the brand of PMTs previously made by EMI Electronics [90], thus the EMI 9902KSB25FL tube is equivalent to a ET Enterprises 9902B tube [91]. Therefore, the EMI 9902KSB25FL tube is for the sake of simplicity called 9902B tube in the following. The quantum efficiency for all considered PMTs is similar and on the order of ~28% at the light-source wavelength of 365 nm. After extensive studies of the linearity of the PMTs, described in Appendix A.3.1, we decided to employ the 9902B tube as detector for this setup. The operating high voltage is set to 1400 V and the current flow is limited to 500 μA. The geometrical size of the entrance window for the 9902B PMT is 38 mm in diameter, which matches very well the entrance-window size of the FD PMTs. In the following the 9902B tube is, again for

the sake of simplicity, referred to as PMT. The PMT is mounted in a specially constructed holder as visible in the photograph in Fig. 6.8. The front side of that holder, which is facing towards the light source, is covered with a non-reflecting flock paper to avoid any reflections. To also reduce the sensitivity of the PMT to potentially reflected photons within the experimental area, its field-of-view (FoV) is reduced by attaching a ~15 cm-long plastic tube, as indicated in Fig. 6.8. For all measurements discussed in the following, if not stated otherwise, the operating voltage of the PMT is set to 1.4 kV and we switched on the high-voltage supply several hours before the actual data taking has started.

The integrating-sphere light source is located on the other side of the setup. The integrating sphere is mounted onto an L-shaped metal structure as visible in the photograph in Fig. 6.8, but the versatile setup allows us the straightforward mounting of the light source as discussed in Section 6.3. This L-structure is equipped with two rotational stages made by Standa [92], which enables independent rotation of the light sources around two axes. One of the rotation axes is vertical, going through the center point of the exit window of the light source. This rotation is performed by an 8MR191 motorized rotary stage. The other rotation axis is the optical axis of the light source itself (normal vector of the exit-window surface through the exit-window center) and this rotation is carried out by a motorized rotary stage of the 8MR151 type. Both rotational axes are indicated by the orange lines in Fig. 6.8. In the following, we denote the rotation around the vertical axis by an angle α and the rotation around the optical axis by an angle β, as indicated in the schematics in Fig. 6.8. For the orientation of $\alpha = \beta = 0°$ the light-source exit-window surface and the PMT entrance-window are parallel, while for the integrating-sphere light source the LED- and PHD-head are in exactly the same position as for measurements at the FD telescopes. The two rotation stages are connected to a Standa 8SMC5-USB-B9-2 two-axis motor controller which itself is connected through USB to the DAQ computer.

The light source itself is operated by its own electronics board as described in Section 6.2. Due to network restrictions in the experimental area it was not possible to host a wireless network and establish a wireless communication between the DAQ computer and the light source. Therefore, we connected the light-source electronics via USB to the DAQ computer. For most of the measurements discussed in the following and if not otherwise stated, flashing the light source is triggered internally by the sphere electronics and the trigger is then forwarded to the PicoScope to initiate capture of the PMT output. On the DAQ computer a custom-developed software manages setting up and reading of the parameters of operation for the light source, acquiring and storing the data captured by the PicoScope, and steering of the two rotation-axes motors.

6.5.2. EMISSION PROFILE OF KIT INTEGRATING SPHERE

With the experimental environment being set up, we performed the first measurements of the KIT integrating sphere in 2021. For these measurements, we observe the emission of the light source with the PMT for various orientations of the sphere. The number of photons reaching the entrance window of the PMT is directly proportional to the collected charge Q and therefore we use the relative charge $q = Q/Q_{\alpha=0°}$ as a proxy for the intensity of the light source in any other given direction. We show the relative charge q collected by the PMT as a function of the rotation angle α and five different settings of β in Fig. 6.9. The measurement procedure is the following: For each of the five β orientations, α was scanned from $\alpha_{min} = -90°$ to $\alpha_{max} = +90°$ in steps of $\Delta\alpha = 1°$ for $|\alpha| < 20°$ or else $\Delta\alpha = 2°$. At each orientation the light source was flashed 500 times for 5 μs with a LED current of 2.7 mA, the pulsing period was set to 0.1 s. The LED under test was LED #2, which is the very same LED used for calibration measurements at the observatory site. These settings of the light-source parameters are equivalent to the parameters we set up for the calibration measurements at the FD telescopes, except the pulsing period is larger at the telescopes since the readout of the 440 pixel-PMTs requires significantly more time than the single PMT in the laboratory. A test of the influence of the pulsing period (flashing frequency) is attached in Appendix A.3.2.

In Fig. 6.9 we present the measured emission profile of the KIT integration sphere. In this plot, the different colored lines represent different rotations β of the light source around its optical
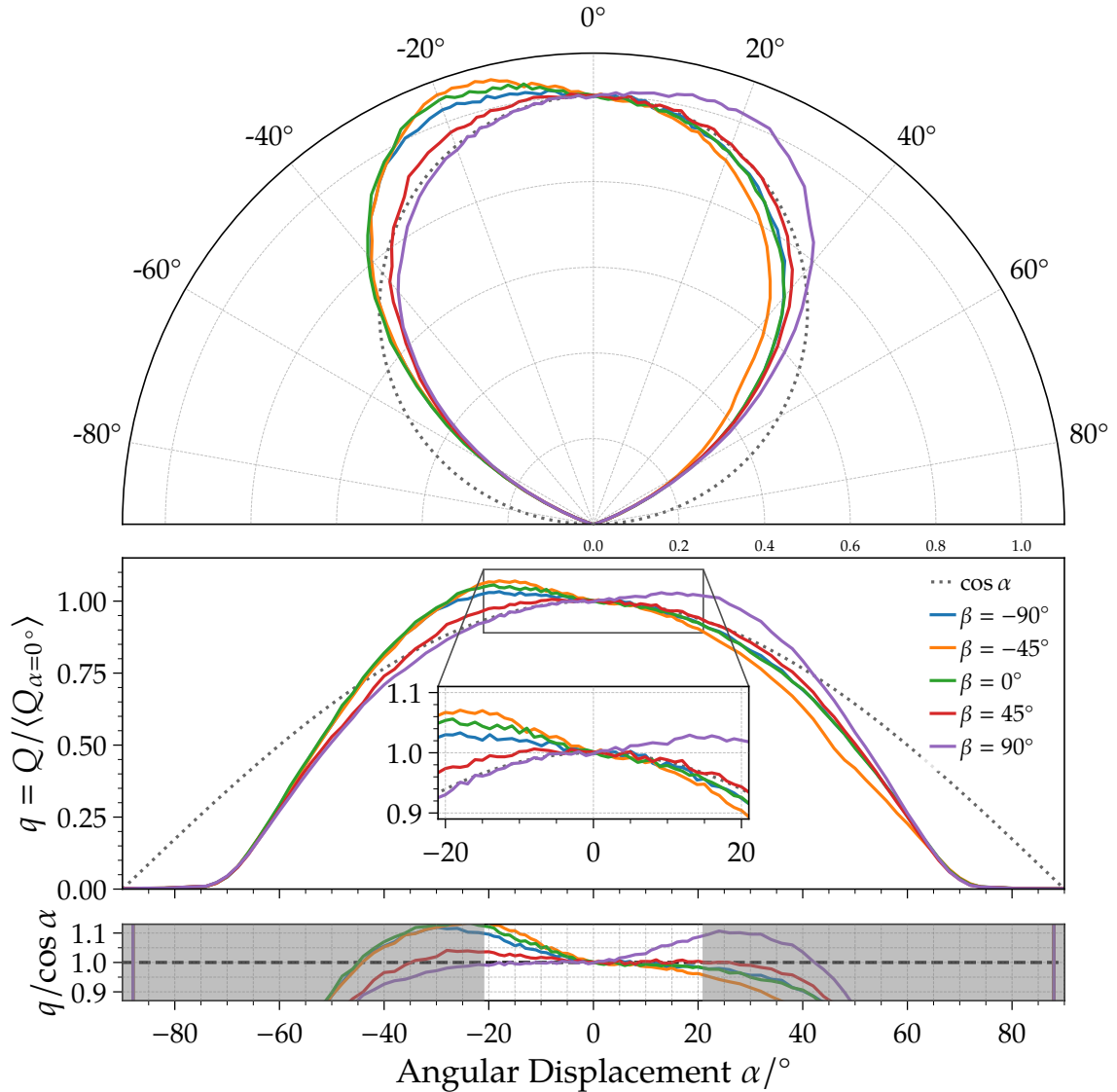
Figure 6.9: Measured emission profile of the KIT integrating sphere (first generation sphere with first generation LED head). LED #2 was flashed for this data. Plotted are the relative charges collected by the PMT for $-90° \leq \alpha \leq +90°$ and $\beta = \{0°, \pm45°, \pm90°\}$. The expected profile of an ideal Lambertian light source ($q \propto \cos\alpha$) is plotted as gray dotted line.

axis. The two upper plots in the Fig. 6.9 display the same data, but for a better illustration in different representations. The most relevant part of the measurement is the emission into the angular acceptance of a FD telescope ($|\alpha| \lesssim 21°$). We show this part as a zoomed-in inset.

For an ideal Lambertian emission of the light source, we expect the observed intensity to be proportional to the cosine of the viewing angle, in particular $I \propto q \propto \cos\alpha$. This case is plotted as gray dotted line in Fig. 6.9. The ratio of the measured relative charge q and the expectation for ideal Lambertian emission is plotted in the bottom plot of Fig. 6.9. The gray shaded area illustrates the parts outside the angular acceptance of a telescope.

Depending on the rotation β around the optical axis, we observe a deviation on the order of up to ~10% between the measurement and the expectation for an ideal Lambertian emitter within the angular acceptance of an Auger FD telescope. We attribute this observed deviation
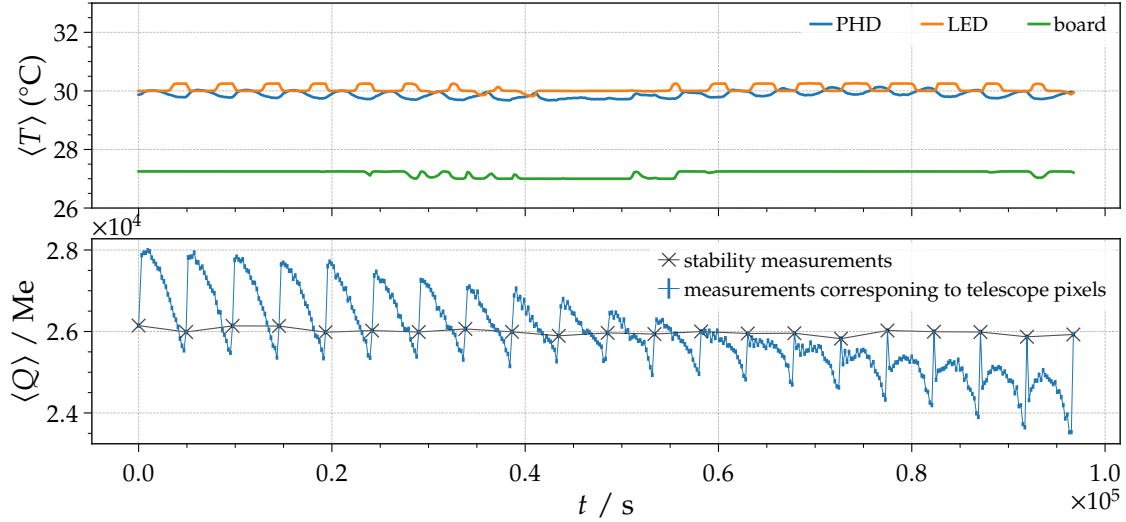
Figure 6.10: Various quantities captured during an emission scan of the KIT sphere light source, each data point represents the mean of 1000 captures. *Top:* Temperatures measured during the data taking at the electronics board, LED-head, and PHD-head. *Bottom:* Mean charge accumulated in the PMT for each measurement and its standard deviation are drawn in blue. In black the control measurements at $\alpha = \beta = 0°$ are shown.

to be a consequence of the large shielding baffle (introduced in Section 6.2) which is installed in the KIT integrating sphere (first generation of spheres). This hypothesis is strengthened by the fact that we observe the closest agreement of data and expectation at the rotation $\beta = 45°$. For this particular orientation the LED head and therefore also the baffle are at the top position in the sphere, and we thus expect to observe a minimal influence of the baffle. On the contrary, the maximal deviation is observed while the sphere is rotated to $\beta = -45°$. Here the LED and baffle lie in the scanning plane and therefore the maximal effect of the baffle is excepted. This observed deviation of the KIT-sphere emission from the ideal cosine dependence will directly introduce an under- or over-estimation of the calibration for the telescope pixels of the same order of magnitude.

In the following we present a procedure for individually measuring the emission into the direction observed by each telescope pixel and thus directly estimate a correction for the non-Lambertian emission of this light source on a telescope-pixel level.

Emission into Direction Observed by Telescope Pixels. We use the same experimental setup to measure the directional emission of the light source into the direction observed by each pixel of the telescope camera. Therefore, we calculate the measuring angles α_i and β_i that correspond to telescope pixel i as

$$\alpha_i = \varphi_i \sqrt{\left(\frac{\delta_i}{\varphi_i}\right)^2 + 1} \qquad \text{and} \qquad \beta_i = -\text{atan2}\left(\delta_i, \varphi_i\right) \tag{6.3}$$

with[2] the azimuth φ_i and the elevation δ_i of pixel i of the camera according to Eq. (3.9) and Eq. (3.8) with the telescope axis set to $\alpha_m = 0°$ as we explain in Section 3.2.

For the measurement we present here, we employed the KIT Sphere. It was flashed 1000 times at each of the 440 pairs of angles (α_i, β_i). We kept the current for the LED constant at $I_{\text{LED}} = 2.7\,\text{mA}$, the pulse length fixed to $t_{\text{pulse}} = 5\,\mu\text{s}$, and we set the flashing frequency to $f = 10\,\text{Hz}$. These are

---

[2] $\theta = \text{atan2}(x, y)$ gives θ with $-\pi < \theta \leq \pi$, for $\theta = \arctan(x/y)$
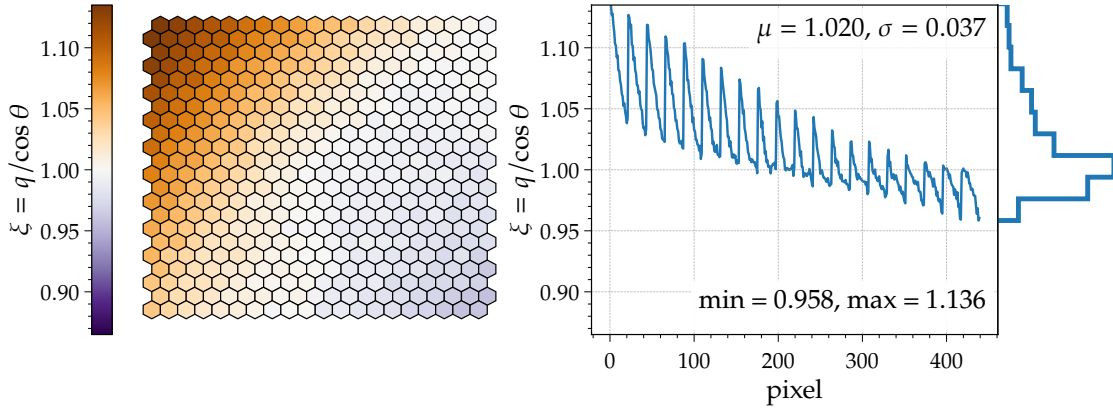
Figure 6.11: Measured correction factor ξ of the KIT integrating-sphere light source for each pixel of the FD camera. *Left:* ξ as pixel matrix. *Right:* ξ is shown as linear plot over the pixel number. The distribution of ξ is drawn at the right edge of the plot while the mean μ, standard deviation σ, and minimal and maximal value are printed within the plot.

the same parameters we set for measurements at the telescopes, except the flashing frequency is lower due to the time needed to readout an entire telescope camera (~ 1.2 s). For an estimate of the stability of the measurements, we additionally rotate the light source to the $\alpha = \beta = 0°$ orientation after each completed 22 positions (corresponding to a column of pixels of the telescope camera). Here also 1000 flashes are fired. We show various quantities captured during that measurement in Fig. 6.10. The temperatures of all components (LED, PHD, electronics board) are stable within $\Delta T = \pm 0.25$ K during the entire duration of the measurement.

For the stability measurements at $\alpha = \beta = 0°$ we estimate the average charge collected by the PMT to be $\langle Q_{\alpha=\beta=0°} \rangle \approx 25\,990$ Me with a standard deviation of 82 Me. The maximal and minimal measured charges differ less than 0.7% from the average. We therefore conclude that the signal output of the PMT is stable for the entire duration of the presented measurement.

Since the charge Q collected by the PMT is proportional to the number of photons reaching its entrance window, we use this charge directly to calculate a correction factor for the discrepancy between the emission of the light source and an ideal Lambertian emitter. Therefore, we first normalize the charge to the average $\alpha = \beta = 0°$ measurement and we define $q = Q/\langle Q_{\alpha=\beta=0°} \rangle$. We then obtain the correction factor ξ by building the ratio of the relative charge q and the cosine of the pixel zenith angle θ. We show the estimated correction factors ξ for the KIT sphere light source in Fig. 6.11. We observe a maximal correction of $\sim 14\%$, but on average the correction factor is compatible with one. Without applying this correction, the calibration constants for pixels in the upper left (in the representation of Fig. 6.11-left) corner, would be underestimated by more than 10%. While the pixels in the opposite corner would experience an overestimation of 4%.

Emission Profile for Simulation. For an accurate simulation of the emission of the integrating-sphere light sources we need to precisely know their directional emission. For an ideal Lambertian source the directional emission pattern is known, but as we show above, we observe a significant deviation of the first generation integrating-sphere light source (KIT sphere) form an ideal Lambertian emission. Therefore we performed a dedicated measurement to estimate the emission of the light source at combinations of orientations with $-32° \leq \alpha \leq 32°$ and $-90° \leq \beta \leq 90°$. The light source parameter were kept as above: pulse length of 5 µs, 2.7 mA LED current, and 0.1 s flashing period.

We transform the laboratory angles α and β to the azimuth angle θ and the zenith angle φ
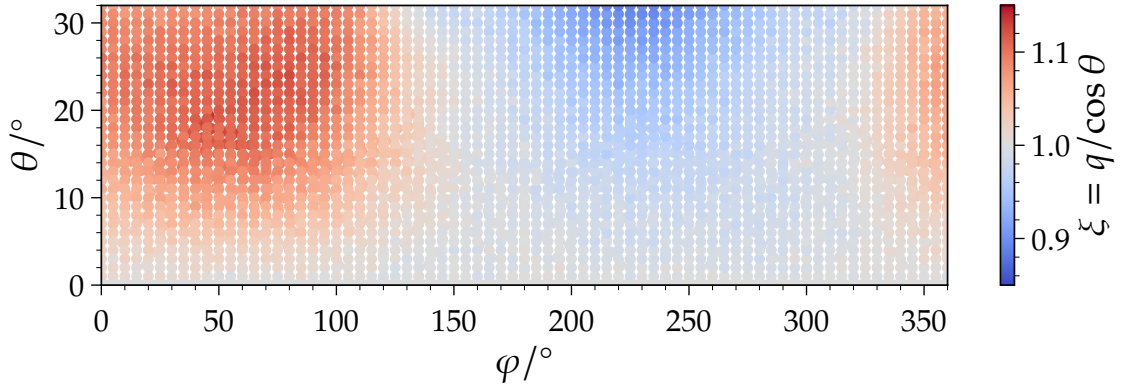
Figure 6.12: Dedicated measurement of the directional emission of the KIT integrating-sphere light source.

relative to the optical axis of the integrating sphere itself. We thus calculate θ and φ as

$$\varphi = \begin{cases} \beta + 270°, & \text{if } \alpha > 0 \\ \beta + 90°, & \text{if } \alpha \leq 0 \end{cases}$$ (6.4)

$$\theta = |\alpha|.$$ (6.5)

In Fig. 6.12 we show the measured correction ξ to the Lambertian emission. A linear interpolation between this data points is used to implement the source emission profile into the XY-Scanner simulation, see Section 4.4.3.

6.5.3. EMISSION PROFILE OF IMPROVED INTEGRATING SPHERE

Similarly to the measurements of the KIT sphere described in Section 6.5.2, we studied the emission profiles of the optimized integrating-sphere light source (introduced in Section 6.2.2). We mounted the second-generation sphere together with the second-generation LED head (Olomouc sphere) into the same setup and performed a measurement scan with the same settings for the angles α and β. For light-source parameters we set the flashing frequency to $f = 10\,\text{Hz}$, the pulse duration to $t_{\text{pulse}} = 5\,\mu\text{s}$, and the LED current to $I_{\text{LED}} = 15.9\,\text{mA}$. For the measurements presented here, only LED #2 was flashed. We choose the LED current again to match the value we set for the calibration measurements at the FD telescopes. Note that the LED #2 of the second generation of LED heads is covered by an opal glass disk and therefore the LED current has to be drastically increased in comparison with the KIT sphere to archive a comparable light output of the sources. In addition, we mounted the sphere in a way the $\alpha = \beta = 0°$ is equal to the orientation on the XY-Scanner. Particularly for this source this means that the LED head is at the top position of the sphere.

The results of measuring the emission profile are shown in the top plots of Fig. 6.13. As mentioned above, for an ideal Lambertian source we expect the intensity to decease with the cosine of the viewing angle. We plot this ideal behavior again as gray dotted line in Fig. 6.13. Compared to the unmodified first-generation integrating sphere (KIT sphere, Fig. 6.9) we observe a profile which closely matches an ideal Lambertian profile. Within the angular acceptance of an FD telescope ($|\alpha| \lesssim 21°$) we observe a maximal deviation of ~2.7%. Even though the size of the baffle for this integrating sphere is drastically reduced and the homogeneity is thus increased, we still observe the influence of the LED position on the emission profile. Specially for the $\beta = \pm 90°$ orientation we observe an excess of ~5% at $\alpha \approx 30°$. However, the maximum of this excess lies outside of the angular acceptance of an FD telescope.

For this source we also measure directly the emission into the direction observed by the telescope pixels and we calculated a correction factor ξ for the deviation from the cosine dependence.
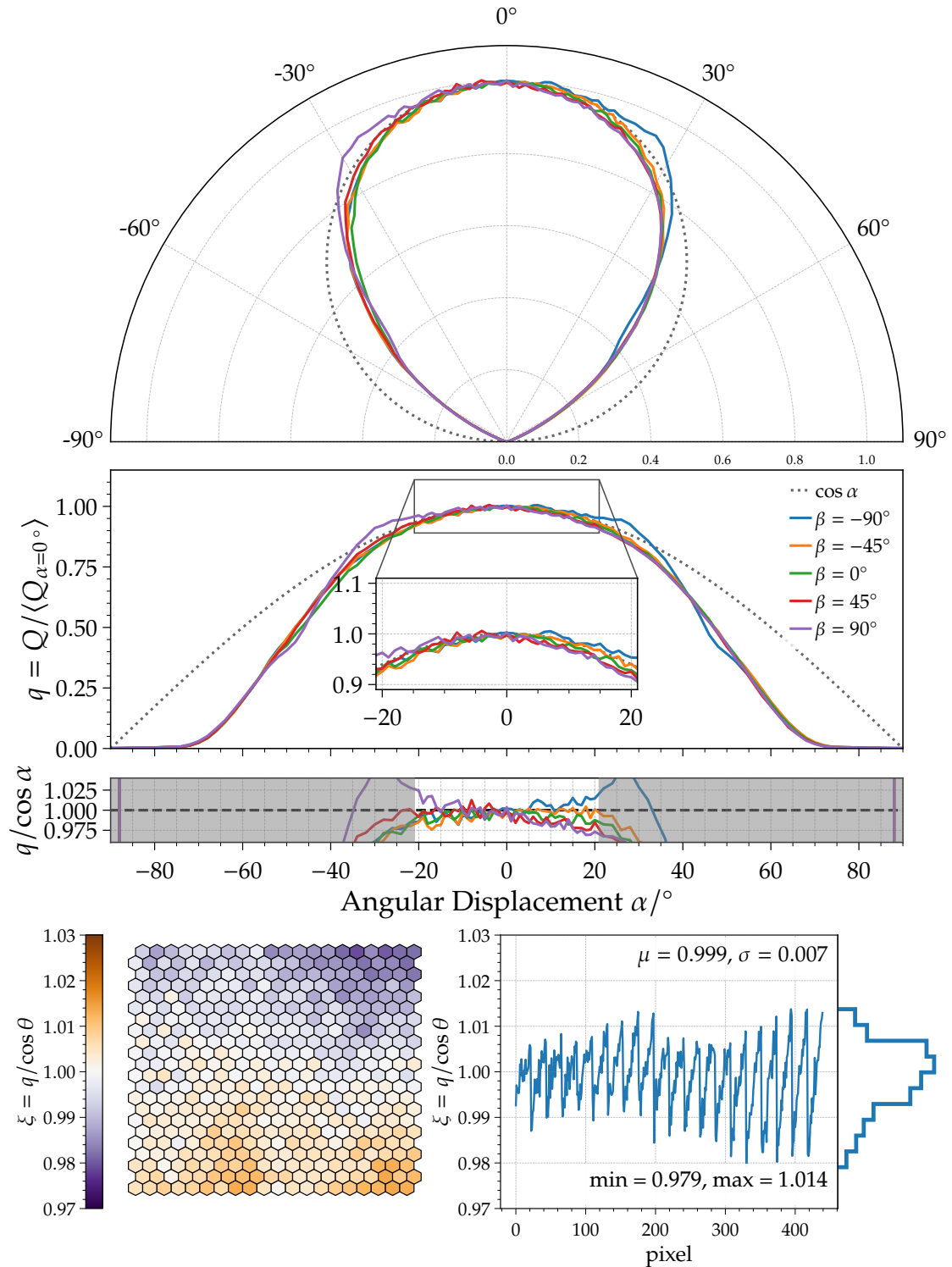
Figure 6.13: *Top plots:* Measured emission profile of the second-generation integrating sphere. Plotted are the relative charges collected by the PMT, similar to Fig. 6.9. *Bottom plots:* Estimated correction of the source emission to an ideal cosine dependence. Similar to Fig. 6.11.
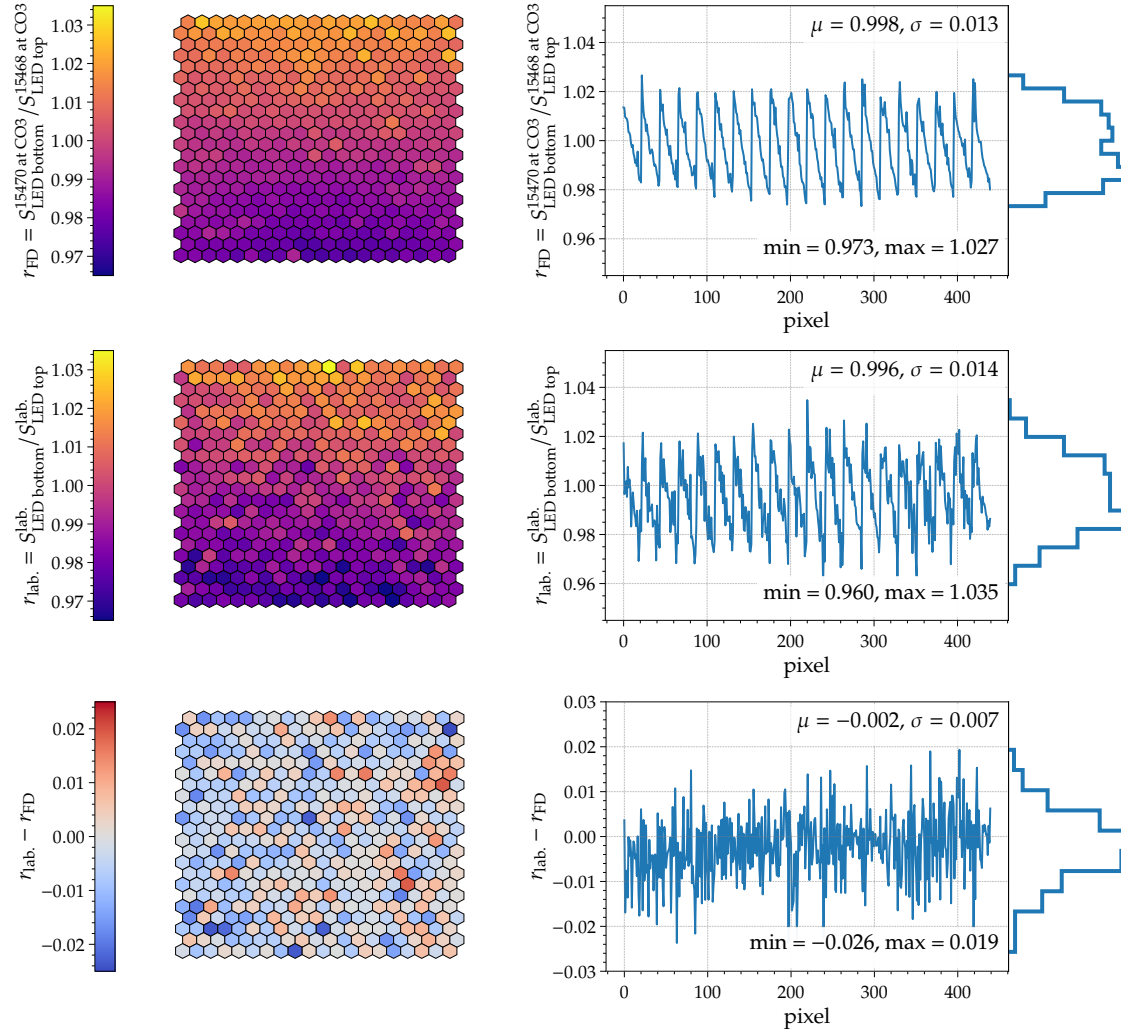
Figure 6.14: *Top:* Ratio of the telescope-pixel signal for XY-Scanner measurements with the improved integrating-sphere light source (Olomouc sphere) with the LED located either at the top or bottom position. *Middle:* Similar to the top-row plots, but here the data was taken in the laboratory setup (explained in Section 6.5) by rotating the source and observing the emission into the direction seen by the telescope pixels. *Bottom:* Difference between the laboratory and telescope measurements.

We estimate the stability of the measurements by comparing the average charges collected by the PMT at $\alpha = \beta = 0°$. We calculate the average charge to $\langle Q_{\alpha=\beta=0°} \rangle \approx 28\,193$ Me with a standard deviation of 90 Me. The maximal and minimal measured charges differ less than 0.7% from the average.

We show the estimated correction factor in the bottom of Fig. 6.13. We observe a maximal correction factor ξ for the Olomouc sphere of ~2%, while on average the correction factor is compatible with one. Due to the LED being located at the top position of the sphere, we observe a vertical gradient in the correction factor. Therefore, we would overestimate the calibration constants for the top part of the camera, while the bottom part would be underestimated. Top and bottom refer to the representation of Fig. 6.13.

Additional Measurements with Rotated Light Source. For the Olomouc sphere we additionally performed dedicated measurements at the FD telescopes to investigate the directional emission properties of this light source. We performed XY-Scanner measurements with this improved integrating-sphere source in different orientations of the latter. We took data of four standard XY-Scanner calibrations scans with the light source rotated each time by 90°, thus the LED of the source was located in the top/left/right/bottom positions. This light source is mounted in a holder which enables us the straightforward rotation of the integrating sphere around its optical axis without the need to remove the source from the XY-Scanner. We present the effects of a rotated source in Fig. 6.14. Herein, the signal ratio per telescope pixel of the two measurements with the LED in the top and bottom position is plotted in the top row. We present a similar study with the LED at the left and right positions in Fig. 6.15. We observe a vertical gradient in the ratio throughout the entire camera with a maximal deviation of ~2.7% for the pixels at the highest and lowest edge of the camera. On average, for the whole camera the ratio is compatible with one. For a comparison and as a crosscheck we performed a similar measurement at the rotation setup in the optics laboratory at KIT. We measured the light emission from the source with the LED in the top and bottom position into the direction observed by each of telescope pixels, similarly as described above. The ratio of the two laboratory measurements is displayed in the middle row of Fig. 6.14. We observe a similar gradient as for the measurement at the FD. The statistical noise in the laboratory measurements may be reduced by repeating this measurement with a larger number of flashes per pixel orientation. The presented laboratory data only contains 200 flashes per pixels, which is ~12% of the flashes in a standard XY-Scanner measurement. In the bottom row of Fig. 6.14 we show the difference between the laboratory and telescopes measurements and we estimate the average difference to be in agreement with zero.

Fig. 6.15 presents equivalent measurements of the same source for the LED being located at the left or right position in the source. The top row shows the measurement at the telescope, the center row illustrates the laboratory measurement, and the bottom row displays the difference between the two measurements. We observe a horizontal gradient in the captured image of the telescope camera with a similar magnitude (±2%) as for the previously shown measurements. Also here the average difference between the telescope and the laboratory measurements are compatible with zero.

From these measurements we draw two conclusions. First, the emission of this light source is not homogeneous into the direction of all pixels of an FD telescope. We observe a gradient with a magnitude of roughly on the order of ±2%. And second, the difference between the measurements performed at the setup in the optics laboratory and at the FD telescopes on site is on average compatible with zero, validating the alignment of the laboratory setup.

We use these measurements in the laboratory and at the FD telescopes to estimate the uncertainty on the correction factor ξ. Since we observe an average difference of ~0.3%, we conclude and define the uncertainty of ξ to be less than 0.5%.

6.5.4. Emission Profile of Tube Source

For the tube source (introduced in Section 6.3) we performed a similar set of measurements in the laboratory setup as for the integrating-sphere light sources. We set the flashing frequency of the source to $f = 10\,\mathrm{Hz}$ and the pulse duration to $t_{\mathrm{pulse}} = 5\,\mu s$. For the LED current we choose $I_{\mathrm{LED}} = 20\,\mathrm{mA}$, for this current setting we observe approximately the same signal in the PMT as for the integrating-sphere sources at their nominal current setting. We choose this current also for the measurements at the FD telescopes. We present the results of this measurements in Fig. 6.16. Herein the top plots show the relative charge collected by the PMT for different orientations of the light source. We observe a maximal deviation of ~1.7% between the light source emission and the excepted cosine dependence.

In the bottom part of Fig. 6.16 we again present the results obtained by measuring directly the emission into the directions observed by each FD telescope pixel. Here we obtain an average ratio of the relative charge q and the cosine of the pixel zenith angle $\cos\theta$ which is compatible with one. We estimated a maximal correction factor of 0.981 for the pixels on the right edge of
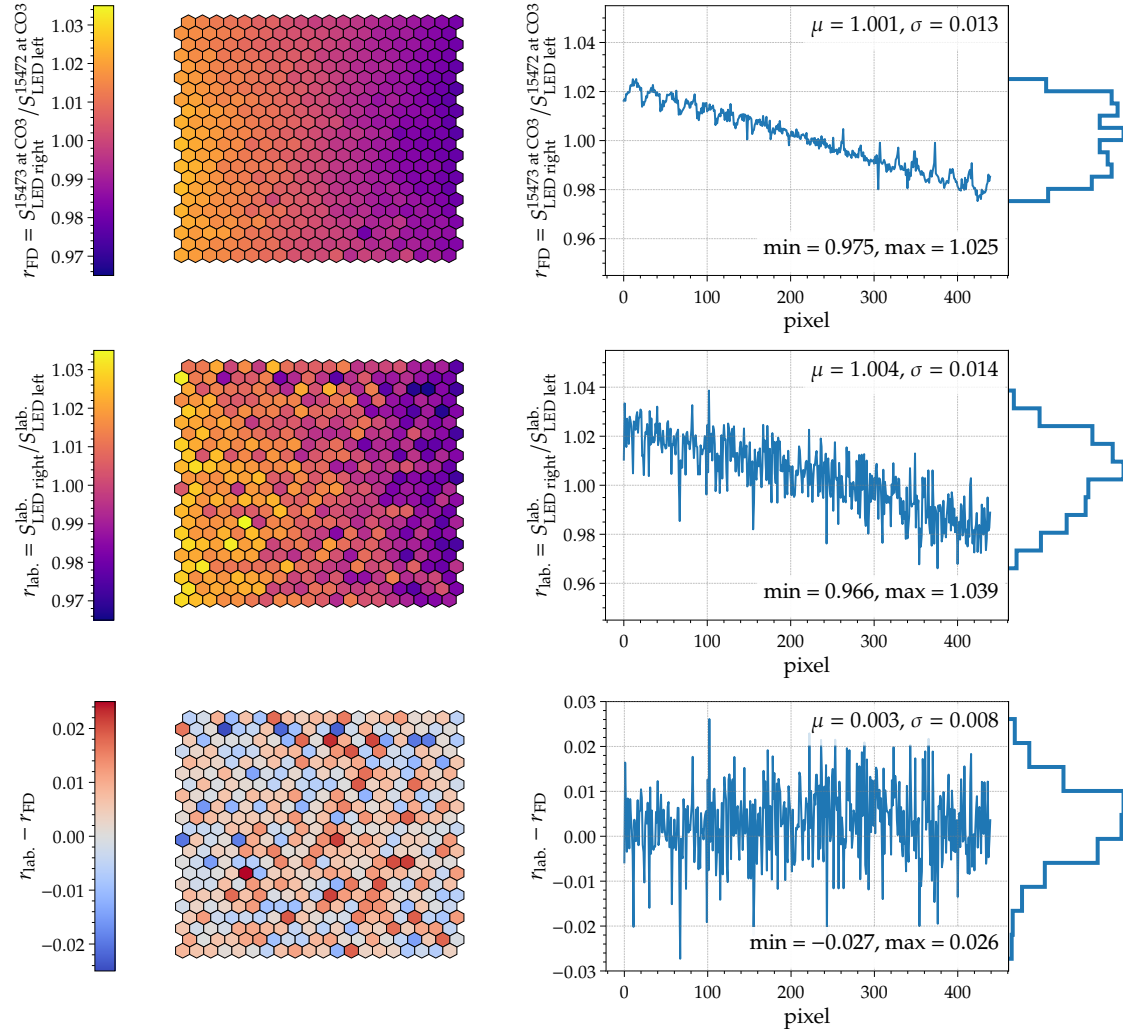
Figure 6.15: Plots equivalent to Fig. 6.14, but with the LED of the integrating sphere located either at the left or right position.

the camera.

The accumulation of pixels with the smaller corrections ξ on the right side of the camera and the discrepancy at $\alpha \approx 20°$ (Fig. 6.16-top) suggests a possibly slight misalignment of the optical axis of the source and the detector for this measurement.

From these measurements we conclude that the emission of tube source shows the closest agreement with an ideal Lambertian emitter, considering all discussed calibration light sources.

6.6. EMISSION SPECTRA OF CALIBRATION LIGHT SOURCES

We measured the spectral emission of all calibration light sources in the laboratory with an Ocean Optics [93] SD2000 spectrometer. This type of the spectrometer has a sensitive wavelength range from 200 nm to 850 nm. The uncertainty of the spectrometer wavelength was measured in the year 2000 by the manufacturer and we show this calibration results in Appendix A.4.1. Within the region of interest (~250 nm to ~450 nm) the maximally measured derivation is 0.11 nm.

Since this calibration measurement was performed more than 20 years ago, we inspect the spectrometer wavelength calibration in a dedicated measurement. For this we coupled a gauged

Figure 6.16: *Top plots:* Measured emission profile of the tube source. Plotted are the relative charges collected by the PMT, similar to Fig. 6.9. *Bottom plots:* Estimated correction of this source emission to an ideal cosine dependence. Similar to Fig. 6.11.
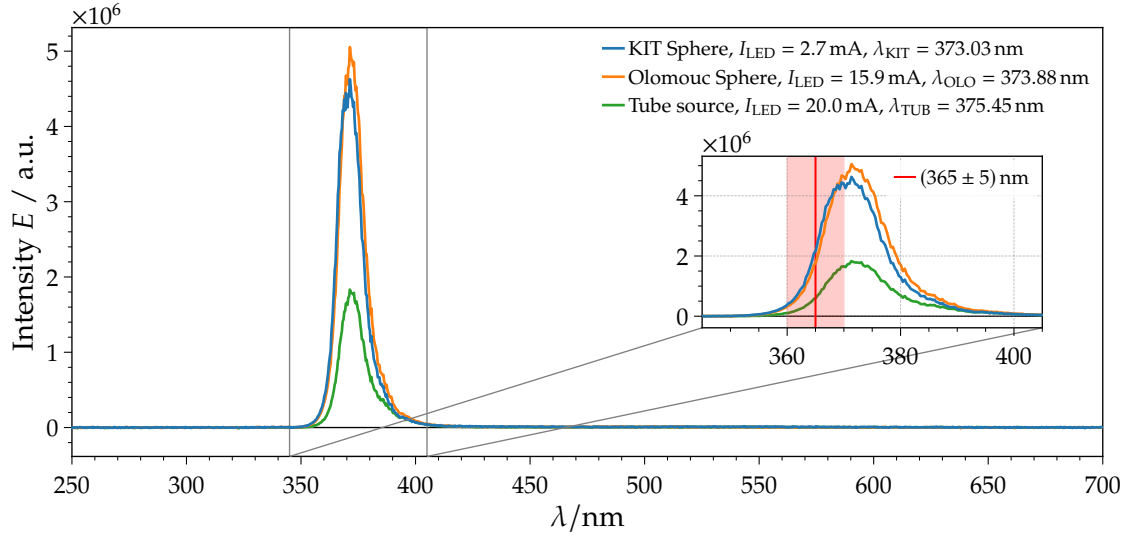
Figure 6.17: Light emission spectra of the XY-Scanner calibration light sources measured with an Ocean Optics [93] SD2000 spectrometer. Different color lines represent different sources. The wavelength range of the typical emission peak for this type of LEDs (360 to 370 nm) is drawn in red in the zoomed-in inset.

Mercury-Argon light source to the input of the spectrometer and recorded the spectrum. We present the results of this measurement in Appendix A.4.1. We observed an offset of $\Delta\lambda \approx 1\,\text{nm}$ between the expected emission lines of the light source and the measurement obtained from the SD2000 spectrometer. In the following we correct all spectrometer measurements by this measured offset and we assume an accuracy of the SD2000 spectrometer to lie within 2 nm.

All XY-Scanner calibration light sources are equipped with same type of LED, UVLED365-110E made by Roithner Lasertechnik [78]. According to the data sheet of this type of LED [79] the peak wavelength emission λ_p lies between 360 nm and 370 nm and is typically located at ~365 nm. The spectrum half width is given as ~15 nm at $T = 25°\text{C}$.

In Fig. 6.17 we show the measured emission spectrum of the three calibration sources: the KIT sphere, the Olomouc sphere, and the tube source. We define the effective wavelength of the sources as

$$\lambda_\text{src}^\text{eff} = \frac{\int_{340\,\text{nm}}^{440\,\text{nm}} \lambda\, E_\text{src}(\lambda)\, \text{d}\lambda}{\int_{340\,\text{nm}}^{440\,\text{nm}} E_\text{src}(\lambda)\, \text{d}\lambda} \tag{6.6}$$

with the measured spectral intensity E_src of each source. The effective wavelengths are printed within Fig. 6.17 and listed below

$$\lambda_\text{KIT sphere}^\text{eff} = (373 \pm 2)\,\text{nm} \tag{6.7}$$

$$\lambda_\text{Olomouc sphere}^\text{eff} = (374 \pm 2)\,\text{nm} \tag{6.8}$$

$$\lambda_\text{tube source}^\text{eff} = (375 \pm 2)\,\text{nm} \tag{6.9}$$

These measurements show that the effective wavelengths of all sources are in agreement with each other, but we observe the peak emission slightly above the range provided by the manufacturer of the LEDs. We assume an uncertainty on the wavelength measurements of 0.5%.
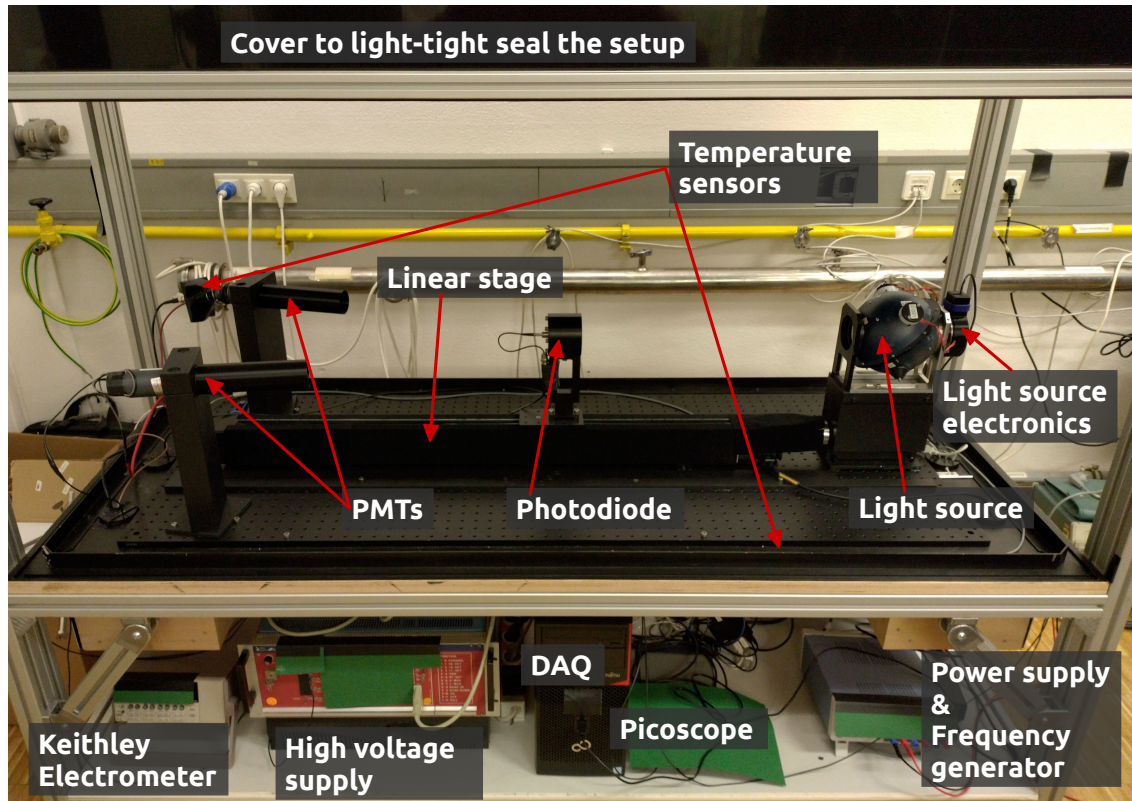
Figure 6.18: Photograph of the absolute-calibration setup of the XY-Scanner light sources installed in the IAP laboratory at KIT. Crucial components of the setup are labeled.

6.7. Absolute Calibration of Light Sources

In the following we introduce a method for the absolute radiometric calibration of the light sources. First, we describe the components we employed for the experimental setup and describe the measuring procedure, then we discuss the analysis, and we conclude by giving absolute calibration results for the light sources employed for the XY-Scanner.

6.7.1. Experimental Setup

The basic idea for the radiometric calibration setup is to employ an absolutely calibrated photodiode to estimate the radiance of the light source. Photodiodes are ideal detectors for measuring the photon flux emitted from rather strong light sources in continuous operation mode. However, for the absolute-calibration measurements of the FD telescopes on site, we need to operate the sources in pulsed mode and, additionally, we are limited to a flashing frequency of the light sources of ~1 Hz, due to the time needed to readout the telescope camera. The light emitted during a single 5 μs-long pulse of the sources is not enough to induce a measurable signal in the photodiode. Fast photodiodes which are able to resolve the 5 μs-long pulse exists (e.g. the diodes included in the sphere light-sources), but the absolutely calibrated diodes we employed for this setup do not have this ability. To overcome this obstacle, we operate the light source at higher flashing frequencies during the absolute-calibration measurements mimicking a continuous illumination of the photodiode. Then, we use the single pulse resolution of PMTs to estimate the pulse-to-pulse stability for high and low frequencies.

The setup for the radiometric calibration of the light sources consists of several light detectors on one side and the light source under test on the other side of the setup. A photograph of the

assembled setup is shown in Fig. 6.18. The entire setup is installed within a light tight enclosure. We covered the inner walls and the ceiling of the enclosure with non-reflecting flock paper made by Edmund Optics [81]. Additionally, we have the ability to mount a ~30×25 cm^2 M-UG 6 filter glass in front of the light source. The distance between the light source and the filter glass is equal to the corresponding distance of the XY-Scanner stage. We tested whether a misalignment of the filter plane and the emitting plane of the light source has any influence on the calibration of the source, but none was observed. In the photograph of Fig. 6.18 the M-UG 6 filter is not mounted. By including the same type of a filter, which is mounted on the entrance window of the FD telescopes in the source calibration-setup, we ensure that all light detectors in the laboratory setup observe the source under the same conditions as the PMT camera in a FD telescope. Furthermore, the optical properties of the M-UG 6 filter glass were studied in great detail and these results are used in the reconstruction of air-shower events by the FD. Another advantage of using the filter in the setup is, that all possible photon reflections on the filter back towards the light source are automatically included by the source calibration, albeit this effect is of the order of less than ~0.4% [57]. Two temperature sensors are located on each end of the enclosure and measure the ambient temperature. On the right side of the setup we place the light source. The sources are equipped with the same electronics board and, for the integrating-sphere light-sources, the LED head is in the same positions as for the calibration measurements at the FD telescopes.

The left side of the setup hosts two PMTs, which are placed with a horizontal offset of ~22 cm relative to the optical axis. The centers of the PMT entrance windows and the center of the sphere exit port are aligned in a horizontal plane. We employed two different types of PMTs both made by Hamamatsu [94], one is an R9420 tube [95] while the other is an R11102 tube [96]. The R9420 tube is the type of PMT which is used in the surface scintillator detector (SSD) for the Auger Prime [21] upgrade of the observatory. This tube was already employed for validation measurements of the SSDs assembled at KIT. The R11102 tube was purchased for the very same validation setup, but this particular PMT was never used in any measurements before. High voltage for both PMTs is generated by a CAEN SY127 High Voltage supply and is set to U_{R9420} = 1.15 kV and U_{R11102} = 0.60 kV. The output of the PMTs is digitized by a PicoScope 6404D PC Oscilloscope [85] which is connected via USB to the DAQ computer.

As photodiode we employ an OSI Optoelectronics Silicon Photodiode Model UV-100 (SN 1062) absolutely calibrated by the National Institute of Standards and Technology (NIST [97]) in the wavelength range from 200 nm to 500 nm. The spectral power responsivity as provided by NIST is shown in Fig. 6.20. The effective area of the photodiode is reduced by a circular iris with a precisely measured radius r_{diode} = (4.004 ± 0.003) mm. The center of the diode is aligned to the optical axis of the light source and the diode is placed onto a Standa [92] 8MT195 long-travel motorized linear stage. This allows us to change the distance between the photodiode and the sphere exit-port remotely and without the need to open the light-tight enclosure. We can set the distance between $d_{min} \approx 0.25$ m and $d_{max} \approx 1.05$ m with a 12.5 µm step resolution. The photodiode is connected to a Keithley 6514 System Electrometer [98].

As mentioned above, we need to operate the light source at higher frequencies as for the FD measurements. The electronics of the sources allows for internally triggered operation with a maximal flashing frequency of $f_{max}^{internal}$ = 10 Hz. With external trigger input we can reach a maximal flashing frequency of $f_{max}^{external} \approx 125$ Hz. An operation at even higher frequencies is not possible, due to the time needed to readout the internal photodiode and temperature sensors (which is done for every flash) and to transfer the captured data to the DAQ computer exceeds the time between triggers. For the latest firmware version of the source electronics this readout of the internal photodiode and temperature sensors can be disabled and thus enabling us to operate the sources at even higher frequencies up to ~1 kHz. However, we did not yet update the firmware on the KIT sphere, thus only the Olomouc sphere and the tube source are able to flash at frequencies higher than ~125 Hz. For the setup discussed here, we use an HP 33120A Function Generator as a trigger source for flashing the light sources.

6.7.2. Data Acquisition

All previously introduced devices are connected to a single DAQ computer. On this machine a custom developed software is running, which handles the initialization of and the communication with the individual components of the setup, and stores the acquired data. In the following we introduce the measuring procedure for the absolute calibration of light sources. After the light source is installed on the test bench, we close the enclosure and ramp up the high voltage of the PMTs. Typically, the high voltage of the PMTs is turned on approximately one hour before we start the data-taking procedure, allowing the PMTs to reach a stable state of operation.

The data taking itself is split into events. Each event contains a certain number of light pulses and a background estimation. An event is split into three equally long parts, first background estimation, second the actual measurement, and third another background estimation. Before starting an event, the DAQ moves the photodiode on the linear stage to a desired position. During the duration of this event the diode is fixed at this position. Once the diode reached the measuring position, the Keithley Electrometer and the PicoScope are initialized and set into acquiring operation. The electrometer is set to charge-measuring mode and starts to collected background data. After one third of the total event duration, the DAQ software starts the function generator to trigger the light-pulse emission from the light source. Capturing the PMTs output by the PicoScope is triggered by the light source. For each trigger arriving, the PicoScope captures a 1000 bin-long trace with a sampling time of 100 ns for each of the PMTs. The light-source electronics measures for every emitted pulse the temperatures of the LED- and PHD-heads and transfers the measurement to the DAQ computer where it is stored in the event file. If operated at high frequencies $f \gtrsim 100\,\text{Hz}$, only temperatures for every X pulse are measured, with X on the order of ~10. After another third of the event duration, the total number of requested flashes were fired, and the electrometer continues to measure the background for the last third of the event. After the total event duration, the captured data from the electrometer and the PicoScope are transferred to the DAQ machine and stored in the event file.

For an absolute-calibration measurement of a light source, we typically measure several events with a higher frequency (typically ~100 Hz) at a multitude of different distances between the source and the diode. Additionally, we drive the diode completely out of the field of view of the PMTs (to the left most position (in Fig. 6.18) on the linear stage) and capture additional events with the high and low (1 Hz) frequency. These events are then used to estimate the pulse stability between the two different flashing frequencies.

6.7.3. Estimation of Absolute Calibration

Electrometer Charge Estimation. In the following, we describe the estimation of the charge accumulated in the photodiode and measured by the electrometer. In Fig. 6.19 we show a typical event. The red line represents the charge as measured by the electrometer. By building the derivative of the charge we obtain the current which is plotted as green line in the same plot. The three parts of the event (background, signal, background) become visible as different slopes of the charge and consequentially as different levels of current. We estimate the collected charge during the signal part of the event as follows: We perform four linear fits to the charge measurements. For two of the fits we use a fraction of data taken before and after the light-source flashing-interval. These two fits describe the background of the measurement. Similarly, we perform another two fits after starting and before stopping to flash the source. Likewise, these two fits describe the signal of the measurement. The parts of data used for the fits are marked in blue in Fig. 6.19. The resulting fits are drawn as black solid lines, additionally their slopes are drawn as horizontal green-dashed lines. For the event we present here, the fitted slopes for the signal (and background) part hardly differ and therefore the four horizontal green-dashed lines appear as two in this plot. We discard an event if the slopes estimated for the signal or the background part differ significantly or the slope of one background estimate is negative. We show a selection of discarded events in Appendix A.4.3. Therefore, we obtain each two linear fitted estimates of the signal and the background part of the event, close to the begin and the end of flashing interval.
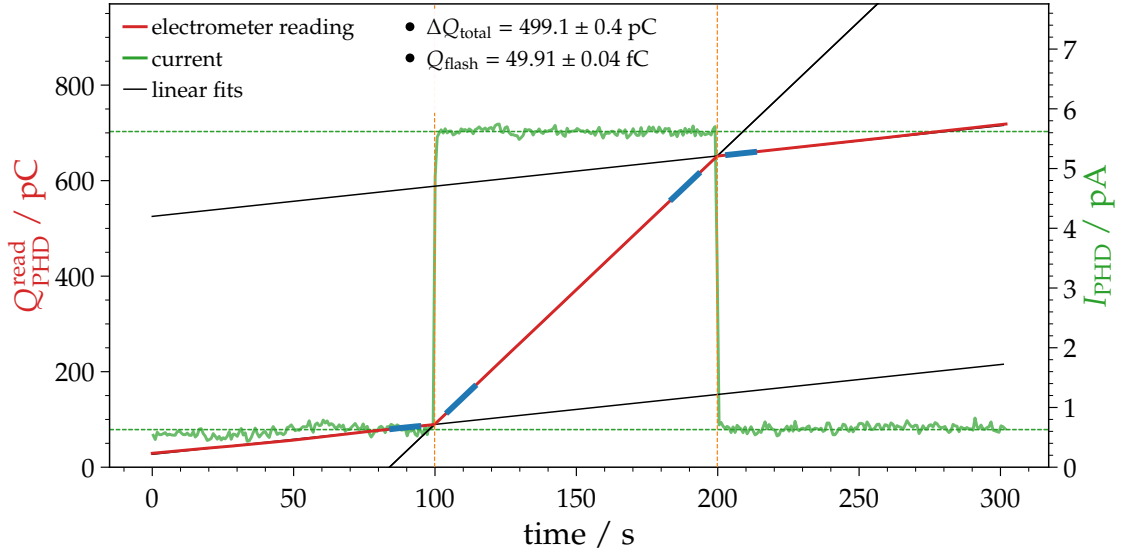
Figure 6.19: Typical event of a calibration measurement as captured by the photodiode and readout by the electrometer. The red lines represents the reading of the electrometer, the green line is its derivative. Black solid lines are linear fits to the parts of the data marked in blue. More details given in the text. This event contains 10^4 light flashes, emitted at frequency of 100 Hz from the KIT integrating-sphere source. The printed are statistical uncertainties.

From the intersection of the first pair of signal and background fits we directly obtain the signal begin time t_0 and the corresponding charge reading Q_0. Equivalently, from the second two fits we obtain the signal end time t_1 and the charge reading Q_1. Signal begin and end time are indicated by the vertical orange-dashed lines in Fig. 6.19. We calculate the total change in charge to

$$\Delta Q_\text{total} = (Q_1 - Q_0) - I_\text{bkg}\,(t_1 - t_0) \tag{6.10}$$

with the mean slope of the two background fits I_bkg. We calculate the average collected charge per light flash as

$$Q_\text{flash} = \frac{\Delta Q_\text{total}}{N_\text{flashes}} \tag{6.11}$$

with the number of emitted flashes from the light source N_flashes. We estimate the statistical uncertainty of this procedure to be on average less than 0.1% for distances below 0.5 m between the diode and the source, and less than 0.3% for distances up to 1.0 m for the light-sources operated at their nominal LED current. We neglect the statistical uncertainty of the charge estimation in the following.

For the smallest possible charge range setting of the electrometer, which we set for the measurements discussed here, the manual of the electrometer [98] gives an accuracy of 0.4% and 50 counts for the first year of operation, an acquisition duration less than 1000 s, and temperatures between 18°C and 28°C. For the used charge range, 50 counts correspond to 0.5 pC. We operate the electrometer within the given temperature range and the acquisition time is set below the 1000 s limit. But since the electrometer was bought in 2013 (10 years ago) we are operating it well outside the one year margin. We assume conservatively a linear decrease of the accuracy of ~0.4% per year and therefore we adopt a total accuracy of 4% for the electrometer charge estimation. A new calibration of the electrometer will probably reduce this uncertainty drastically and is planned for the foreseeable future.

Additionally, we performed a crosscheck with another Keithley electrometer of the same type and roughly the same age, but we observed no significant difference in the charge measurement.

We present these observations in Appendix A.4.4.

Photon Flux on Photo-Diode.   We describe the conversion between the measured charge collected by the photodiode and flux of photons through the diode in the following.

First, the current flow I through the photodiode is given as

$$I = \epsilon\, P \tag{6.12}$$

with the incident radiant power P and responsivity ϵ of the photodiode. We eliminate time by considering per-flash quantities so that

$$Q_{\text{flash}} = \epsilon\, E_{\text{flash}} \tag{6.13}$$

with the collected charge Q_{flash} and the radiant energy E_{flash} deposited in the diode per light flash. We express the radiant energy E_{flash} as

$$E_{\text{flash}} = \frac{hc}{\lambda_{\text{src}}^{\text{eff}}}\, \phi \tag{6.14}$$

where the product of the Planck constant and the speed of light $hc = 1.986{\times}10^{-25}\,\text{J m} = 1240\,\text{eV nm}$, the wavelength of the source is $\lambda_{\text{src}}^{\text{eff}}$, and the photon flux is ϕ (number of photons per flash). By combining Eq. (6.13) and Eq. (6.14) we estimate the photon flux ϕ through the photodiode per flash emitted by the light source as

$$\phi = \frac{Q_{\text{flash}}\, \lambda_{\text{src}}^{\text{eff}}}{\epsilon\, hc}. \tag{6.15}$$

Next, we need to estimate the effective spectral responsivity ϵ^{eff} of the photodiode for the different light sources. The responsivity ϵ for the employed photodiode as function of wavelength is shown in Fig. 6.20 as provided by NIST [99]. Within the wavelength region of interest NIST gives a relative uncertainty on the spectral responsivity measurement of ~0.9% on average. Within the same plot we draw the measured emission spectra of the calibration-light sources.

We used the measured wavelength spectra of all sources (see Section 6.6) together with the NIST provided responsivity $\epsilon(\lambda)$ of the photodiode to calculate the effective responsivity $\epsilon_{\text{src}}^{\text{eff}}$ of the different light sources as

$$\epsilon_{\text{src}}^{\text{eff}} = \frac{\int_{340\,\text{nm}}^{440\,\text{nm}} \epsilon(\lambda)\, E_{\text{src}}(\lambda)\, \mathrm{d}\lambda}{\int_{340\,\text{nm}}^{440\,\text{nm}} E_{\text{src}}(\lambda)\, \mathrm{d}\lambda} \tag{6.16}$$

with the measured spectral intensity $E_{\text{src}}(\lambda)$ of each source. For the three calibration-light sources we obtain the following effective spectral responsivities:

$$\epsilon_{\text{KIT sphere}}^{\text{eff}} = 0.128\,\text{A/W}, \tag{6.17}$$

$$\epsilon_{\text{Olomouc sphere}}^{\text{eff}} = 0.129\,\text{A/W}, \tag{6.18}$$

$$\epsilon_{\text{tube source}}^{\text{eff}} = 0.131\,\text{A/W}. \tag{6.19}$$

When we include the M-UG6 filter into the setup we estimate the effective responsivity as

$$\epsilon_{\text{src}}^{\text{eff, M-UG6}} = \frac{\int_{340\,\text{nm}}^{440\,\text{nm}} T_{\text{M-UG6}}(\lambda)\, \epsilon(\lambda)\, E_{\text{src}}(\lambda)\, \mathrm{d}\lambda}{\int_{340\,\text{nm}}^{440\,\text{nm}} E_{\text{src}}(\lambda)\, \mathrm{d}\lambda}, \tag{6.20}$$

additionally accounting for the wavelength-dependent transmittance $T_{\text{M-UG6}}(\lambda)$ of the filter. We obtain for each source

$$\epsilon_{\text{KIT sphere}}^{\text{eff, M-UG6}} = 0.102\,\text{A/W}, \tag{6.21}$$

$$\epsilon_{\text{Olomouc sphere}}^{\text{eff, M-UG6}} = 0.102\,\text{A/W}, \tag{6.22}$$

$$\epsilon_{\text{tube source}}^{\text{eff, M-UG6}} = 0.100\,\text{A/W}. \tag{6.23}$$
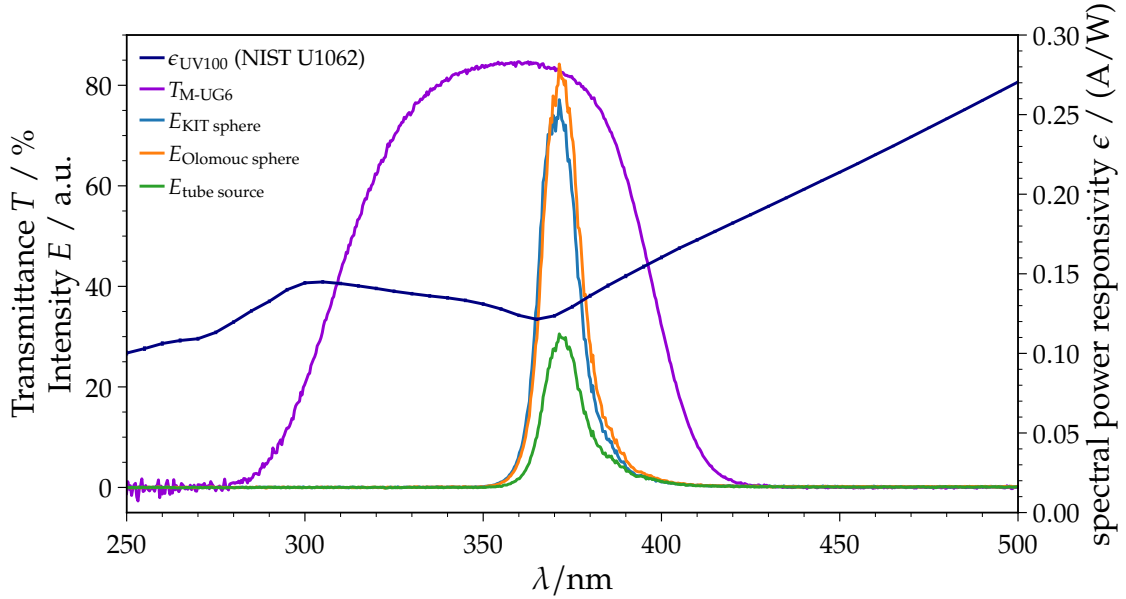
Figure 6.20: Spectral power responsivity of the photodiode ϵ_{UV100} used in the absolute calibration setup as provided by NIST [99]. Also shown are the measured emission spectra of the calibration light-sources ($E_{\text{KIT sphere}}$, $E_{\text{Olomouc sphere}}$, $E_{\text{Tube source}}$) and the transmitivity $T_{\text{M-UG6}}$ of the M-UG6 filter.

For this calculation we used the measured transmittance $T_{\text{M-UG6}}(\lambda)$ of the M-UG6 filter glass which is presented in Fig. 6.20.

We estimate the uncertainty on the effective responsivity of the photodiode to 1%, including the uncertainty on the NIST calibration of the diode (0.9%) and the uncertainties on the spectrometer measurements of the source wavelengths and filter transmittance (0.5%).

Concluding, we calculate the photon flux ϕ through the photodiode per light flash of the light source (similar to Eq. (6.15)) as

$$\phi = \frac{Q_{\text{flash}} \, \lambda_{\text{src}}^{\text{eff}}}{\epsilon_{\text{src}}^{\text{eff}} \, hc} \tag{6.24}$$

with the effective spectral responsivity $\epsilon_{\text{src}}^{\text{eff}}$ depending on the setup and the source.

The dominant uncertainty of ϕ is the uncertainty on charge measurement of the photodiode Q_{flash} which is 4%. Other contributions are the uncertainties of the wavelength of the sources with ~0.5% and the effective responsivity of the photodiode with ~1%. We assign the systematic uncertainty of the photon flux ϕ as the quadratic sum of the uncertainties listed above to be 4.2%.

Determination of Source Radiance. In general we define the radiance L of any given source to be

$$L = \frac{\mathrm{d}\phi}{\cos\theta \, \mathrm{d}A \, \mathrm{d}\Omega} \tag{6.25}$$

where ϕ is the emitted photon flux, A is referring to the area in the surface of the light source, θ is the angle to the normal of the surface, and the solid angle $\mathrm{d}\Omega$ into which the light is emitted. According to Ref. [100], we can express the transfer of radiant power ϕ between two surfaces as

$$\phi = \iint \frac{(L_{12} - L_{21}) \cos\theta_1 \cos\theta_2}{d_{ij}^2} \, \mathrm{d}A_1 \, \mathrm{d}A_2 \tag{6.26}$$

with the radiance of surface i into direction of surface j as L_{ij}, the distance between the two surfaces d_{ij}, and the angles θ_i and θ_j between the ray d_{ij} and the surfaces normals. If we consider
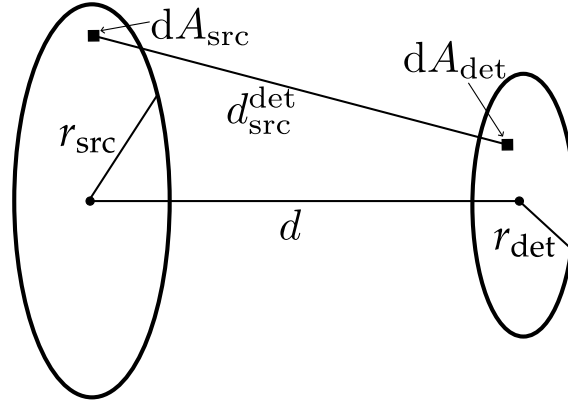
Figure 6.21: Sketch of two parallel circular surfaces with the radii r_{src} and r_{det} at a distance d.

a scenario where one of the surfaces acts as a source while the other surface is a detector, Eq. (6.26) becomes

$$\phi_{\mathrm{det}} = \iint \frac{L_{\mathrm{src}} \cos \theta_{\mathrm{src}} \cos \theta_{\mathrm{det}}}{(d_{\mathrm{src}}^{\mathrm{det}})^2} \, \mathrm{d}A_{\mathrm{src}} \, \mathrm{d}A_{\mathrm{det}} \tag{6.27}$$

and if we additionally assume the source has an uniform radiance across its entire surface and L is independent of the viewing direction (Lambertian source) we get

$$\phi_{\mathrm{det}} = L_{\mathrm{src}} \iint \frac{\cos \theta_{\mathrm{src}} \cos \theta_{\mathrm{det}}}{(d_{\mathrm{src}}^{\mathrm{det}})^2} \, \mathrm{d}A_{\mathrm{src}} \, \mathrm{d}A_{\mathrm{det}}. \tag{6.28}$$

The double integral in Eq. (6.28) is defined by the geometry of each setup and is most commonly referred to as the *configuration factor*.

The configuration factors for different geometries can be found in e.g.   Ref. [101]. For a geometry with a parallel circular detector and a circular source and their center points are aligned on the same optical axis at a distance d (see Fig. 6.21) the configuration factor is given in Ref. [100] as

$$\iint \frac{\cos \theta_{\mathrm{src}} \cos \theta_{\mathrm{det}}}{(d_{\mathrm{src}}^{\mathrm{det}})^2} \, \mathrm{d}A_{\mathrm{src}} \, \mathrm{d}A_{\mathrm{det}} = \frac{2 \left(\pi r_{\mathrm{src}} r_{\mathrm{det}}\right)^2}{r_{\mathrm{src}}^2 + r_{\mathrm{det}}^2 + d^2 + \sqrt{(r_{\mathrm{src}}^2 + r_{\mathrm{det}}^2 + d^2)^2 - 4 r_{\mathrm{src}}^2 r_{\mathrm{det}}^2}} \tag{6.29}$$

$$= \frac{(\pi r_{\mathrm{src}} r_{\mathrm{det}})^2}{D^2 \left(r_{\mathrm{src}}, r_{\mathrm{det}}, d\right)} \tag{6.30}$$

where r_{src} is the radius of the source and r_{det} is the radius of the detector. For $d^2 \gg (r_{\mathrm{src}}^2 + r_{\mathrm{det}}^2)$ we can approximate

$$D^2 \left(r_{\mathrm{src}}, r_{\mathrm{det}}, d\right) \approx d^2. \tag{6.31}$$

Summarizing, we express the photon flux through the detector as a product between a distance-depended factor (provided the radii of the source r_{src} and detector r_{det} are constant) and the source radiance L_{src}, thus Eq. (6.28) becomes

$$\phi_{\mathrm{det}}^{\mathrm{a}} (d) = \frac{(\pi r_{\mathrm{src}} r_{\mathrm{det}})^2}{D^2 \left(r_{\mathrm{src}}, r_{\mathrm{det}}, d\right)} L_{\mathrm{src}} \tag{6.32}$$

or

$$\phi_{\mathrm{det}}^{\mathrm{b}} (d) = \frac{(\pi r_{\mathrm{src}} r_{\mathrm{det}})^2}{d^2} L_{\mathrm{src}} \tag{6.33}$$

if we apply the approximation in Eq. (6.31). In the following, we fit Eq. (6.32) and Eq. (6.33) to the measured photon flux on the photodiode and thus estimate the radiance L_{src} of the light source under test. In the following we give an example of this procedure in a real measurement.
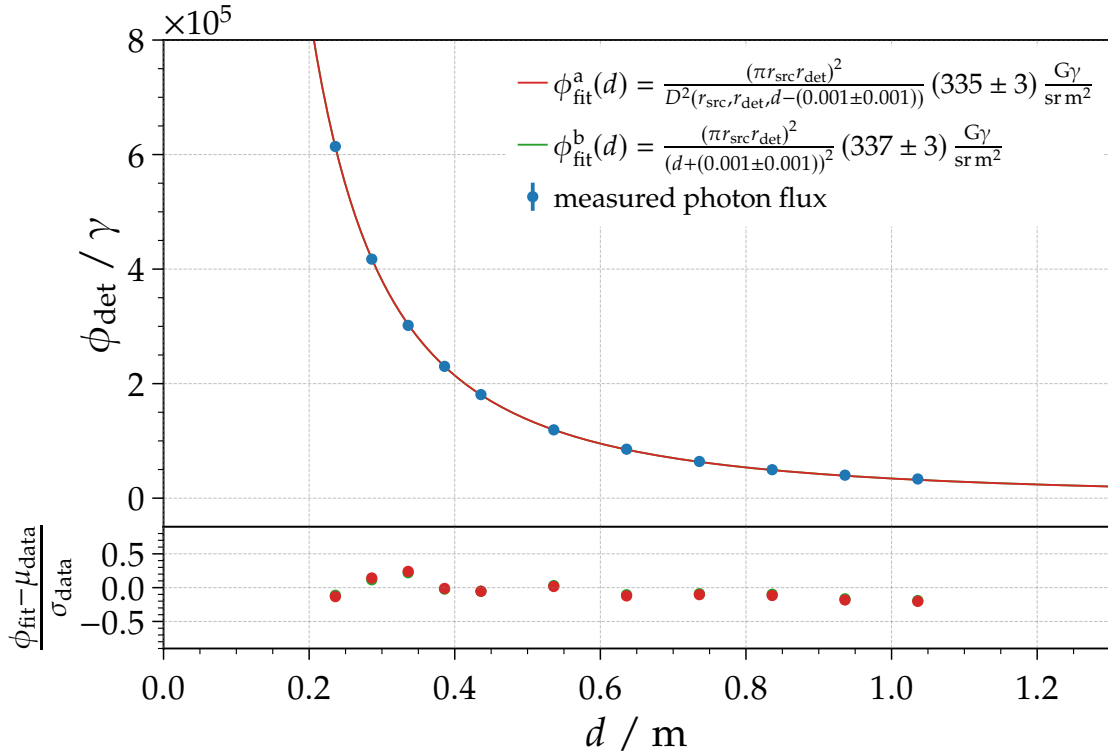
Figure 6.22: Estimation of the source radiance. *Top:* Measured mean photon flux through the photodiode per position as blue marker. Error bars depict the standard error of the mean, but only barely visible. The fitted photon flux is drawn as red or green line depending on the function. *Bottom:* Residuals between each fitted function and the measured data.

Actual Measurement of Radiance of Calibration Light Source. In the following we discuss a radiance measurement of the first-generation integrating-sphere light-source (KIT sphere). For this measurement we estimate the photon flux through the photodiode at 11 different measuring points distributed over various distances d between the light source and the photodiode. The absolute distance between the latter two reaches from $d_{min} \approx 0.25$ m to $d_{max} \approx 1.05$ m. We set the distance between measuring positions to 5 cm for absolute distances below 0.5 m and to 10 cm for absolute distances above 0.5 m. At each distance we capture 25 events each containing 10 000 light pulses from the source captured with a flashing frequency of $f = 100$ Hz. The measured charge collected by the photodiode in a typical event is shown in Fig. 6.19. To minimize the influence of any possible temporal effects we scan 25 times through all measuring positions rather than immediately capturing all events at a given position. The temperature of all source components and the ambient temperatures in the light-tight enclosure are continuously measured and were found to be stable within $\Delta T = 1$°C for the entire duration of the measurement procedure. We show the measured temperatures in Fig. A.9 of the appendix.

In Fig. 6.22 we show the average photon flux detected by the diode (estimated according to Eq. (6.24)) as function of the distance d between the source and the detector. The relative distance between measuring points is known precisely as a result of the single step resolution of 12.5 μm for motor of the linear stage. We measured the absolute distance between the source and detector with a laser tool and a caliper tool, reaching an accuracy of roughly ~1 mm. To counteract this inaccuracy, we extend the fit function of Eq. (6.32) and Eq. (6.33) by adding a constant distance
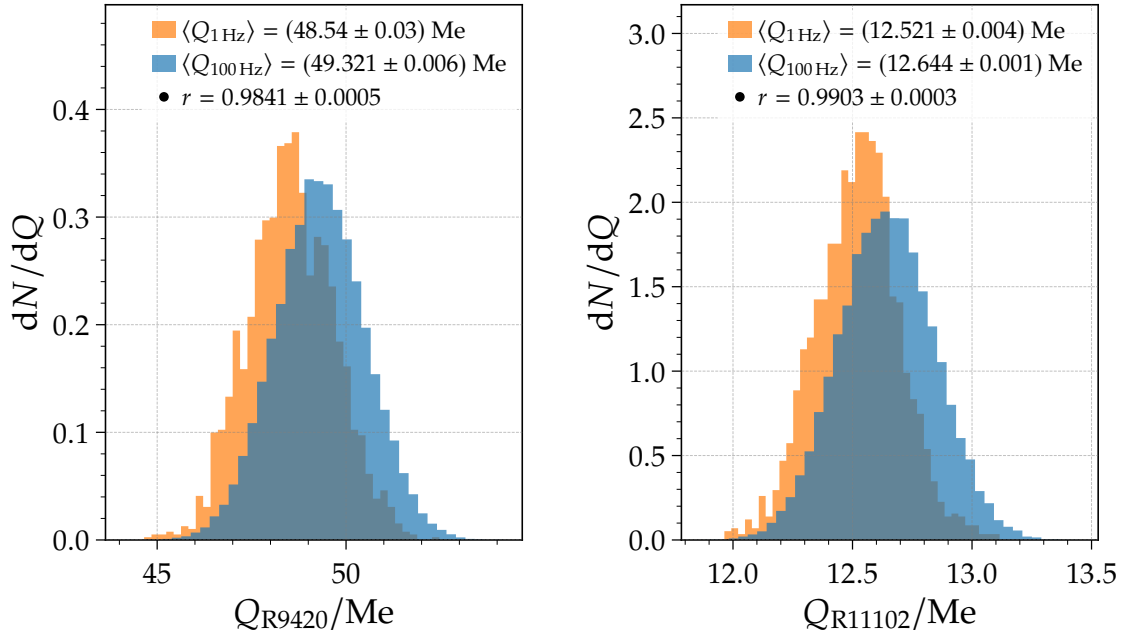
Figure 6.23: Distribution of the charges collected by the two PMTs (*left:* R9420, *right:* R11102) in the calibration setup. Different colors indicate different flashing frequencies of the source, 1 Hz in orange, 100 Hz in blue. Mean of the distribution, the standard error of the mean, and the ratio between the means for the two frequencies are printed within the plots.

offset Δd as free parameter, thus obtaining

$$\phi_{\mathrm{det}}^{\mathrm{a}}(d) = \frac{(\pi r_{\mathrm{src}} r_{\mathrm{det}})^2}{D^2 (r_{\mathrm{src}}, r_{\mathrm{det}}, d + \Delta d)} L_{\mathrm{src}}, \tag{6.34}$$

$$\phi_{\mathrm{det}}^{\mathrm{b}}(d) = \frac{(\pi r_{\mathrm{src}} r_{\mathrm{det}})^2}{(d + \Delta d)^2} L_{\mathrm{src}}. \tag{6.35}$$

In the next step, we fit these functions to the measured photon flux and thus obtain the radiance of the source L_{src} and the distance offset Δd. We plot the resulting functions and their residuals in Fig. 6.22. The optimal parameters returned from the fitting procedure are given within Fig. 6.22. Note here that the uncertainties on L_{src} and Δd are of purely statistical nature. We calculate the residuals of this fit to be smaller than $\pm 0.5\sigma$ for the entire range of measurements. The obtained radiance parameters L_{src} for both functions are in agreement within the statistical uncertainties of the fit. We therefore decide to use Eq. (6.34) to describe the photon flux. The estimated distance offset Δd is compatible with zero which we interpret as a validation of the measurement of the absolute distance between the source and detector. We estimate the statistical uncertainty of the source radiance L_{src} as the uncertainty we obtain from the fitting procedure and is ~0.8%.

Pulse-to-Pulse Stability. As mentioned above, it is not possible to perform the calibration of the light sources at the same flashing frequency as we operate them for the XY-Scanner measurements at the FD telescopes. The time needed to readout the telescope camera allows for a maximal frequency of only $f_{\mathrm{max}}^{\mathrm{FD}} \approx 1\,\mathrm{Hz}$. For the radiance measurement we operate the light source at a frequency of $f_{\mathrm{lab}} = 100\,\mathrm{Hz}$, which is a factor 100 larger than the frequency for the calibration of the FD telescopes.

To validate a consistent light emission per light flash from the sources at higher and lower flashing frequencies we make use of the single pulse resolution of PMTs. We installed two PMTs in

the calibration setup left and right of the optical axis of the light source, as shown in Fig. 6.18. The signal output of each PMT is connected to the PicoScope, which is triggered to capture the signal traces of both PMTs for every light flash emitted by the source. A light-flash event containing typical signal traces from both PMTs is shown in Fig. A.12 of the appendix.

For each source-calibration measurement we include several events for which we move the photodiode entirely out of the field of view of both PMTs. These events are partly taken with the higher (f_{lab}^{high} = 100 Hz) and lower (f_{lab}^{low} = 1 Hz) flashing frequency. For every light flash emitted by the source we estimate the collected charge Q_{PMT} by each PMT as the integral over the relevant part of the trace. We used a similar pulse finding algorithm as we use on the signal traces captured by the FD camera, which we introduce in Section 7.1.1.

In Fig. 6.23 we show the distributions of the collected charge Q_{PMT} for the different flashing frequencies. The two panels in Fig. 6.23 correspond to the two employed PMTs, the R9420 tube on the left and the R11102 tube on the right. Additionally, the mean charge and its standard error, as well as the ratio between the mean charges collected for different flashing frequencies are printed within the plots.

We observe a ~1% difference in the charges collected by the R11102 PMT. However, for the R9420 tube we observe on average a ~2% lower charge if we operate the source at the lower flashing frequency.

Since the two PMTs observe exactly the same light pulses from the source but measure a different charge ratio, we attribute the detected difference between the charge ratios to a property of the employed PMTs. See also the discussion in Appendix A.4.6.

Therefore, we conclude that with this setup we are unable to measure any frequency dependent difference of the light-source emission and take the larger observed difference of ~2% in the R9420 PMT measurement as the uncertainty on the stability of the light-source operation at higher and lower frequencies. With new and better suited PMT we may be are able to reduce this uncertainty.

6.7.4. UNCERTAINTIES ON RADIANCE MEASUREMENTS

We estimate the statistical uncertainty of the radiance to ~0.8%, as explained above. However, the main contribution to the uncertainty are of systematic nature. We enumerate the individual contributions in the following.

Since the radiance of the source L_{src} depends linearly on the photon flux ϕ_{det} measured by the photodiode, we assign the same systematic uncertainty of 4.2% on ϕ_{det} to the radiance L_{src}.

The radius of the detector is limited by a precisely measured pinhole to r_{det} = (4.004 ± 0.003) mm resulting in a relative uncertainty on $A_{det} = \pi\, r_{det}^2$ of ~0.15%. We estimate the radius of the exit port of the integrating-sphere light-sources to r_{src} = (25.4 ± 0.1) mm, leading to a relative uncertainty on $A_{src} = \pi\, r_{src}^2$ of 0.8%. We take the same relative uncertainty on the source area for all light sources. With the current setup, we estimate the uncertainty of the pulse-to-pulse stability of the light sources to be 2%.

We list the individual contributions to the systematic and statistical uncertainties of the estimation of the source radiance L_{src} in the following:

Photon flux on photodiode	4.2%
Photo-diode surface area	0.15%
Source surface area	0.8%
Pulse-to-pulse stability	2%
Unaccounted uncertainty budget	1%
Fitting the source radiance	0.8%
Total	**4.9%**

Combining these contributions in a quadratic sum we are able to estimate the source radiance to an uncertainty level of 4.9%.
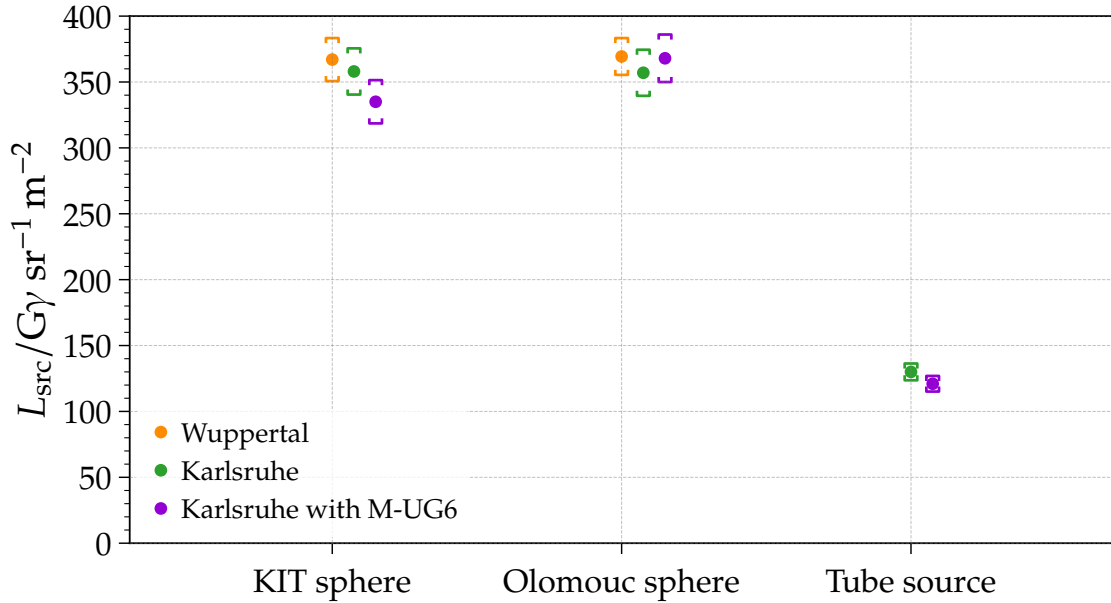
Figure 6.24: Radiance of the calibration light-sources of the XY-Scanner. Different colors depict the different setups, which are labeled regarding their location. Brackets represent the total uncertainty on the measurements.

We emphasize again that the dominant contribution to this uncertainty is the accuracy of the Keithley electrometer, which we conservatively estimate to be 4%. A re-calibration of the electrometer to an accuracy level of ~0.4% as quoted in the manual of this electrometer [98] and a better suited PMT to estimate the pulse-to-pulse stability will reduce the total uncertainty of the source calibration to the order of ~2%.

6.7.5. Radiance Measurements of Calibration Light Sources

A similar approach for a light-source calibration-setup was independently developed and assembled by our collaborators at the Bergische Universität Wuppertal. The underlining method is equivalent to the one described above and will not be discussed here, a description is given in Ref. [102]. The two integrating-sphere light sources were last calibrated in Wuppertal in April 2020. For this calibration a relative uncertainty on the order of 4% was estimated [103, 104]. So far, it was not possible to calibrate the tube source in the Wuppertal setup. At the current time the setup in Wuppertal is being upgraded and we plan to perform the calibration measurements of all light sources in the foreseeable future.

In Fig. 6.24 we show the radiance measured in the setup discussed above and the results obtained in Wuppertal for all calibration light sources employed by the XY-Scanner. Comparing the calibrations obtained in Wuppertal with the results from this setup, we observe a difference of ~3% between the two setups for both integrating-sphere sources. Since this difference is within the uncertainties of each setup we conclude that the source calibrations obtained by the two setups are in agreement. Additionally, we estimate the difference between the radiance of the KIT and Olomouc sphere to be less than ~1% for both setups. The small difference between the two integrating-sphere light source is not a coincidence, the LED current for the operation of the Olomouc sphere was chosen in such a way that the light output (measured in the Wuppertal setup) for both spheres was matching.

Nevertheless, we observe a larger difference between these two sources in the charges collected by the PMTs within the calibration setup. Since the PMTs are located on either side of the optical axis with an offset of ~22 cm, the PMTs do observe the source under an angle of ±11°. As discussed
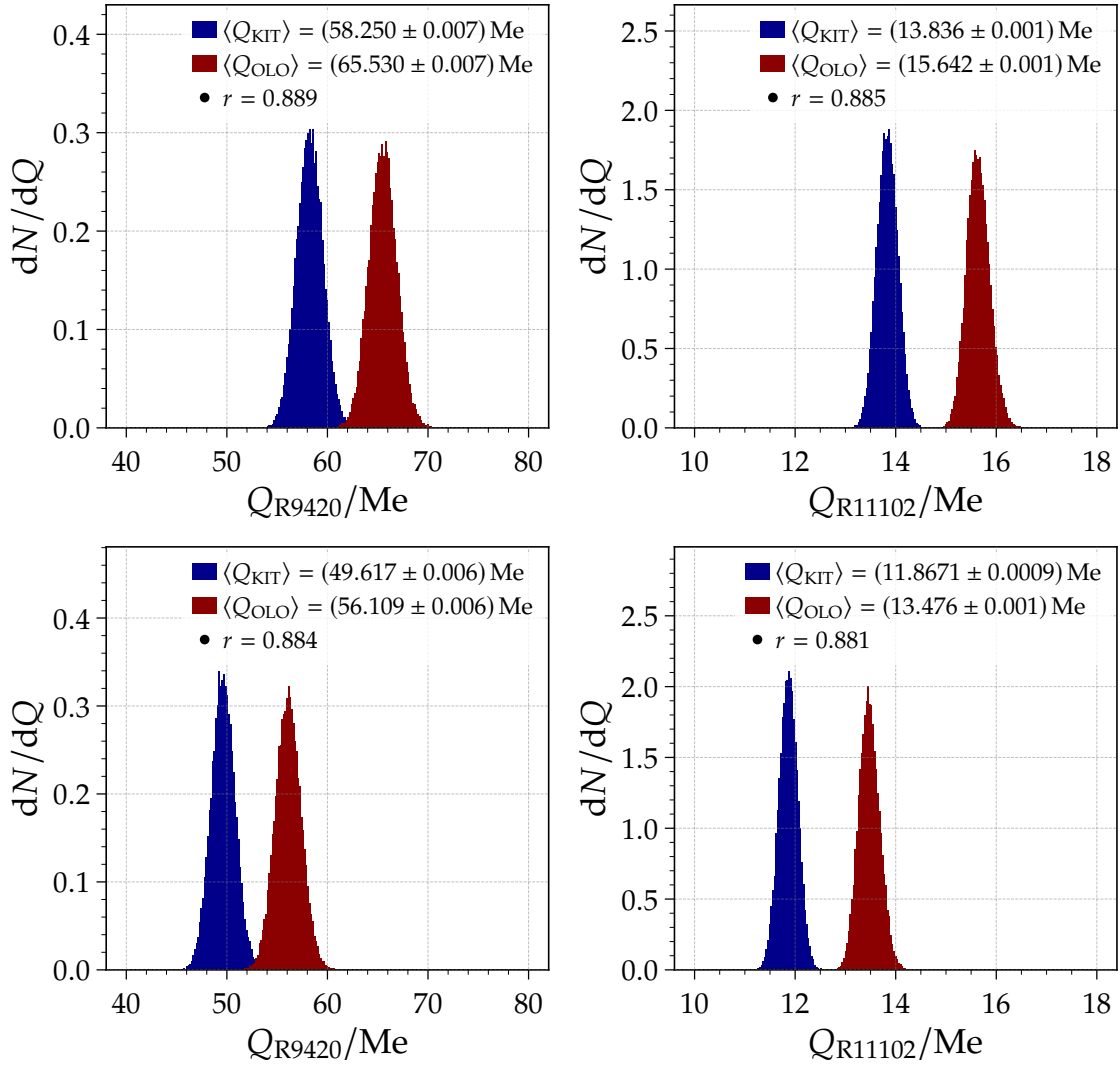
Figure 6.25: Distributions of the PMT charges captured during calibrations of the integrating-sphere light sources. *Left* and *right* show the two PMTs of the setup. *Top:* Measurement without the M-UG6 filter. *Bottom:* M-UG6 filter is installed. Mean and standard error of the mean are printed for each distribution. The ratio of the means is given as well.

in Section 6.5 the two light sources have different angular emission patterns. We corrected the collected charges of the PMTs for this effect. The top row of Fig. 6.25 shows the charge distributions for the two PMTs and the two sphere light sources. The mean and its standard derivation of each distribution is given within the plot together with the ratio between the means. For both PMTs we observe a difference between the KIT sphere and the Olomouc sphere of the order of ~10%, which is in disagreement with the before-discussed ratio of the estimate for the source radiance.

We make here a short excursion to compare these observations with the XY-Scanner measurements we performed at the FD telescopes. In Fig. 6.26 we show the pixel-signal ratio between two XY-Scanner measurements, which used either of the two integrating-sphere light sources. The left side of these plots shows the ratio as pixel matrix, while the right side illustrates the same data as a function of the pixel number. Minimum, maximum, mean, and standard derivation of the ratio are printed within the plot. The pixels which observe the light source under approximately
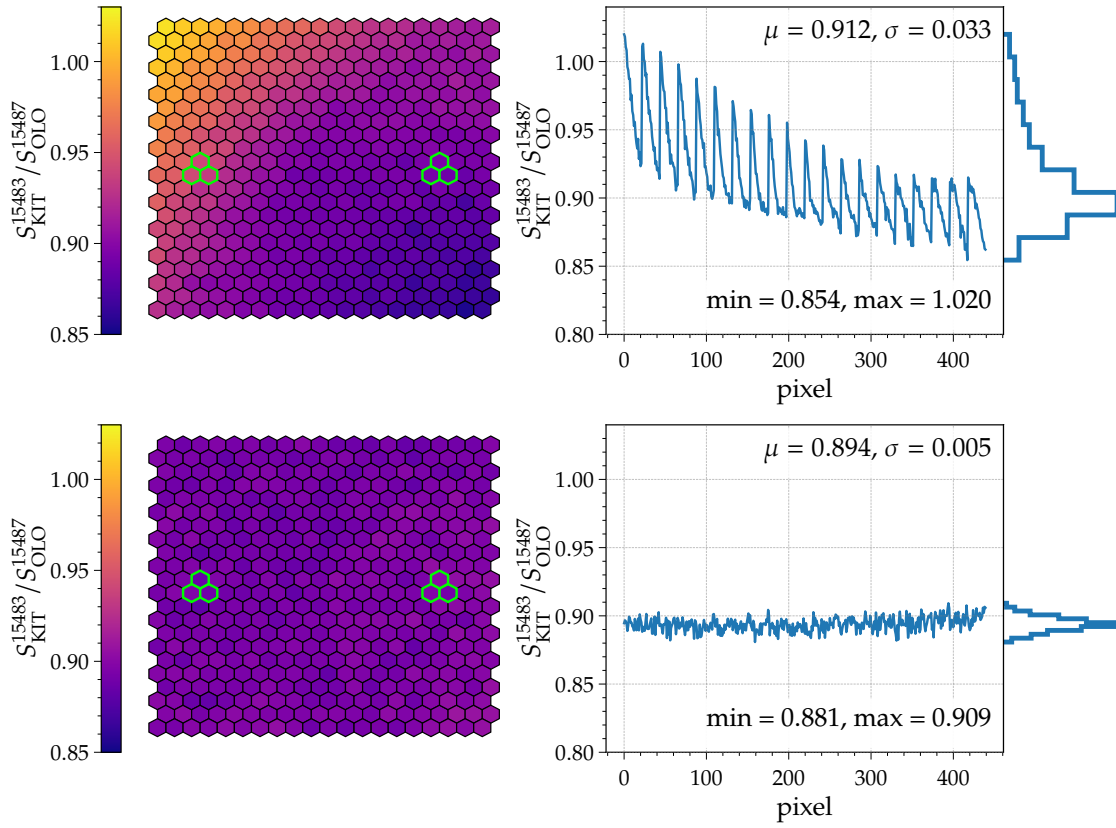
Figure 6.26: Signal ratio for the FD camera pixels between XY-Scanner measurements with the KIT and Olomouc sphere. The marked pixels observe the light source under roughly the same angles as the PMTs in the calibration setup. *Top:* Signals as captured by the FD camera-PMTs. *Bottom:* The emission correction for both sources is applied. *Left:* Pixel matrix. *Right:* Plot as function of the pixel number with distribution attached to the right. Values of the mean, standard derivation, minimum, and maximum are printed within the plot.

the same angles as the PMTs in the laboratory setup are framed in green. The plots in the top row show the ratios as captured, while for the bottom row we applied in Section 6.5 derived emission correction to each measurement. With and without applying this emission correction we observe on average a ~10% higher signal in the telescope camera for the measurements which employed the Olomouc sphere as a light source. This coincides with the ratio obtained for the PMT signals in the source calibration setup. After applying the emission correction for both spheres, we estimate the ratio between the KIT and Olomouc sphere measurements to 0.89, which agrees with the laboratory measurement presented in Fig. 6.25.

When including the M-UG6 filter into the calibration setup and accounting for its transmission the analysis however seems to have a different influence on the obtained radiance depending on measured light source, as we show in Fig. 6.24. While for the tube source and the KIT sphere we observe a decrease in the radiance, on the opposite we observe an increased radiance estimate for the Olomouc sphere. We calculate the radiance ratio between the two integrating-sphere light sources to 0.91 ± 0.06. The ratio of the PMT signals between the sources is not affected by including the M-UG6 filter as shown in the bottom row of Fig. 6.25. If we include the filter into the setup, we observe a similar ratio between the two integrating-sphere light-sources in the PMT signals and the estimated radiance. Additionally, the measured ratio coincides with the measurements at the FD telescopes on site.

In the following we speculate about a possible explanation for this observation. The simplest and most straightforward explanation is an additional light emission from either of the soucres in the wavelength range ($\lambda \gtrsim 650\,\mathrm{nm}$) where neither the PMTs in the calibration setup nor the PMTs of the FD camera are sensitive anymore. However, the sensitive range of the photodiode exceeds wavelengths of $\lambda_{\mathrm{diode}}^{\max} \approx 1000\,\mathrm{nm}$. See Fig. A.14 of the appendix for an illustration of the efficiency of the individual components. By including the M-UG6 filter we remove this long-wavelength component and consequently measure the expected ratio between the source radiances estimated with the photodiode.

This additional light contribution could originate from an afterglow of one of the LEDs itself or come from a phosphorescence-light emission of components, which are only present in either of the integrating-sphere sources. The LED within the Olomouc sphere is covered with a diffusive layer (opal glass) and, additionally, the sphere opening is equipped with a protective glass. In contrast, the KIT sphere is equipped with neither of these two. A detailed description of the light sources is given above in Section 6.2. Assuming that one of these additional glasses, either the diffusive layer directly on the LED or the protective layer on the exit port, is producing phosphorescence with wavelengths $\lambda \gtrsim 650\,\mathrm{nm}$, it may explain our observations. However, in the spectrometer measurements we do not observe any significant emission from the light sources with $\lambda_{\mathrm{src}}^{\max} \gtrsim 440\,\mathrm{nm}$, see Fig. A.14 of the appendix. Nevertheless, the sensitive range of the Ocean Optics SD2000 spectrometer ends at $\lambda_{\mathrm{SD2000}}^{\max} \approx 860\,\mathrm{nm}$. A measurement of the light-source emission spectrum using a spectrometer with a sensitive range reaching into or covering the infrared part of the electromagnetic spectrum could validate or falsify our assumption. Due to time constraints and unavailability of such a spectrometer in the inventory of the laboratory, we did not perform such measurements yet.

Since we cannot explain this discrepancy between the observed ratios in the PMT signals and the measured radiance for the setup without the M-UG6 filter, we decided to include the M-UG6 filter for the final estimation of the radiance of the calibration light sources. In the following we list the obtained radiance of each source:

$$L_{\mathrm{KIT\ sphere}} = (335 \pm 16)\ \mathrm{G\gamma\, sr^{-1}\, m^{-2}}, \tag{6.36}$$

$$L_{\mathrm{Olomouc\ sphere}} = (368 \pm 18)\ \mathrm{G\gamma\, sr^{-1}\, m^{-2}}, \tag{6.37}$$

$$L_{\mathrm{Tube\ source}} = (121 \pm 6)\ \mathrm{G\gamma\, sr^{-1}\, m^{-2}}, \tag{6.38}$$

where we estimate the total uncertainty to be 4.9%, as discussed in Section 6.7.4.

NOVEL CALIBRATION OF FLUORESCENCE TELESCOPES

Contents

In the following chapter we first describe the analysis of the XY-Scanner measurements performed at the fluorescence telescopes of the Pierre Auger Observatory. We then evaluate the reproducibility of the method and estimate the relative differences between various telescopes. We conclude by describing the method of estimation of the absolute end-to-end calibration constants of the telescopes via the XY-Scanner technique and present the results of the latest XY-Scanner calibration campaigns.

7.1. DATA FROM FLUORESCENCE TELESCOPES

As described in Section 4.2, for the calibration measurements at the FD telescopes we trigger the readout of the entire FD camera for each position of the light source on the scanning grid. For one position we store an event containing 480 traces for each flash of the light source. Out of these, 440 traces correspond to real telescope pixel-PMTs, while the remaining 40 are virtual channels, which can be used to recover the actual signal for saturated pixels, as described in Section 3.3. For the standard FD telescopes, the captured traces contain 1000 time bins and are sampled with a period of 100 ns. The HEAT telescopes are sampled faster (every 50 ns), nevertheless that the traces contain 2000 time bins. Therefore, the traces of all FD telescopes are 100 μs long. We present
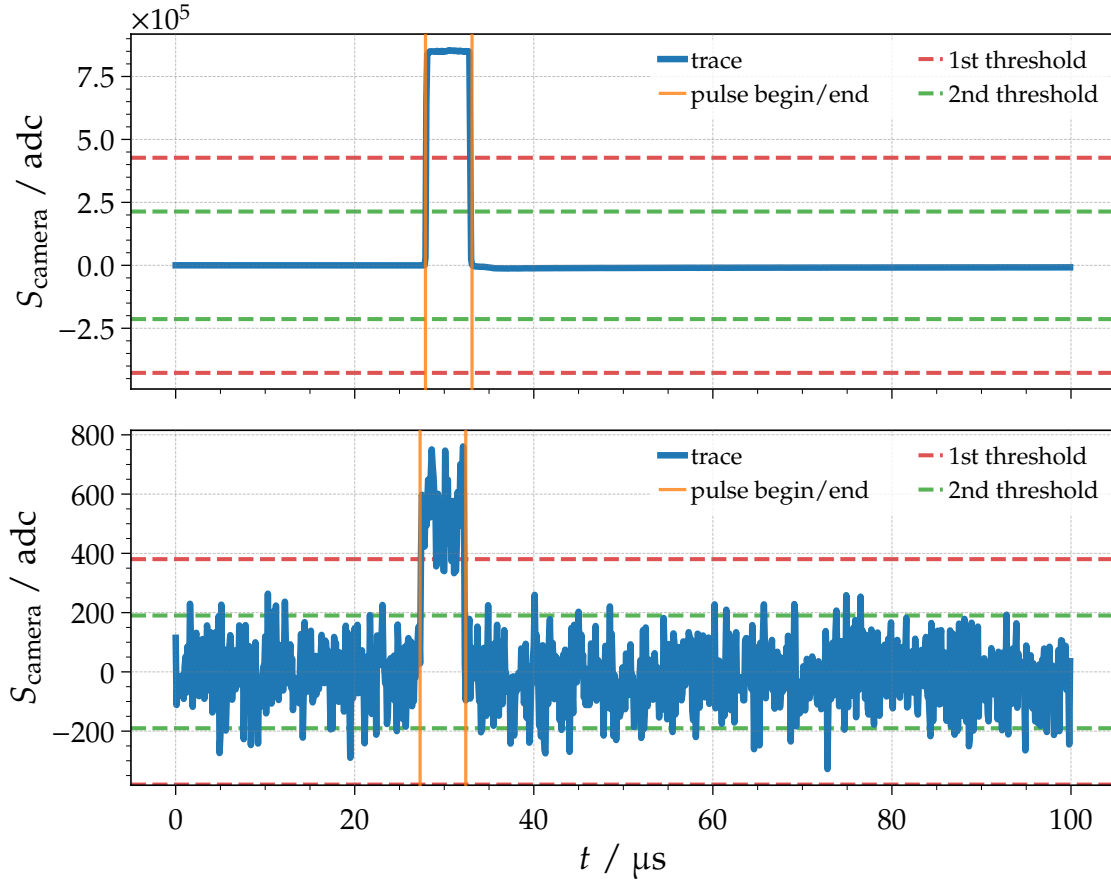
Figure 7.1: Typical trace captured by the telescope camera for an event during an XY-Scanner measurement. The plotted trace is the sum of all 440 pixel-PMT traces for a single event. Additionally we draw the thresholds for the pulse-finding algorithm as horizontal lines and the determined pulse begin/end as vertical lines. *Top:* The light source is well contained in the aperture opening. *Bottom:* Light source is located at a large radius, already partially obscured by the telescope diaphragm. Note the large change if the signal scale between the two plots.

the measuring procedure in Section 4.2. In the following we introduce the tools and methods we employ to analyze the captured data from the FD telescopes.

7.1.1. SIGNAL TRACES AND PULSE FINDING

The first step in analyzing the captured PMT traces is the pedestal subtraction. For this purpose we build an average of the signal in the first ~13 μs of a given trace. This is long enough to obtain a meaningful estimate of the mean, but still short enough to avoid including any possible parts of the signal pulse. While varying this parameter we did not observe an significant impact on the pedestal subtraction as long as no parts of the signal pulse are included. For most XY-Scanner measurements the pulse induced by the light source appears between 25 μs and 35 μs. The pulse length is 5 μs, similar to the one used for the drum calibration.

In a second step, for each event (flash of the light source) the bin-by-bin sum of all 440 pixel-PMT signal traces is calculated and on the resulting trace a pulse-finding algorithm is run. The search for signal pulses is described below. The rising edge of all signal pulses within an event is at the same temporal location for all PMTs. Fig. 7.1 shows the event traces for two events with
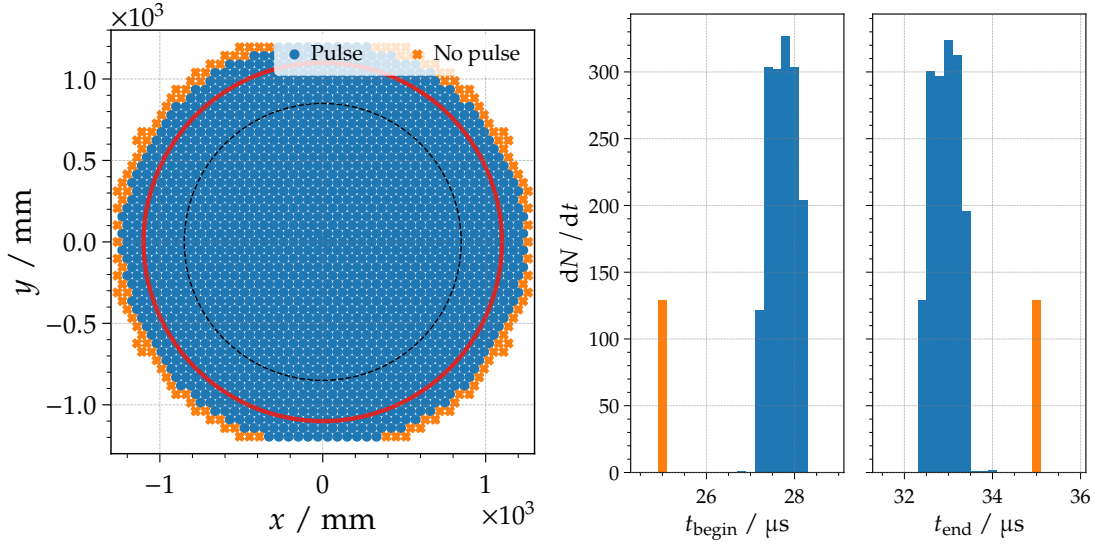
Figure 7.2: Positions of the light source during an XY-Scanner calibration measurement at LA3. The red and dashed-back concentric circles represent the edge of the aperture opening and the corrector lens, respectively. *Left:* Color and style of the marker indicate whether the pulse-finding algorithm was able to find a pulse (blue circle) or not (orange cross). *Right:* Distribution of the found begin and end time bins for all events of an XY-Scanner run. Blue bins represent events where a pulse was found, the orange bins represent the default pulse window.

the light source at different positions of the XY-Scanner. The upper trace is captured while the light source is placed well inside the aperture window, while for the lower trace the light source is located at the outer part of the scanning grid. For the second position the light source is already partially obscured by the diaphragm of the telescope and thus only a fraction of photons emitted by the source actually enters the telescope. We still observe a prominent signal pulse in both of the traces, but the pulse amplitude differs by a factor ~1600. One challenge for the pulse-finding algorithm is to reliably find pulses in all events regardless of the position of the light source and thus nearly independently of the absolute pulse height. We introduce an algorithm capable of finding all those signal pulses in the following.

Pulse-Finding Algorithm. This algorithm was not originally developed for the analysis of the XY-Scanner measurements, but was adapted from Refs. [88, 105].

First, the algorithm estimates the mean μ and the standard deviation σ of all bins b_i within the event trace. The event trace is the bin-by-bin summed traces of all 440 pixel PMTs and is conveniently called trace in following. Then, all trace bins b_i with $|b_i| > (\mu + 5\sigma)$ are excluded and once again the mean μ_{trunc} and the standard deviation σ_{trunc} of the truncated trace are calculated. Afterwards, two threshold parameters t_1 and t_2 with $t_1 \geq t_2$ are defined. For the traces analyzed within this work, these threshold parameters are set to half, $t_1 = 0.5\,b_{\text{max}}$, and quarter, $t_2 = 0.25\,b_{\text{max}}$, of the trace maximum b_{max}, respectively. Exceptions are traces where $b_{\text{max}} < 2\,\sigma_{\text{trunc}}$, for such traces we set the thresholds to $t_1 = \sigma_{\text{trunc}}$ and $t_2 = 0.5\,\sigma_{\text{trunc}}$. However, in most of the analyzed traces we observe a rather large maximum b_{max} and the condition for this exception above is rarely met and occurs exclusively just for positions of the light source far outside the aperture of the telescope. In Fig. 7.1 both thresholds for two different traces are drawn as red and green dashed horizontal lines, respectively.

Next, the algorithm scans the trace and whenever the trace exits the window $w_1 = \mu_{\text{trunc}} \pm t_1\,\sigma_{\text{trunc}}$ the pulse finding is triggered. We define the first bin with an entry outside the window w_1 as a starting point for the next step of the algorithm.

Once the pulse candidate is found by exiting the w_1 window, the next step is to search for the begin and the end of the pulse candidate. We define another parameter d which describes the minimal requirement for the pulse length. Now, the algorithm scans left and right of the previously found starting point until d consecutive bins of the trace inside the smaller threshold window $w_2 = \mu_{\text{trunc}} \pm t_2\, \sigma_{\text{trunc}}$ are found. For the here discussed measurements we set the pulse extent to $d = 4$ bins. If a begin and end of the pulse is found, the pulse finding for this pulse candidate is finished and the algorithm continues searching for more possible pulses within the trace.

We filter away any baseline fluctuations by discarding any pulses with an average height smaller than $2\,\sigma_{\text{trunc}}$. In addition, all pulses, which occur outside the expected time window, are discarded. We accept only pulses, which start between 17.5 µs and 32.5 µs and end between 27.5 µs and 42.5 µs. If no pulse is identified by the algorithm for a given trace, the default pulse begin of $t_{\text{begin}} = 25$ µs and pulse end $t_{\text{end}} = 35$ µs is set for this event. With this procedure we ensure that for each event one and only one pulse begin and end time is returned by the pulse-finding algorithm. In Fig. 7.1 the found begin and end times are indicated by orange vertical lines.

In Fig. 7.2-left we show the positions of an XY-Scanner run and depict the outcome of the pulse finder with different colors. Orange crosses indicate positions where no pulse is found and thus the default pulse window is used. As is visible from the plot, only in positions far outside of the aperture no pulse is found. In the measurement presented here, these positions where no pulse is found account for ~8% of the total number of positions. Nevertheless, the signal captured in the telescope camera for these positions (default pulse window) account for only ~0.0005% of the total signal captured during an entire XY-Scanner measurement. On the right side of Fig. 7.2 the distributions of the determined begin and end times of all events of the same XY-Scanner measurement are plotted. The average pulse length estimated by the pulse-finding algorithm is ~5.2 µs. The nominal length of the light pulses from the source is 5 µs, thus the algorithm overestimates the pulse length on average by only two time bins.

Finally, the pulse-finding algorithm has determined the begin t_{begin} and end t_{end} of the signal pulse for an event by analyzing the bin-by-bin summed trace of all 440 pixels of the telescope camera.

Estimating Charge of Individual PMT Pulses. For an accurate estimation of the charge accumulated during a PMT pulse, the integral over the suitable portion of the trace has to be determined with high precision. For that, it is mandatory to know and estimate the baseline of the whole captured trace. However, in most use cases the baseline is not constant during the time of the whole trace, but depends on the past current flowing through the PMT. Fig. 7.3 presents a typical PMT pulse captured by an FD pixel during an XY-Scanner calibration measurement. In the upper plot, the whole amplitude range of the signal pulse is visible between the times 20 µs and 40 µs. A zoomed view around the baseline of the trace (bottom plot) reveals a rather large undershoot of the trace right after the end of the pulse. This undershoot persists until the end of the captured trace and only slowly decays so that at the end of the trace it still does not reach the initial state. An assumption about a constant baseline would thus result in an underestimation of the charge of the pulse.

In a more advanced approach we assume the baseline is constant before and after the pulse while during the duration of the pulse we use a linear interpolation between the two pieces. The baseline before the pulse, b_{before}, is taken as a mean of the trace starting at the beginning of the captured trace up until 7 µs before the estimated beginning of the signal pulse. The baseline after the pulse, b_{after}, is estimated as a mean of the trace between 2 µs and 5 µs after the estimated end of the pulse. Within the pulse we assume that the baseline drops linearly from the level before the pulse to the level after the pulse. In Fig. 7.4 the trace and the linear baseline model are plotted as blue and orange curve, respectively. The parts of the trace that were used to estimate the two levels of the baseline are marked in red. We estimate the charge signal $S_{\text{ADC}}^{\text{pixel}}$ accumulated in a
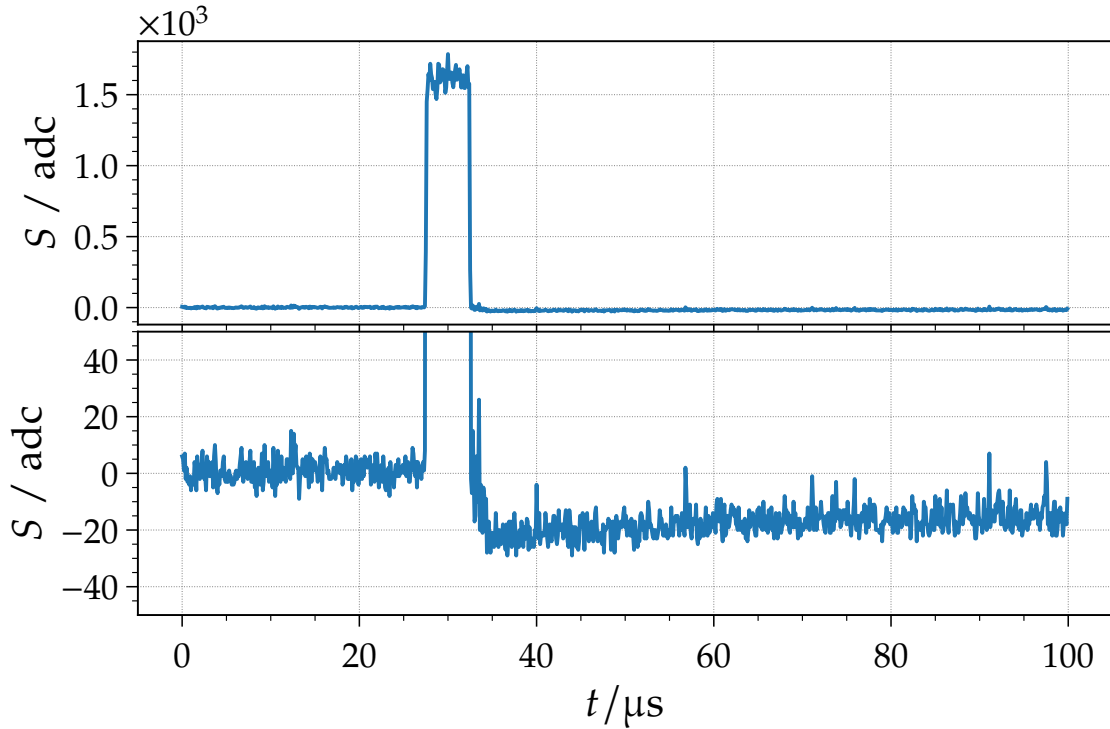
Figure 7.3: Typical pulse captured by a telescope-camera pixel during an XY-Scanner calibration data-taking. The bottom plot is a magnified version of the upper plot to highlight the baseline.

PMT during a light pulse as a sum over the baseline corrected bins b_i of a trace,

$$S_{\text{ADC}}^{\text{pixel}} = \frac{1}{2}\Delta t\,\Delta b + \sum_{t_{\text{begin}}}^{t_{\text{end}}} b_i \tag{7.1}$$

with the pulse begin t_{begin} and end t_{end} estimated by the pulse-finding algorithm, the pulse duration $\Delta t = t_{\text{end}} - t_{\text{begin}}$, and the baseline difference $\Delta b = b_{\text{before}} - b_{\text{after}}$ between the baseline before and after the pulse.

The weakness of this linear-baseline approximation is that the parts of the trace, which determine the two baseline levels, are chosen in a rather arbitrary way. Changes in the number of bins included in the determination of the two means will affect the resulting baseline estimation. For example, if the second level is estimated in a different window, the baseline and thus the calculated charge of the pulse will change. In Section 7.1.2 we discuss a more sophisticated baseline model.

7.1.2. Advanced Baseline Model for FD Photomultipliers

This following part is already available as an Auger internal note [106].

Full Reconstruction of Baseline. Our aim here is to eliminate any arbitrary choices of parameters that can affect the charge estimation of the XY-Scanner signal pulses. We thus have to take into account the whole trace. The model of the time dependence of the actual baseline $b(t)$ on the
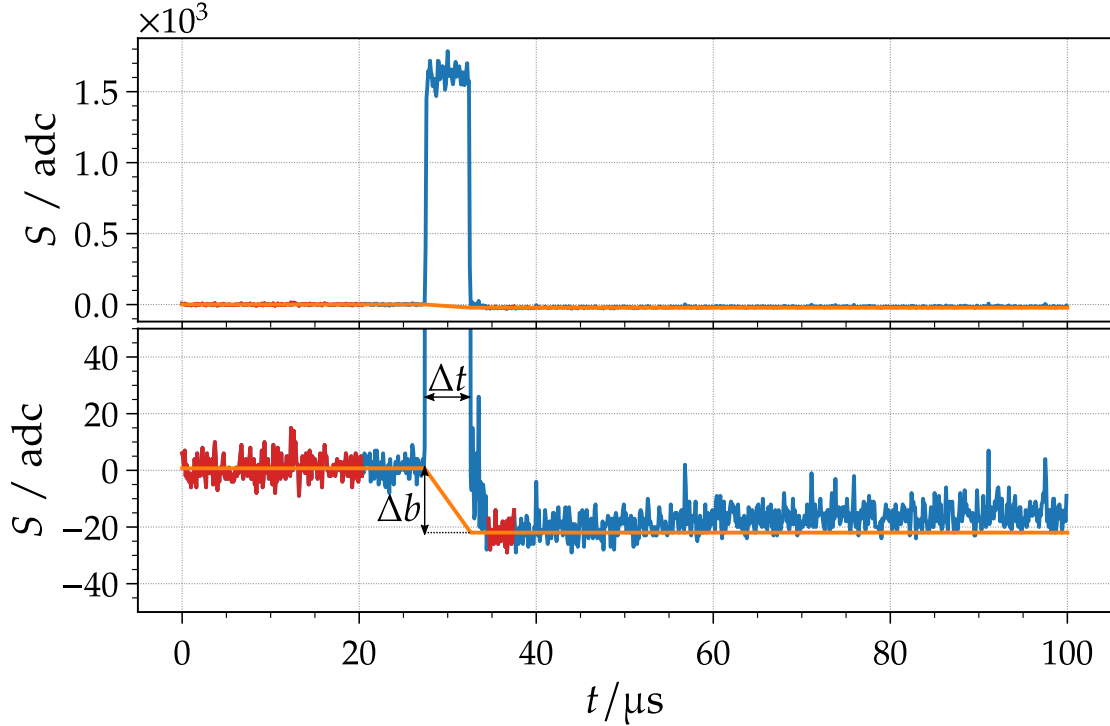
Figure 7.4: Linear-baseline model. The mean of certain parts of the trace (marked in red) give two levels of the baseline before and after the pulse. The baseline in between is estimated as a linear interpolation between the two.

time-dependent "true" signal $S(t)$ is written as

$$b(t) = b_{\text{nom}} + \frac{\alpha}{\tau} \int_{-\infty}^{t} \exp\left(-\frac{t - t'}{\tau}\right) S(t') \, dt' \tag{7.2}$$

where b_{nom} is the nominal baseline (i.e. baseline in the absence of any signal) and where we introduce α as a proportionality factor between the baseline distortion and the pulse signal, and where τ is the decay time of the distortion. Both parameters α and τ will be explained separately below. The huge advantage of this model is that there are almost no arbitrary choices of parameters, which could influence the baseline. How the parameters α and τ of this model are estimated from real measured traces of the XY-Scanner measurements is discussed in the following.

Decay Constant and Undershoot Amplitude. For the relaxation of the trace $T(t)$ after the pulse, i.e. for $t > t_1$, an exponential decay is assumed,

$$T(t) - b_{\text{nom}} = \frac{q_u}{\tau} \exp\left(-\frac{t - t_1}{\tau}\right), \tag{7.3}$$

where q_u is the charge amplitude of the baseline distortion and τ its decay time. Note that for undershoot the distortion amplitude q_u is going to be negative and that the functional form of Eq. (7.3) is chosen so that $\int_{t_1}^{\infty} T(t) \, dt \equiv q_u$. For the fitting of this particular example of pulses the beginning of the decay was set at the end of the pulse $t_1 = 35\,\mu s$. An example of the performed fit is plotted in Fig. 7.5. In this figure the trace $T(t)$ is plotted as a blue line and the result of the fitting Eq. (7.3) is shown in green. The fitted part of the trace after the pulse is marked with orange.
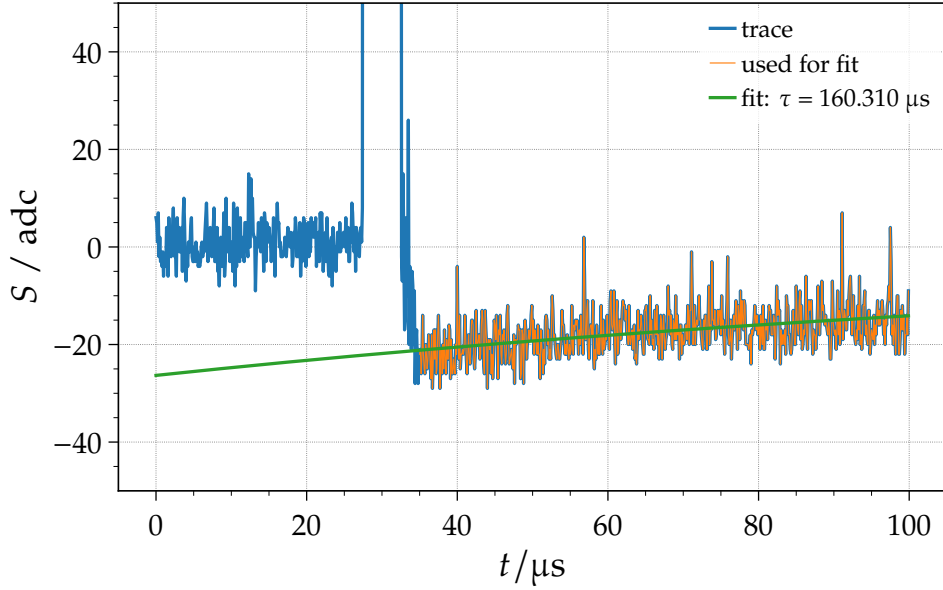
Figure 7.5: Plot of a typical PMT trace in blue with the fitted decay function from Eq. (7.3) in green. The part of the trace used for the fit is marked in orange.

The fits were performed on a dataset containing ~700 000 traces (~1600 events × 440 pixels) and resulted in ~700 000 different values for q_u and τ.

The distribution of the fitted decay-time parameter τ is shown in Fig. 7.6. To clean the data from all low-charge pulses a quality cut was applied to the data (orange curve) which removes all pulses with a charge q less than 30% of the maximal observed charge q_{max} in the whole dataset, i.e. $q > 0.3\, q_{max}$. As can be seen in Fig. 7.6, the decay constant τ in the cleaned dataset is peaked and narrowly distributed around a short interval of values.

To estimate this one single global decay-time constant τ that would on average describe well all the pixel PMTs, a fit of the normal distribution $\mathcal{N}(\tau; \bar{\tau}, \sigma_\tau)$ is performed to the peak of the cleaned dataset. The variation between the telescopes is not large enough to justify keeping separate values of the decay constant so that once $\bar{\tau}$ was estimated from the whole cleaned dataset, the parameter τ in Eq. (7.3) was fixed to $\bar{\tau} = 158.505\,\mu s$. The trace after the pulse can thus be well described by

$$T(t) - b_{\mathrm{nom}} \approx \frac{q_u}{\bar{\tau}} \exp\left(-\frac{t - t_1}{\bar{\tau}}\right). \tag{7.4}$$

With this modified function (with fixed parameter $\bar{\tau}$), the fit of the whole dataset was repeated and a new and final set of baseline-distortion amplitudes q_u was obtained.

Correlation of Pulse Charge and Subsequent Undershoot.   We are interested in the correlation of the pulse charge q and the associated undershoot q_u. The pulse charge q is defined as the integral of the signal $S(t)$ between the pulse begin and end,

$$q = \int_{t_{\mathrm{begin}}}^{t_{\mathrm{end}}} S(t)\, \mathrm{d}t = \Delta t \sum_{i=i_{\mathrm{begin}}}^{i_{\mathrm{end}}} S_i \approx \Delta t \sum_{i=i_{\mathrm{begin}}}^{i_{\mathrm{end}}} (T_i - b_{\mathrm{before}}), \tag{7.5}$$

where we approximated the unknown S_i with the baseline-subtracted trace $T_i - b_{\mathrm{before}}$. In the FD the sampling period of the traces is $\Delta t = 0.1\,\mu s$. The begin t_{begin} and the end t_{end} of the pulse are obtained by a pulse-finding algorithm (discussed in Section 7.1.1). The charge of the undershoot q_u is given by the fits of Eq. (7.4) to the trace, which is now, with the decay fixed to
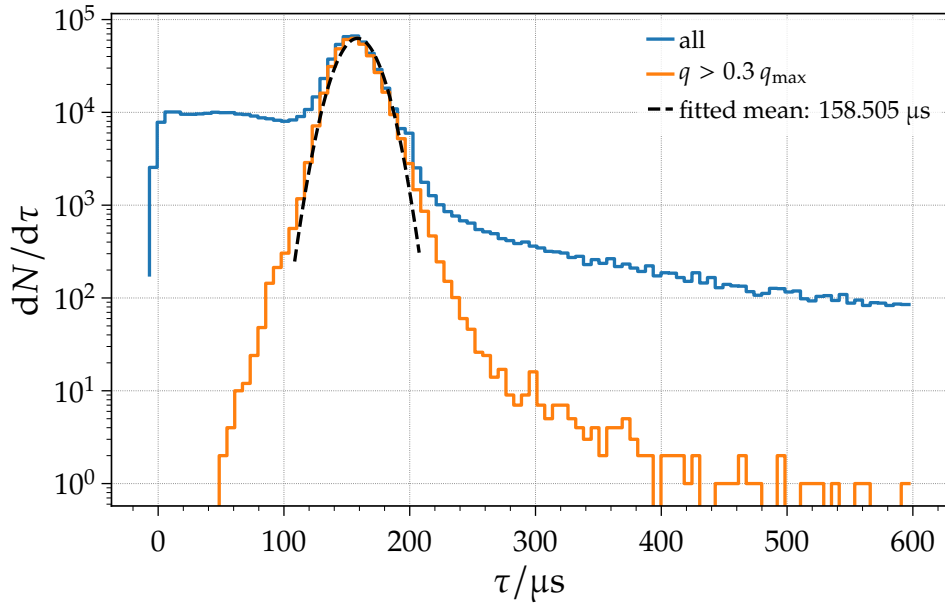
Figure 7.6: The distribution of the decay time τ from fits of Eq. (7.3) to the entire data set of ~700 000 traces is shown in blue. The cleaned data set with the cut $q > 0.3\, q_{max}$ is shown in orange. The black dashed line is a fit of a normal distribution to the orange histogram.
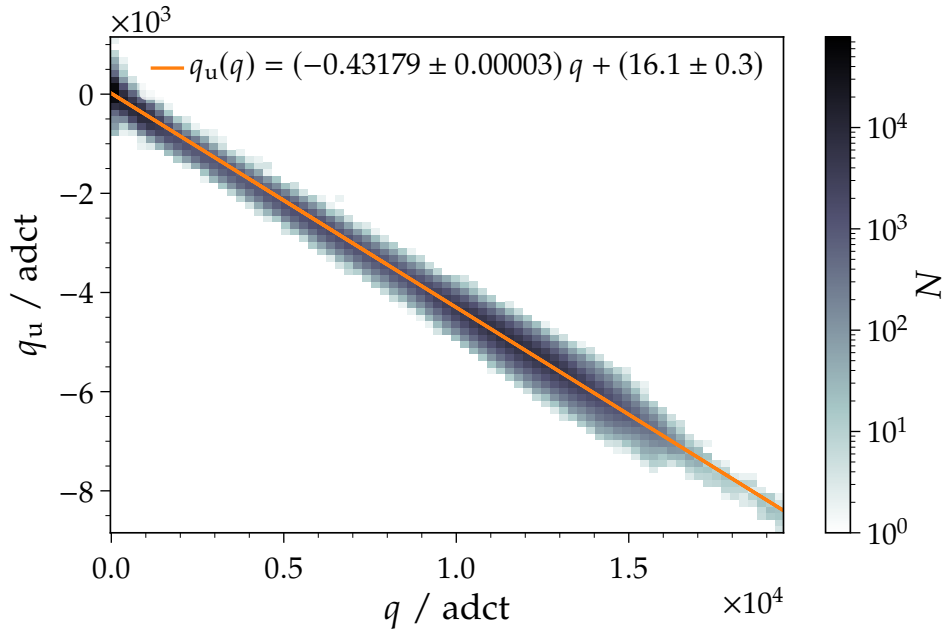
Figure 7.7: The two dimensional distribution of the pulse charge q and the baseline-distortion amplitude q_u. The amplitude of the undershoot scales linearly with the pulse charge. The orange line represents a linear fit to the data.
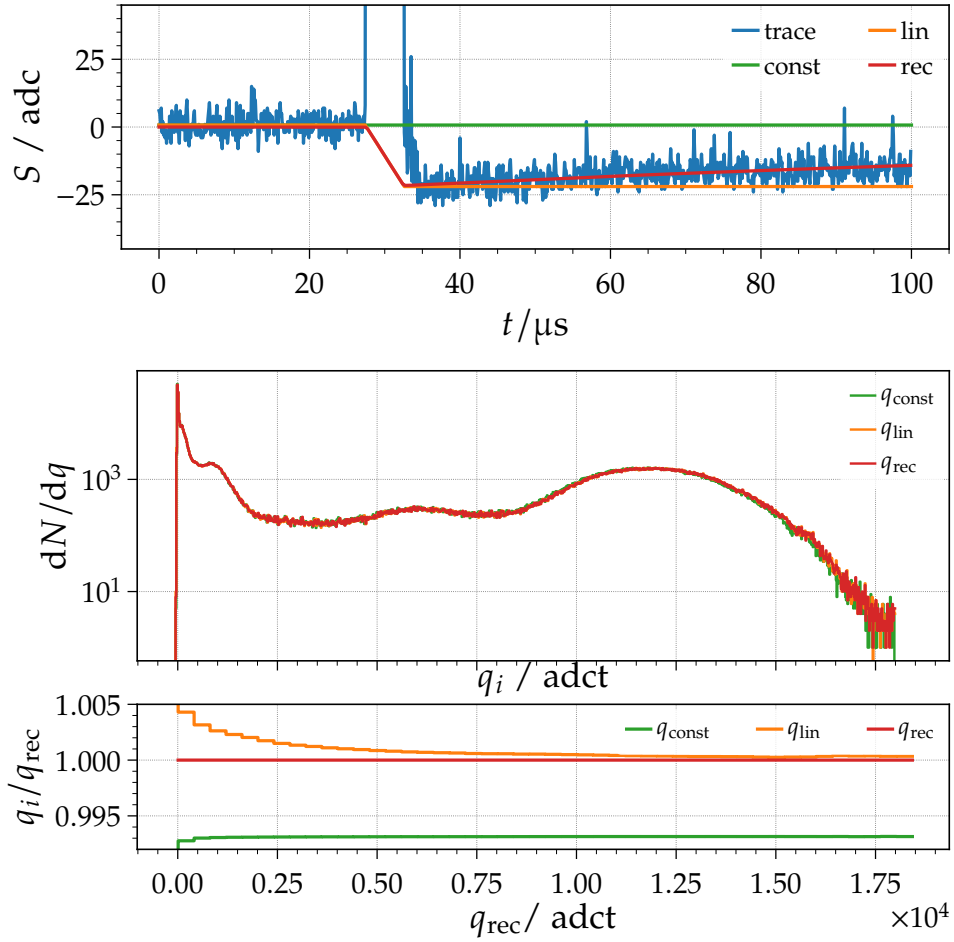
Figure 7.8: *Top:* Comparison of baseline models. The measured trace T_i is drawn in blue. The linearly-interpolated baseline approximation is shown in orange. The baseline according to the full reconstruction in Eq. (7.8) is plotted in red. *Center:* Distributions of the pulse charges q when using the different baseline models: q_{const} for assuming constant baseline throughout the trace (in blue), q_{lin} for assuming linearly-interpolated baseline between two values (in orange), and q_{rec} for the full reconstruction (in green). *Bottom:* Mean ratio of the estimated pulse charges q_{const}/q_{rec} and q_{lin}/q_{rec} as a function of q_{rec}.

$\bar{\tau}$, only a single-parameter fit. The two-dimensional distribution of obtained pulse charges q and corresponding baseline-distortion amplitudes q_u is plotted in Fig. 7.7. From this distribution we can easily conclude that the distortion amplitude scales linearly with the pulse charge. Therefore a linear fit in the form

$$q_u(q) = \alpha\, q + n \tag{7.6}$$

was performed, obtaining the proportionality factor $\alpha = -0.43179$ and the offset $n = 16.1$. While the latter is not exactly compatible with zero, it is negligible in terms of the actual sizes of q and q_u encountered in the dataset so that it can be safely assumed to be zero from now on.

Reconstruction of Baseline. Now we can return to the model of the time dependence of the baseline from Eq. (7.2). Expressing the integral with a sum over discrete time bins, the model

becomes

$$b_i = b_{\text{nom}} + \beta \sum_{j=-\infty}^{i} \exp\left(-\frac{t_i - t_j}{\bar{\tau}}\right) S_j$$

$$= b_{\text{nom}} + \beta S_i + \beta \sum_{j=-\infty}^{i-1} \exp\left(-\frac{t_i - t_j}{\bar{\tau}}\right) S_j$$

$$= b_{\text{nom}} + \beta(T_i - b_i) + \beta \sum_{j=-\infty}^{i-1} \exp\left(-\frac{\Delta t(i - j)}{\bar{\tau}}\right) S_j, \qquad (7.7)$$

with the signal S_i in time bin i obtained from the raw trace T_i as $S_i = T_i - b_i$. We also introduced a dimensionless parameter $\beta = \alpha \Delta t / \bar{\tau}$. As a suitable approximation for b_0 we can simply use T_0 or a mean over the beginning of the trace. Solving the final equation for b_i leaves us with an explicit expression

$$b_i = \frac{1}{1 + \beta}\left(b_{\text{nom}} + \beta T_i + \beta \sum_{j=-\infty}^{i-1}\left[\gamma^{(i-j)}(T_j - b_j)\right]\right), \qquad (7.8)$$

where $\gamma = \exp(-\Delta t / \bar{\tau})$. With this the baseline b_i in each time bin i can be reconstructed. Note that in the sum above, technically the expression $j = -\infty$ means that the sum should run from the beginning of the trace T. An example of the various baselines is shown in Fig. 7.8-top. The *constant* baseline assumes one value of the baseline for the whole trace, the *linear* model assumes linear interpolation between the two baseline values on each side of the pulse, and the *reconstructed* baseline is obtained with Eq. (7.8). The associated pulse charges obtained with the different baselines are denoted with q_{const}, q_{lin}, and q_{rec}, respectively. Their distributions are for the whole dataset shown in Fig. 7.8-center. The ratios of $q_{\text{const}}/q_{\text{rec}}$ and $q_{\text{lin}}/q_{\text{rec}}$ as a function of q_{rec} are shown in Fig. 7.8-bottom. When compared to the pulse charges q_{rec}, the two simpler estimates q_{const} and q_{lin} exhibit deviations on the order of 0.7% and ~0.2%, respectively. For rectangular pulses, like for instance emitted by flashers of the XY-Scanner light sources or by the CalA setup, assuming a linear interpolation between the two baselines is usually a good enough approximation.

Therefore, we decide to apply the linear interpolation model for the baseline of the PMT traces to estimate the charge signal $S_{\text{ADC}}^{\text{pixel}}$ according to Eq. (7.1) throughout this work. We assign the difference between the signal determined with the reconstructed and the linear baseline model (~0.2%) as the uncertainty of the estimated signal $S_{\text{ADC}}^{\text{pixel}}$.

7.1.3. SIGNAL DISTRIBUTION OF XY-SCANNER MEASUREMENTS

In the following we discuss the signal captured by the telescope camera for the light source being placed at different positions on the scanning grid.

The left side of Fig. 7.9 shows the signal captured in the entire telescope camera for the various positions (~1700) of the light source for an entire XY-Scanner calibration measurement. Each filled circle in the plot represents the location of the light source, while the colors of each circle indicate the signal captured in the entire telescope camera. The red circle drawn in the plot presents the edge of the aperture, which has a radius of $r_{\text{aperture}} = 1100\,\text{mm}$. The dashed-black circle demonstrates the edge of the corrector lens. The dark vertical and horizontal lines visible in that plot are shadows cast by the filter support structure of the telescope.

Most of the signal collected in the camera is captured for positions of the light source within the aperture. The flashes of the light source from the positions outside the aperture account only for ~3% of the entire captured signal during this XY-Scanner measurement. Furthermore, 99.9% (99.99%) of the total signal is produced by positions within a radius of $r \approx 1167.9\,\text{mm}$ (1213.2 mm). The right plot of Fig. 7.9 displays the cumulative sum of the signal
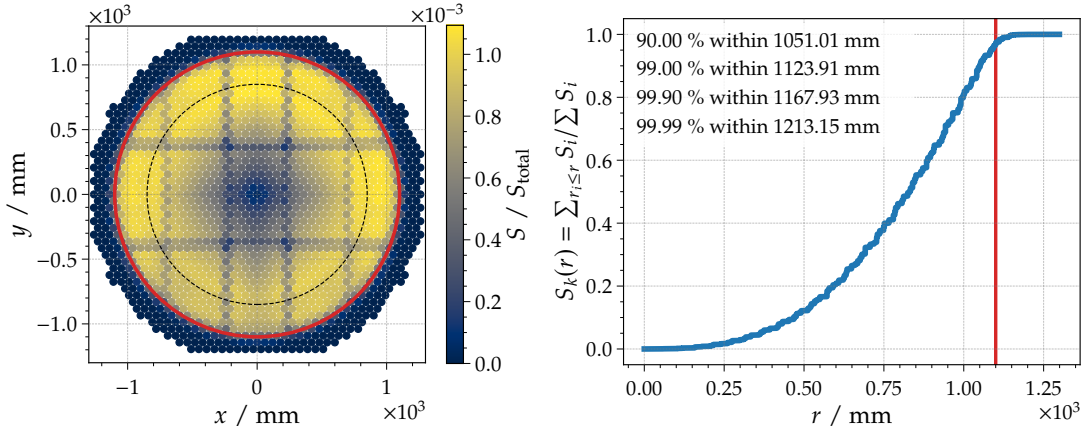
Figure 7.9: *Left:* Signal captured by the entire FD camera for each position is drawn as circle, the color of the circle gives the signal strength. The red and black-dashed concentric circles represent the edge of the aperture and the corrector lens, respectively. *Right:* Cumulative signal sum over the radial distance ($r = \sqrt{x^2 + y^2}$) between the light source and the optical axis of the telescope.

captured for the light source being within a given radius r. The radius of the aperture edge r_{aperture} is drawn as a red vertical line. The slow increase of the signal sum for small radii, $r \lesssim 500$ mm, is due to the shadow cast by the camera itself. This shadow also appears as the dark area in the center of the plot on the left of Fig. 7.9. A collection of radii, which contain a certain signal amount are also shown within the plot.

From these observations, we conclude that the radius $r_{\text{grid}} \approx 1300$ mm of XY-Scanner grid is large enough to encompass all positions, which make a non negligible contribution to the total signal. Hence, the contribution of any additional positions further outside the aperture opening is insignificant.

7.1.4. Statistical Uncertainties of XY-Scanner measurements

Since we assume an identical light emission from the light source at each position on the XY-Scanner grid, the main contribution to the statistical uncertainty on a measurement run arises from the signal captured by the telescope camera. For a standard XY-Scanner measurement with the step size of $\Delta s = 6$ cm, we capture $S_{\text{ADC}}^{\text{pixel}} \approx 8 \times 10^6$ adc per pixel or $S_{\text{ADC}}^{\text{camera}} \approx 3.5 \times 10^9$ adc in the entire camera during a complete calibration measurement. See Fig. 4.4 for an illustration of the total signal captured during a measurement.

For an estimation of the statistical uncertainty on the dataset (signal in each of the 440 pixels for an entire XY-Scanner measurement run) we use a bootstrap method [107]. We build a bootstrap dataset by randomly selecting n light source positions with n equal to the number of positions $n_{\text{pos}} \approx 1700$ within the original dataset. We draw the n positions with replacement, which allows for duplicated or missing positions in the bootstrap dataset with respect to the original dataset. The bootstrap dataset thus most probably differs from the original dataset. Then we compute the signal in each pixel by building the sum over all n positions. With this procedure we end up with a signal estimate $S_{\text{boots}}^{\text{pixel}}$ for each individual pixel for an entire measurement run. Repeating these steps several hundred times results in a signal distribution for each individual pixel. Next, we estimate the mean μ_{boots} and the standard deviation σ_{boots} of each distribution. We define the relative uncertainty for an XY-Scanner measurements as $\sigma_{\text{boots}}/\mu_{\text{boots}}$.

We perform this analysis for different XY-Scanner measurements performed at different telescopes, with different calibration-light sources, and using different step sizes. In Fig. 7.10 we show the average of the estimated uncertainties for the different XY-Scanner measurements. We observe
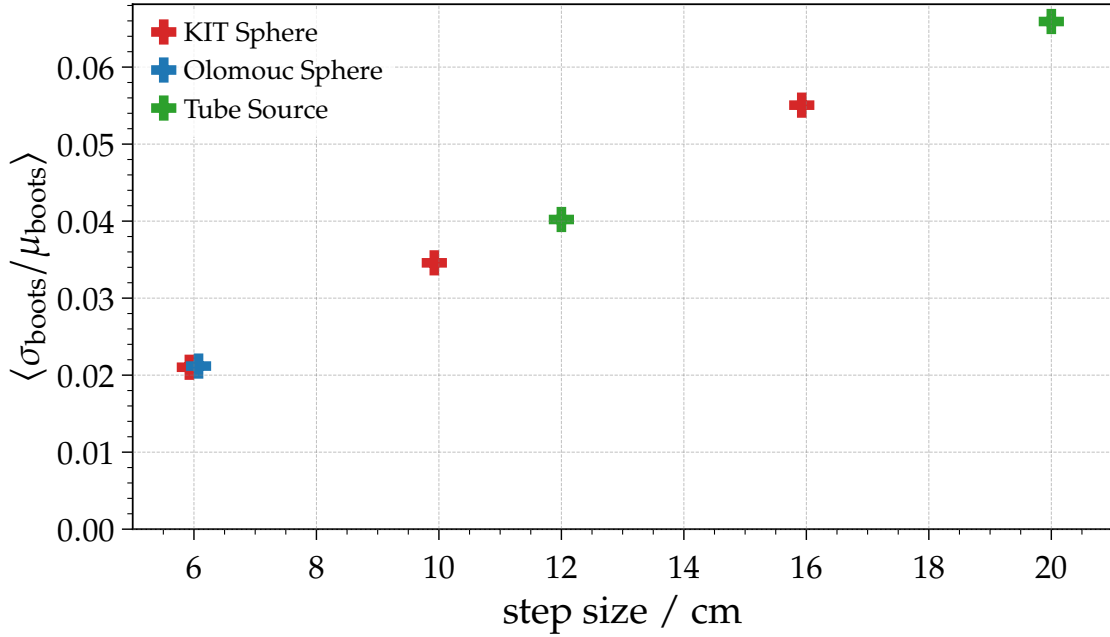
Figure 7.10: Average uncertainties of the pixel signal for a XY-Scanner measurement as function of the step size. Estimates obtained via the bootstrap method as explained in the text. Different colors represent different calibration-light sources.

the smallest uncertainties of ~2.1% for measurements with the smallest step size of $\Delta s = 6$ cm and with either of the two integrating-sphere light sources. Increasing the step size will reduce the number of positions on the scanning grid and therefore also increase the statistical uncertainty. The estimated uncertainties are:

	step size Δs	uncertainty	measurement duration
integrating spheres	6 cm	2.1%	~46 min
	10 cm	3.5%	~21 min
	16 cm	5.5%	~10 min
tube source	12 cm	4.0%	~15 min
	20 cm	6.6%	~7 min

In addition we list the duration needed to complete a certain measurement. With 6 cm-steps we manage to calibrate one FD building (six telescopes) within two measuring nights. If we want to reduce the measuring time needed for the XY-Scanner, it only makes sense to reduce it to the point where we are able to calibrate an entire building in one night. Otherwise two trips to the FD building are necessary anyway. Therefore we need to reduce the measurement time and following the number of positions by roughly a factor of two, which on the other hand increases the uncertainty of the calibration. Choosing 8 cm-steps reduces to number of positions by ~40%. Assuming a similar reduction for the measuring duration we may able to calibrate six telescopes in a single night and keep the uncertainty below ~3%. However, a more detailed study of the consideration of uncertainty and time consumption is not presented here.

Since former simulation studies [57] concluded that a step size of 6 cm is convenient for the calibration measurements, we performed the bulk of measurements with this setting. For these measurements we estimate the statistical uncertainty via the bootstrap technique to be ~2.1%.

Figure 7.11: Reproducibility of the results on short timescales. Ratio of the calibrated pixel signal captured during the XY-Scanner measurements, which were performed ~8 days apart in October 2022 at CO3. *Left:* Ratio illustrated as pixel matrix with the colors indicating the magnitude. *Right:* Plot of the signal ratio as function of the pixel number.

7.2. Reproducibility of XY-Scanner Measurements

The absolute calibration of the FD telescopes is only reliable if the procedure itself provides reproducible results within its statistical uncertainty. Therefore, we repeatedly performed measurements with the identical settings and identical hardware at the same telescope. In the time between the measurements we uninstalled all parts of the XY-Scanner mechanics and stored them inside the FD telescope building. This includes the light source, the horizontal X-axis, and the scanner control box. Only the vertical scanner axis, which are permanently mounted left and right of the aperture windows remained installed.

Short Timescales. We estimate the reproducibility of the XY-Scanner results on timescales of days by comparing measurements performed within the same calibration campaign but during different measuring nights. In Fig. 7.11 we present the ratio of the calibrated pixel signal

$$S_{\text{pixel}}^{\text{calib}} = S_{\text{pixel}}^{\text{ADC}} \, C_{\text{pixel}}^{\text{std}} \tag{7.9}$$

with the pixel signal $S_{\text{pixel}}^{\text{ADC}}$ and its standard calibration constant $C_{\text{pixel}}^{\text{std}}$, between two XY-Scanner measurements performed eight days apart. The left side of the plot presents the ratio as a 2D-pixel matrix where each hexagon corresponds to a telescope pixel PMT. The color indicates the magnitude of the ratio. The very same data is displayed as a function of pixel index in the right plot. The values of the mean μ, standard deviation σ, minimum, and maximum of the data are given in the figure. Comparing the calibrated signal of the two measurements, we observe also no significant change in the whole-camera average signal. The mean pixel-signal ratio is compatible with one. For individual pixels we estimate a maximal difference between the two measurements to be on the order of ~2%. However, the difference is below ~0.5% for the majority of pixels and only ~10% of the pixels show a larger than ~0.5% difference. Therefore, we conclude that the XY-Scanner calibration measurements are stable on time scales of days.

Long Timescales. Similarly to above, we compare XY-Scanner measurements separated by a longer time interval. We selected measurements, which were performed ~7 months apart in 2019 for the telescopes of Los Leones. Fig. 7.12 presents the ratio of the calibrated pixel signals,
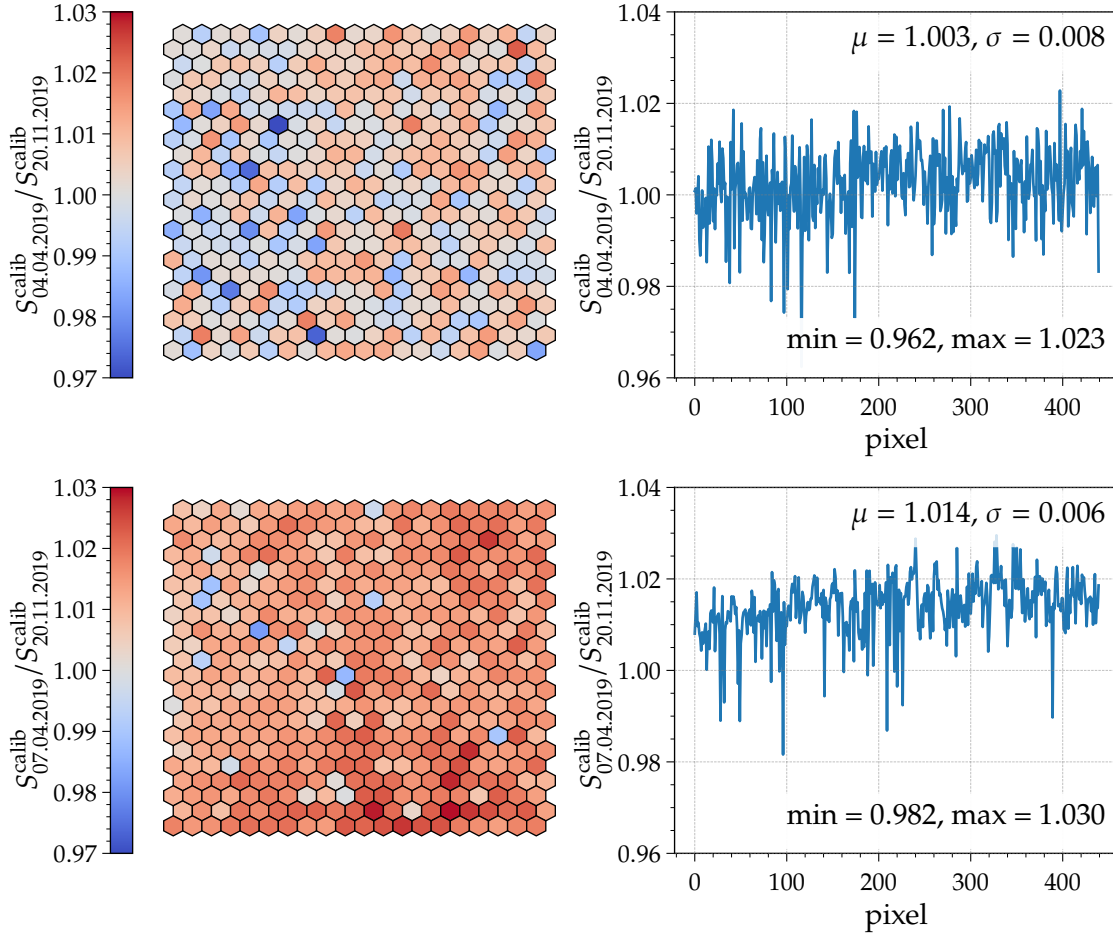
Figure 7.12: Ratio of the calibrated pixel signal captured during XY-Scanner measurements, which were performed ~7 months apart in April and November 2019 at the FD site of Los Leones. Plots are similar to Fig. 7.11. *Top:* LL3 telescope. *Bottom:* LL4 telescope.

according to Eq. (7.9), as captured by the telescope camera. The plots in the top row show the measurements at LL3 while the bottom row presents the equivalent measurements at LL4.

For the LL3 telescope we observe an average change in the telescope pixel signal of ~0.3% for the time interval of ~7 months, which is below the statistical uncertainty of XY-Scanner measurements as discussed in Section 7.1.4. However, this would correspond to a signal drift of ~0.5% per year. We assume an identical light source for both measurements and ignore any systematic effects of the XY-Scanner measurements or the telescope calibration and attribute the change in signal entirely to a change of the telescope. This observed signal drift in the XY-Scanner measurements coincides with the observed drift of the energy ratio between the FD and SD measurements. In Ref. [70] a drift of $(-0.68 \pm 0.28)\%$ per year of this energy ratio is reported for measurements after the year 2014, which is the time when we operate the XY-Scanner.

However, for the LL4 telescope (plots in the bottom row of Fig. 7.12) we observe a larger difference between the two measurements. We estimate a maximal ratio for individual pixels to be ~3% and an average signal drift of ~1.4% within the same time period. However, this observation is within the statistical uncertainty of a 6 cm-run with an integrating sphere as a light source, as discussed in Section 7.1.4. Nevertheless, the observed ratio corresponds to a rather large signal drift of ~2.4% per year, but this coincides with an older estimate [108] where an FD energy drift of $(-2.4 \pm 0.4)\%$ per year is reported. For this estimate data taken in between 2004

and 2008 is analyzed.

In the following we speculate about a possible explanation for this apparent contradiction of these observations. The mirror of the telescope LL4 was cleaned on 05 April 2019, right before we performed the XY-Scanner measurement. We describe the cleaning procedure and this effect on the XY-Scanner measurements in Section 5.1. But note that both measurements of LL4 presented in Fig. 7.12 were performed after the mirror cleaning. The last cleaning of the mirror of LL3 was performed 11 years prior, in the year 2008. If, after a certain time duration, the accumulation of dirt or dust on the mirror surfaces reaches a kind of saturation then the reflectance of the mirror will not change significantly after this point. The saturation could explain the smaller drift of the LL3 telescope seen in the analysis of the XY-Scanner data and in the latest analysis of the FD/SD energy ratio due to the fact that this mirror is "saturated" on dust. On the other hand, cleaning the mirror puts it back into similar (or more clean) conditions as it was the case in the early days of the observatory. During that time the FD/SD energy ratio revealed the larger $((-2.4 \pm 0.4)\%$ per year) drift. If the relative change of reflectance depends on the total amount of dust accumulated, the influence on a clean mirror is higher than on an already dusty mirror. This could potentially explain the larger FD energy drift seen in the years 2004 to 2008 and likewise explain the larger signal ratio observed in the XY-Scanner measurements after the cleaning of the mirror.

Nevertheless, we conclude that the XY-Scanner measurement procedure is stable within its statistical uncertainty (~2.1% for the measurements presented here) on time scales of several months.

7.2.1. Influence of Telescope Shutter Status

Up to now, we performed the standard XY-Scanner measurements for the absolute calibration of the FD telescopes while the telescope shutter was kept open. There is no specific reason, which forces the XY-Scanner to be operated with the opened shutters. All hardware components of the scanner setup are located within the aperture box and are thus technically allowing us to operate the XY-Scanner with the shutters closed. At least, this is the case for the standard FD telescopes. Due to a different design of the three telescopes of HEAT, the shutter cannot be closed there while the XY-Scanner is installed. Even though the FD camera is additionally illuminated due to the persistent night-sky background, the XY-Scanner calibration technique should be insensitive to this DC background. First of all, the telescope PMTs are AC coupled to the readout system and are therefore insensitive to a constant photon flux. Secondly, any potential shift of the PMT signal baseline is accounted for in the pulse-finding algorithm, as we discuss in Section 7.1.1. Nevertheless, photons emitted from the light source, which get reflected on the filter or other components within the aperture box leave the telescope while the shutter is opened. On the other hand, for a closed shutter operation these photons may get reflected back into the telescope where they can contribute and increase the signal.

We studied the influence of the shutter status in the XY-Scanner campaign of November 2019, during which we performed a dedicated measurement program with opened and closed telescope shutters at the telescope 4 of Loma Amarilla (LA4). Right after the standard XY-Scanner measurement with opened shutters was completed, we closed the shutter and repeated the measurements with identical parameters. The time interval between the last flash of the open-shutter run and the first flash of the closed-shutter run was ~6 min. This data enables us to study the influence of the shutter status on the XY-Scanner procedure.

In Fig. 7.13 we present the ratio of the captured signal per telescope pixel for the XY-Scanner measurements with closed and open shutter. The left side of Fig. 7.13 shows the signal ratios as a pixel matrix. The magnitude of the ratio is encoded by color. On the right, the same data is shown as a function of the pixel number. The mean μ, standard deviation σ, minimum, and maximum of the measured ratios are also given within the plot.

In this analysis we observe an average increase in the pixel signals of ~3% by comparing the XY-Scanner measurements with the closed and open shutter. This observed increase may be explained by reflected light at the inner shutter walls. Any photons, which get reflected either directly at the telescope filter or at any interior component of the telescope, may leave the telescope
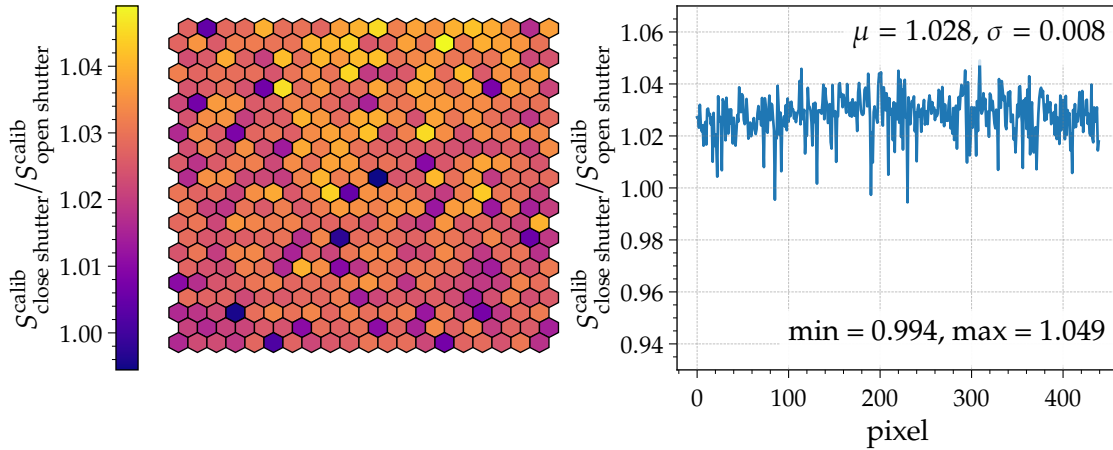
Figure 7.13: Influence of the telescope shutter status on XY-Scanner measurements at LA4. Shown is the signal ratio per pixel for two XY-Scanner runs with open and closed shutter. *Left:* Pixel matrix of the camera. *Right:* Signal ratio as a function of pixel number.

when the shutter is open. For a closed shutter some of these photons can possibly get reflected on the inner walls of the shutter and return into the telescope. Also note that the inner walls of the shutters are equipped with the highly-reflecting Tyvek sheets of the relative calibration system Cal C, as explained in Section 3.4.2. Therefore, these reflected photons can lead to an increase of the measured signal. To avoid necessary corrections for these reflected photons, it is advisable to perform the calibration measurements with the XY-Scanner while the telescope shutter is open.

If not stated otherwise all XY-Scanner measurements discussed throughout this work were performed while the telescope shutters were open.

7.2.2. STABILITY OF TELESCOPE CAMERA DURING XY-SCANNER MEASUREMENTS

Former observations and studies [40, 53, 109] have shown, that the response of the telescope pixel PMTs to the illumination of the Cal A light flashes changes over the course of a night. See also the discussion in Section 3.4.2 and particularly Fig. 3.15. The response to the Cal A illumination at the beginning of a measuring night is on average ~1% to ~5% lower than to the Cal A at the end of the night. These changes in the response of the PMTs are probably due to changes in PMT gains, which are induced by the additional illumination from the night-sky background.

To ensure the stability of the telescope camera for the entire duration of a full XY-Scanner calibration measurement (up to ~60 min), we execute the Cal A procedure right before the start and right after the finish of an XY-Scanner measurement run. We validate the stability of the telescope camera by analyzing these Cal A measurements. The results of a selection of measurements are presented in Fig. 7.14. Fig. 7.14 shows the distributions of the ratios between the captured pixel signal during the Cal A procedure before (and after) the XY-Scanner measurement and the standard Cal A measurement performed at the beginning of the measuring night. The mean of the ratio distributions $\langle r_{\mathrm{b}} \rangle$ ($\langle r_{\mathrm{a}} \rangle$) for the Cal A before (after) the XY-Scanner measurement as well as their difference are given within the plots. The standard Cal A measurement at the beginning of the data-taking night is performed with closed shutters, while the two Cal A runs surrounding the XY-Scanner measurements are executed while the shutter is open. We summarize the influence of the shutter status on the Cal A procedure in Appendix A.5, but we observe no significant influence of the shutter status on the recorded pixel signals during Cal A measurements.

For the measurements presented in Fig. 7.14, we estimate the difference in the average relative pixel signals before and after an XY-Scanner measurement to be $\langle r_{\mathrm{b}} \rangle - \langle r_{\mathrm{a}} \rangle \lesssim 0.6\%$. From this observations we conclude that the telescope cameras are stable for the entire duration of a complete XY-Scanner measurement run.

Figure 7.14: Distributions of the ratios between the FD pixel response to Cal A procedure (before (blue) and after (orange) XY-Scanner runs with open shutter) and the standard Cal A procedure (with closed shutter) at the start of the measuring night. Different plots show different telescopes, only a selection of telescopes is shown here.

7.3. Cross Calibration between Telescopes

The calibration measurements we performed during the various XY-Scanner campaigns offer additional the unique possibility to directly estimate a cross-calibration between different telescopes. We use such a cross-calibration to validate the current standard calibration procedure of the FD telescope cameras. In this context we refer to the standard calibration as the absolute calibration constants obtained by the latest drum calibration campaign (Section 3.4.1), which are propagated to any point in time with the relative calibration system (Section 3.4.2).

For ordinary XY-Scanner calibration measurements the light source is driven across the whole aperture of the telescope. At each of the ~1700 positions (depending on the step size), the light source emits a light pulse with the same intensity. We give a detailed description of the XY-Scanner measurement procedure in Section 4.2 and discuss the stability of the measurements in Section 7.2.

We estimate the total signal S_{tel} captured by the entire camera of a telescope during a complete XY-Scanner measurement as the sum over all light-source positions P_{xy} on the XY-Scanner grid
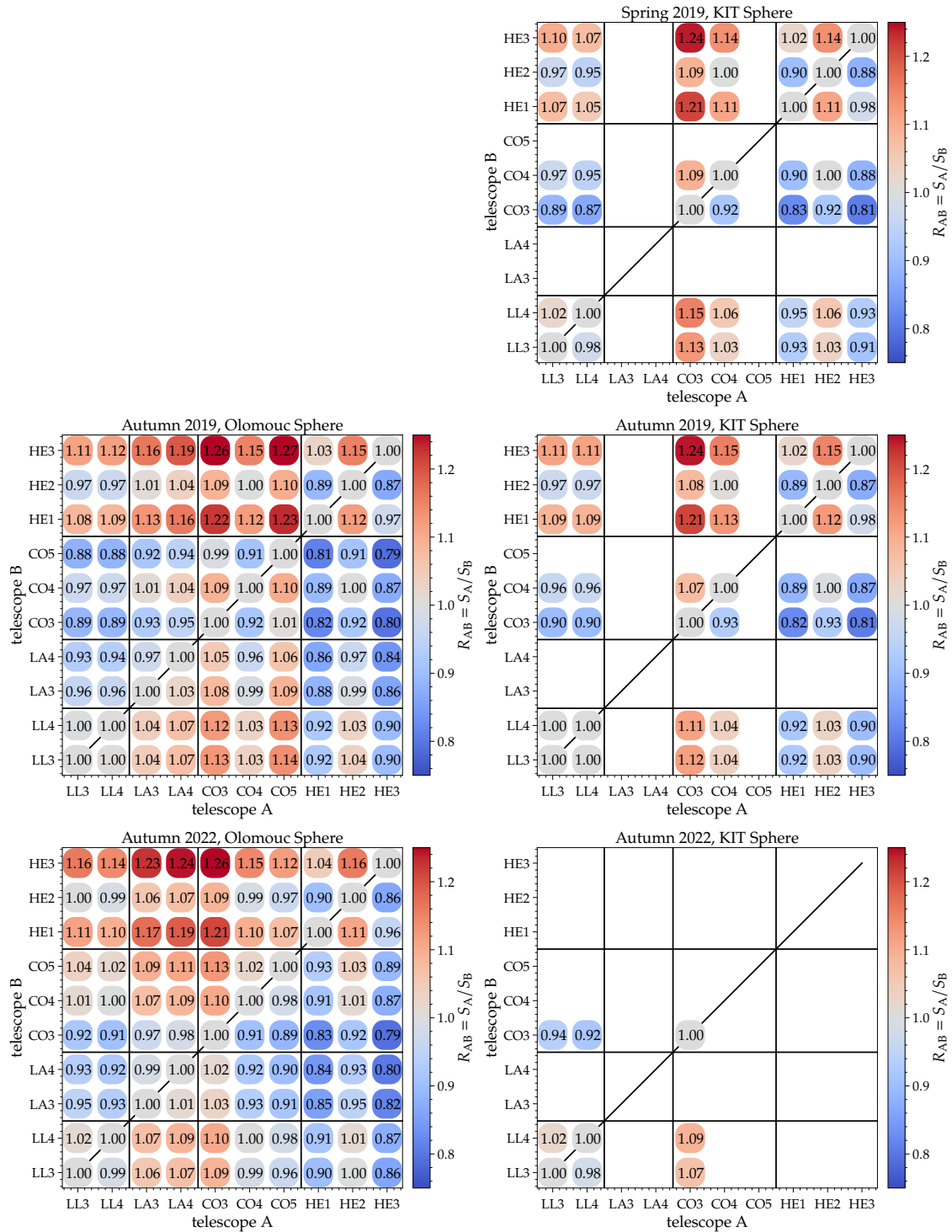
Figure 7.15: Cross-calibration factors R_{AB} between different telescopes A and B. Values are obtained from the XY-Scanner measurements. Rows show different campaigns, columns show different light sources (Olomouc sphere left, KIT sphere right).

and over all camera pixels as

$$S_{\text{tel}} = \sum_{\text{pixel}} \left(C_{\text{pixel}}^{\text{std}} \sum_{P_{xy}} S_{\text{pixel}}^{\text{ADC}}(P_{xy}) \right) \tag{7.10}$$

with the pixel signal $S_{\text{pixel}}^{\text{ADC}}(P_{xy})$ at the positions P_{xy} and the standard calibration constant $C_{\text{pixel}}^{\text{std}}$ of the pixel during the night of the XY-Scanner measurement.

Assuming an identical light emission of each individual calibration source for all XY-Scanner measurements, we can directly compare the different FD telescopes and estimate their cross-calibration factors. We define the cross-calibration factor as a ratio between the total camera signal for the different telescopes A and B as

$$R_{\text{AB}} = \frac{S_{\text{A}}}{S_{\text{B}}}. \tag{7.11}$$

Any systematic uncertainties of the XY-Scanner measurements cancel and we can use the uncertainty of ~2.1% for each $S_{\text{A,B}}$ (see Section 7.1.4) to estimate the uncertainty of R_{AB} as a sum in quadrature of the contributions amounting to ~3%.

For an ideal absolute calibration of the telescopes in the past and an ideal extrapolation of that calibration through time we expect these ratios R_{AB} to be very close to one. Nevertheless we emphasize that the absolute calibration performed with the drum (Section 3.4.1) (as well as the XY-Scanner) does include the optical properties of all components of the telescopes (e.g. filter, corrector lens, mirror, camera), they are end-to-end calibrations of the whole telescope. On the other hand, the relative calibration system (see Section 3.4.2), which extrapolates this absolute calibration in time, accounts only for the changes in the camera and is entirely blind to any changes in all other components.

We show the results of comparing a selection of telescopes in Fig. 7.15. Herein each square represents the total signal ratio R_{AB} as explained above. The numerical value is shown inside of each square, while the color of the square visually illustrates its magnitude. The black horizontal and vertical lines group the telescopes by FD site.

For the standard telescopes we estimate a maximal deviation of ~15% between different telescopes, but in general telescopes within one site show a smaller deviation. Including the HEAT telescopes we measure differences of up to ~25%. An increased accumulation of dust and other debris on the optical components (e.g. mirrors and filters) of HEAT due to its tilted operation may explain this disagreement with the other telescopes.

There are other techniques and methods to determine the cross calibration between the telescopes. For example, air-shower events recorded simultaneously with two different telescopes (FD stereo events) can be analyzed, but these events are rather rare and thus the statistics is very low. Therefore, the cross calibrations are estimated on a level of entire FD buildings rather than for individual telescopes, see e.g. Ref. [110].

Another method is the comparison between the reconstructed shower energy obtained by the SD and the FD. Since the SD is calibrated via FD measurements, such an analysis yields only the deviation of individual telescopes with respect to the average telescope, see e.g. Ref. [111].

During ordinary data-taking nights each telescope monitors the night-sky brightness (NSB). Each telescope captures the NSB every 30 s during measuring nights. Even though the telescopes are equipped with UV filters there is still significant background present from the emission from the night sky. The NSB is mainly composed of airglow and zodiacal light [112]. These continuous NSB measurements are analyzed to also estimate a relative cross calibration between the individual telescopes [112, 113].

The above mentioned methods were only analyzed for the times before the XY-Scanner was installed and the first measurements were performed. Therefore, a direct comparison between the cross calibrations obtained via the different methods with the results of the XY-Scanner measurements is not possible yet. Nevertheless, an analysis, which compares these cross calibrations obtained in the past with the measurements of the XY-Scanner can be found in Ref. [57].
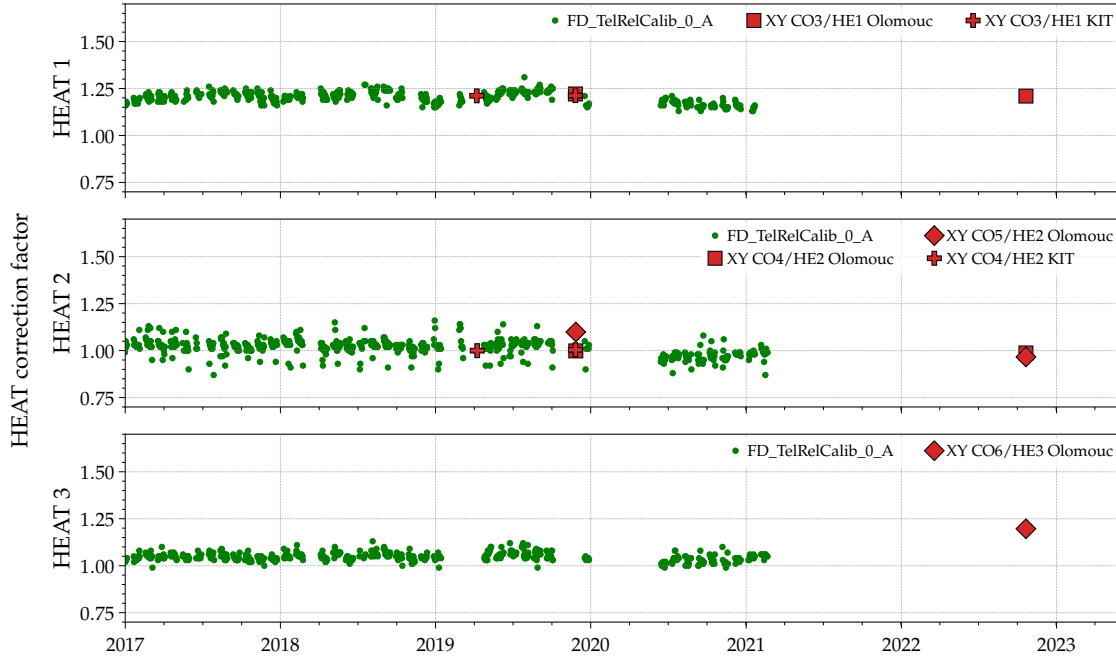
Figure 7.16: HEAT correction factors as stored in the `FD_TelRelCalib_0_A` (v0-AS) database shown in green. In red the cross calibration estimated from the XY-Scanner measurements. Different markers represent different light sources or telescope combinations. Each row displays one of the three telescopes of HEAT.

HEAT and Coihueco.   The standard FD telescopes of the Pierre Auger Observatory cover a field of view of ~2° to ~30° in elevation. Three additional telescopes (HEAT) are installed next to the FD site Coihueco at a distance of 150 m. These telescopes extend the field of view of this FD site to higher elevations, additionally covering elevations from ~30° to ~60°. Since the telescopes of HEAT and Coihueco are able to observe the same air shower during different stages of its development, their cross calibration is of exceptional interest.

The special design of the HEAT telescopes allows for these telescopes to change their field of view between two operation modes. Switching the operational mode of a HEAT telescope changes the pointing direction of the optical axis of the telescope in elevation, the azimuth of the axis is unchanged. For the first mode, as explained above, the telescopes cover a elevation between ~30° and ~60°. Conveniently, we refer to this mode as the *upward* mode. Most of the time the HEAT telescopes are operated in the upward mode. For the second mode, the *downward* mode, the field of view the HEAT telescopes is overlapping with the field of view of the Coihueco telescopes. In the downward mode, the field of views of HEAT and Coihueco are arranged as follows: HE1 overlaps with CO3, the center of HE2 is on the edge between CO4 and CO5, and HE3 coincides with CO6.

The NSB ratio between HEAT and Coihueco is constantly evaluated and stored in a database (`FD_TelRelCalib_0_A`), which can be used for event reconstruction. In Fig. 7.16 we show the correction factors for the three HEAT telescopes from 2017 until they are still available. These correction factors are the NSB ratio between the corresponding pairs of Coihueco and HEAT telescopes [114]. In addition, we plot the cross calibration obtained with XY-Scanner measurements as explained above.

The cross-calibration factors estimated from the XY-Scanner measurements are of the same order as the HEAT correction factors obtained from the NSB observations. Therefore, we give an independent validation of the HEAT correction factors obtained via the NSB analysis for the telescopes HE1 and HE2. Since the XY-Scanner was installed at CO6 only in Autumn 2022 and

the NSB analysis is not yet available for 2022, we cannot yet directly compare the HE3 correction factor of the two techniques.

7.4. Absolute End-to-End Calibration of Telescopes

In the following we derive the procedure of obtaining the absolute end-to-end calibration for a fluorescence telescope of the Pierre Auger Observatory with the XY-Scanner technique. The calibration constant of a telescope pixel is defined as the conversion factor between the measured signal output in adc units of the pixel PMT and the number of photons entering the telescope aperture within the solid angle observed by that pixel. Similarly as already described in Section 3.4, the underlying principle of the absolute end-to-end calibration is to expose the telescope to a precisely known flux of photons and capture the signal response of each pixel in the camera. For this purpose, we define the calibration constant for a given FD camera pixel as

$$C_{\text{abs}}^{\text{pixel}} = \frac{N_\gamma^{\text{pixel}}}{S_{\text{ADC}}^{\text{pixel}}} \tag{7.12}$$

where $S_{\text{ADC}}^{\text{pixel}}$ is the signal output recorded by the pixel (given in adc units) within the duration of a light pulse and N_γ^{pixel} is the total number of photons emitted from the light source within the angular acceptance of that pixel per emitted light pulse. The signal $S_{\text{ADC}}^{\text{pixel}}$ captured by a pixel is estimated as we explained in Section 7.1.1 and defined in Eq. (7.1).

In the following we describe two conceptually different methods of estimating the number of photons N_γ^{pixel} and thus the absolute calibration $C_{\text{abs}}^{\text{pixel}}$.

Individual Light-Source Positions. For the first method, we calculate the total number of injected photons N_γ^{pixel} from all positions of the light source in the scanning grid as follows. The radiance of the source L_{src} is measured as presented in Section 6.7. We estimate the intensity I_{src} of the source to be

$$I_{\text{src}} = \int L_{\text{src}} \, dA = L_{\text{src}} \int dA = L_{\text{src}} A_{\text{src}}, \tag{7.13}$$

with the area of the emitting surface of the light source A_{src}. We obtain the combined intensity I_{XY} for all positions of the source in the XY-Scanner grid by multiplying with the number of positions n,

$$I_{\text{XY}} = n \, I_{\text{src}}. \tag{7.14}$$

The number of injected photons N_γ^{pixel} per pixel is given as

$$N_\gamma^{\text{pixel}} = I_{\text{XY}} \, \Omega_{\text{pixel}} \, \xi_{\text{pixel}} \tag{7.15}$$

$$= n \, I_{\text{src}} \, \Omega_{\text{pixel}} \, \xi_{\text{pixel}}, \tag{7.16}$$

with the solid angle Ω_{pixel} covered by a pixel (introduced in Section 3.2) and the correction for the deviation of the source from a Lambertian emitter ξ_{pixel} (discussed in Section 6.5). The Eq. (7.12) becomes

$$C_{\text{abs}}^{\text{pixel}} = \frac{n \, I_{\text{src}} \, \Omega_{\text{pixel}} \, \xi_{\text{pixel}}}{S_{\text{ADC}}^{\text{pixel}}}. \tag{7.17}$$

This approach rises one issue, namely the actual number of positions contributing to the total signal n is a priori not known. We cannot simply use the total number of positions of the XY-Scanner since positions far outside the aperture do not contribute to the signal captured by the camera, as we pointed out in Section 7.1.3. Including these positions would increase the number
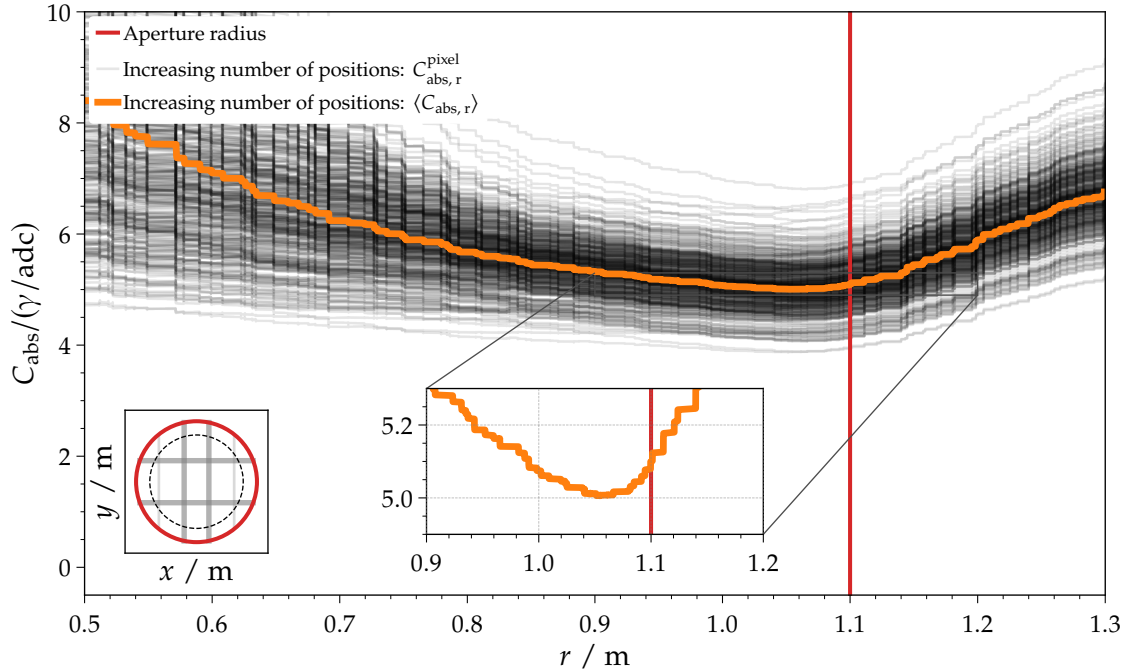
Figure 7.17: Absolute calibration constants obtained from XY-Scanner measurements as function of the radius of included light-source positions. Black lines show calibrations of individual pixels, the orange line their mean, and the red vertical line marks the edge of the aperture opening.

of injected photons N_γ^{pixel} but not change the captured pixel signal $S_{\text{ADC}}^{\text{pixel}}$ and thus the calibration constant is overestimated.

We illustrate this issue in Fig. 7.17. Herein we show the calibration constant C_{abs} derived according to Eq. (7.17) as a function of the radius r of included light-source positions. The number of included positions n is proportional to the square of the radius, $n \propto r^2$. Fig. 7.17 shows the constants for individual pixels as well as the mean for the entire camera. With increasing radius r we observe a decreasing calibration constant C_{abs} up to a minimum close the aperture radius $r_{\text{aperture}} = 1.1\,\text{m}$ (red vertical line in Fig. 7.17). For larger radii the calibration constant increases due to the fact that photons emitted at these positions are blocked by the telescope diaphragm and thus do not reach the camera, leading to an overestimation of the calibration as mentioned above. On the other hand, for positions close to the optical axis of the telescopes (small r) photons are absorbed by the back plane of the camera, thus causing an overestimated calibration for similar reason as above. Therefore, the absolute calibration according to Eq. (7.17) depends on the number and positions of the light source included in the estimation.

In the following we present a different approach for the estimation of N_γ^{pixel}, which is independent of the number of included light-source positions.
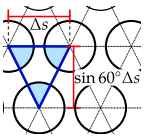
Figure 7.18: Illustration of the coverage factor f_{cov}.

Entirety of Light-Source Positions. While for the drum calibration (Section 3.4.1) the entire aperture of the telescope is illuminated, with the XY-Scanner technique we illuminate only a certain fraction of the aperture. Since we are avoiding to generate scanning positions where the exit windows of the light sources would overlap, we calculate the fractional area, which is actually illuminated by the light source as

$$f_{\text{cov}} = \frac{A_{\text{src}}}{\Delta s^2 \, \sin 60°}, \tag{7.18}$$

where A_{src} is the area of the emitting surface of the light source and Δs is the step size of the triangular scanning grid. This coverage factor f_{cov} depends on the geometry of the scanning grid, nevertheless within this thesis we discuss calibration measurements performed only with a triangular grid and therefore we do not discuss any coverage factors for other grid configurations. Fig. 7.18 illustrates the determination of the coverage factor. In Fig. 7.18 each circle represents the positions of the emitting surface of the light source. The blue equilateral triangle has a side length of the scanner step-size Δs and contains three 60°-wedges of the source area. We define the ratio of area of the light source and the blue triangle as the coverage factor f_{cov}. Depending on the employed light source and the step size Δs of the scanning grid, we estimate the coverage factors f_{cov} for different setups to be

	step size Δs	f_{cov}
integrating spheres	6 cm	0.650
	10 cm	0.234
	16 cm	0.091
tube source	12 cm	0.596
	20 cm	0.215

We validate this estimation of the coverage factor by simulations as presented in Section 4.4.4. The uncertainty of f_{cov} is derived from the uncertainties of the light-source emitting area A_{src} and the step size Δs of the XY-Scanner measurement. We measure the emitting area A_{src} to a 0.8% precision level and estimate the relative accuracy of the XY-Scanner to be 0.7%. We use the propagation of uncertainties and assign an uncertainty of 1.3% to the coverage factor f_{cov}. We assume the same uncertainty for all measurements employing different light sources or scanner step sizes.

The combined intensity I_{XY} for all XY-Scanner positions of the light source is estimated as

$$I_{\text{XY}} = L_{\text{src}} \, f_{\text{cov}} \, A_{\text{aperture}} \tag{7.19}$$

for a FD telescope with a aperture area A_{aperture} and a light source with radiance L_{src}. The nominal aperture area of the FD telescopes of the Pierre-Auger Observatory is defined to be $A_{\text{aperture}} = \pi \, (1.1 \, \text{m})^2$. Next, the total number of photons N_γ^{pixel} emitted by the light source into the angular acceptance Ω_{pixel} of the pixel is then calculated as

$$N_\gamma^{\text{pixel}} = I_{\text{XY}} \, \Omega_{\text{pixel}} \, \xi_{\text{pixel}} \, c_{\text{pixel}}^{\text{halo}} \tag{7.20}$$

$$= L_{\text{src}} \, \Omega_{\text{pixel}} \, \xi_{\text{pixel}} \, c_{\text{pixel}}^{\text{halo}} \, f_{\text{cov}} \, A_{\text{aperture}} \tag{7.21}$$

where ξ_{pixel} is the correction for the deviation of the source from an ideal Lambertian emitter as discussed in Section 6.5. We also directly include the correction factors $c_{\text{pixel}}^{\text{halo}}$ for the reflections on the camera surface, as discussed in Section 4.4.5. This is not the case of the absolute calibration obtained with the drum measurements, but rather the camera reflection is accounted for in the tracking method. It makes no difference at which point we include this correction, but we have to be careful to not count it twice.

In the following, we combine Eqs. (7.12) and (7.21) and define the absolute calibration constant as

$$C_{\text{abs}}^{\text{pixel}} = \frac{N_\gamma^{\text{pixel}}}{S_{\text{ADC}}^{\text{pixel}}} \tag{7.22}$$

$$= \frac{L_{\text{src}} \, \Omega_{\text{pixel}} \, \xi_{\text{pixel}} \, c_{\text{pixel}}^{\text{halo}} \, f_{\text{cov}} \, A_{\text{aperture}}}{S_{\text{ADC}}^{\text{pixel}}} \tag{7.23}$$

for any pixel of an FD telescope as a function of the source radiance L_{src}, the pixel solid angle Ω_{pixel}, the source emission correction ξ_{pixel}, the correction factor for camera reflections c_{pixel}^{halo}, the coverage factor f_{cov}, the aperture area of the telescope $A_{aperture}$, and the signal captured by each pixel S_{ADC}^{pixel}.

7.4.1. DISCUSSION OF UNCERTAINTIES

The uncertainty of the current absolute calibration of the FD telescopes with the drum method is 9%, [115, 116]. Even though there were efforts made by the drum team to reduce this calibration uncertainty to a 5% level [42, 43], the Auger Collaboration did not implement this improvement to avoid including further uncertainties related to the stability of the FD/SD energy ratio [117].

Since the area of the aperture $A_{aperture}$ and the pixel solid angle Ω_{pixel} are defined to be a fixed value for all telescopes and pixels respectively (see discussion in Section 3.2), we will, for the subsequent discussion on uncertainties, treat the absolute calibration as a photon density rather than a photon number. Therefore, the absolute calibration becomes

$$D_{abs}^{pixel} = \frac{C_{abs}^{pixel}}{A_{aperture}\,\Omega_{pixel}} = \frac{L_{src}\,f_{cov}\,\xi_{pixel}\,c_{pixel}^{halo}}{S_{ADC}^{pixel}}. \tag{7.24}$$

We list the relative uncertainties of the individual contributions as

contribution	uncertainty
Radiance of the light sources L_{src}	4.9%
Coverage factor f_{cov}	1.3%
Light-source directional emission ξ_{pixel}	1%
Back-reflection on telescope camera c_{pixel}^{halo}	0.5%
Signal in the pixel-PMTs S_{ADC}^{pixel}	0.2%
Statistical uncertainty (bootstrap)	2.1%
Unaccounted uncertainty budget	2%
Total	**5.9%**

and calculate the total uncertainty on the absolute calibration of each individual pixel of a FD telescope as a sum in quadrature of the individual contributions as ~5.9% for an XY-Scanner measurement with a step size of $\Delta s = 6$ cm and an integrating sphere as light source. Increasing the step size to $\Delta s = 10$ cm (16 cm), but keeping the same light source, results in a larger total uncertainty of ~6.5% (~7.7%) due to the increased statistical uncertainty, see Section 7.1.4. For the tube source we generally measure with a larger step size of 12 cm or 20 cm and thus obtain uncertainties on the ~6.8% or ~8.6% level, respectively.

We once again emphasize that the dominant contribution to this overall uncertainty is the uncertainty on the measurement of the source calibration. The improvements, introduced in Section 6.7.5, will probably reduce this uncertainty on the source radiance measurement to a ~2% level. We thus reach a total uncertainty on the order of ~3.9% for the absolute calibration of the telescopes with an integrating sphere as a light source and a step size of $\Delta s = 6$ cm.

The second-largest contribution originates in the statistical uncertainty of the XY-Scanner measurement method. Possibilities to reduce this statistical uncertainty are either to increase the number of positions of the light source on the XY-Scanner or to increase the number of light flashes emitted at each position. On the other hand, both actions would drastically increase the time needed to perform an XY-Scanner measurement, since the limiting time factor is the readout of the telescope camera.

Concluding, with the above described technique, we reach an uncertainty of ~6% on the absolute end-to-end calibration with the XY-Scanner, which is smaller than the currently used

uncertainty of 9% of the drum calibration. However, improvements of the source calibration may enable us to reach an uncertainty of the absolute end-to-end calibration below ~4%.

7.4.2. RESULTS OF RECENT XY-SCANNER CAMPAIGNS

In the right plots of Fig. 7.19 we present the absolute calibration constants $C_{\mathrm{abs}}^{\mathrm{XY}}$ of each pixel of a telescope camera obtained from a typical XY-Scanner measurement. In the very same plot we draw the standard calibration $C_{\mathrm{abs}}^{\mathrm{CalA}}$ of the same night as evaluated with the Cal A tracking. We emphasize that these two calibrations are independent, $C_{\mathrm{abs}}^{\mathrm{CalA}}$ is obtained with the last drum measurement and the relative calibrations, while for $C_{\mathrm{abs}}^{\mathrm{XY}}$ we use only the XY-Scanner measurement and the measured source radiance and emission profile as input. We observe a similar behavior for both calibration constants as a function of pixel number and determine an almost constant mean offset $\langle C_{\mathrm{abs}}^{\mathrm{XY}} - C_{\mathrm{abs}}^{\mathrm{CalA}} \rangle$ for all individual pixels with sizes between 0.7 to 1.1 γ/adc, depending on the telescope. The left plot of Fig. 7.19 illustrates the ratio between the XY-Scanner and the standard calibration as pixel matrices. We observe a homogeneous ratio of the calibration across the entire camera, except for the measurement at HEAT where a faint vertical gradient is visible. This gradient may indicate an increased accumulation of dust on the bottom part of the HEAT mirrors, due to the tilted operation.

As discussed in Section 3.4.2, the tracking of the absolute calibration with the Cal A system is not sensitive to changes in any components of the telescope except for the pixel PMTs of the camera. Therefore, any loss of efficiency in either the filter, the corrector lens, or the mirror since the last absolute calibration is not taken into account when estimating the calibration constants $C_{\mathrm{abs}}^{\mathrm{CalA}}$. Note that the last absolute end-to-end calibration, which is actually tracked, was performed in the year 2010 with the drum. Nevertheless, the Cal A tracking system very reliably monitors the gain of each telescope pixel, as concluded in e.g. Ref. [44] for the 2013 drum calibration campaign. Assuming the evolution of the telescope response is dominated by the evolution of the pixel gains, it is valid to neglect the contributions of the other telescope components and rely only on the relative calibration Cal A. On the other hand, the XY-Scanner calibration is an end-to-end calibration of the entire telescope and therefore accounts for all components of the telescope.

We conclude that the almost-constant difference of the calibration of individual pixels observed between the Cal A-tracked drum calibration and the XY-Scanner end-to-end calibration can be explained by an additional efficiency loss of some telescope components to which the Cal A tracking is not sensitive to. Therefore, both calibrations show a similar behavior as function of pixel number, since they are dominated by the gain of the individual pixels, which is taken into account in both calibrations. However, the XY-Scanner measurements reveal a constantly higher calibration due to the sensitivity of the technique to all components of the telescope.

Telescope Average. In Fig. 7.20 we show the ratio of the average calibration constant per telescope between the XY-Scanner calibration and the drum calibration tracked with Cal A during the night of the XY-Scanner measurement. A similar plot presenting the individual pixel calibrations of all telescopes is shown in Fig. A.17 of the appendix. For the analysis of both campaigns we use the identical source radiance estimates as presented in Section 6.7.5. The brackets in Fig. 7.20 represent the total uncertainty on the XY-Scanner calibration as discussed above in Section 7.4.1. The gray band in Fig. 7.20 illustrates the 9.9% uncertainty on the current FD calibration, which includes 9% on the absolute calibration with the drum, 2% on the relative nightly calibration, and 3.5% on the optical efficiency [116].

For each individual telescope we observe compatible calibrations of XY-Scanner measurements regardless of the employed light source. The maximal difference we observe for a calibration (telescope average) using different light sources is on the order of ~3% and thus within the uncertainty of the XY-Scanner calibration technique.

However, the calibration constants obtained with the XY-Scanner measurements are consistently larger than the Cal A-tracked calibration. For the measurements performed in November 2019, we observe an average offset on the order of ~22% for the XY-Scanner calibration w.r.t. the
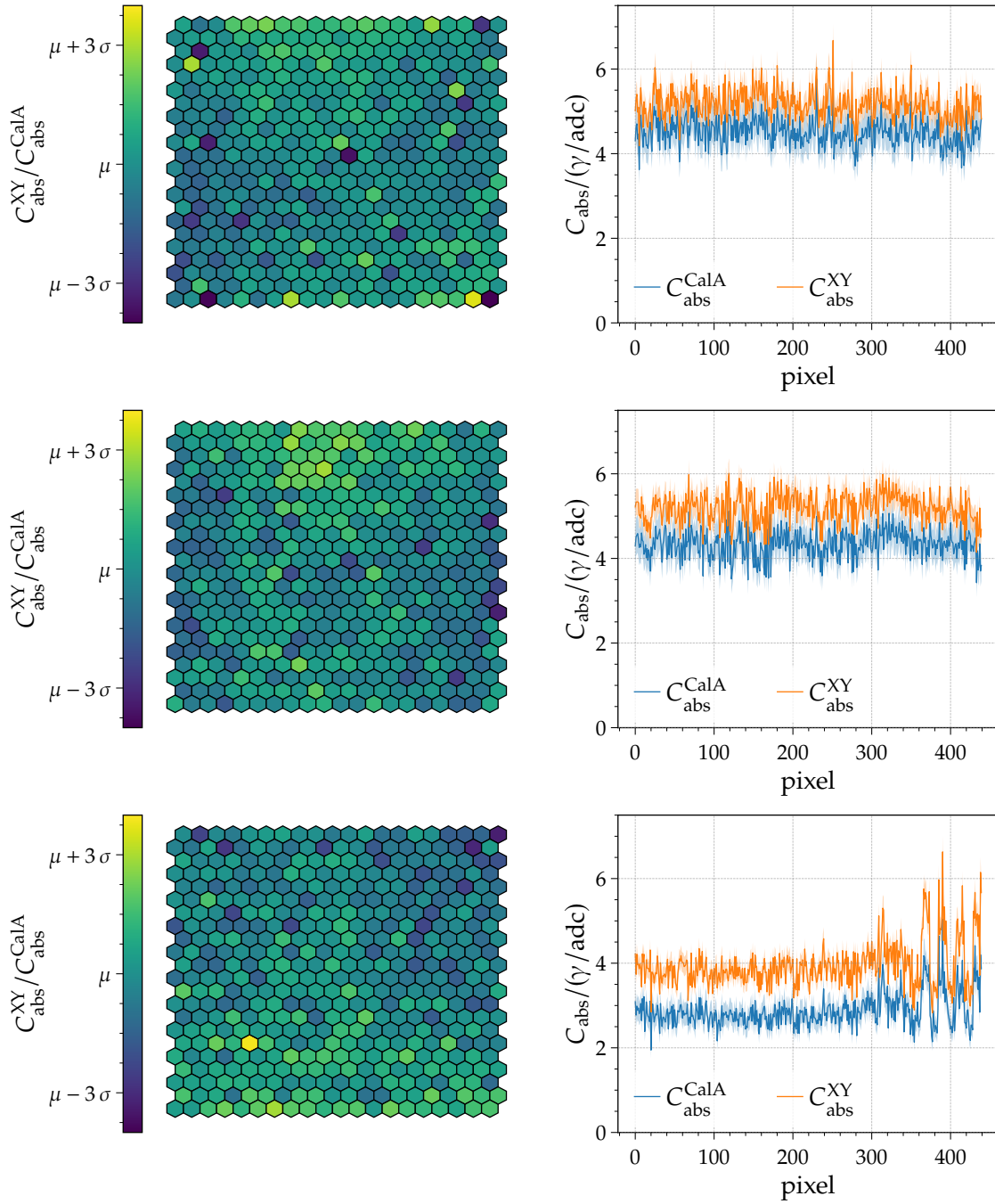
Figure 7.19: Calibration constants for a selection of telescope. *Left:* Ratio of the XY-Scanner calibration and the standard calibration with Cal A tracking shown as a pixel matrix. *Right:* Absolute calibration constants C_{abs}^{XY} obtained from XY-Scanner measurements (orange) and calibration constants C_{abs}^{CalA} obtained with the Cal A tracking (blue). The shaded areas surrounding each line represent the total uncertainty of each calibration. *Top:* LA4 with the Olomouc sphere in November 2019. *Center:* CO4 with the KIT sphere in November 2019. *Bottom:* HE3 with the Olomouc sphere in November 2019.
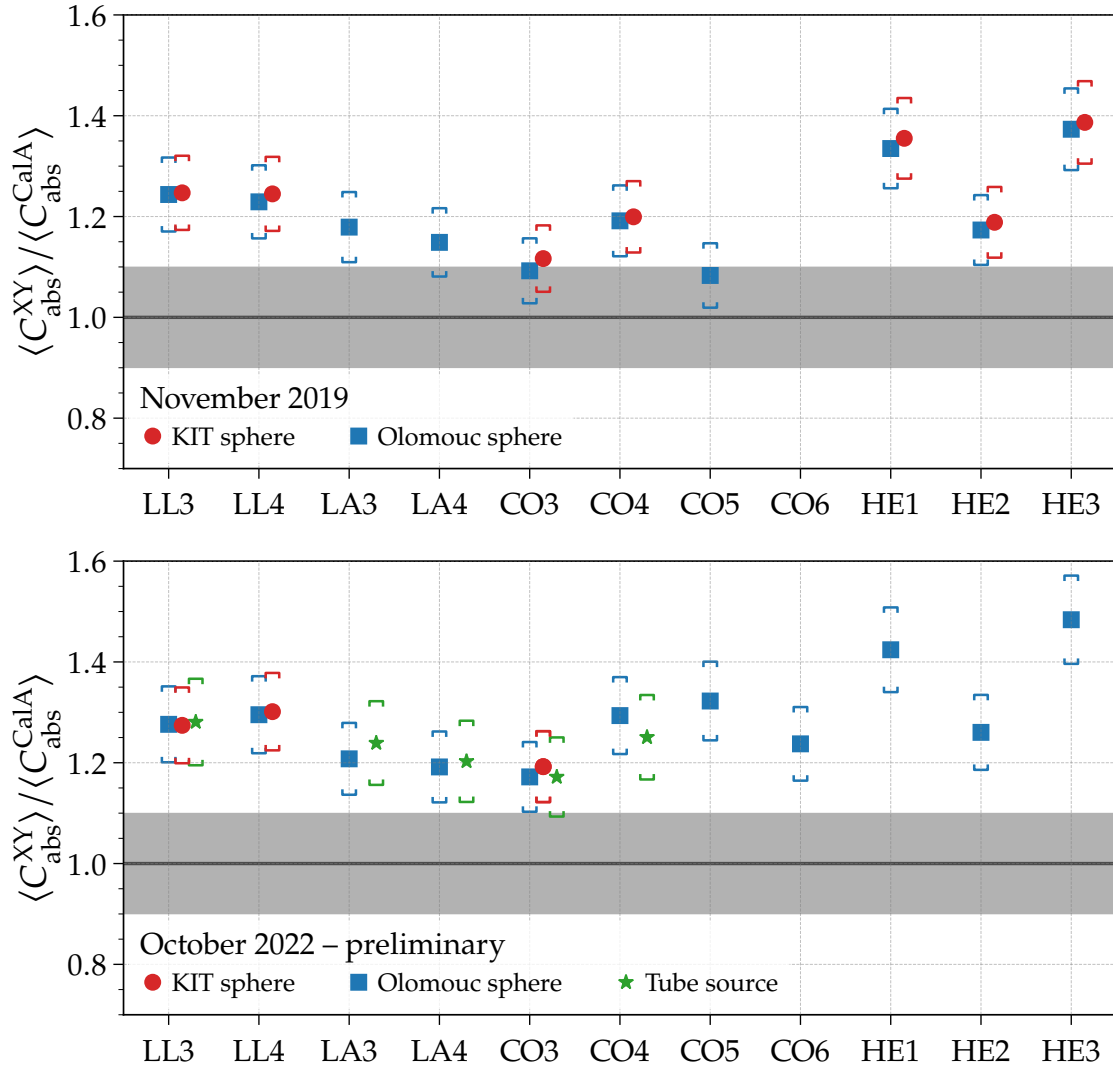
Figure 7.20: Ratio between the average absolute pixel calibration of FD telescopes obtained from the XY-Scanner measurements $\langle C_{abs}^{XY} \rangle$ and the average calibration $\langle C_{abs}^{CalA} \rangle$ obtained with the Cal A tracking of the relative calibration system. Different markers depict different light sources and the brackets indicate the total uncertainty on the XY-Scanner calibration. The gray band illustrates the current total uncertainty on the FD calibration. *Top:* Calibration measurements performed in November 2019. *Bottom:* Data from October 2022. Here a custom implementation of the Cal A tracking is used, since the official calibration is not yet available.
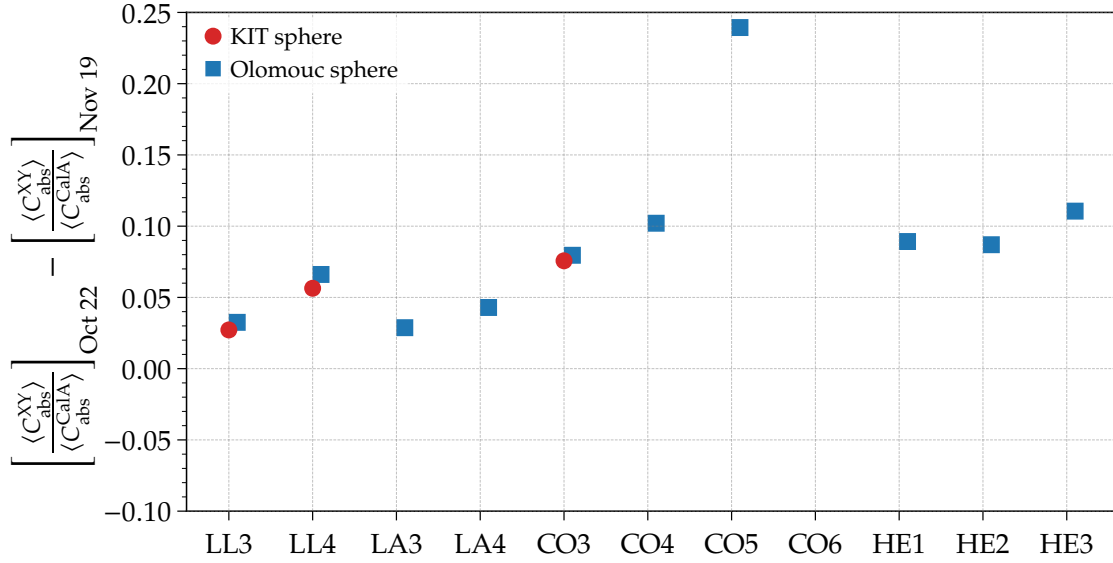
Figure 7.21: Difference between the ratio of the XY-Scanner calibrations and Cal A-tracked calibrations for measurements performed in October 2022 and November 2019.

Cal A tracking. The maximal and minimal differences are observed for the HE3 telescope with ~38% and CO5 telescope with ~8%, respectively. The XY-Scanner calibration of the CO5 telescope lies within the uncertainty of the current FD telescope calibration. Similarly, for the campaign of October 2022 we observe an average difference of ~26% comparing the two calibrations. Again, the maximal difference is estimated for the HE3 telescope with ~48% while having the minimal difference in CO3 of about ~18%. However, the results of the October 2022 campaign are still preliminary since the official calibration constants are not yet available. We present here the results we obtain by our custom implementation of the calibration tracking with Cal A measurements. In Fig. A.16 of the appendix we show a comparison between the calibration obtained from our implementation and the preliminary official Cal A tracking. We discussed a possible reason for the observed differences between the XY-Scanner calibration and the Cal A tracking above. The different evolution of the individual telescopes manifests as a non-constant difference between the two calibrations across all telescopes.

In the following, we estimate the aging of each individual telescope by comparing the difference between the XY-Scanner calibration (relative to the Cal A-tracked calibration) for measurements performed in October 2022 and November 2019. We plot this difference for measurements employing the KIT and Olomouc spheres in Fig. 7.21. A brief study of the elevation dependency of the aging is given in Appendix A.8. We observe a larger calibration ratio in October 2022 than in November 2019 and estimate the effect to be on average of the order of 8% for the investigated telescopes. However, the CO5 telescope shows a particularly large difference of more than 20%. If we treat the measurement at CO5 as an outlier and thus exclude this measurement, we estimate the average difference to be 6.6% within three years. This corresponds to a drift of ~2% per year. Additionally, excluding the three telescopes of HEAT, because of their different design and operational mode, does not change this result significantly.

If we very roughly assume a degradation of each telescope efficiency on average by ~2% per year to which the Cal A system is not sensitive, we estimate a total shift of ~18% between the time of the 2010 drum measurements and the 2019 XY-Scanner campaign. Equivalently, for the latest XY-Scanner campaign in 2022 we obtain a shift of ~24%. We include this average drift of 2% per year for the Cal A calibration C_{abs}^{CalA} and present in Fig. 7.22 again the ratio of the average telescope calibration between the XY-Scanner calibration and the Cal A tracking. If we increase the Cal A calibration by the 2% per year, we observe an agreement between the telescope average
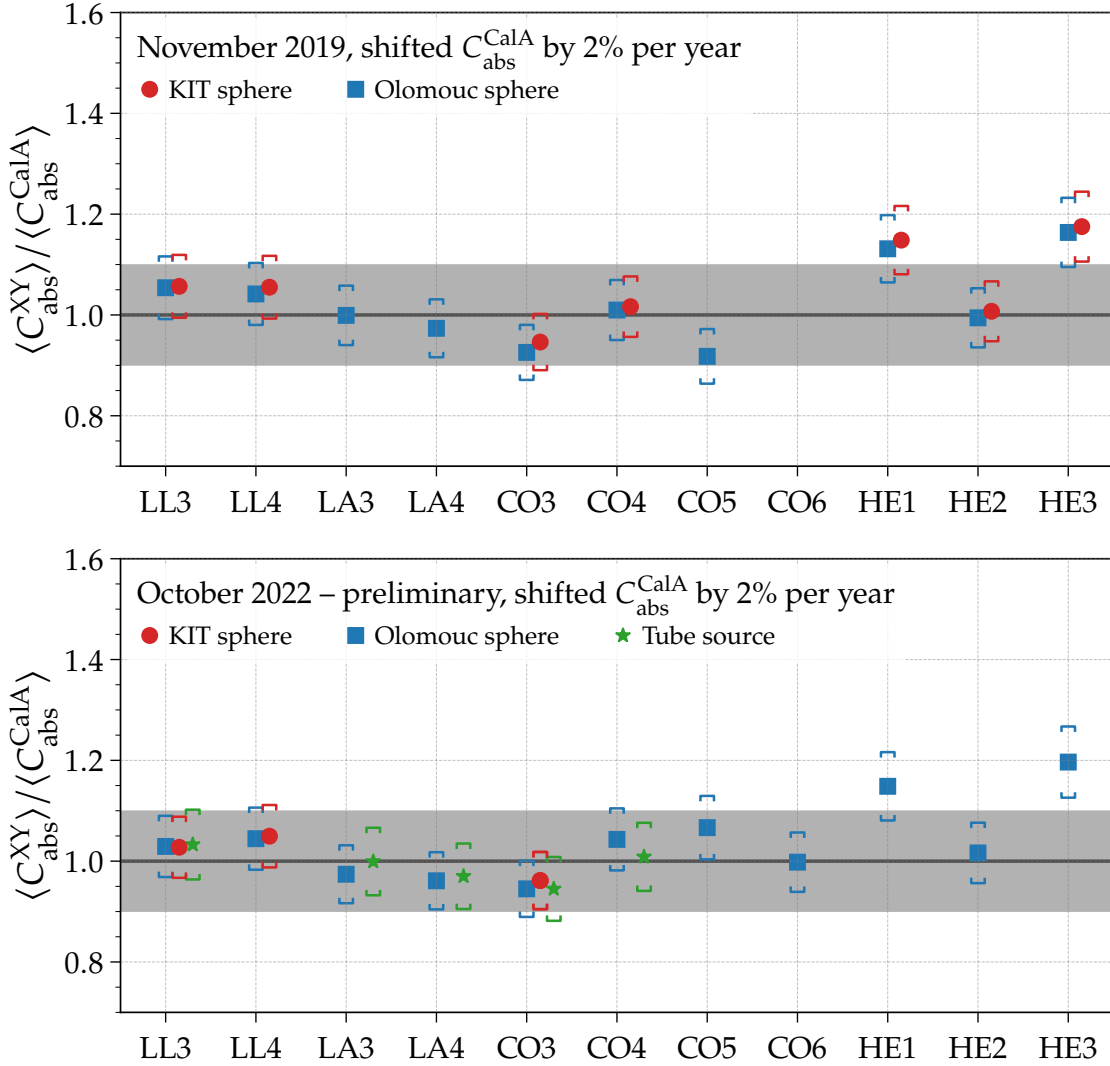
Figure 7.22: Similar plots as in Fig. 7.20, but the standard calibration C_{abs}^{CalA} is here scaled with a 2% per year drift.

of the XY-Scanner calibration and the Cal A-tracked constants within the uncertainty of the FD standard calibration for all FD telescopes, except HE1 and HE3. This again might be explained by the tilted orientation of the HEAT telescope mirrors and thus increased accumulation of dust.

In conclusion, we presented the results of the last two XY-Scanner calibration campaigns, which took place in November 2019 and October 2022. We compare the XY-Scanner calibration with the current standard (drum) calibration of the telescopes and observe a significant difference, on average on the order of ~22% for the November 2019 campaign. However, we performed the calibration of the light source employed by the XY-Scanner in early 2023 and assume that the calibration of the source was identical in the year 2019. For future campaigns it is highly advisable to perform the light-source calibration in the laboratory shortly before and after the XY-Scanner calibration campaign on the observatory site. The average difference between the calibrations is larger for the October 2022 campaign, but for this campaign the standard calibration is not yet available and we have to rely on a custom implementation of the Cal A tracking. However, our implementation of the Cal A tracking is in good agreement with the preliminary official Cal A tracking, as shown in Fig. A.16 of the appendix.

Nevertheless, if we consider a 2% per year loss of the telescope efficiency to which the standard calibration is not sensitive, we observe an agreement between the telescope-averaged XY-Scanner calibration and the standard calibration for most of the telescopes.

SUMMARY

In this work we presented a novel tool for the absolute end-to-end calibration of fluorescence telescopes – the XY-Scanner. This tool employs a portable calibrated light source mounted on a motorized rail system, which is moved across the aperture of each telescope. In the past the whole aperture was illuminated at once by a large-diameter light source. Due to the high amount of work and person-power required for this procedure, it was only carried out roughly once every three years. A relative calibration of the telescope is performed every night to track short-term changes. However, the relative calibration is only sensitive to changes of the telescope camera and is blind to any other component of the telescope. Since 2013, only the relative calibration has been performed.

For the calibration measurements with the XY-Scanner we drove the light source over ~1700 positions in front of the telescope aperture. At each position we captured and readout the entire telescope camera. The accurate knowledge of the light source emission pattern and the readout of the camera then provides the absolute end-to-end calibration of each pixel-PMT of the camera. We verified our understanding of the performed measurements with ray-tracing simulations of the light sources of the XY-Scanner and the telescope. These simulation studies revealed a sensitivity of the XY-Scanner measurements to the filter support structure of the telescope. In simulations, we showed that the scanning grid of the XY-Scanner can be optimized to reduce the aforementioned sensitivity.

The versatile setup of the XY-Scanner is able to employ a variety of different light sources. We introduced and discussed the standard calibration light sources made of integrating spheres as well as the modifications, which were applied to improve their emission characteristics. We briefly demonstrate the possibilities of measurements using a collimated beam source. In addition, we developed, constructed, and tested a viable alternative calibration light source – the tube source. The tube source consists predominantly of 3D-printed parts but has the same form factor as the integrating sphere sources, which allows us the uncomplicated installation of all calibration light sources into the same setup. However, the main advantage of the tube source is its ~3.5 times larger emitting surface in comparison to the integrating spheres. This reduces the time needed to perform a calibration measurement with the XY-Scanner at the telescopes by roughly the same factor.

In future campaigns, the calibration light sources could also be equipped with a LED emitting at different wavelengths and therefore the XY-Scanner measurements can be used to obtain the relative telescope response at various wavelengths.

We measured the directional emission profiles of the calibration light sources in a specially designed setup. This setup employs two motorized rotational stages allowing the independent rotation of the sources around two axes. We use a PMT to observe the emission under a variety of directions and use these measurements to estimate the emission into the direction observed by individual telescope pixels.

In addition, we built a dedicated calibration setup combining a NIST-calibrated photodiode and a pair of PMTs. In this setup, we use the photodiode to measure the average photon emission during a light pulse and the PMTs to estimate the pulse-to-pulse stability. With this setup we were able to calibrate the light sources of the XY-Scanner to a ~5% accuracy level. The uncertainty on the source calibration is dominated by the uncertainty of the employed electrometer. A novel calibration of this device will further improve the accuracy of the light source calibration.

Distributed over several instrumentation campaigns we installed XY-Scanner systems on all 27 fluorescence telescopes of the Pierre Auger Observatory. We performed an absolute calibration of 11 telescopes. We plan to calibrate all telescopes within the foreseeable future. We presented the method of estimating the absolute calibration constants from the XY-Scanner measurements and derived the uncertainty on this novel calibration to be on the order of ~6%. The obtained calibration results for the fluorescence telescopes are consistent between all employed calibration light sources. The largest contribution to the total uncertainty of the telescope calibration is the calibration of the employed light sources. With an improved light-source calibration setup, an uncertainty below 4% becomes reachable. Despite that the current calibration uncertainty of the XY-Scanner technique is well below the uncertainty level of 9% of the current standard calibration with the large-diameter light source. Therefore, the here presented XY-Scanner calibration is increasing the accuracy of the estimation of the cosmic-ray energies for all events gathered by the Pierre Auger Observatory.

Comparing the novel absolute end-to-end calibration with XY-Scanner and the standard calibration obtained via the relative calibrations, we on average observe a significant difference on the order of ~25%. However, including a 2% efficiency loss per year of operation of the fluorescence telescopes, which is not accounted for in the relative calibration, brings the XY-Scanner calibration and the standard calibration into agreement within the uncertainties of both methods.

Concluding, we showed that the XY-Scanner is a viable method to calibrate the fluorescence telescope of the Pierre Auger Observatory. With the current XY-Scanner setup we were able to estimate the absolute end-to-end calibration of each telescope pixel with an uncertainty of ~6%. This uncertainty is smaller than the 9% uncertainty of the currently used absolute calibration. We attribute the difference between the XY-Scanner calibration and the standard calibration to the insensitivity of the relative calibration system to any changes on the telescope except the pixel-PMTs.

APPENDIX

Contents

A.1.   Additional Drawings and Figures concerning Fluorescence Telescopes

Figure A.1: Technical drawing of an FD telescope. Taken from Ref. [118].

Figure A.2: Schematic drawing of the readout system for an FD site. Taken from Ref. [10].

A.2. Missing Protection on Y-Axes
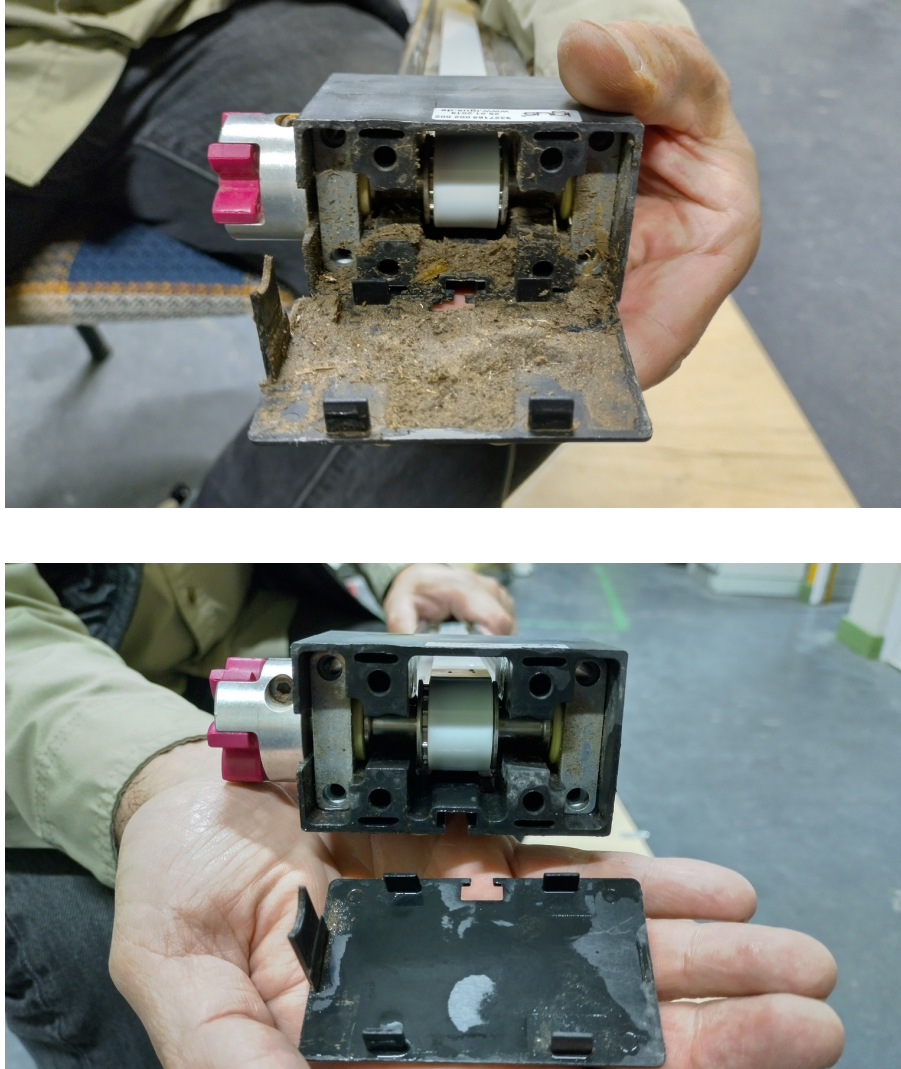
Figure A.3: Photographs of one of the y-axes for the HE 1 telescope. *Top:* Accumulated dirt after leaving the y-axes installed without the protective cover for ~2.5 years. *Bottom:* After cleaning.

A.3. Additional Measurements in Optics Laboratory

A.3.1. PMT Linearity Studies
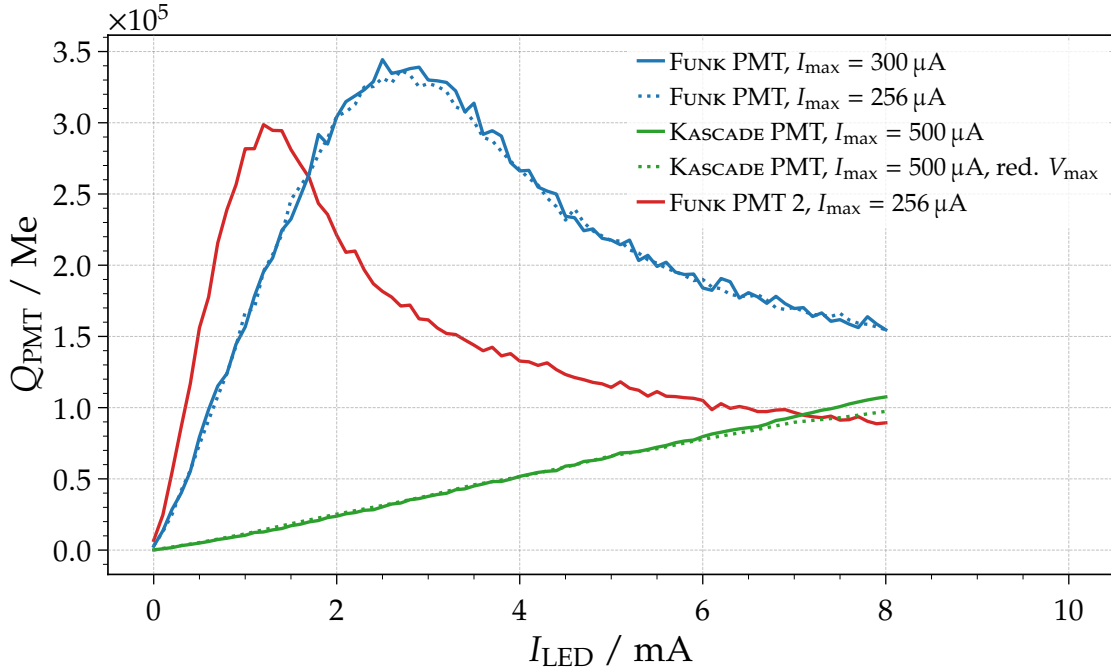
Figure A.4: Comparison of the collected charge Q_{PMT} of the different PMTs for an increasing LED current I_{LED}.

For the selection on the optimal PMT for the laboratory setup introduced in Section 6.5, the linearity of various PMTs was studied. The intensity per light flash of the light source at a fixed distance was gradually increased and the captured signal in the PMT analyzed. Three different PMTs were studied, two of the same type ET Enterprises 9107QB (Funk PMTs) and one EMI 9902KSB25FL (Kascade PMT) which is similar to an ET Enterprises 9902B. The results are shown in Fig. A.4.

The response of both Funk PMTs is linear up to a LED current of only ~1.0 mA and ~2.5 mA, respectively. As demonstrated by the red and blue curves in Fig. A.4. For the blue-dotted curve the current limit of the high-voltage crate supporting the PMT was increased to investigate a possible influence of this current limit on the linearity range, but no significant influence was observed.

On the other hand, the Kascade PMT delivers a linear response for the entire range of measurements, as illustrated by the green solid line in Fig. A.4. An additional measurement with a reduced voltage range of the digital oscilloscope is shown as a green-dotted line. This measurements ran into saturation of the voltage range at above ~6 mA of LED current.

Most of the measurements in the laboratory and at the FD telescopes were performed with $I_{LED} = 2.7$ mA.

From these measurements we concluded that the Kascade tube is the most suitable PMT for the laboratory setup as explained in Section 6.5.

A.3.2. FLASHING-FREQUENCY OF LIGHT SOURCE
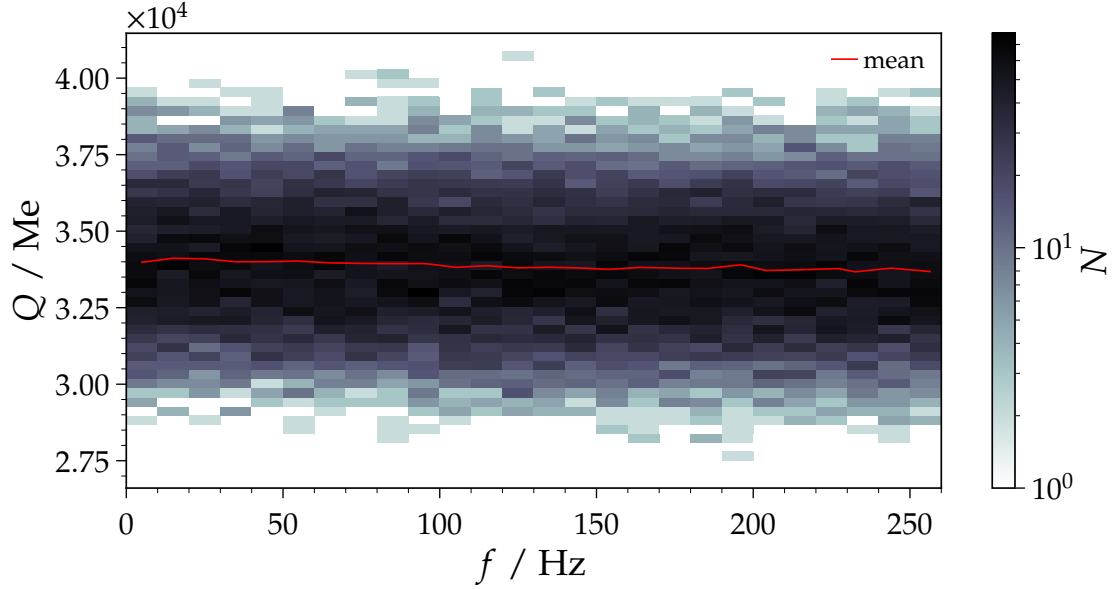
Figure A.5: Distributions of the charge Q collected by a PMT for different flashing frequencies of the KIT sphere. The red line indicates the mean of each distribution. The flashing of the source and readout of the PMT are triggered by an external frequency generator.

Here we study the stability of the light source on the flashing frequency in a dedicated measurement. For this purpose we mounted a PMT at a distance of several meters in front of the light source. We operated the light source with a constant LED current and increased the flashing frequency from ~1 Hz to ~250 Hz. A frequency generator was used to trigger the light flashes and the readout of the PMT. The PMT signal is digitized by the PicoScope. We observe no significant change in the average collected charge per flash for the entire frequency range.

A.3.3. Correlation between PMT and Photo-Diode Signals
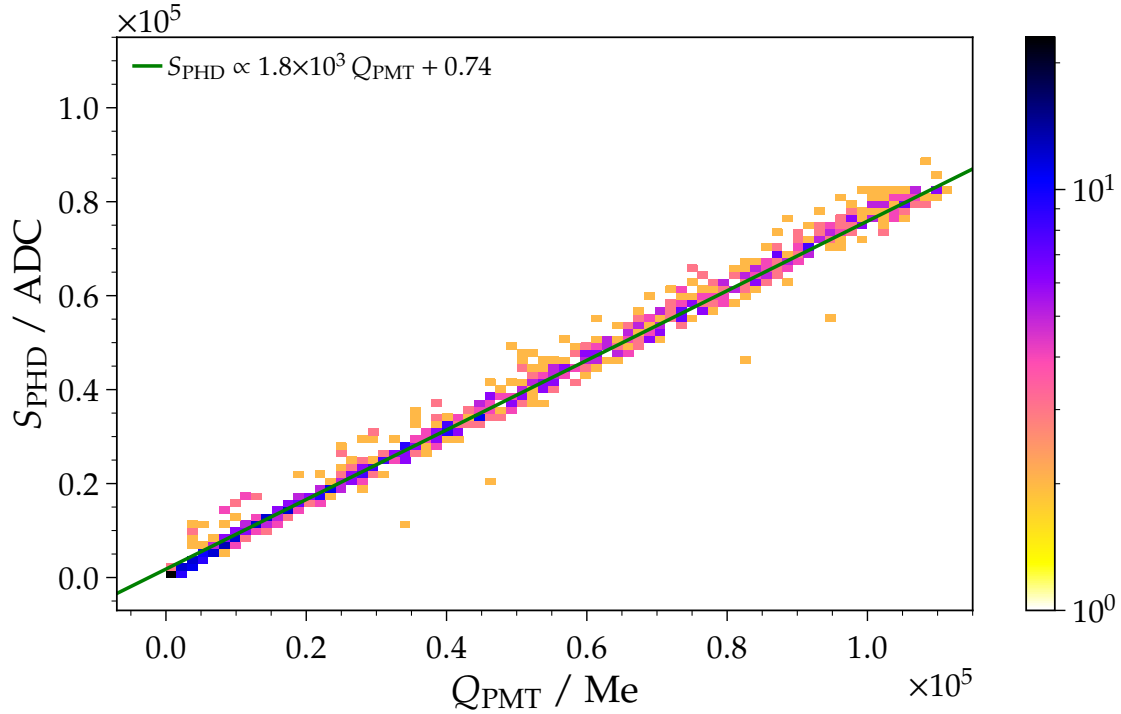
Figure A.6: Distribution of the signals recorded by the photodiode and the PMT for increasing LED currents.

In Fig. A.6 we present a validation study of the internal photodiode installed within the integrating-sphere light sources. Similarly to the study in Appendix A.3.2, we observed the light source with a PMT. We increased the LED current of the light source and captured the signals recorded by this PMT and the internal photodiode. The joint distribution of the captured data is plotted in Fig. A.6 indicating the very linear correlation of the two detectors.

A.4. Light-Source Calibration

A.4.1. Wavelength Calibration of SD2000 Spectrometer
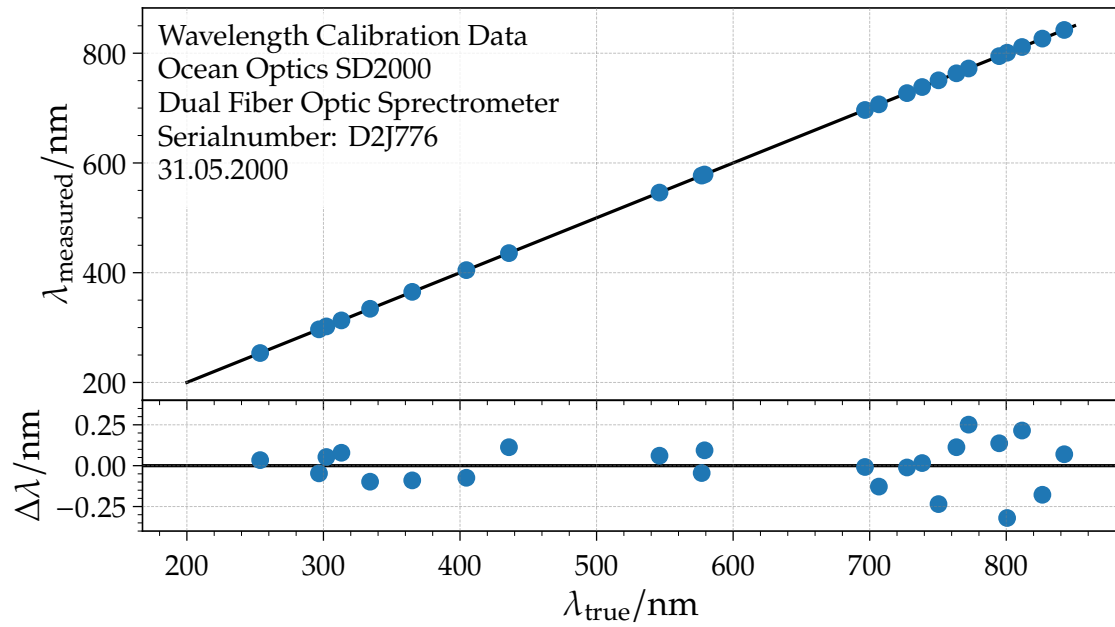
Figure A.7: Wavelength Calibration of the SD2000 Spectrometer. These values were provided by Ocean Optics Inc. [93] from measurements they performed in the year 2000.
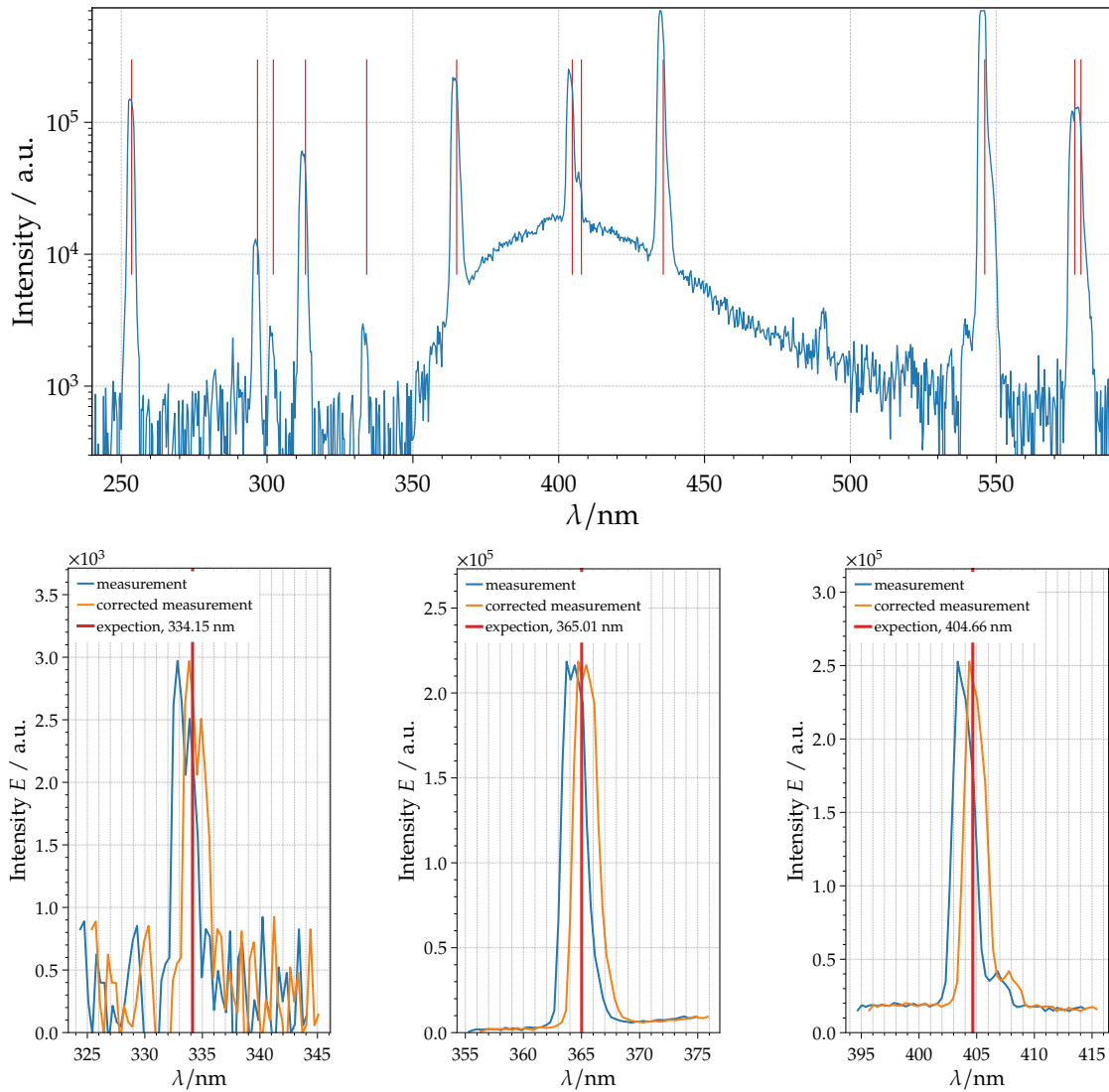
Figure A.8: Spectrum of the mercury-argon light source (CAL2000) measured with the Ocean Optics SD2000 spectrometer. *Top:* Measured spectrum in blue. The expected emission peaks of the mercury-argon light source are plotted as red vertical lines. *Bottom:* Zoomed-in plots of the three emission lines which are closest to the nominal wavelength of the XY-Scanner light-source (365 nm).

A.4.2. Temperature during Source Calibration Measurement
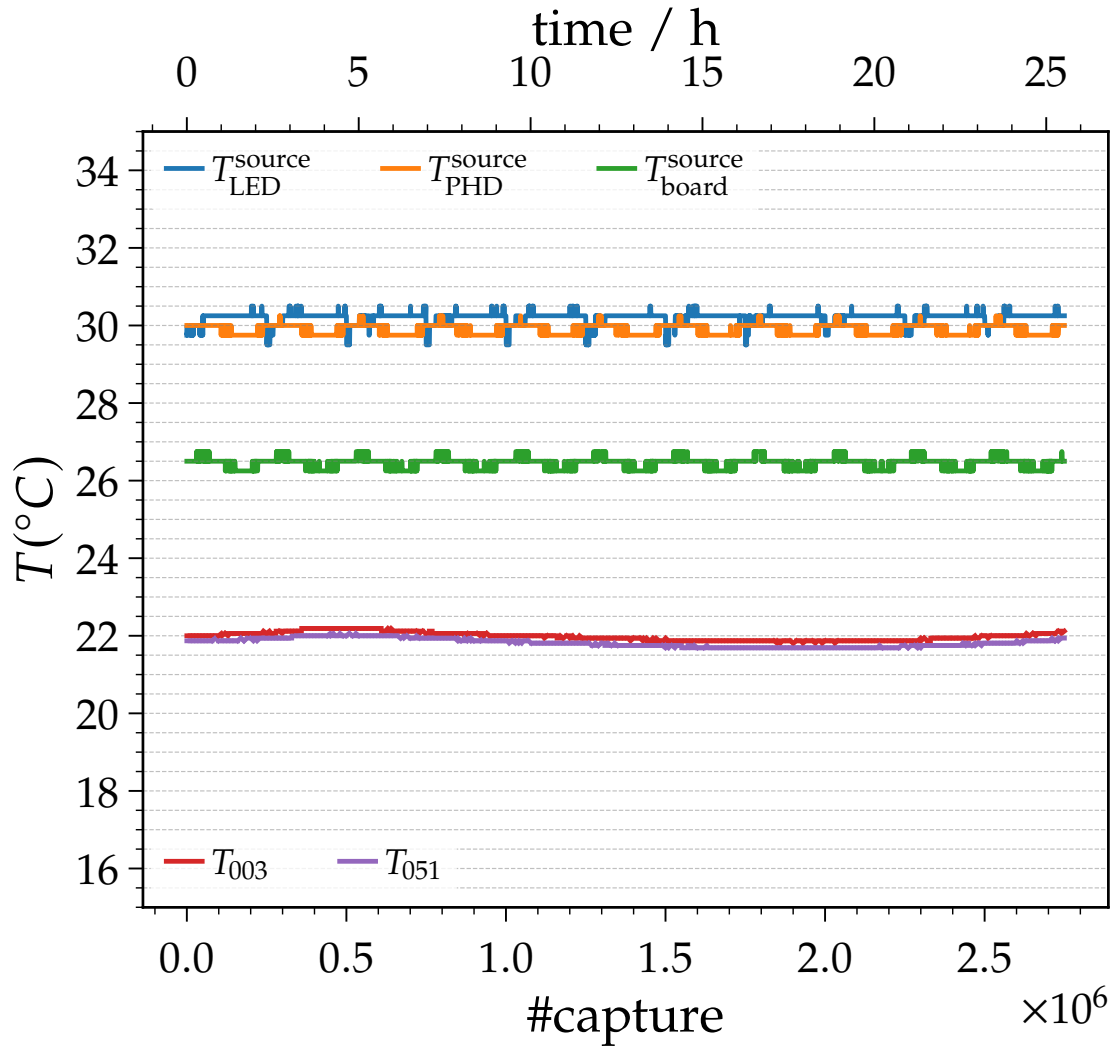
Figure A.9: Temperatures measured at source components (LED, photodiode, and electronics board) and by the two temperature sensors (T_{003} and T_{051}) within the light-tight enclosure during a calibration measurement of a XY-Scanner light source.

A.4.3. TYPICAL DISCARDED SOURCE-CALIBRATION EVENTS
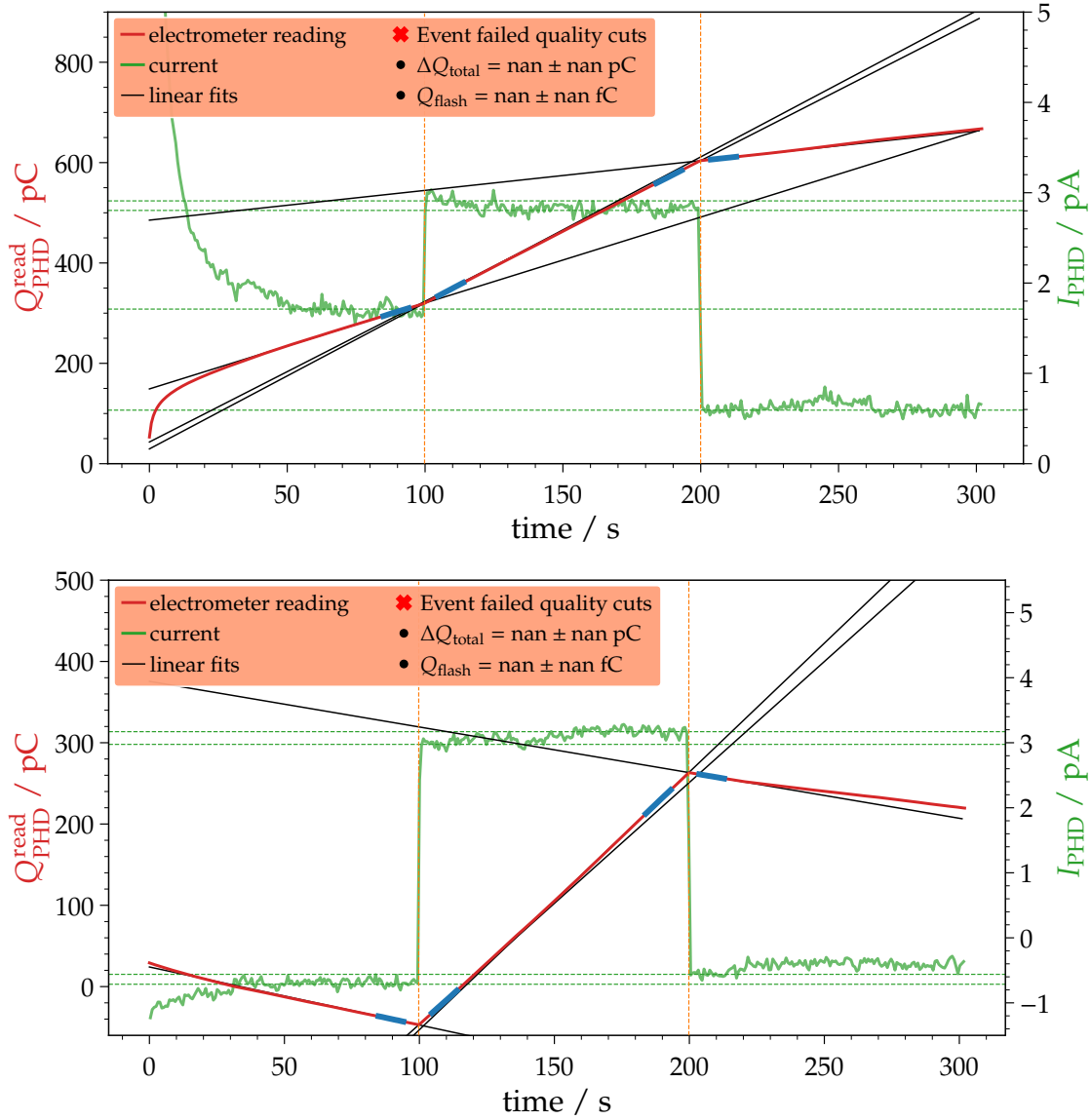
Figure A.10: Typical events of a source-calibration measurement as captured by the photodiode and read out by the electrometer which failed to pass the quality cuts. Plots are similar to Fig. 6.19.

In Fig. A.10 we show two events which failed to pass the event selection. The event in the top plot shows a significant difference in the background estimate before and after the signal part of the event. For the event in the bottom plot we observe a consistent but negative slope of the charge reading for the background part.

A.4.4. Crosscheck of Keithley 6514 Electrometers
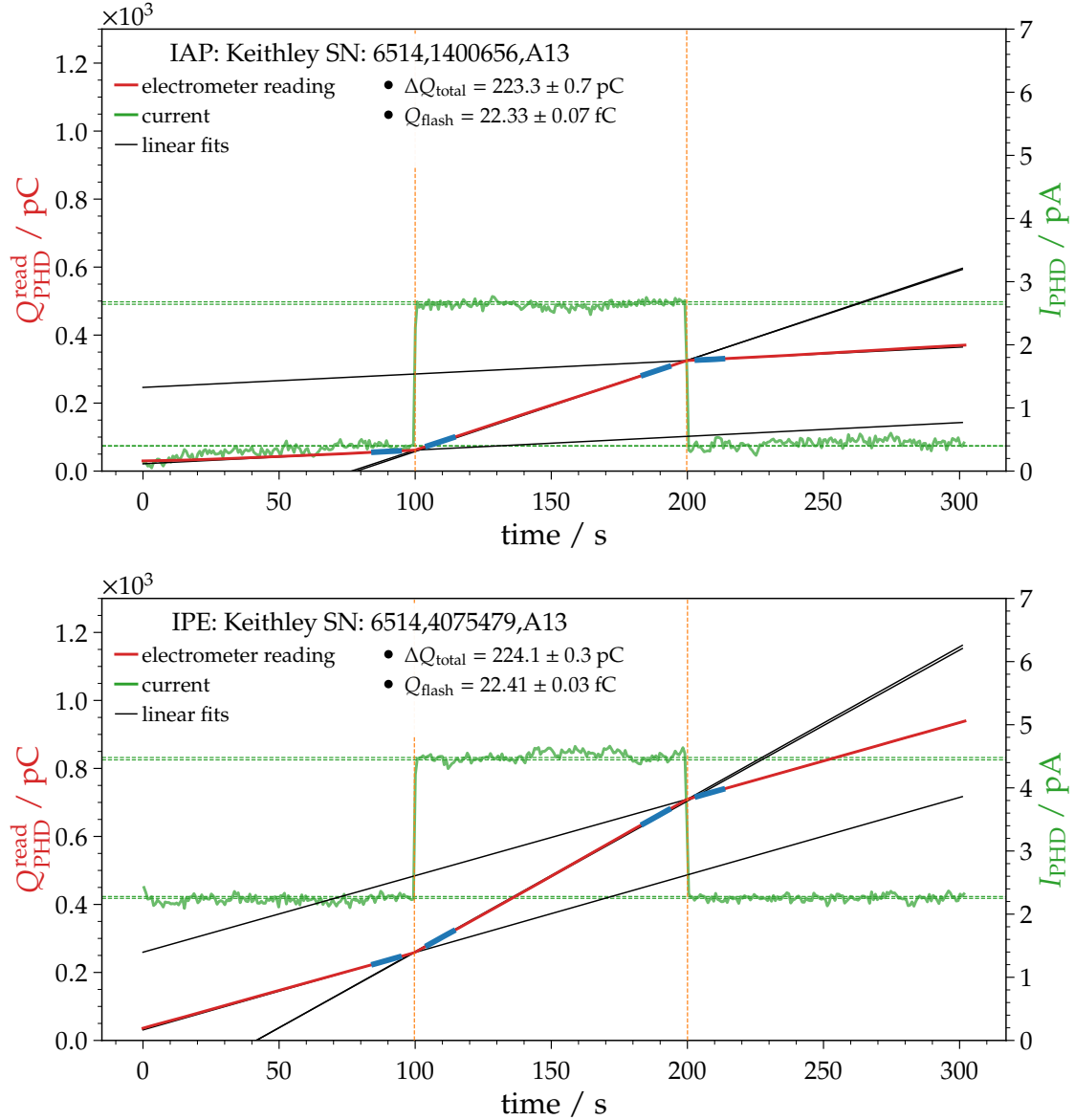
Figure A.11: Source calibration events taken with two different Keithley 6514 System Electrometers. Plots are similar than in Fig. 6.19.

In Fig. A.11 we present two events of a source-calibration measurement (see Section 6.7) which were captured with two different electrometers. The electrometers are approximately of the same age as both are operating a firmware version build on 2011 Aug. 30. For both events we used the same light source, operated at the same LED current, and set the same distance between the source and diode. For the event in the bottom plot of Fig. A.11 we observe a ~5.5 times higher background current. However, the charge estimates for both measurements differ less than 0.5% and agree within their statistical uncertainties. We therefore conclude, first, that the algorithm of estimating the charge is robust against an increased level of dark current and, second, that the electrometers if so aged in an identical manner.

A.4.5. PMT Traces of Source-Calibration Setup
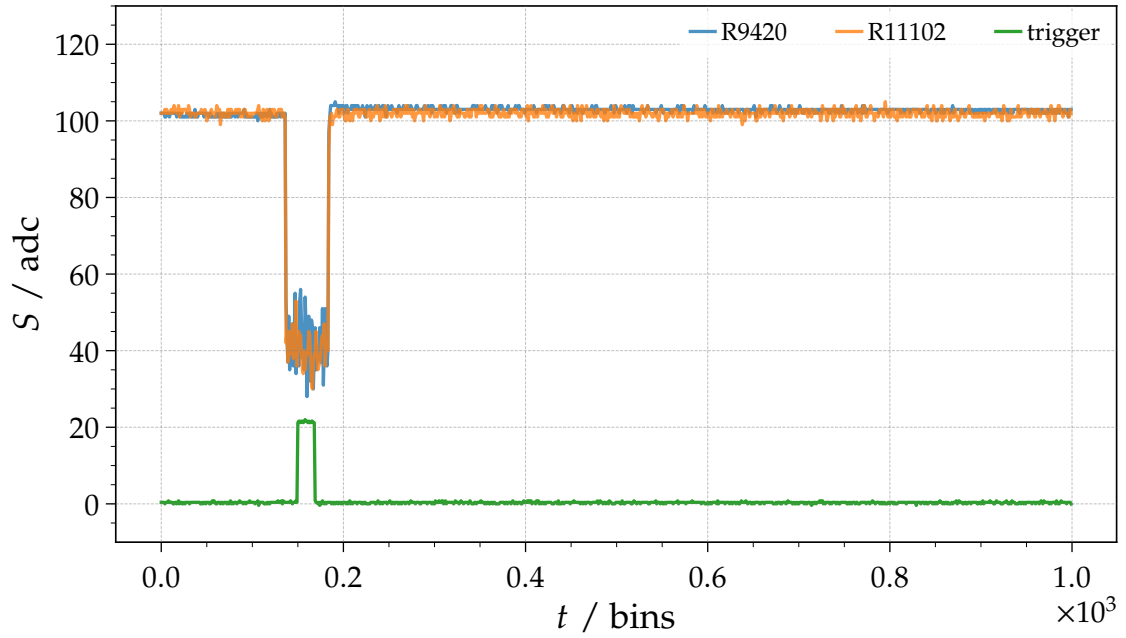
Figure A.12: Typical traces of the two PMTs in the source-calibration setup captured by the PicoScope.

A.4.6. Frequency Dependence of PMTs in Source-Calibration Setup
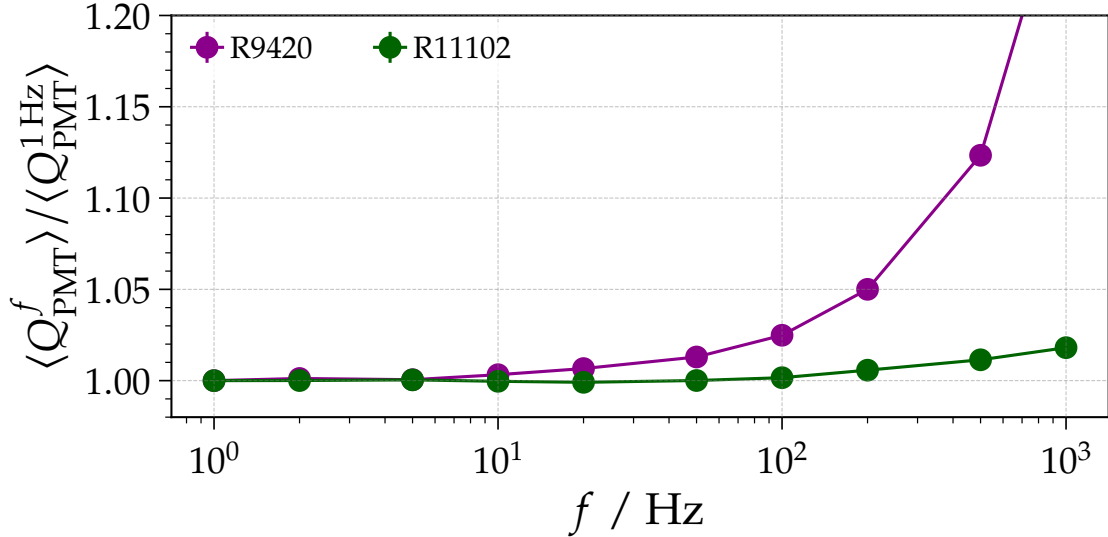
Figure A.13: Mean charge collected by the two PMTs in the light-source calibration setup relative to the 1 Hz measurement. Plotted are the mean and the standard error of the mean, the latter is very small and not really visible. Different colors depict different PMTs.

Fig. A.13 presents a dedicated study of the frequency behavior of the PMTs in the light-source calibration setup. We discuss this setup in Section 6.7. For this study we installed the Olomouc sphere and moved the photodiode out of the field of view of the PMTs. We operated the source at a constant LED current of $I_{LED} = 15.9$ mA and scanned through flashing frequencies between 1 Hz and 1 kHz. At each frequency we flashed the light source several 1000 times. The average charge collected per light flash by each PMT relative to the measurement at 1 Hz is plotted in Fig. A.13. Both PMTs show an increasing charge for an increasing flashing frequency. However, for the R9420 PMT we observe a faster and larger increase.

The average charge difference observed with the R11102 PMT is below ~1% (~2.5% for the R9420) for frequencies up to ~100 Hz. Flashing with 1 kHz the R11102 PMT sees a ~2% difference while in the R9420 PMT we observe a difference of ~28%. Therefore, and due to the fact that the firmware in the source electronics of the KIT sphere does not allow frequencies higher than 100 Hz, for the source calibration we decided to operate all sources at a maximal frequency of 100 Hz.

Operating the sources at higher frequencies would introduce a need for correction between higher and lower flashing frequencies, depending on the choice of the PMT.

A.4.7. Efficiency of Components for Source-Calibration Setup
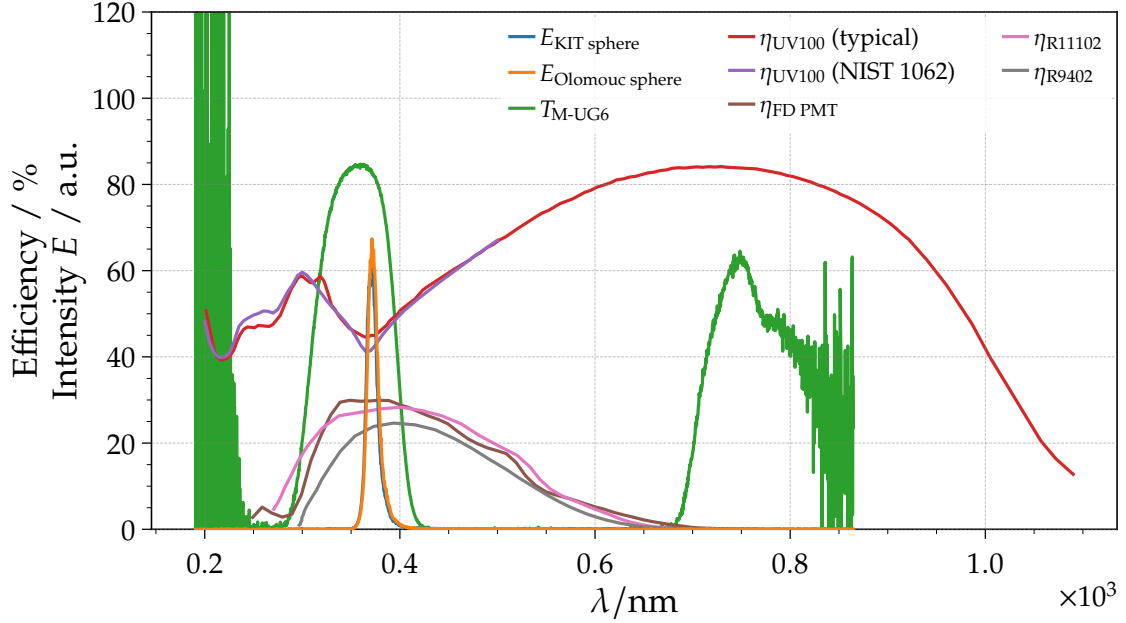
Figure A.14: Efficiency of various optical components included in the light-source calibration-setup. More details are given in the text.

In Fig. A.14 we show the efficiency of the components employed for the estimation of the light-source radiance. We plot the transmittance $T_{\text{M-UG6}}$ of the M-UG6 filter and the emission of the two integrating-sphere light sources (KIT sphere $E_{\text{KIT sphere}}$ and Olomouc sphere $E_{\text{Olomouc sphere}}$) as measured with the Ocean Optics SD2000 spectrometer. The quantum efficiency η of each PMT is taken from $\overline{\text{Off}}\underline{\text{line}}$ [58] in case of the FD PMT or the corresponding datasheets [96, 95]. We convert the measured (by NIST [99]) and typical responsivity ϵ_{UV100} [119] of the UV100 photodiode to a quantum efficiency η_{UV100} with

$$\eta_{\text{UV100}} = \epsilon \, \frac{hc}{\lambda \, e} \tag{A.1}$$

with the Planck constant h, the speed of light c, the wavelength λ, and the elementary charge e.

A.5. Influence of Telescope Shutter on Cal A
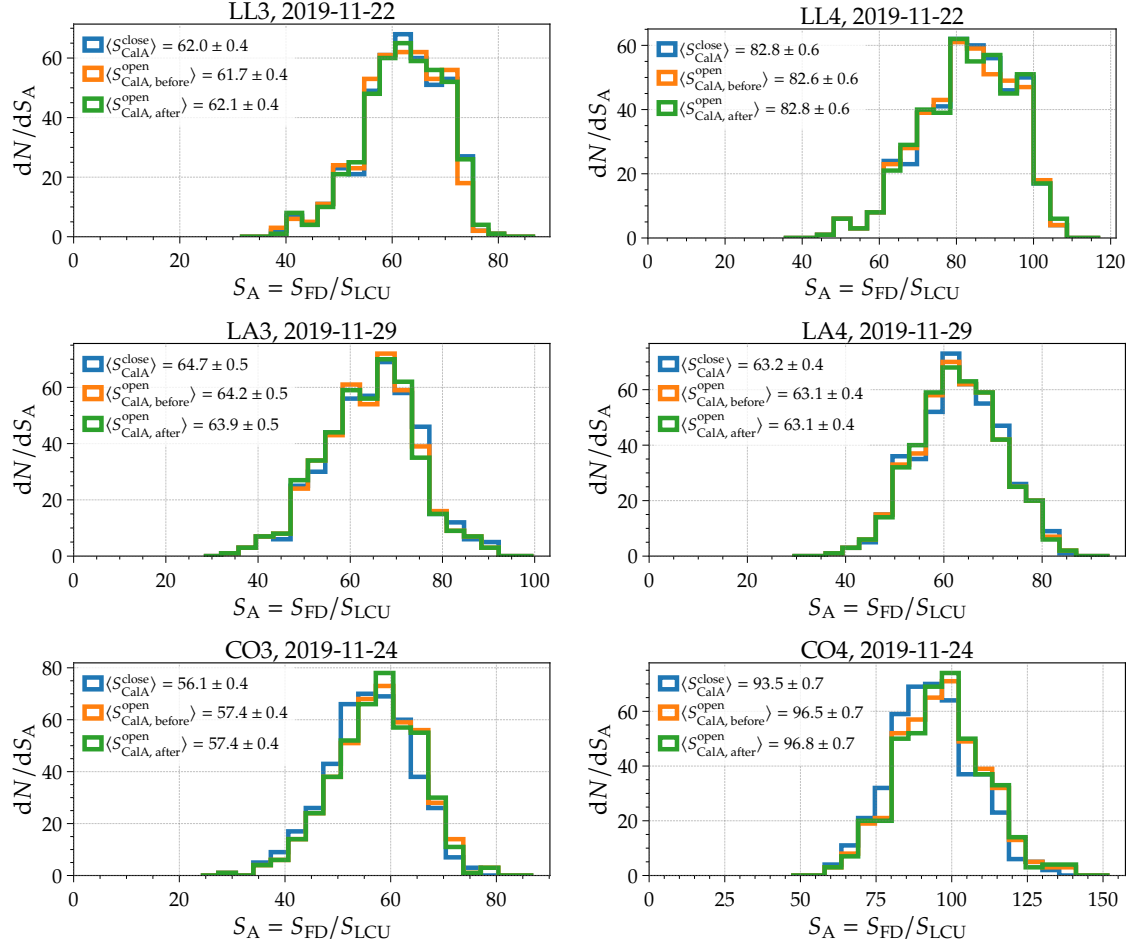
Figure A.15: Distributions of signals captured by telescope pixels during Cal A measurements relative to the signal recorded by the LCU. Data taken with closed shutters $\langle S_{\mathrm{CalA}}^{\mathrm{close}} \rangle$ is shown in blue. Open shutter measurement before $\langle S_{\mathrm{CalA, before}}^{\mathrm{open}} \rangle$ and after $\langle S_{\mathrm{CalA, after}}^{\mathrm{open}} \rangle$ an XY-Scanner measurement are drawn in orange and green, respectively. Data taken in November 2019. Different plots represent different telescopes.

In Fig. A.15 we present a study on the influence of the telescope shutter status on the pixel signals recorded during the Cal A calibration. Herein each plot represents the measurements at a certain telescope, as written above the plot. Each plot shows three distributions of pixel signals during different Cal A measurements. We show the standard Cal A at the beginning of a night which is performed with closed telescope shutter, as well as the two Cal A measurements we do before and after each XY-Scanner measurement. The mean and the standard error of the mean of each distribution are included within each plot. Comparing the mean of the measurements of open (before and after the XY-Scanner measurement) and closed shutter we observe no significant difference and therefore conclude that there is no significant influence of the telescope shutter status on the Cal A measurements.

A.6. Comparison between Individual and Official Cal A Tracking
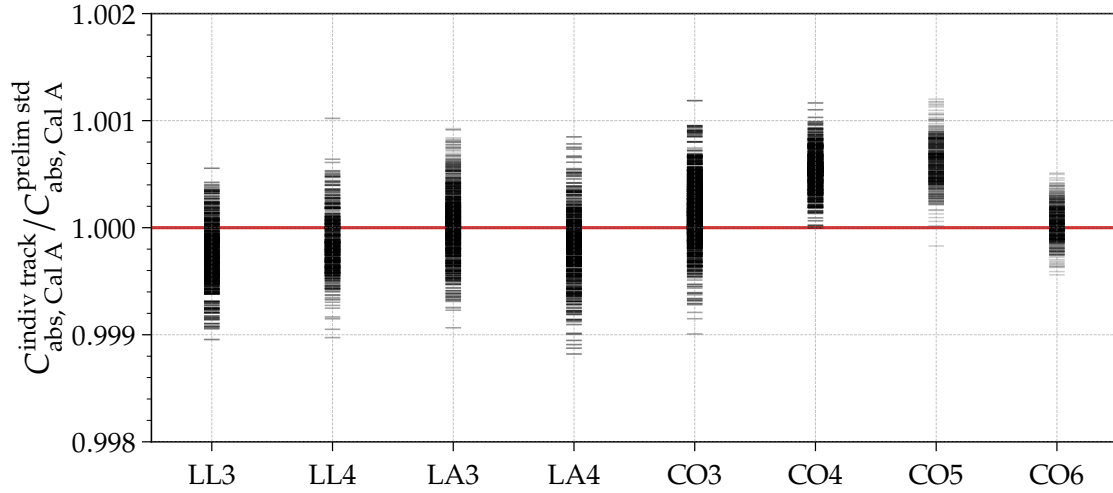
Figure A.16: Comparison between the calibration obtained from our implementation $C_{\text{abs, CalA}}^{\text{indiv track}}$ and the preliminary official Cal A tracking $C_{\text{abs, CalA}}^{\text{prelim std}}$. Each black bar represents an individual telescope pixel.

In Fig. A.16 we show a comparison between the calibration obtained with the Cal A from our implementation of Eq. (3.18) and the preliminary official values. The plot contains the Cal A calibrations performed during the XY-Scanner campaign of autumn 2022. We observe a maximal difference between the two methods of less than ~0.15%. Therefore, we conclude that the methods agree within numerical accuracy.

A.7.   ABSOLUTE CALIBRATION OF TELESCOPE PIXELS
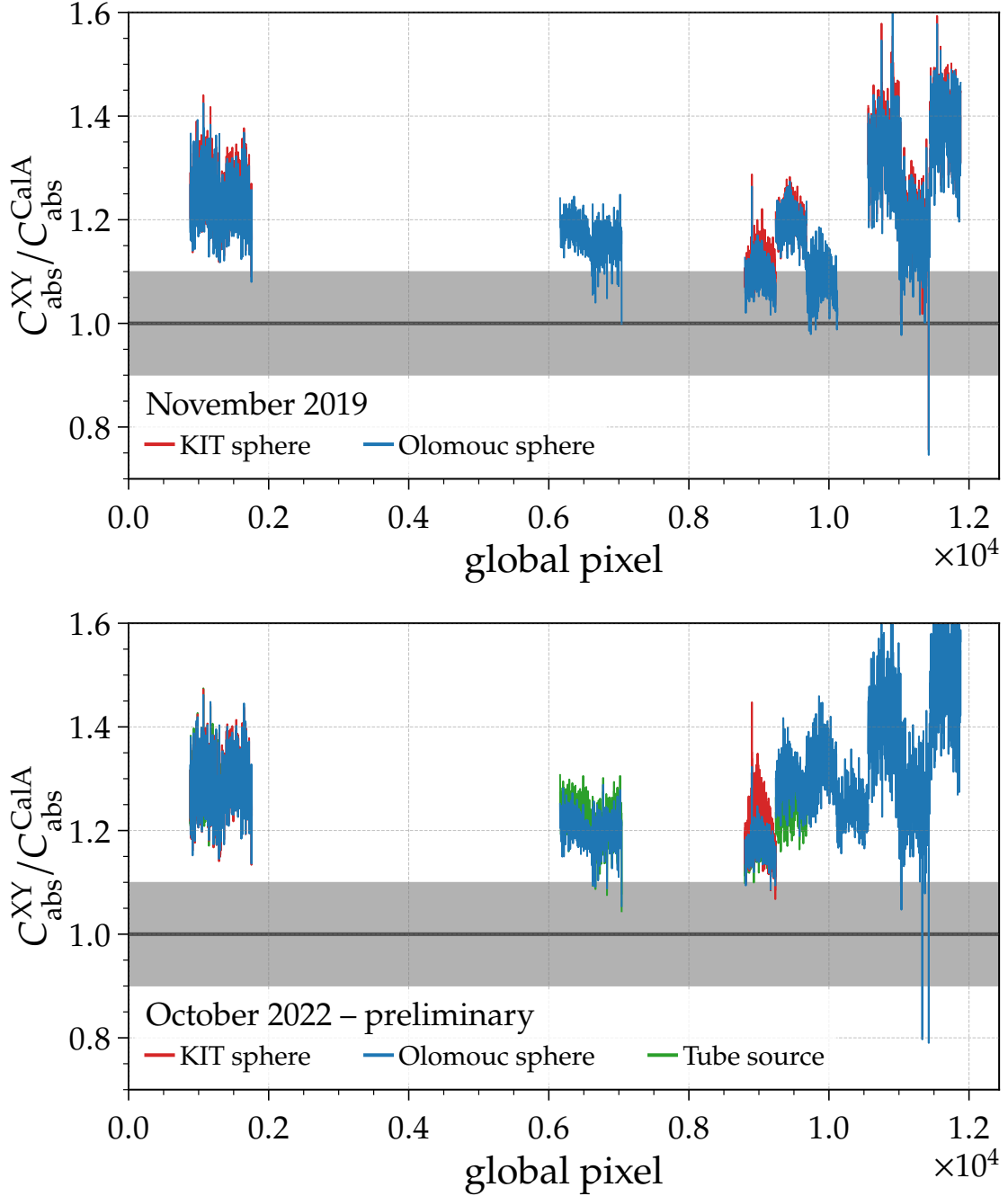
Figure A.17: Ratio between the absolute pixel calibrations of FD telescopes obtained from the XY-Scanner measurements C_{abs}^{XY} and with the tracking of the relative calibration system C_{abs}^{CalA}. Different colors depict different light sources. The gray band illustrates the current uncertainty on the FD calibration. *Top:* Calibration measurements performed in November 2019. *Bottom:* Data from October 2022. Here a custom implementation of the Cal A tracking is used.

Below we list examples of absolute calibration constants for each individual pixel obtained from the XY-Scanner measurements. Measurements were taken during the Autumn 2022 XY-Scanner campaign with the Olomouc sphere.

LL3 2022-10-24

col/row	1	2	3	4	5	6	7	8	9	10	11	12	13	14	15	16	17	18	19	20
1	6.19	5.96	6.18	6.06	6.38	6.22	6.40	6.68	6.85	6.53	6.30	6.53	6.41	6.57	6.44	6.22	6.41	6.30	6.31	5.83
2	6.33	6.51	6.29	5.91	6.22	6.15	6.35	6.61	6.78	5.84	6.54	6.99	6.47	6.48	6.33	6.34	6.19	6.48	6.35	6.88
3	6.77	6.69	6.66	6.47	6.45	6.77	6.46	6.52	6.29	6.44	6.44	7.02	6.62	6.34	6.11	6.42	6.41	6.29	6.22	6.32
4	6.23	6.01	6.53	6.35	6.37	6.73	6.59	6.76	5.75	6.80	6.45	6.76	6.51	6.75	6.59	6.36	6.15	5.92	6.48	6.42
5	6.42	6.29	5.93	6.51	6.67	6.61	6.58	6.36	7.06	6.27	6.41	6.45	6.05	6.66	6.54	6.06	6.63	6.49	6.10	6.44
6	6.85	6.48	6.14	6.70	6.15	6.63	6.58	6.57	6.19	6.49	6.20	6.59	6.72	6.58	6.23	6.44	6.01	6.00	6.58	6.39
7	5.90	6.68	6.63	6.78	6.64	5.78	6.45	6.33	6.19	6.28	6.58	6.59	6.29	6.66	5.94	6.04	6.50	6.66	6.69	6.40
8	6.15	6.36	6.13	6.47	6.31	6.58	6.63	6.62	6.78	6.37	6.90	6.53	6.62	6.72	6.20	5.66	6.73	6.58	6.63	6.38
9	6.37	6.35	6.29	6.45	6.49	6.14	6.35	6.57	6.62	6.57	6.77	6.36	6.28	6.41	6.63	6.37	6.43	6.34	6.15	6.14
10	6.23	6.52	5.90	6.44	6.53	6.57	6.53	6.73	6.87	6.43	6.18	6.80	6.00	6.42	6.83	6.72	6.75	6.05	6.34	6.84
11	6.52	6.63	6.43	5.77	6.66	6.76	6.18	6.79	6.15	6.62	7.22	7.05	6.89	5.99	6.55	6.38	6.10	6.44	6.21	5.83
12	6.60	6.53	6.73	6.45	5.96	6.12	6.47	6.57	6.58	5.97	6.25	6.32	6.30	6.12	6.85	6.39	6.48	6.50	6.01	6.51
13	6.72	6.08	6.93	7.00	7.13	6.49	6.49	6.98	6.25	6.45	7.02	6.18	6.05	6.50	6.80	6.56	6.42	6.82	6.78	6.35
14	6.20	6.53	6.52	6.29	7.04	6.37	6.51	6.56	6.56	6.71	6.48	6.94	6.62	6.34	5.93	6.30	6.56	6.45	6.74	6.56
15	6.79	6.46	6.87	6.50	6.52	6.10	7.36	6.58	7.00	6.46	6.57	6.42	6.89	5.98	6.53	6.80	6.46	6.47	5.85	5.71
16	5.83	5.81	6.24	6.27	6.40	6.27	6.45	6.44	6.25	6.55	6.37	6.21	6.25	6.58	6.26	6.36	6.28	6.07	5.89	6.02
17	6.16	6.16	6.97	6.13	6.61	6.58	6.28	6.65	7.02	6.68	6.99	6.08	6.65	6.67	6.35	6.26	6.58	6.49	5.86	6.09
18	6.77	6.47	6.87	5.88	6.65	6.51	6.31	6.52	6.27	6.27	6.74	6.92	6.05	6.80	6.25	6.06	6.44	6.74	7.13	6.68
19	6.77	5.86	6.32	6.74	6.95	6.79	6.73	6.62	6.64	6.70	6.60	6.46	6.60	6.08	6.64	5.91	6.36	6.50	6.19	6.15
20	6.36	6.88	6.47	6.35	6.39	6.72	6.27	6.67	6.93	6.70	6.62	6.53	6.54	6.61	6.41	6.09	6.42	7.04	7.22	6.31
21	6.07	6.60	5.94	6.02	6.50	6.79	7.04	6.28	6.90	6.78	6.50	6.65	6.68	6.70	6.03	6.06	6.61	6.44	6.47	6.49
22	6.32	5.87	6.17	5.96	7.07	6.89	6.95	6.91	6.64	6.99	6.89	6.80	6.32	6.55	6.15	6.57	6.79	6.15	5.75	6.15

LL4 2022-10-24

col\row	1	2	3	4	5	6	7	8	9	10	11	12	13	14	15	16	17	18	19	20
1	6.24	5.87	6.27	6.56	6.29	6.85	6.54	6.37	6.58	6.73	6.22	6.57	6.56	6.56	6.79	6.75	6.28	6.08	6.46	6.64
2	6.45	6.05	6.28	6.16	6.31	6.62	6.80	6.30	6.44	6.42	6.22	6.41	6.71	6.45	6.63	6.43	6.44	6.21	6.07	6.36
3	6.19	6.06	6.15	6.18	6.35	6.58	6.44	6.34	6.26	6.68	6.51	6.21	6.48	6.31	6.25	6.59	6.32	6.12	6.14	6.48
4	6.33	6.36	6.47	6.32	6.58	6.18	6.48	6.53	6.44	6.81	6.43	6.28	6.43	6.35	6.39	6.40	6.16	5.89	6.34	6.51
5	6.01	6.28	6.21	6.24	6.61	6.67	6.64	6.58	6.64	7.03	6.42	6.52	6.49	6.67	6.21	6.49	5.91	6.08	6.50	5.95
6	6.06	6.05	6.05	6.47	6.46	6.52	6.47	6.79	6.30	6.31	6.36	6.17	6.56	6.52	6.56	6.34	6.20	6.07	6.24	6.22
7	5.95	5.85	5.85	6.16	6.59	6.52	6.55	6.80	6.85	6.26	6.38	5.99	6.61	6.38	6.65	6.28	6.17	6.44	6.48	6.67
8	5.92	6.03	6.43	6.44	6.70	6.38	6.50	6.22	6.52	5.94	6.28	6.59	6.81	6.37	6.38	6.36	5.96	6.15	6.27	6.18
9	6.06	6.51	6.14	6.25	6.23	6.20	6.80	6.62	6.50	6.62	6.30	6.51	6.50	6.58	6.24	6.62	6.34	6.26	6.14	6.25
10	6.29	5.99	6.46	5.99	6.58	6.51	6.44	6.97	6.28	6.39	6.42	6.22	6.79	6.64	6.34	6.30	6.67	6.84	6.99	6.20
11	6.03	6.01	6.29	6.56	6.67	6.76	6.48	6.88	6.48	6.49	6.35	6.44	6.49	6.62	6.56	6.25	6.25	6.45	6.28	6.22
12	6.40	6.37	6.37	6.33	6.33	6.26	6.70	6.25	6.02	5.96	5.95	5.99	6.17	6.20	6.10	6.44	6.63	6.37	6.65	6.53
13	6.41	6.36	6.71	6.29	6.82	6.15	6.29	6.21	6.49	6.41	6.28	6.28	6.14	6.39	5.95	6.54	6.52	6.78	6.63	6.62
14	6.09	6.48	6.16	6.83	6.07	6.51	6.15	6.37	6.48	6.05	6.15	6.45	6.18	6.14	6.41	6.17	6.25	6.52	6.32	6.80
15	6.60	6.40	6.28	6.79	6.20	6.30	6.38	5.92	6.09	6.34	6.27	6.49	6.41	6.14	6.35	6.16	6.42	6.47	6.89	6.58
16	6.53	6.41	6.54	6.39	6.39	5.84	5.97	6.04	5.99	5.93	6.31	6.68	6.09	6.45	6.18	6.31	6.52	6.25	6.67	6.27
17	6.45	6.34	6.39	6.12	6.21	6.27	6.30	6.76	6.18	6.31	6.24	6.71	6.60	6.06	5.94	6.49	6.35	6.25	6.30	6.51
18	6.38	6.26	6.48	5.97	6.31	6.73	6.30	6.69	6.52	6.53	6.19	6.39	5.96	6.10	6.37	6.50	6.37	6.40	6.25	6.37
19	6.11	6.32	6.60	6.48	6.10	6.49	5.99	6.63	6.32	6.47	5.98	6.35	6.29	6.25	6.26	6.23	6.27	6.67	6.56	6.45
20	6.59	6.09	6.54	6.57	6.03	6.47	6.43	6.38	6.53	6.25	6.17	6.00	6.63	6.33	6.24	6.27	6.58	6.37	6.19	6.34
21	6.53	6.03	6.57	6.68	6.12	6.17	6.25	5.79	6.30	6.59	6.44	6.33	6.48	5.99	5.98	6.27	6.27	6.15	6.65	6.54
22	6.67	6.35	6.60	6.21	6.46	6.22	6.24	6.09	6.27	6.32	6.05	6.04	6.56	6.33	6.55	6.00	6.27	6.14	6.93	5.90
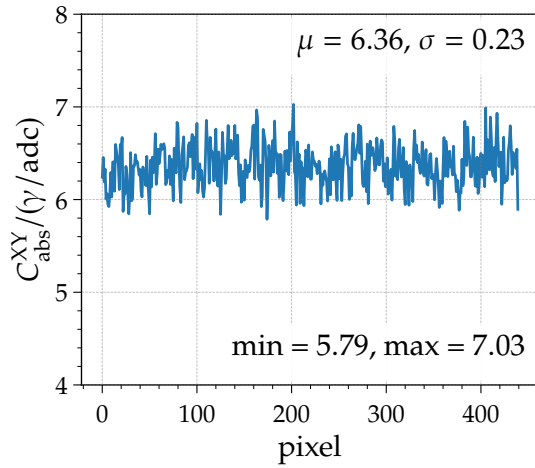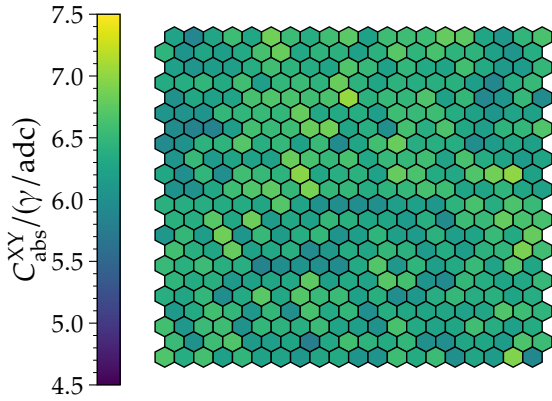
LA3 2022-10-19

col / row	1	2	3	4	5	6	7	8	9	10	11	12	13	14	15	16	17	18	19	20
1	5.24	5.71	5.51	6.16	5.63	5.61	6.28	5.93	6.03	5.75	5.86	6.13	5.31	6.49	5.64	4.93	5.71	6.17	6.11	5.03
2	5.99	6.49	6.08	6.24	5.16	5.14	6.09	5.57	5.95	5.99	5.55	5.60	5.67	6.16	6.33	5.93	5.50	5.68	5.61	5.97
3	5.19	5.89	6.16	5.23	4.98	6.47	5.52	6.03	6.32	6.14	5.98	5.62	5.85	6.08	5.96	5.72	5.41	5.21	5.28	5.25
4	5.74	5.42	5.86	5.34	5.44	5.49	6.62	5.47	5.77	5.58	5.68	6.14	5.14	5.62	5.41	5.12	5.20	5.91	5.68	5.62
5	6.01	5.14	5.68	5.53	5.57	5.79	6.53	5.62	5.85	5.11	6.21	5.76	5.40	5.49	5.83	5.10	5.71	5.67	6.32	6.31
6	6.47	6.65	5.83	5.49	5.69	5.47	5.35	5.42	5.80	5.93	5.62	6.16	5.19	5.25	6.37	6.43	5.74	6.10	6.27	6.89
7	5.91	5.77	6.25	5.23	6.89	5.82	6.13	5.59	6.20	5.62	6.06	5.47	6.44	5.76	5.23	6.15	5.29	6.67	6.10	5.09
8	5.95	6.43	5.68	6.28	5.72	5.52	5.89	6.14	6.93	6.45	5.47	5.28	5.99	5.76	5.43	5.37	4.97	6.03	5.26	6.57
9	5.58	6.48	5.82	5.89	5.62	5.79	6.83	6.91	6.15	5.58	5.59	6.10	5.64	5.89	5.22	4.95	4.86	5.60	5.55	5.69
10	5.08	5.83	5.60	5.44	5.47	5.55	5.47	6.26	6.41	5.08	5.81	6.15	5.23	5.38	5.53	6.48	5.22	5.67	5.25	5.82
11	5.16	5.25	6.53	5.86	6.48	5.87	5.62	5.39	5.75	5.50	5.14	4.79	5.95	5.01	5.61	6.17	6.22	6.04	6.54	4.68
12	5.03	5.85	5.30	5.85	5.23	5.64	6.02	4.73	5.22	6.10	5.66	5.92	5.85	4.57	5.36	4.64	5.34	6.08	5.58	6.51
13	6.92	5.51	7.17	5.55	5.73	6.07	6.08	4.97	5.48	5.01	5.74	6.81	6.29	6.03	5.06	4.83	5.19	5.31	5.49	5.33
14	4.63	6.28	5.72	5.57	6.00	5.38	5.61	6.10	5.35	5.09	6.60	6.64	5.10	5.14	5.16	4.50	5.48	5.76	5.57	5.06
15	5.70	4.98	6.29	6.10	4.66	6.54	6.17	6.31	5.54	5.97	6.20	5.70	5.84	4.70	5.66	5.62	6.22	6.16	4.46	6.18
16	6.17	5.95	6.68	5.11	5.20	5.78	6.01	5.94	7.11	7.46	5.88	6.18	5.75	5.59	5.32	5.18	5.02	6.14	4.75	6.03
17	5.65	6.76	5.67	5.43	5.49	6.02	5.16	4.89	5.93	5.87	5.68	5.56	5.25	5.96	4.34	5.20	4.95	5.85	5.91	6.04
18	5.28	5.09	5.02	4.89	5.46	5.51	5.73	5.13	5.46	5.44	5.55	6.11	5.84	5.28	5.67	6.42	5.49	5.11	5.07	5.71
19	5.24	5.39	5.38	5.29	6.18	5.19	5.60	5.53	7.26	5.33	5.48	6.28	5.02	5.20	5.44	5.41	5.46	5.63	7.49	4.54
20	5.48	5.16	4.61	5.84	4.65	5.84	4.67	5.06	5.84	5.36	6.61	6.10	7.65	5.30	5.32	5.16	6.08	6.10	5.51	7.42
21	5.81	5.53	5.17	4.51	5.57	5.54	4.58	5.99	5.15	5.56	5.15	5.59	5.31	5.41	6.00	5.22	5.25	5.55	5.28	5.73
22	6.92	5.57	4.90	5.27	5.93	5.51	5.48	5.65	6.53	4.59	6.21	5.80	4.71	4.92	4.68	4.47	5.29	4.92	6.20	5.52
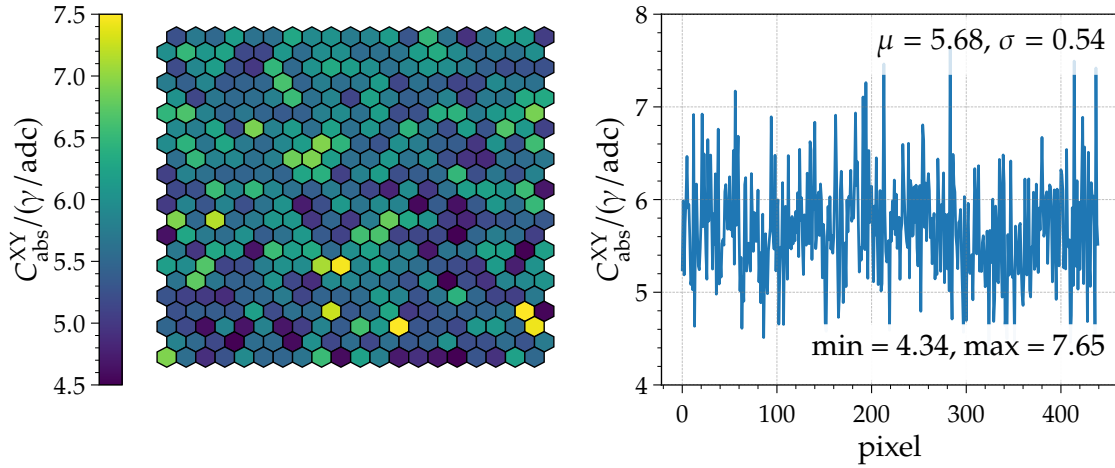
LA4 2022-10-20

col / row	1	2	3	4	5	6	7	8	9	10	11	12	13	14	15	16	17	18	19	20
1	5.68	5.73	5.08	6.26	6.25	5.54	6.31	6.16	6.43	6.00	5.61	6.38	5.95	5.53	6.14	5.60	5.54	5.41	5.77	4.87
2	5.87	6.40	6.29	5.42	5.43	5.81	6.20	5.76	5.47	5.67	6.27	5.74	5.59	5.68	5.66	6.72	5.32	5.67	5.15	5.50
3	6.25	5.94	5.65	6.03	6.16	6.37	6.53	5.70	5.89	6.35	5.68	6.03	6.01	5.82	5.74	5.37	5.56	5.60	5.12	6.34
4	5.48	6.77	6.39	5.82	6.29	5.64	5.91	6.37	5.72	5.80	5.77	6.74	5.58	5.58	5.63	5.75	5.71	5.52	5.05	5.75
5	5.75	6.44	5.92	6.11	5.64	6.80	6.28	6.23	6.86	5.99	6.26	6.95	5.43	5.60	6.72	5.35	5.96	5.75	5.29	5.06
6	4.70	5.73	6.10	6.84	5.04	5.73	5.75	5.98	6.25	5.42	6.20	6.35	5.61	5.77	6.12	5.74	5.41	5.52	5.18	5.48
7	5.86	6.22	5.53	6.11	6.41	5.37	6.35	6.76	5.93	5.65	5.80	6.09	6.39	6.18	5.54	5.81	5.63	5.39	5.00	5.47
8	6.20	5.42	6.01	6.30	5.63	5.31	6.34	5.99	5.81	5.38	5.89	5.60	5.75	6.28	5.75	6.12	5.67	5.32	5.09	5.31
9	6.10	6.09	5.52	6.04	5.90	6.25	5.23	5.79	5.99	5.75	5.49	6.06	5.37	5.36	5.66	5.90	5.79	5.46	5.50	4.89
10	5.87	5.32	5.86	6.51	6.00	6.44	6.22	6.54	5.81	5.62	6.70	7.80	5.86	5.90	6.14	6.12	5.64	5.88	5.59	5.56
11	5.22	6.31	5.70	5.77	6.49	6.79	5.29	5.99	6.52	5.51	6.89	5.04	5.23	6.30	5.54	6.52	6.22	5.57	5.31	6.43
12	5.88	6.00	6.00	5.99	5.74	6.12	5.75	5.75	5.77	6.02	6.31	5.48	6.76	5.56	5.78	6.02	6.12	6.31	5.18	5.34
13	5.39	6.03	4.98	6.56	6.01	5.52	5.80	6.47	6.02	5.30	5.80	5.76	5.13	5.81	5.84	5.46	6.04	5.69	6.14	6.09
14	5.74	5.25	5.17	5.97	5.58	6.11	5.58	6.64	5.92	5.93	5.30	5.47	5.42	6.15	5.54	5.93	5.24	4.92	5.09	6.02
15	5.56	5.41	6.33	5.44	5.79	5.34	6.16	5.81	5.93	5.39	5.44	5.61	5.09	4.98	5.91	5.39	6.00	5.16	5.84	5.68
16	5.10	5.44	6.34	5.77	6.29	6.36	5.78	5.50	5.55	5.42	5.46	5.67	4.72	5.26	5.56	5.70	5.59	5.41	5.77	6.10
17	5.01	4.87	6.18	5.68	5.43	6.32	5.73	5.63	5.71	5.58	5.63	5.62	6.02	5.58	6.22	5.70	5.81	4.94	5.37	5.95
18	5.47	5.99	5.77	5.50	5.81	5.64	7.01	5.54	6.03	5.78	5.50	5.70	5.01	6.27	5.96	6.09	6.17	5.26	6.31	6.01
19	5.53	6.05	6.13	5.85	6.63	6.22	6.39	5.43	6.04	5.79	5.62	6.28	4.95	5.28	5.17	5.69	5.98	5.57	4.90	5.69
20	5.82	5.82	6.39	5.40	5.91	5.47	5.88	5.37	6.01	5.70	6.24	5.12	5.56	5.79	5.42	6.46	6.11	5.73	5.60	5.85
21	5.29	6.15	6.41	6.20	5.74	6.39	6.26	6.09	5.00	5.62	5.19	5.54	5.51	6.11	5.40	7.03	5.80	5.42	5.41	6.08
22	4.96	5.87	5.90	6.27	5.44	5.32	6.64	5.52	5.61	5.67	5.50	5.61	5.74	6.20	5.09	5.25	5.50	5.20	5.19	5.36

$\mu = 5.80, \sigma = 0.44$

min = 4.70, max = 7.80
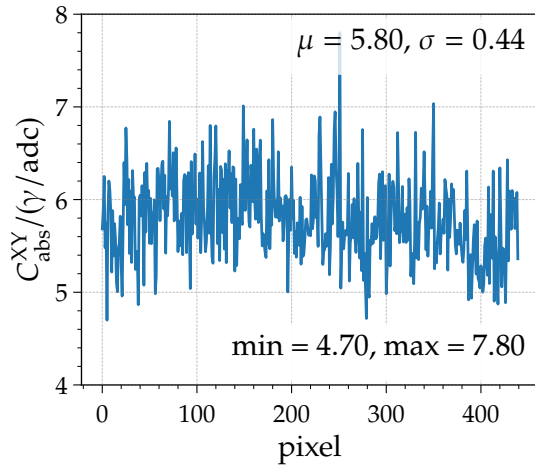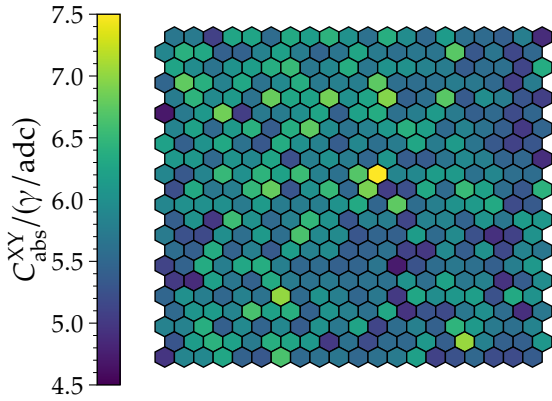
CO3 2022-10-14

$\frac{col}{row}$	1	2	3	4	5	6	7	8	9	10	11	12	13	14	15	16	17	18	19	20
1	5.74	5.65	6.07	6.01	6.42	6.14	6.03	6.33	6.41	6.86	6.19	6.06	6.26	5.90	6.34	6.63	5.89	5.81	6.35	6.30
2	6.03	5.93	5.66	5.76	5.77	5.69	6.06	5.93	5.62	6.41	6.73	6.25	5.92	6.26	6.32	5.97	6.53	6.39	6.38	6.34
3	6.05	6.00	6.41	5.62	6.61	6.11	6.65	6.25	5.59	6.51	6.89	5.87	6.38	6.29	6.57	6.29	6.14	6.17	6.10	6.44
4	6.13	5.64	6.19	6.08	6.10	6.55	6.65	6.34	6.13	6.18	6.48	6.20	6.23	6.12	5.27	6.15	6.58	6.04	6.60	5.91
5	5.73	6.31	6.02	6.65	6.12	6.38	6.38	6.25	5.72	6.50	6.15	5.74	6.36	6.03	6.10	5.52	6.25	5.81	6.00	6.21
6	5.49	6.05	5.86	5.84	5.82	6.06	6.06	6.41	6.43	6.07	6.08	6.23	6.29	5.61	6.14	6.66	6.11	6.62	6.49	5.71
7	5.97	6.66	6.25	5.61	6.26	6.66	5.77	6.20	6.24	6.36	6.10	6.41	5.62	6.25	6.10	6.09	5.92	6.44	5.74	5.76
8	5.63	6.20	6.07	6.46	6.38	6.13	6.22	6.47	5.84	6.27	6.08	6.21	6.61	5.99	5.33	6.61	5.82	6.05	5.63	5.56
9	5.95	5.56	5.23	6.23	6.33	5.86	5.84	5.29	5.59	6.33	6.10	5.54	6.07	6.68	6.31	6.68	6.07	5.84	5.96	5.67
10	5.03	5.11	6.26	5.58	6.06	5.91	6.61	6.21	6.84	5.22	5.98	5.73	6.38	6.64	6.29	5.68	6.65	6.10	5.85	5.60
11	5.94	5.44	6.36	5.20	6.04	6.26	6.18	6.33	7.09	5.93	5.80	5.50	6.67	5.87	6.21	5.39	6.41	5.95	5.83	5.97
12	5.33	5.48	6.15	5.79	6.70	5.78	6.12	5.74	5.54	6.96	6.76	6.80	6.41	5.63	6.12	6.89	6.55	6.56	5.37	6.02
13	6.49	5.93	5.01	6.12	7.19	6.93	5.75	5.54	6.09	5.75	6.36	5.81	6.25	6.78	6.25	6.34	6.68	6.49	6.59	6.66
14	6.31	5.00	5.79	6.05	5.63	5.39	6.97	5.99	6.66	5.87	6.07	5.89	5.79	6.03	5.95	6.11	6.41	6.10	5.17	6.48
15	5.51	5.86	5.89	6.13	6.42	5.90	5.33	6.04	6.61	6.43	6.48	6.64	5.93	6.44	5.80	6.08	6.28	6.11	6.24	5.62
16	5.63	5.90	6.16	6.34	6.44	6.46	5.57	7.00	6.60	5.87	5.51	6.73	6.65	6.55	6.98	5.53	6.54	5.43	5.78	6.24
17	5.63	6.85	6.59	6.24	6.67	6.03	6.12	6.90	6.18	6.15	6.44	6.16	6.44	5.85	5.94	6.05	6.74	6.25	6.42	5.58
18	5.25	5.79	5.90	6.43	5.33	5.84	6.31	6.00	5.89	6.52	5.28	5.61	6.01	6.07	5.31	5.84	7.01	5.53	5.72	6.74
19	7.06	5.98	6.24	5.46	6.22	5.86	6.92	6.10	6.00	5.84	6.61	5.64	5.75	6.48	6.68	6.07	7.39	5.75	4.50	6.34
20	5.84	5.66	6.08	5.37	6.08	5.76	6.55	5.89	6.20	6.01	5.70	6.12	5.94	6.63	6.08	5.85	7.30	5.58	6.07	5.76
21	6.16	6.00	6.36	6.43	5.57	6.02	6.99	6.10	5.99	5.95	5.65	6.03	6.25	7.14	6.48	6.58	5.65	6.30	6.61	5.89
22	5.60	6.57	6.59	5.98	5.76	6.42	6.42	6.38	6.85	7.14	6.33	6.01	5.97	5.91	5.24	5.89	5.56	5.89	5.03	6.10
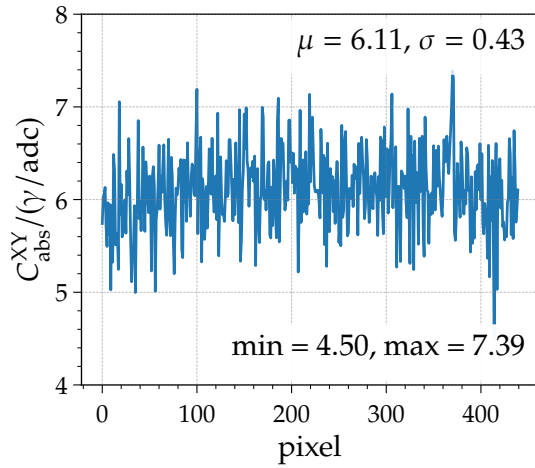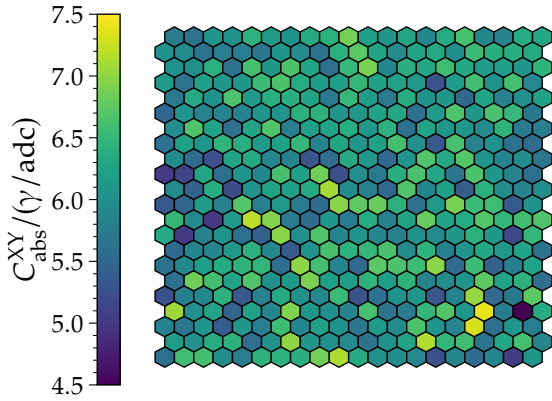
CO4 2022-10-15

col row	1	2	3	4	5	6	7	8	9	10	11	12	13	14	15	16	17	18	19	20
1	6.24	6.12	6.48	6.35	6.55	6.38	6.87	5.41	6.89	6.27	6.61	6.34	6.36	6.21	5.62	6.49	6.69	6.63	6.18	4.98
2	6.14	6.42	6.13	6.17	6.63	5.92	6.39	5.49	6.86	6.44	6.06	6.35	6.30	6.14	6.39	6.71	5.85	6.35	6.49	6.63
3	6.27	6.00	5.92	7.18	6.46	6.16	6.97	5.96	6.45	6.54	6.28	5.49	6.46	6.28	6.76	6.35	6.57	6.42	6.06	5.92
4	6.12	5.95	6.58	5.49	6.67	6.34	6.82	5.73	6.21	6.16	6.06	6.61	6.46	5.98	6.49	6.40	6.21	6.01	5.96	6.13
5	6.30	6.50	6.23	6.43	6.24	5.53	5.77	5.44	6.89	6.48	6.53	6.56	6.86	6.84	6.60	6.66	5.74	5.97	6.80	6.21
6	5.98	6.64	6.43	6.25	6.06	6.77	6.13	6.40	6.68	6.93	5.79	6.65	6.39	6.58	6.74	6.91	6.59	6.39	6.30	6.35
7	6.24	6.07	6.73	6.84	6.00	6.46	5.70	6.55	6.32	6.90	6.27	6.10	5.60	6.34	7.01	6.18	5.87	6.48	6.41	6.27
8	5.80	6.37	5.68	6.35	5.89	5.75	5.50	6.14	6.55	5.91	5.96	5.64	6.42	6.15	6.18	6.59	6.23	5.61	6.04	6.56
9	6.99	6.55	5.69	5.97	6.39	7.06	5.86	5.79	6.16	6.78	6.06	6.52	6.44	7.00	7.14	5.76	6.36	6.38	6.15	5.72
10	6.16	6.34	5.96	6.22	5.93	7.07	6.88	5.91	7.22	6.33	6.49	5.78	6.44	6.40	6.46	6.35	6.52	5.98	6.33	5.67
11	6.25	6.07	6.00	6.40	5.99	5.52	6.31	5.39	6.53	6.13	6.65	6.08	6.49	6.87	6.80	6.08	6.18	6.53	6.46	5.66
12	5.64	6.47	6.55	6.23	6.22	6.61	5.40	5.97	6.14	6.60	6.04	6.59	5.39	6.90	6.48	6.18	5.93	5.86	5.82	5.57
13	5.97	5.91	5.84	6.50	5.92	5.35	6.58	5.26	6.23	6.54	5.97	5.94	6.60	6.70	6.36	6.81	5.43	6.94	5.53	6.64
14	6.23	6.42	5.43	6.56	6.27	5.53	6.58	6.71	6.46	5.81	6.26	6.31	5.69	5.88	6.75	6.00	6.17	5.73	6.09	6.43
15	6.10	6.66	6.75	5.82	6.37	5.72	6.36	5.71	6.43	5.94	5.80	5.78	6.81	6.29	7.24	6.50	6.53	5.87	5.95	6.64
16	5.94	6.19	6.34	6.21	6.63	6.74	6.98	5.36	5.89	5.93	4.98	5.63	5.79	6.39	6.53	6.45	6.11	5.97	5.57	5.03
17	5.60	6.52	5.86	5.90	6.56	6.28	6.83	7.21	6.86	6.44	5.73	6.11	6.51	6.52	6.51	7.03	6.05	5.46	5.92	6.08
18	6.07	6.66	6.41	6.88	6.51	6.45	6.43	7.68	6.20	6.54	5.25	6.38	5.35	6.55	6.72	6.51	5.57	6.05	6.65	5.62
19	6.10	6.15	6.45	6.66	6.68	6.65	5.66	5.48	6.73	6.43	5.88	5.50	5.74	6.83	6.48	6.65	6.05	5.90	5.84	5.47
20	5.63	6.33	6.08	6.62	5.81	6.57	6.93	6.25	7.02	6.11	6.27	6.45	5.93	6.20	7.08	5.79	5.90	5.61	6.08	6.31
21	6.49	6.57	6.54	5.31	5.97	6.89	5.57	6.30	5.57	6.47	5.93	6.09	6.41	7.40	6.64	6.40	6.37	6.01	5.79	5.60
22	6.20	5.80	6.34	6.10	6.30	6.56	6.38	6.24	6.57	6.05	6.39	6.50	6.40	6.26	6.68	6.48	5.84	5.88	6.19	5.97
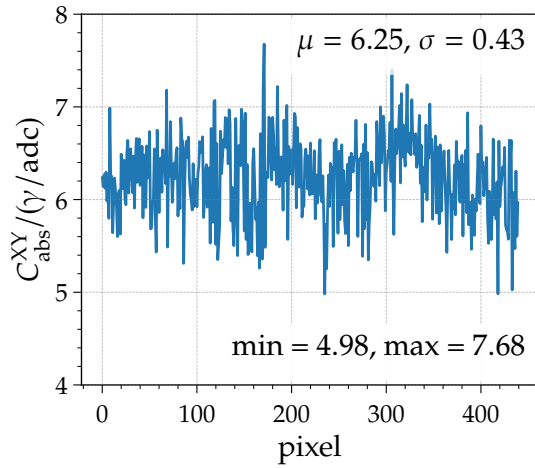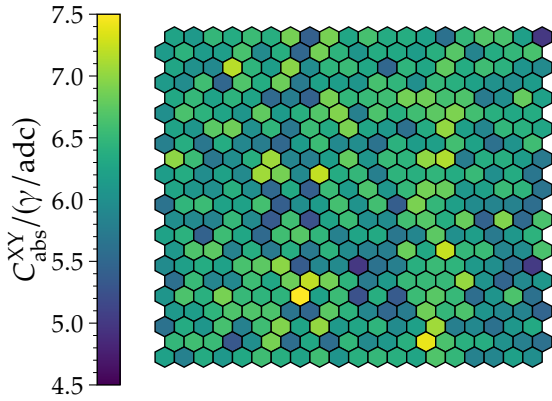
CO5 2022-10-15

col row	1	2	3	4	5	6	7	8	9	10	11	12	13	14	15	16	17	18	19	20
1	6.61	7.61	7.50	6.44	7.40	7.29	6.62	6.46	7.08	7.26	6.43	7.03	7.31	7.25	6.55	7.11	6.74	6.59	6.23	6.12
2	6.46	7.21	5.67	7.31	7.04	7.71	7.33	7.86	6.78	7.41	7.45	7.52	6.77	7.26	6.76	7.14	6.79	6.60	6.34	6.36
3	6.68	7.11	6.53	6.86	7.11	6.89	6.33	7.13	7.08	7.69	7.44	7.35	7.14	7.00	6.00	6.20	7.52	6.94	6.37	6.24
4	6.29	6.78	6.56	6.43	6.60	6.55	6.81	6.64	6.99	7.05	6.94	7.54	6.55	6.38	7.04	6.58	7.32	6.88	7.25	6.21
5	6.22	5.75	6.89	6.49	6.33	5.89	6.43	7.58	7.48	6.66	6.72	6.26	7.39	6.97	7.25	6.84	7.00	6.75	6.31	6.90
6	7.22	7.14	6.92	7.62	6.26	6.33	6.23	6.82	6.77	7.33	6.69	6.95	6.77	6.44	6.59	6.84	7.18	7.17	5.64	7.10
7	6.58	5.75	6.26	7.03	6.29	6.34	7.46	6.56	7.42	7.05	7.44	6.36	6.34	5.99	7.38	6.28	6.94	6.41	7.58	6.23
8	6.85	6.76	6.53	6.38	6.15	7.28	7.28	6.42	7.52	6.98	7.25	7.39	6.75	6.67	6.07	6.83	6.54	6.21	6.25	6.17
9	6.13	5.57	6.48	7.43	6.69	6.40	6.57	6.49	7.30	6.92	6.66	6.32	6.78	6.40	7.28	6.60	6.66	6.43	6.37	6.37
10	6.74	7.02	6.29	7.20	7.28	6.81	7.04	6.16	6.40	7.46	6.81	6.81	6.18	6.87	7.28	7.16	7.37	6.07	6.50	6.71
11	6.13	6.89	6.55	6.83	7.19	6.29	6.86	6.95	6.94	6.64	7.40	6.78	7.01	6.98	7.39	6.38	6.49	5.98	6.23	6.67
12	6.76	7.05	6.13	7.10	6.89	6.10	6.43	6.59	6.68	6.48	7.19	5.99	6.47	7.40	6.32	6.96	6.56	7.25	6.20	5.73
13	6.03	7.28	6.36	6.39	7.00	6.86	7.47	7.01	6.12	6.58	7.29	4.96	6.52	5.95	6.39	6.99	7.01	6.13	6.66	6.29
14	6.83	7.00	6.33	6.82	6.50	6.15	6.79	7.03	7.04	6.04	7.13	7.25	6.91	6.45	7.29	6.15	5.76	6.48	6.10	6.38
15	6.46	6.97	6.57	7.52	6.53	6.44	6.24	6.06	6.77	7.02	6.77	7.03	6.53	6.44	6.17	6.04	6.24	6.84	6.88	6.50
16	6.74	6.47	6.22	6.02	6.29	6.92	6.70	6.33	6.72	7.08	6.59	6.78	7.00	6.34	6.49	6.75	6.77	6.28	6.35	6.98
17	7.01	6.55	6.29	6.67	7.77	6.23	6.71	6.41	7.15	7.09	7.15	6.53	7.40	6.66	7.11	6.75	6.05	6.68	6.16	7.44
18	6.62	6.98	6.25	5.97	6.63	6.79	6.26	6.50	7.35	7.24	6.60	6.10	6.90	7.13	7.01	6.66	6.89	6.77	6.34	7.17
19	6.23	6.79	6.84	6.22	6.93	6.50	6.91	7.64	7.03	6.88	6.32	6.86	7.02	6.23	7.42	6.94	6.12	5.90	6.42	6.00
20	6.05	7.43	6.63	7.15	6.84	7.12	6.41	6.43	7.53	6.54	6.04	6.70	6.56	5.85	6.46	7.17	6.27	6.37	6.58	7.68
21	6.80	7.50	6.57	6.72	6.53	7.33	7.81	6.71	7.31	6.53	6.95	7.12	6.39	6.71	6.34	7.32	6.79	6.66	6.36	5.50
22	6.43	5.92	6.05	7.05	6.42	6.67	7.60	6.75	6.27	7.26	6.65	6.56	6.75	6.93	6.78	6.65	5.99	6.51	6.17	6.18
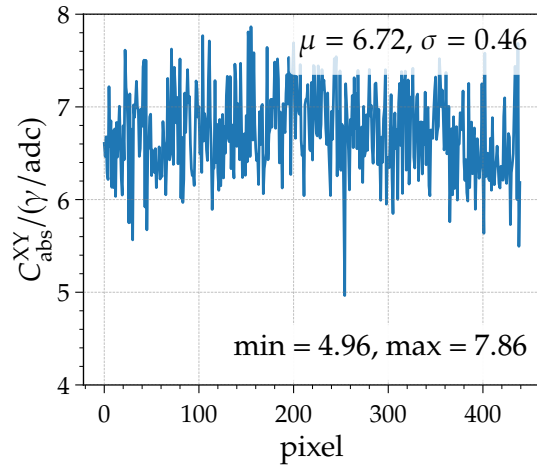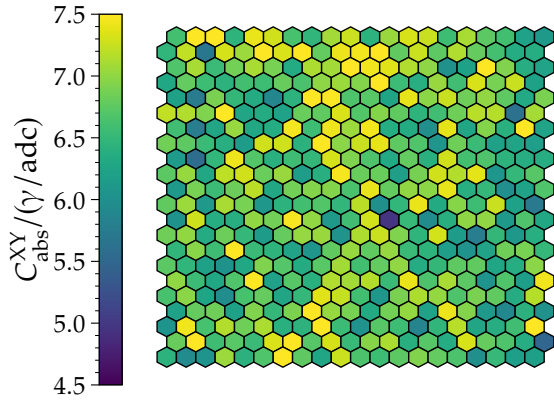
CO6 2022-10-22

col / row	1	2	3	4	5	6	7	8	9	10	11	12	13	14	15	16	17	18	19	20
1	6.06	5.27	5.29	5.13	5.35	6.08	5.19	5.74	6.04	5.14	5.38	6.01	4.65	5.06	5.53	5.61	5.69	4.82	5.40	5.97
2	5.59	5.82	5.65	5.38	5.71	5.81	5.28	5.17	5.80	5.47	5.87	6.35	5.45	5.90	5.77	5.34	6.00	5.28	5.82	6.01
3	5.41	5.36	5.14	5.68	5.49	5.31	5.49	5.94	5.99	5.69	5.01	5.95	4.54	5.48	5.80	5.64	5.53	6.00	5.02	5.36
4	5.63	5.80	6.02	5.38	5.48	5.58	4.88	5.91	6.16	6.23	5.71	5.41	5.52	5.38	5.06	5.72	5.36	5.38	5.98	5.86
5	6.12	6.11	6.08	4.91	5.99	5.99	5.07	5.48	5.64	5.86	6.11	5.27	5.47	5.25	5.82	4.66	5.16	5.05	4.95	5.38
6	5.08	5.43	5.92	5.37	5.64	5.92	5.34	5.31	4.92	6.19	5.79	5.69	4.90	5.41	4.85	5.29	6.55	4.53	5.99	5.49
7	4.96	6.28	5.39	5.03	5.93	5.60	5.19	5.13	6.08	5.01	5.63	5.73	5.20	6.34	5.29	5.28	5.08	5.33	5.54	4.87
8	5.90	5.79	5.20	5.33	5.25	6.05	5.22	5.57	5.55	5.98	6.09	5.77	4.60	5.27	6.00	5.29	5.79	4.99	5.77	5.59
9	6.50	5.08	5.10	5.85	5.55	5.55	5.37	5.50	5.45	4.99	5.91	5.86	5.04	5.73	5.40	5.51	6.07	5.33	5.47	5.59
10	5.81	6.44	5.50	4.62	5.96	5.81	5.07	5.36	6.42	4.87	5.55	5.43	5.44	5.05	5.72	5.40	4.71	5.43	5.07	5.35
11	5.95	5.16	5.40	5.04	6.04	5.42	5.19	5.23	5.87	5.82	6.07	5.42	5.57	5.29	5.07	5.85	5.24	4.61	4.48	5.57
12	5.67	5.49	5.20	5.83	5.29	5.29	4.99	5.53	5.40	5.52	6.03	5.75	6.05	5.26	6.01	5.90	5.41	6.13	4.86	5.50
13	5.43	5.31	5.78	4.93	6.05	5.51	4.95	5.27	4.92	5.28	5.36	4.82	5.49	5.25	5.61	5.62	4.98	5.07	6.05	5.07
14	5.62	5.05	5.68	5.32	5.68	5.98	4.85	5.88	5.06	5.10	5.41	4.51	5.26	6.20	5.32	4.77	5.84	6.27	5.72	5.15
15	5.52	5.41	5.35	5.65	5.60	5.82	4.95	4.72	6.62	5.14	5.90	4.65	5.77	5.16	5.57	5.40	5.17	6.01	5.05	5.30
16	5.20	5.60	5.96	5.43	5.00	6.07	5.36	5.39	6.02	6.17	5.69	5.70	5.96	5.96	4.94	5.04	6.17	5.65	5.73	5.15
17	5.53	4.98	5.82	5.97	5.48	5.74	5.32	5.09	5.30	5.47	5.81	5.00	5.12	5.60	4.96	5.91	6.15	6.14	5.94	6.34
18	5.77	4.89	5.70	5.73	5.43	5.21	5.40	5.11	5.21	5.82	6.05	4.72	5.31	5.36	5.33	5.60	5.98	5.90	5.31	5.16
19	5.75	5.42	5.19	5.84	4.93	5.21	5.30	4.91	4.94	5.71	5.53	5.80	6.17	5.78	5.72	5.27	5.34	6.26	5.16	5.62
20	5.27	5.74	6.19	5.64	4.89	5.94	5.42	6.31	5.62	5.94	5.43	6.03	6.06	6.35	5.34	5.61	6.24	6.01	5.66	5.59
21	5.03	5.18	5.64	6.08	5.85	5.35	5.84	5.83	5.52	5.83	5.74	5.69	5.75	6.10	5.74	5.35	4.97	6.32	6.40	4.57
22	5.48	5.16	6.18	6.03	4.07	5.43	4.85	6.35	4.37	5.32	5.57	6.13	5.02	5.22	6.22	6.22	6.01	5.65	5.98	6.16
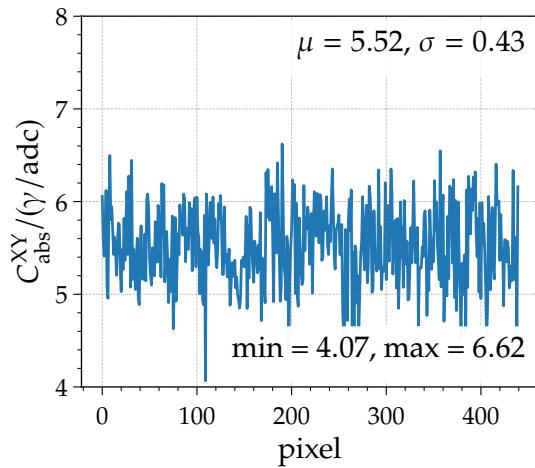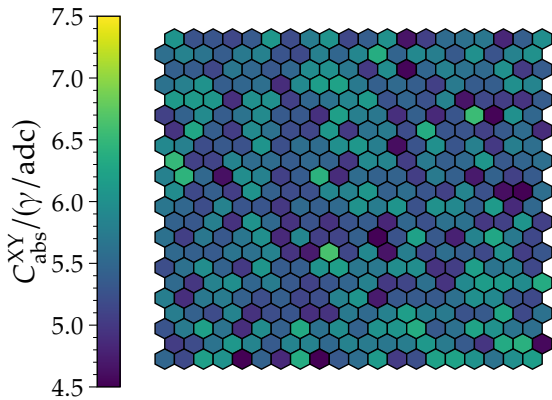
HE1 2022-10-21

col / row	1	2	3	4	5	6	7	8	9	10	11	12	13	14	15	16	17	18	19	20
1	4.74	3.30	3.83	4.53	4.51	4.24	4.54	3.43	5.25	4.05	5.17	3.94	5.32	4.78	3.67	4.20	5.26	4.82	5.74	6.26
2	3.70	4.45	4.90	5.05	4.61	4.65	4.63	4.52	4.53	4.19	4.68	4.28	3.90	4.83	4.49	4.70	5.20	5.52	4.82	5.10
3	4.28	4.89	4.23	4.75	5.11	5.14	4.63	3.85	4.58	4.67	4.76	4.02	4.87	5.16	4.53	3.71	5.01	5.91	5.49	4.86
4	4.09	3.90	4.27	4.49	4.40	4.33	4.97	3.90	4.61	4.43	4.39	4.60	4.82	4.45	4.06	3.96	6.25	5.65	4.69	4.67
5	5.29	3.41	4.76	5.17	4.40	4.90	4.90	4.37	4.70	3.33	1.54	4.41	4.12	4.80	3.52	5.39	6.10	4.85	5.83	3.61
6	4.27	3.68	4.22	5.05	5.16	4.80	4.25	3.92	3.86	4.30	4.10	4.92	4.13	5.43	4.38	4.56	6.15	5.53	5.10	5.62
7	3.75	4.02	3.80	4.77	4.58	4.06	3.88	4.10	5.07	4.18	3.67	4.96	3.91	4.12	3.73	3.47	4.92	4.86	6.75	3.63
8	3.76	3.79	5.57	4.92	5.51	4.69	4.30	5.07	4.51	4.20	4.30	5.27	3.83	5.20	4.29	4.13	5.32	5.23	7.23	4.36
9	3.69	3.59	4.40	3.63	4.14	4.16	4.46	3.76	4.04	3.62	4.82	5.17	4.18	4.94	4.07	4.59	5.73	5.67	5.97	3.75
10	3.79	3.50	5.02	4.93	3.60	4.11	4.06	4.00	4.31	4.33	5.83	5.14	3.86	4.50	3.95	4.10	6.12	4.67	6.49	4.72
11	3.65	3.56	4.87	4.31	3.69	4.64	4.13	4.36	4.95	3.84	3.96	4.88	4.59	5.02	4.09	3.44	5.91	5.02	5.44	4.38
12	3.52	4.20	4.39	4.28	4.41	4.19	3.46	4.37	5.00	3.77	4.92	5.38	4.49	4.36	4.40	3.73	3.39	4.56	4.42	4.16
13	4.59	4.20	4.11	3.89	4.06	4.50	4.38	4.48	5.16	4.28	4.34	3.77	3.53	3.50	4.08	2.88	5.47	4.47	4.57	4.64
14	4.76	3.62	5.04	3.83	4.90	4.66	4.41	4.34	5.03	4.73	5.02	3.74	4.20	4.21	3.57	3.53	3.96	3.79	3.85	5.50
15	4.46	4.16	4.37	4.83	4.81	5.51	4.30	4.87	4.64	3.35	4.24	4.82	3.65	4.11	4.11	4.53	4.59	5.43	4.07	4.40
16	3.10	3.71	4.01	4.23	4.57	4.77	4.09	4.03	6.16	4.40	3.45	3.84	4.66	4.87	3.82	3.89	4.29	4.85	4.39	4.76
17	3.94	3.24	3.72	4.20	4.51	4.02	3.26	4.28	5.01	8.27	4.03	4.07	3.96	3.59	3.17	4.51	4.57	4.47	4.44	5.23
18	4.81	4.29	4.54	3.16	6.02	4.96	3.34	5.63	5.24	4.39	3.90	4.36	3.79	4.48	3.46	3.79	4.22	5.04	3.71	4.26
19	4.09	3.67	3.88	4.70	4.82	3.99	3.48	4.83	5.10	3.73	5.38	3.64	3.57	4.12	126.01	3.47	4.03	4.06	5.60	4.02
20	4.67	4.22	3.70	4.39	5.00	3.69	3.95	4.29	6.01	3.35	5.13	4.70	3.55	4.20	3.93	1.85	4.46	5.31	4.01	4.16
21	4.60	4.22	4.36	4.28	3.77	3.49	4.60	4.48	4.69	4.71	5.13	4.31	3.64	4.38	3.33	3.25	5.37	4.96	4.60	2.85
22	4.83	3.81	4.76	4.21	4.63	3.61	4.35	4.23	5.31	5.19	5.29	5.09	5.18	4.08	4.65	3.83	5.61	5.87	4.02	9.48

$\mu = 4.73$, $\sigma = 5.84$

$\text{min} = 1.54$, $\text{max} = 126.01$
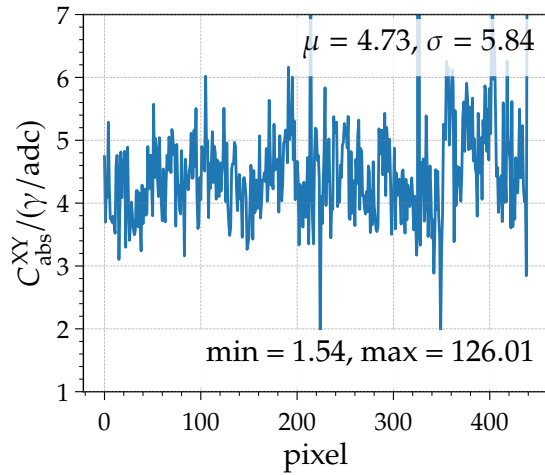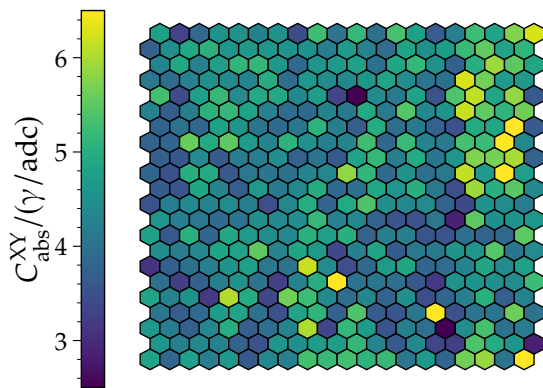
Appendix A. Appendix

HE2 2022-10-21

col / row	1	2	3	4	5	6	7	8	9	10	11	12	13	14	15	16	17	18	19	20
1	2.77	3.27	3.31	3.58	3.37	4.34	3.39	3.72	4.29	4.03	3.83	4.16	4.05	4.50	4.25	3.22	3.60	3.70	3.14	2.93
2	3.50	3.69	3.48	3.10	3.01	3.38	2.83	3.69	3.81	4.39	3.84	3.85	3.73	4.28	3.73	3.49	3.69	3.43	3.36	3.32
3	3.34	2.95	3.70	3.44	3.76	3.42	3.80	4.36	3.84	4.42	3.70	4.24	4.02	3.86	3.81	6.99	3.46	3.72	4.01	3.33
4	3.26	3.06	3.89	3.82	3.60	3.76	3.43	4.33	4.02	3.94	4.50	4.68	3.72	4.38	4.33	3.67	3.40	3.20	3.86	3.54
5	3.26	3.63	3.19	4.34	3.96	3.20	3.54	3.83	4.19	3.87	4.32	3.76	3.51	4.91	4.37	3.27	3.65	3.62	3.55	3.54
6	3.67	3.43	3.31	3.67	3.33	3.68	3.73	4.90	4.33	4.93	4.26	4.04	3.28	4.06	4.09	3.67	3.76	3.43	3.80	3.72
7	3.22	3.54	3.90	3.88	3.53	4.04	3.37	4.46	4.34	3.72	4.37	4.18	3.68	4.41	4.35	3.97	4.09	3.79	3.77	3.22
8	3.29	3.79	4.29	2.64	4.27	4.39	3.82	4.09	4.23	4.32	4.25	4.43	4.07	4.78	4.37	4.01	3.66	3.38	3.68	3.21
9	3.71	3.34	3.51	2.98	4.25	3.24	4.89	3.84	3.02	4.23	4.50	4.50	3.64	4.07	4.07	3.52	3.64	3.75	3.81	3.25
10	3.44	3.36	4.20	3.03	3.46	4.42	3.40	4.49	4.92	3.36	3.99	4.19	3.83	3.91	4.66	4.37	3.75	3.26	3.07	3.29
11	3.94	4.01	3.96	3.55	3.87	4.30	3.34	4.08	4.02	3.56	4.26	4.05	3.63	4.19	4.58	4.16	3.79	3.51	3.21	3.23
12	3.10	3.63	3.54	3.33	4.56	3.37	4.28	2.89	3.98	3.48	3.67	3.77	3.29	3.13	3.68	3.44	3.55	3.40	3.40	4.38
13	3.08	3.18	3.20	2.44	4.64	3.51	3.25	3.17	3.19	3.75	4.15	4.06	3.59	4.45	3.58	3.67	3.32	3.91	4.33	3.26
14	3.50	3.17	3.33	3.22	4.89	4.03	3.51	3.48	4.80	3.73	3.38	3.73	3.71	3.14	3.99	3.35	3.70	3.93	4.35	3.04
15	3.20	3.17	3.39	3.25	3.68	3.02	3.67	3.34	3.81	3.71	3.63	4.07	4.06	3.62	2.84	3.67	3.29	3.18	4.24	3.59
16	4.52	2.98	3.71	2.84	4.49	3.96	3.08	3.71	4.40	3.71	3.81	3.75	3.43	3.90	3.90	3.72	3.88	3.33	3.48	3.67
17	3.52	3.23	3.12	2.54	3.99	3.77	4.36	3.78	4.25	4.34	3.52	3.51	3.77	3.79	3.97	3.81	3.29	3.45	3.50	4.29
18	4.18	2.94	3.41	4.28	3.49	3.34	4.37	3.50	3.51	3.51	4.11	3.33	3.34	3.48	3.52	3.90	3.24	3.77	4.65	4.12
19	3.41	4.22	3.62	2.68	3.99	4.19	4.83	3.27	4.08	3.21	3.63	3.20	3.43	3.16	3.97	3.90	2.73	3.40	4.40	3.68
20	3.31	4.23	3.61	2.96	3.92	3.50	4.17	3.64	3.92	4.37	3.16	2.45	3.32	3.06	3.10	3.54	2.81	3.54	3.66	3.49
21	3.82	2.89	2.90	2.53	4.54	3.39	3.63	3.21	4.04	4.12	4.04	3.52	3.14	3.35	3.41	3.82	3.76	3.88	3.27	3.85
22	2.77	3.72	4.05	2.88	4.65	3.75	3.67	3.39	3.32	3.45	2.86	3.70	3.41	3.39	3.79	3.89	3.38	3.53	3.39	3.70
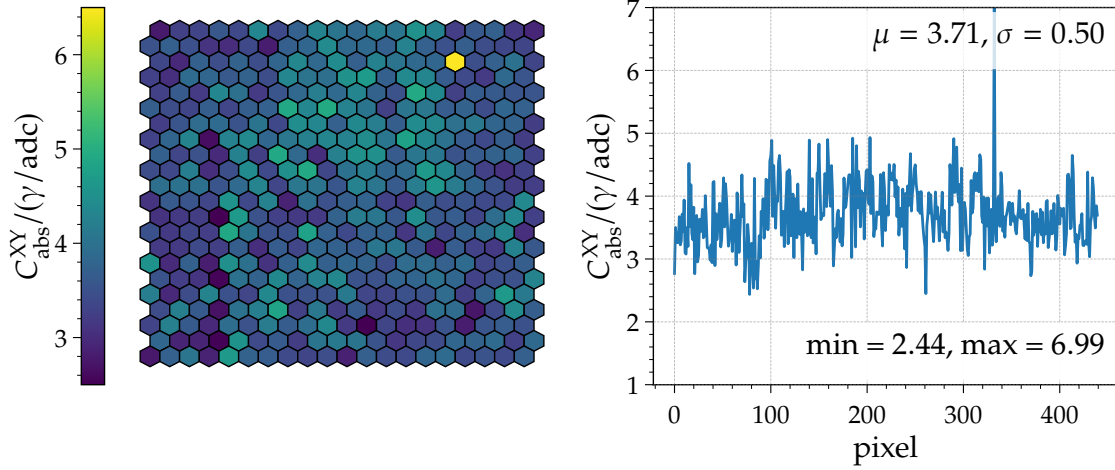
HE3 2022-10-21

$\frac{\text{col}}{\text{row}}$	1	2	3	4	5	6	7	8	9	10	11	12	13	14	15	16	17	18	19	20
1	4.78	4.12	4.20	4.69	4.15	4.86	4.47	4.47	4.06	4.38	3.83	4.52	4.71	3.90	5.05	3.83	3.28	4.10	4.56	3.50
2	4.09	4.22	4.50	3.34	4.59	3.90	4.35	3.85	4.79	4.48	3.58	4.09	4.24	4.25	6.03	4.93	3.94	3.96	3.79	4.34
3	4.66	3.85	4.47	3.95	4.78	4.31	4.08	4.18	4.65	4.60	4.27	4.46	4.63	4.61	4.01	4.90	3.18	3.40	3.99	3.65
4	4.42	4.06	3.74	4.06	4.10	4.26	4.04	3.65	3.85	3.37	4.19	4.72	4.37	4.80	4.20	4.02	4.09	3.17	3.95	4.35
5	4.42	4.19	4.40	3.72	3.92	4.23	4.34	4.21	4.33	3.83	4.54	4.50	4.92	4.63	5.07	4.78	3.92	3.93	3.65	4.59
6	4.22	4.03	3.95	4.82	3.56	4.33	3.96	3.69	4.13	3.67	3.88	4.55	3.80	4.52	5.41	4.58	3.86	3.88	3.88	4.15
7	4.43	4.59	4.29	3.72	4.15	4.11	3.82	4.16	3.76	3.61	4.57	4.27	4.56	4.09	6.02	4.51	4.89	3.61	3.37	3.50
8	4.38	4.44	3.84	3.91	4.05	4.04	4.30	3.88	4.77	4.55	4.29	3.89	3.70	4.75	6.03	5.58	3.81	3.76	3.64	3.22
9	3.78	3.86	3.65	4.26	4.33	3.99	3.94	4.30	4.41	3.46	4.35	4.04	4.28	4.57	4.56	5.09	3.66	3.78	4.88	4.11
10	4.65	3.58	3.65	3.78	4.38	4.10	3.86	4.32	3.96	4.20	4.10	4.73	3.76	5.10	5.04	4.75	4.21	3.50	3.56	3.84
11	4.58	4.51	4.13	3.69	3.60	4.62	3.98	4.67	4.51	3.66	3.94	4.16	4.57	4.90	4.45	4.41	3.87	4.42	4.39	3.71
12	4.75	4.06	4.44	4.67	4.28	4.16	4.34	4.29	4.56	4.46	3.89	4.27	3.65	4.51	4.60	3.54	5.29	6.86	4.93	6.19
13	3.83	3.89	4.69	4.29	4.38	4.30	4.20	4.28	4.25	4.54	4.11	3.87	4.20	4.98	5.46	5.03	5.35	5.23	5.90	5.98
14	4.01	4.12	4.62	4.12	3.80	4.53	4.24	3.64	4.71	4.37	4.37	4.17	4.96	4.38	3.97	4.31	5.42	5.46	5.84	6.69
15	4.57	4.17	4.69	4.28	4.39	4.25	4.69	3.96	4.29	4.65	4.20	4.77	4.31	5.27	5.08	4.59	6.69	5.43	5.25	5.68
16	4.35	4.26	4.46	5.02	4.57	3.99	4.77	4.43	3.81	3.93	4.48	4.47	5.05	4.48	5.00	4.77	6.45	5.82	4.71	5.99
17	4.25	4.03	4.59	4.15	3.78	4.77	4.13	3.55	4.65	4.17	4.02	4.59	4.55	4.81	5.19	4.97	6.55	7.87	5.51	6.09
18	4.31	4.18	4.47	4.89	4.15	3.93	4.91	4.27	4.77	4.88	4.30	3.73	3.54	4.63	4.32	4.49	6.61	5.17	5.42	5.39
19	4.14	4.46	4.40	4.26	4.24	4.74	4.41	4.60	4.38	4.36	5.12	4.18	4.92	5.02	4.96	4.83	5.99	6.06	5.41	6.00
20	4.76	4.64	4.51	4.97	3.99	4.15	4.01	3.65	4.62	4.60	5.33	4.25	4.62	4.24	5.23	3.54	5.64	5.02	6.68	4.22
21	3.15	3.80	4.55	3.92	4.01	4.46	4.86	4.43	4.55	4.11	4.45	3.82	4.37	4.27	4.39	4.25	5.74	5.70	5.05	7.18
22	4.28	4.50	4.81	4.46	4.73	4.37	4.51	4.85	4.22	3.94	4.66	4.94	4.76	4.45	5.50	5.18	6.64	5.30	5.70	6.68

$\mu = 4.45, \sigma = 0.67$

$\text{min} = 3.15, \text{max} = 7.87$
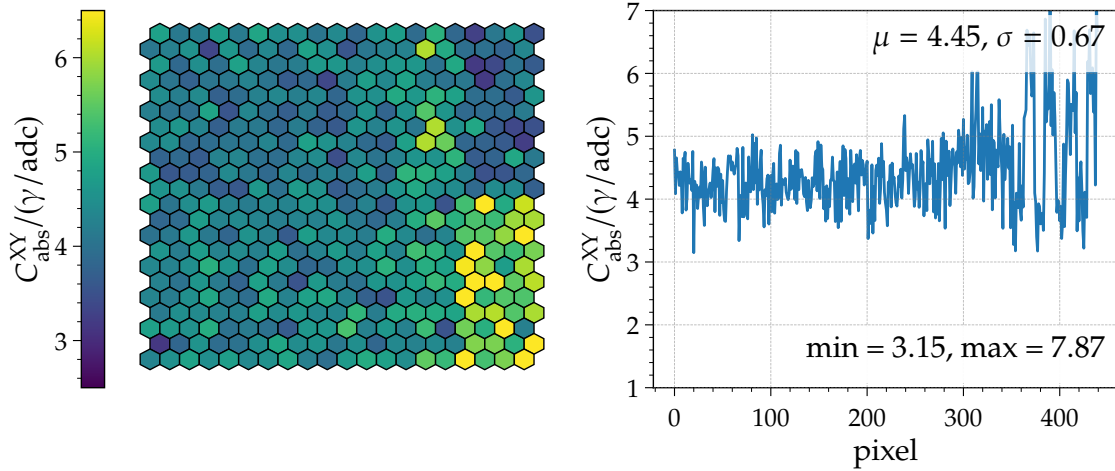
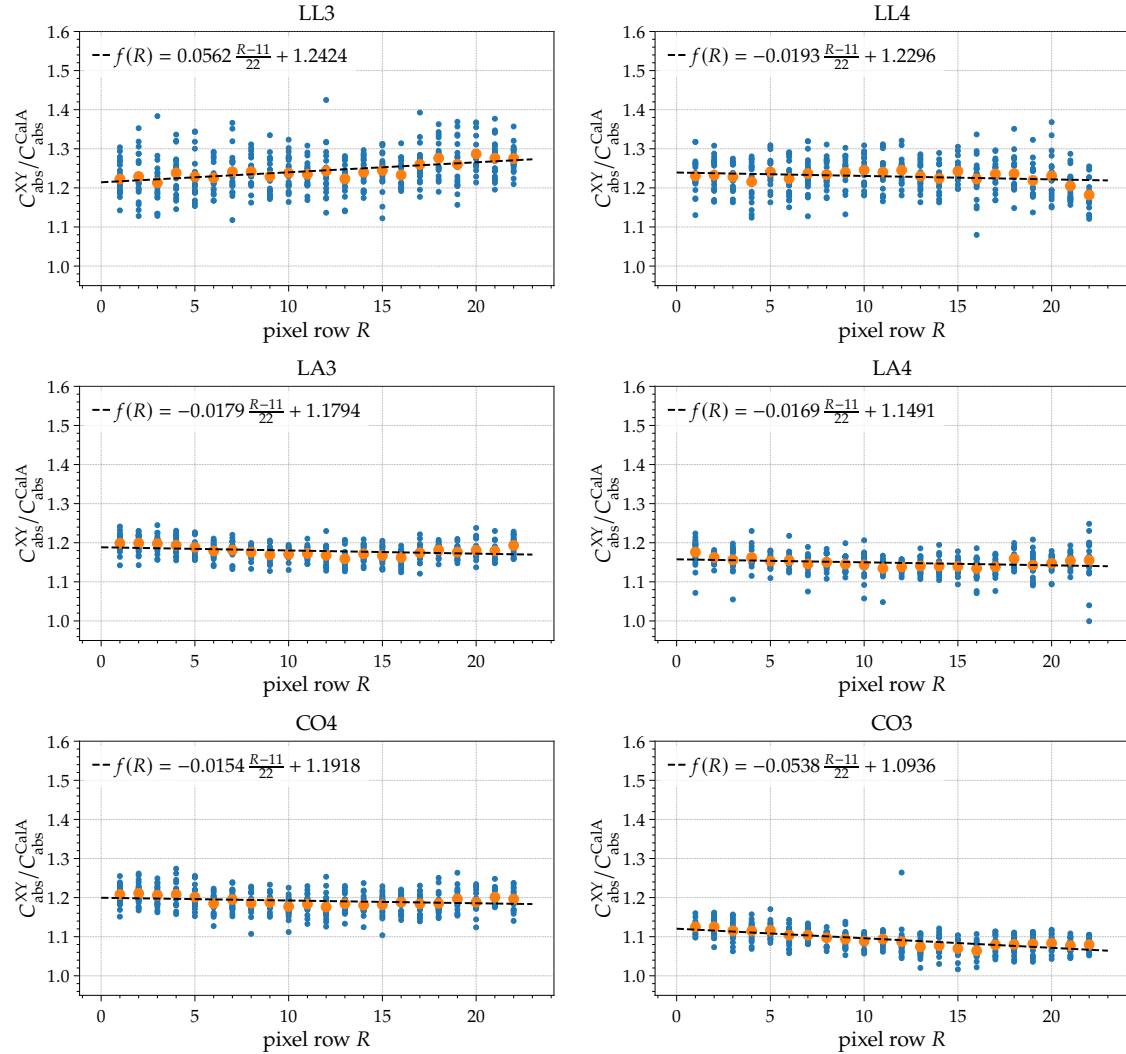## A.8. ELEVATION DEPENDENCY OF TELESCOPE AGING

Figure A.18: Ratio between the XY-Scanner calibration and the standard calibration with Cal A tracking as a function of the pixel row. Individual pixel ratios are shown in blue, the mean per pixel row in orange, and a linear fit is shown as a black line. Different telescopes are shown in different plots. Measurements were performed in the Autumn 2019 campaign with the Olomouc sphere.

We estimate the elevation dependent aging of the telescopes by comparing the absolute end-to-end calibration of the XY-Scanner measurements from Autumn 2019 with the standard tracked calibration obtained with the relative calibration system. In Figs. A.18 and A.19 we show the ratio between the two calibrations as a function of the pixel row in the telescope camera. We estimate the vertical gradient of the aging by fitting a linear function to the data. The slopes of the fitted functions are plotted in the bottom plot of Fig. A.19. For six of the 10 investigated telescopes we observe a negative slope, while the remaining four show a positive slope.

The particularly large slope observed for the HE3 telescope may indicate an increased accumulation of dust on the lower part of the mirror, due to the tilted operation of HEAT. Note that the pixels in the lower camera rows observe the lower part of the mirror. However, on the other hand, for the HE1 telescope we observe a slope, which is compatible with zero, weakening the

Figure A.19: *Top:* Similar plots as shown in Fig. A.18. *Bottom:* The fitted slopes of the gradient for all telescopes shown above.

above made argument.

Appendix A. Appendix

ACKNOWLEDGMENTS

"For the Quest is achieved, and now all is over. I am glad you are here with me. Here at the end of all things, Sam." [120]

Typeset with LaTeX[121].
Analysis performed with C++ and python [122, 123].
Plots and illustrations created using Matplotlib and Inkscape [124, 125] .

BIBLIOGRAPHY

[1] T. K. Gaisser, R. Engel, and E. Resconi, *Cosmic Rays and Particle Physics*. Cambridge University Press, 2 ed., 2016.

[2] R. Engel, D. Heck, and T. Pierog, "Extensive air showers and hadronic interactions at high energy," *Annual Review of Nuclear and Particle Science*, vol. 61, no. 1, pp. 467–489, 2011.

[3] A. Haungs, et. al., "KCDC — the KASCADE cosmic-ray data centre," *Journal of Physics: Conference Series*, vol. 632, p. 012011, 2015.

[4] J. Matthews, "A heitler model of extensive air showers," *Astroparticle Physics*, vol. 22, no. 5, pp. 387–397, 2005.

[5] W. Heitler, *The Quantum Theory of Radiation*. Clarendon Press, 1944.

[6] T. K. Gaisser and A. M. Hillas, "Reliability of the Method of Constant Intensity Cuts for Reconstructing the Average Development of Vertical Showers," in *International Cosmic Ray Conference*, vol. 8 of *International Cosmic Ray Conference*, p. 353, 1977.

[7] M. Ave, et. al., "Spectrally resolved pressure dependence measurements of air fluorescence emission with airfly," *Nuclear Instruments and Methods in Physics Research Section A: Accelerators, Spectrometers, Detectors and Associated Equipment*, vol. 597, no. 1, pp. 41–45, 2008. Proceedings of the 5th Fluorescence Workshop.

[8] T. Waldenmaier, *Spectral Resolved Measurement of the Nitrogen Fluorescence Yield in Air induced by Electrons*. PhD thesis, 2006. Auger internal publication, GAP2006_011.

[9] T. Waldenmaier, J. Blümer, and H. Klages, "Spectral resolved measurement of the nitrogen fluorescence emissions in air induced by electrons," *Astroparticle Physics*, vol. 29, no. 3, pp. 205–222, 2008.

[10] J. Abraham, P. Abreu, M. Aglietta, C. Aguirre, E. Ahn, D. Allard, I. Allekotte, J. Allen, P. Allison, J. Alvarez-Muniz, and et al., "The fluorescence detector of the Pierre Auger Observatory," *Nuclear Instruments and Methods in Physics Research Section A: Accelerators, Spectrometers, Detectors and Associated Equipment*, vol. 620, no. 2-3, pp. 227–251, 2010.

[11] A. Aab, et. al., "Data-driven estimation of the invisible energy of cosmic ray showers with the Pierre Auger Observatory," *Phys. Rev. D*, vol. 100, p. 082003, Oct 2019.

[12] Particle Data Group, "Review of Particle Physics," *Progress of Theoretical and Experimental Physics*, vol. 2022, no. 8, 2022. 083C01.

[13] Y. Tsunesada on behalf of the Pierre Auger and the Telescope Array Collaboration, "Joint analysis of the energy spectrum of ultra-high-energy cosmic rays as measured at the Pierre Auger Observatory and the Telescope Array," in *Proceedings of 37th International Cosmic Ray Conference — PoS(ICRC2021)*, vol. 395, p. 337, 2021.

Bibliography

[14] "The Pierre Auger Cosmic Ray Observatory," *Nuclear Instruments and Methods in Physics Research Section A: Accelerators, Spectrometers, Detectors and Associated Equipment*, vol. 798, pp. 172 – 213, 2015.

[15] H. Kawai, et. al., "Telescope Array Experiment," *Nuclear Physics B - Proceedings Supplements*, vol. 175-176, pp. 221–226, 2008. Proceedings of the XIV International Symposium on Very High Energy Cosmic Ray Interactions.

[16] T. Abu-Zayyad, et. al., "The surface detector array of the Telescope Array experiment," *Nuclear Instruments and Methods in Physics Research Section A: Accelerators, Spectrometers, Detectors and Associated Equipment*, vol. 689, pp. 87–97, 2012.

[17] H. Tokuno, et. al., "New air fluorescence detectors employed in the Telescope Array experiment," *Nuclear Instruments and Methods in Physics Research Section A: Accelerators, Spectrometers, Detectors and Associated Equipment*, vol. 676, pp. 54–65, 2012.

[18] en.wikipedia.org/wiki/File:Southamerica_blank.svg, accessed March 2023.

[19] I. Allekotte, et al., "The surface detector system of the pierre auger observatory," *Nuclear Instruments and Methods in Physics Research Section A: Accelerators, Spectrometers, Detectors and Associated Equipment*, vol. 586, no. 3, pp. 409–420, 2008.

[20] Pierre Auger Collaboration. Flickr Photos.

[21] The Pierre Auger Collaboration, "The Pierre Auger Observatory Upgrade - Preliminary Design Report," 2016. arXiv:1604.03637.

[22] The Pierre Auger Collaboration, "Techniques for measuring aerosol attenuation using the Central Laser Facility at the Pierre Auger Observatory," *Journal of Instrumentation*, vol. 8, no. 04, p. P04009, 2013.

[23] M. Unger, "Mass sensitive observables of the Pierre Auger Observatory," *EPJ Web of Conferences*, vol. 53, p. 04009, 2013.

[24] A. Aab, et al., "Reconstruction of events recorded with the surface detector of the Pierre Auger Observatory," *Journal of Instrumentation*, vol. 15, no. 10, p. P10021, 2020.

[25] The Pierre Auger collaboration, "Reconstruction of inclined air showers detected with the Pierre Auger Observatory," *Journal of Cosmology and Astroparticle Physics*, vol. 2014, no. 08, p. 019, 2014.

[26] A. Aab, et. al., "Measurement of the cosmic-ray energy spectrum above 2.5×10^{18} eV using the Pierre Auger Observatory," *Phys. Rev. D*, vol. 102, p. 062005, 2020.

[27] V. Novotny on behalf of the Pierre Auger Collaboration, "Energy spectrum of cosmic rays measured using the Pierre Auger Observatory," in *Proceedings of 37th International Cosmic Ray Conference — PoS(ICRC2021)*, vol. 395, p. 324, 2021.

[28] Schott Glaswerke, Mainz, Germany. http://www.schott.com, accessed May 2020.

[29] R. Sato and C. O. Escobar, "The performance of the corrector lenses for the Auger fluorescence detector," in *29th International Cosmic Ray Conference*, 2005.

[30] C. Aramo, F. Bracci, G. Gallo, et al., "The camera of the AUGER Fluorescence Detector," *Auger internal publication*, 1999. GAP1999_027.

[31] PHOTONIS. http://www.photonis.com.

[32] M. Giller, J.L. Kacperski, W. Tkaczyk and G. Wieczorek, "Angular Directions of Pixels in the FD Camera," *Auger internal publication*, 2000. GAP2000_032.

[33] Z. Szadkowski, "Second-level trigger in the Pierre Auger Fluorescence Detector," *Nuclear Instruments and Methods in Physics Research Section A: Accelerators, Spectrometers, Detectors and Associated Equipment*, vol. 465, no. 2, pp. 540–549, 2001.

[34] H. Gemmeke for the Pierre Auger Observatory Collaboration, "The Auger Fluorescence Detector Electronics," in *Proceedings of 27th International Cosmic Ray Conference*, 2001. link.

[35] M. Kleifges, "The fluorescene detector electronics of the Pierre Auger Observatory," *Nuclear Instruments and Methods in Physics Research Section A: Accelerators, Spectrometers, Detectors and Associated Equipment*, vol. 518, no. 1, pp. 180–182, 2004. Frontier Detectors for Frontier Physics: Proceedin.

[36] Viviana Scherini, Heiko Geenen, K-H. Kampert, Lorenzo Perrone and Simon Robbins, "The Virtual Channel Reloaded," *Auger internal publication*, 2006. GAP2006_104.

[37] D. Tcherniakhovski, *First Level Trigger Module. – User manual*. Institute of Data Processing and Electronics (IPE), Forschungszentrum Karlsruhe, 3.0 ed., 2002. link.

[38] A. Schmidt, T. Asch, H. Gemmeke, M. Kleifges, H.-J. Mathes, A. Menchikov, F. Schüssler, and D. Tcherniakhovski, "Third level trigger for the fluorescence telescopes of the Pierre Auger Observatory," *Nuclear Instruments and Methods in Physics Research Section A: Accelerators, Spectrometers, Detectors and Associated Equipment*, vol. 601, no. 3, pp. 347–353, 2009.

[39] A. Criss, et. al., "Update on Recent Absolute Calibration Work." Talk at the Auger Collaboration Meeting in March 2010.

[40] L. Tomankova, *Optical Properties and Calibration of the Pierre Auger Fluorescence Detector*. PhD thesis, 2017. Auger internal publication, GAP2017_017.

[41] J. Brack, R. Meyhandan, G. Hofman, and J. Matthews, "Absolute photometric calibration of large aperture optical systems," *Astroparticle Physics*, vol. 20, no. 6, pp. 653 – 659, 2004.

[42] J. T. Brack, R. Cope, A. Dorofeev, B. Gookin, J. L. Harton, Y. Petrov, and A. C. Rovero, "Absolute calibration of a large-diameter light source," *Journal of Instrumentation*, vol. 8, no. 05, pp. P05014–P05014, 2013.

[43] J. Brack, R. Cope, A. Dorofeev, B. Gookin, J. Harton, Y. Petrov, A. Rovero, R. Bruijn, A. Criss, P. Sommers, A. Menshikov, G. La Rosa, "Auger Fluorescence Detector Absolute Calibration January and June 2010," *Auger internal publication*, 2010. GAP2010_118.

[44] A. Dorofeev, B. Gookin, J. Brack, J. Harton, V. Prestes Luzio, M. del Rio, "FD Absolute Calibration, April 2013," *Auger internal publication*, 2013. GAP2013_058.

[45] A. Rovero, P. Bauleo, J. Brack, J. Harton, and R. Knapik, "Multi-wavelength calibration procedure for the Pierre Auger Observatory Fluorescence Detectors," *Astroparticle Physics*, vol. 31, no. 4, pp. 305–311, 2009.

[46] A. Aab, et. al., "Spectral calibration of the fluorescence telescopes of the Pierre Auger Observatory," *Astroparticle Physics*, vol. 95, pp. 44–56, 2017.

[47] J. Brack, M. Sutherland, "Fluorescence Detector Absolute Calibration Database Update," *Auger internal publication*, 2012. GAP2012_095.

[48] B. Gookin, J. Brack, R. Cope, A. Dorofeev, J. Harton, Y. Petrov, "November Absolute Calibration, Addendum to GAP 2010-118," *Auger internal publication*, 2011. GAP2011_037.

[49] A. Menshikov, *LED Calibration Unit – User manual*. Institute of Data Processing and Electronics (IPE), Karlsruhe Institute of Technology. link.

[50] B. Gookin, *Calibration of the Pierre Auger Observatory Fluorescence Detectors and the Effect on Measurements (GAP2015_074)*. PhD thesis, 2015. Auger internal publication, GAP2015_074.

[51] R. Ulrich, D. Pearson, P. Sommers, "Relative FD-Calibration Calibration System and its Stability," *Auger internal publication*, 2010. GAP2010_116.

[52] G. Salina, "New Calibration Task: Some Ideas." Talk at the Golden Auger Analysis Meeting in June 2014.

[53] C.Delle Fratte, G.Matthiae, F.Ortolani, P.Petrinca, J.Rodriguez Martino, G.Salina, V.Tuci, "On the stability of the FD cameras," *Auger internal publication*, 2007. GAP2007_111.

[54] K. Daumiller, M. Del Rio, H.-J. Mathes, R. Smida, L. Tomankova, "Towards a continuous calibration A during FD data taking," *Auger internal publication*, 2016. GAP2016_009.

[55] IGUS. https://www.igus.co.uk/, accessed March 2020.

[56] IGUS – drylin®systems. https://www.igus.co.uk/drylin/linear-guide, accessed March 2020.

[57] J. Debatin, *Preparation of the Operation and Calibration of the Fluorescence Detector of AugerPrime*. PhD thesis, 2020. Auger internal publication, GAP2020_022.

[58] S. Argirò, S. Barroso, J. Gonzalez, L. Nellen, T. Paul, T. Porter, L. P. Jr., M. Roth, R. Ulrich, and D. Veberič, "The offline software framework of the pierre auger observatory," *Nuclear Instruments and Methods in Physics Research Section A: Accelerators, Spectrometers, Detectors and Associated Equipment*, vol. 580, no. 3, pp. 1485–1496, 2007.

[59] S. Agostinelli, et. al., "Geant4—a simulation toolkit," *Nuclear Instruments and Methods in Physics Research Section A: Accelerators, Spectrometers, Detectors and Associated Equipment*, vol. 506, no. 3, pp. 250–303, 2003.

[60] J. Parrisius, R. Ulrich, L. Tomankova, et al., "TelescopeSimulatorKG_DEV." repository.

[61] J. Bäuml, K. Daumiller, R. Engel, H.-O. Klages, H.-J. Mathes, R. Ulrich, M. Unger, "The halo in telescope simulations." Talk at the Auger Collaboration Meeting in March 2011.

[62] D. Mandat, et. al., "Measurements of PMT's reflectivity." Talk at the Auger Collaboration Meeting in June 2010.

[63] J. Parrisius, "Test of the calibration of the Auger fluorescence telescopes with an isotropic UV light source," *Auger internal publication*, 2009. GAP2009_045.

[64] L. Tomankova and M. Bohacova, "Relative FD Calibration - Effect of mirror and filter cleaning procedures," *Auger internal publication*, 2011. GAP2011_113.

[65] Daily Fluorescence Detectors Task Log. https://www.auger.org.ar/FD/fd_task_log.

[66] L. Nozka, P. Schovanek, M. Hrabovsky, D. Mandat, M. Pech, M. Palatka, M. Nyklicek, J. Ridky, P. Travnicek, J. Ebr, M. Prouza, and P. Neesal, "Condition of mirror segments after 5 years of operation in Pierre Auger Observatory," *Auger internal publication*, 2010. GAP2010_040.

[67] L. Nozka, P. Schovanek, M. Hrabovsky, D. Mandat, M. Pech, P. Horvath, M. Palatka, J. Ridky, P. Travnicek, J. Ebr, and M. Prouza, "Scatter measurements of selected mirror segments - examination of dust contamination," *Auger internal publication*, 2012. GAP2012_048.

[68] L. Nozka, H. Hiklova, P. Horvath, M. Hrabovsky, D. Mandat, M. Palatka, M. Pech, J. Ridky, and P. Schovanek, "Monitoring of mirror degradation of fluorescence detectors at the pierre auger observatory due to dust sedimentation," *Journal of Instrumentation*, vol. 13, no. 05, pp. T05005–T05005, 2018.

[69] "List Of Cleanings at LL." `www.auger.unam.mx/AugerWiki/MergedListOfCleanings_LL`, accessed September 2021.

[70] B. Dawson, "Possible effect of dusty FD mirrors on Xmax." Talk at the Auger Collaboration Meeting in November 2019.

[71] H.-J. Mathes for the Pierre Auger Collaboration, "A novel method for the absolute end-to-end calibration of the Auger fluorescence telescopes," *EPJ Web Conf.*, vol. 210, p. 05013, 2019.

[72] Labsphere Inc., 231 Shaker St., North Sutton, NH 03260, USA, *Integrating Sphere Theory and Applications – Technical Guide*.

[73] Labsphere Inc., 231 Shaker St., North Sutton, NH 03260, USA, *Integrating Sphere Uniform Light Source Applications – Technical Guide*.

[74] Labsphere Inc., 231 Shaker St., North Sutton, NH 03260, USA, *Integrating Sphere Radiometry and Photometry – Technical Guide*.

[75] M. Vacula, P. Horvath, L. Chytka, K. Daumiller, R. Engel, M. Hrabovsky, D. Mandat, H.-J. Mathes, S. Michal, M. Palatka, M. Pech, C. M. Schäfer, and P. Schovanek, "Use of a general purpose integrating sphere as a low intensity near-uv extended uniform light source," *Optik*, vol. 242, p. 167169, 2021.

[76] Labsphere Inc., 231 Shaker St., North Sutton, NH 03260, USA. `http://www.labsphere.com`, accessed May 2020.

[77] "Optical-grade Spectralon Reflectance Material." accessed December 2021.

[78] Roithner Lasertechnik GmbH, Wiedner Hauptstraße 76, A-1040 Vienna, Austria. `http://www.roithner-laser.com`, accessed May 2020.

[79] Roithner Lasertechnik GmbH, "UVLED365-110E Technical Data." `http://www.roithner-laser.com/datasheets/led_div/uvled365-110e.pdf`, accessed November 2019.

[80] M. Vacula, "Integrating sphere as a homogeneous light source for FD calibration." Talk at the Auger Collaboration Meeting in November 2019.

[81] Edmund Optics, Ltd Unit 1, Opus Avenue, Nether Poppleton, York, YO26 6BL, UK. `https://www.edmundoptics.com/`.

[82] Edmund Optics, 100mm Dia. White Diffusing Glass. `https://www.edmundoptics.com/p/100mm-dia-white-diffusing-glass/3843/`.

[83] Eljen Technology, *Datasheet – EJ-510 reflective paint*. link, accessed September 2022.

[84] Eljen Technology, 1300 W. Broadway, Sweetwater, TX 79556. `https://eljentechnology.com/`, accessed September 2022.

[85] Pico Technology, *PicoScope 6000 Series*. link, accessed December 2021.

[86] ET Enterprises, *9107B series data sheet*. link, accessed December 2021.

[87] ET Enterprises. `https://et-enterprises.com/`, accessed March 2019.

[88] A. Andrianavalomahefa, C. M. Schäfer, D. Veberič, R. Engel, T. Schwetz, H.-J. Mathes, K. Daumiller, M. Roth, D. Schmidt, R. Ulrich, B. Döbrich, J. Jaeckel, M. Kowalski, A. Lindner, and J. Redondo, "Limits from the funk experiment on the mixing strength of hidden-photon dark matter in the visible and near-ultraviolet wavelength range," *Phys. Rev. D*, vol. 102, p. 042001, 2020.

Bibliography

[89] T. Antoni, et. al., "The cosmic-ray experiment KASCADE," *Nuclear Instruments and Methods in Physics Research Section A: Accelerators, Spectrometers, Detectors and Associated Equipment*, vol. 513, no. 3, pp. 490–510, 2003.

[90] ET Enterprises, "About us." `https://et-enterprises.com/company/about-us`, accessed December 2021.

[91] ET Enterprises, *9902B series data sheet*. link, accessed December 2021.

[92] Standa Opto-Mechanical Products. `https://www.standa.lt`, accessed July 2019.

[93] Ocean Optics, Inc. (rebranded as Ocean Insight in 2019). `https://www.oceaninsight.com/`, accessed November 2022.

[94] Hamamatsu Photonics K.K. `https://www.hamamatsu.com/`, accessed March 2019.

[95] Hamamatsu Photonics K.K., *PHOTOMULTIPLIER TUBE R9420*. datasheet, accessed December 2022.

[96] Hamamatsu Photonics K.K., *PHOTOMULTIPLIER TUBE R11102*. datasheet, accessed December 2022.

[97] National Institute of Standards and Technology (U.S. Department of Commerce), Gaithersburg, Maryland.

[98] Keithley Instruments, Inc, *Keithley 6514 System Electrometer*. link, accessed December 2022.

[99] National Institute of Standards and Technology (U.S. Department of Commerce), Gaithersburg, Maryland., "Report of Calibration NIST Test # 39071C - Specrtal Responsivity for OSI Optoelectronics Silicon Photodiode Model UV-100, S/N U1062, NIST Test No.: 685/280103-11."

[100] E. F. Zalewski, *Chapter 24 in Handbook of Optics, Second Edition Volume II*. McGraw-Hill, Inc.

[101] H. Y. Wong, *Handbook of essential formulae and data on heat transfer for engineers*. London [u.a.]: Longman, 1977.

[102] T. Heibges, "Photometric characterization of a light source used for the absolute calibration of the fluorescence telescopes of the Pierre Auger Observatory," *Auger internal publication*, 2020. GAP2020_020.

[103] T. Heibges, E. Mayotte, J. Rautenberg, "Report of Source Calibration (Olomouc sphere)," 2020.

[104] T. Heibges, E. Mayotte, J. Rautenberg, "Report of Source Calibration (KIT sphere)," 2020.

[105] C. Schäfer, "Search for Hidden-Photon Dark-Matter with a Spherical Mirror," *Master thesis*, 2018.

[106] C. Schäfer, D. Veberič and R. Engel, "Reconstruction of the Baseline Undershoot of FD Photomultipliers," *Auger internal publication*, 2022. GAP2022_012.

[107] B. Efron, "Bootstrap Methods: Another Look at the Jackknife," *The Annals of Statistics*, vol. 7, no. 1, pp. 1 – 26, 1979.

[108] J. Bellido, "Measuring the Energy Scale Stability of the Surface and Fluorescence Detectors," *Auger internal publication*, 2010. GAP2010_014.

[109] P. Huy Nguyen and B. Dawson, "Update on the Seasonal Variations of the Energy Scale." Talk at the Auger Collaboration Meeting in November 2014.

[110] A. Porcelli, *Measurement of the Depth of Shower Maximum in the Transition Region between Galactic and Extragalactic Cosmic Rays with the Pierre Auger Observatory*. PhD thesis, 2014. Auger internal publication, GAP2014_058.

[111] V. Verzi on behalf of the Foundations and Atmospheric Conditions tasks, "Status Report on FD Reconstruction." Talk at the Auger Collaboration Meeting in November 2018.

[112] P. Huy Nguyen, *Energy Systematics and Long Term Performance of the Pierre Auger Observatorys Fluorescence Telescopes*. PhD thesis, 2018. Auger internal publication, GAP2018_011.

[113] P. Nguyen, B. Dawson, J. Bellido, "Cross Check of the Fluorescence Detector Calibration Using the Night Sky Background," *Auger internal publication*, 2016. GAP2016_005.

[114] J. Bellido, I. C. Maris, V. Novotny, J. Rautenberg, A. Segreto, "Cross-calibration of the HEAT and Coihueco telescopes using the night sky brightness," *Auger internal publication*, 2023. GAP2023_013.

[115] B. Dawson on behalf of the Pierre Auger Collaboration, "The Energy Scale of the Pierre Auger Observatory," in *Proceedings of 36th International Cosmic Ray Conference — PoS(ICRC2019)*, vol. 358, p. 231, 2019.

[116] V. Verzi for the Pierre Auger Collaboration, "The Energy Scale of the Pierre Auger Observatory," in *Contributions to the 33th International Cosmic Ray Conference — ICRC2013*, 2013. [arXiv 1307.5059].

[117] V. Verzi, "The Energy Scale of the Pierre Auger Observatory." Talk at the Lisbon Auger Analysis Meeting in June 2013.

[118] The Pierre Auger Collaboration, "The Pierre Auger Project Technical Design Report,"

[119] OSI Optoelectronics, *UV Enhanced Series - Inversion Layer and Planar Diffused Silicon Photodiodes*. link.

[120] J.R.R. Tolkien, *The Lord of the Rings*. HarperCollins (originally published by Allen & Unwin), 1954-1955.

[121] L. Lamport, "A Document Preparation System LATEX," *User's guide & Reference manual*, 1986.

[122] B. Stroustrup, *The C++ programming language*. Pearson Education India, 2000.

[123] G. Van Rossum and F. L. Drake, *Python 3 Reference Manual*. Scotts Valley, CA: CreateSpace, 2009.

[124] J. D. Hunter, "Matplotlib: A 2D graphics environment," *Computing in Science & Engineering*, vol. 9, no. 3, pp. 90–95, 2007.

[125] Inkscape Project, "Inkscape."